Supramolecular Strategies to Control
the Assembly of Organic-Based Materials

Marta Riba Moliner

SUPRAMOLECULAR STRATEGIES TO CONTROL THE ASSEMBLY OF ORGANIC-BASED MATERIALS

Marta Riba Moliner

Director/a

Prof. David B. Amabilino

Dra. Arántzazu González-Campo

Tutor/a

Prof. Mª Luisa Pérez García

Nanoscience PhD Thesis
2016

Institut de Ciència de Materials de Barcelona (ICMAB-CSIC)

Memòria presentada per aspirar al Títol de Doctor per;

Marta Riba Moliner

Vist i plau

Director/a	Codirector/a	Tutor/a
David B. Amabilino	Arántzazu González-Campo	Mª Luisa Pérez García

Barcelona, Gener 2016

TABLE OF CONTENTS

Chapter 7 – Techniques and equipment description 241

Thesis abstract

The focus of this thesis is the use of supramolecular chemistry to functionalize polymers and macromolecules to obtain organic-based materials with a control of their structure and properties.

The non-covalent functionalization of polymers *via* supramolecular chemistry is a potentially efficient route to introduce a particular property with which a new functional molecular material can be originated. This strategy has specially been explored to incorporate conjugated structures in polymeric constructs for new semiconducting materials. Although important advances have been made in this field, the incorporation of π-electron functional units to polymeric backbones with well-controlled arrangement between the donor and acceptor parts is still an area of huge interest for material science.

Following this idea, the supramolecular functionalization of the homopolymer poly(4-vinyl pyridine) (P4VP) with an electron donating unit based on an tetrathiafulvalene (TTF) has been explored. Tetrathiafulvalenes (TTFs) are excellent π-electron donor units that are widely studied in molecular electronic applications due to their *p*-type character and stable doped states. Through complementary hydrogen bonding components of a derivative TTF (TTFCOOH), uniform films incorporating the redox active components have been prepared. When the films were doped using different oxidising agents, Electrostatic Force Microscopy (EFM) studies indicated that a reorganisation at the surface of the films occurred and charges in their surfaces appeared.

Once the application of the P4VP-TTFCOOH films as charge-carrier hybrid material was demonstrated, the next step was to use the block copolymer poly(styrene-*b*-4-vinyl pyridine) (PS-*b*-P4VP) due to its amphiphilic behavior. Therefore, different molar ratios of PS and P4VP blocks have been used to prepare new PS-*b*-P4VP-TTFCOOH thin films. The influence of the phase segregation of the PS-*b*-P4VP-TTFCOOH film

to the charge transportation upon oxidation was performed correlating the Small-Angle X-ray Scattering (SAXS) and EFM results.

On the other hand, microfluidics is a microfabrication technique that relies on the manipulation of fluids, which can be used to control the final microstructure and self-assembly of compounds, by the simple adjusting of the values of the hydrodynamic flow focusing (confinement effect). Moreover, microfluidics offers respect to the bulk conditions important advantages such as larger relation surface-to-volume, lower consumption values and a better control of the concentration gradients. The improvement of the intermolecular contact of disk-shaped C_3-symmetric tris(TTF) system has been studied using microfluidics. This molecule possesses three bonded derivative TTF units through a central aromatic ring that, under determined conditions, large coiled helical fibers could be obtained by their aggregation. A de-doping process of the C_3-symmetric tris(TTF) molecule has been studied using microfluidics, towards the study of the influence of the technique on the supramolecular organization of this compound. Afterwards, a new characterization methodology based on bimodal-Atomic Force Microscopy (bimodal-AFM) was suggested, in order to draw a distinction between electrostatic and mechanical contributions of the coiled fibers and, corroborating that the charge transportation phenomenon occurred

Furthermore, microfluidics has also been used for the control of the structure of an ionically-driven coacervated hydrogel. Hydrogels have been in the spotlight due to their biocompatibility in, for instance, tissue engineering applications. Then, the structural enhancement of an ABA triblock copolymer PEG-based hydrogel was studied using a microfluidics platform by tuning the flow focusing parameters. In a further step, the functionalization of this hydrogel with TTFCOOH molecules under bulk and microfluidic conditions and its charge-carrier character were also analyzed. Additionally, with the objective to immobilize the hydrogel on surfaces, micro-contact printing, technique was tested.

Finally, the organization and phase segregation of the PS-*b*-P4VP block copolymer coordinated with a metalloporphyrin system has also

been approached. Porphyrins, in general, possess exceptional inherent optical and electronic properties that make them suitable for their application in organic-based electronic devices. Moreover, they can be modified with other functional groups, which allows tuning their electrochemical and photophysic properties. Porphyrins can be found free or complexed with metals and in both states their self-assembly occurs. Therefore, the coordination between PS-*b*-P4VP and chiral and an achiral zinc (II) metalloporphyrin has been explored in order to study the chirality transfer from the porphyrin to the hybrid materials. In the last instance, different strategies of surface immobilization of the porphyrin-block copolymer system were also approached by micro-contact printing as an initial study to use porphyrins as molecular rotors.

x

Resum de la tèsi

Aquesta tesi s'emmarca en l'ús de la química supramolecular amb l'objectiu de funcionalitzar polímers i així, obtenir materials orgànics amb estructura i propietats controlades.

La funcionalització no covalent dels polímers via química supramolecular és una ruta potencialment eficient per introduir propietats particulars, amb la que nous materials moleculars funcionals poden originar-se. Aquesta estratègia ha estat especialment explorada a través de la incorporació d'estructures conjugades per l'obtenció de nou materials semiconductors. Encara que ja s'han fet importants avenços en aquesta àrea d'estudi, la incorporació d'unitats π-electròniques a estructures polimèriques amb una bona organització entre la molécula donadora i l'acceptora, és encara una área de gran interés en la ciencia dels materials.

Seguint aquesta idea, s'ha estudiat la funcionalització supramolecular de l'homopolímer de poli(4-vinil piridina) (P4VP) amb unitats donadores d'electrons basades en tetratiafulvalenes (TTFs) els quals són excel·lents π-donadors d'electrons, àmpliament estudiats en aplicacions electròniques moleculars degut als seus estats oxidats/dopats, els quals són estables. Addicionalment, van ser preparats en estat líquid i com a pel·lícula prima (*thin film*) complexos P4VP-TTFCOOH, en els estats neutre i dopat, per mediació de diferents agents de dopatge. El dopatge d'aquests sistemes, la seva organització i capacitat de transport de càrrega van ser estudiats a través d'espectroscòpia d'UV-Visible i Microscòpia Electrostàtica de Força (EFM).

Una vegada vista la viabilitat dels films de P4VP-TTFCOOH, es va treballar amb el copolímer tipus bloc poli(estirè-*bloc*-4-vinil piridina) (PS-*b*-P4VP), ja que es tracta d'un copolímer de caràcter amfifílic molt prometedor degut als punts reactius (nitrògens dels anells piridínics) dels què disposa, per on els quals s'hi pot coordinar el TTFCOOH per

enllaços d'hidrogen. Seguidament, es va fer la síntesi de PS-*b*-P4VP, amb diferents fraccions molars tant de PS com de P4VP. En vista dels prometedors resultats obtinguts en forma de pel·lícula prima en el sistema P4VP-TTFCOOH, el nou sistema PS-*b*-P4VP-TTFCOOH va ser també estudiat en forma de pel·lícula prima i se'n va determinar l'efecte del TTFCOOH en l'auto-assemblatge del PS-*b*-P4VP en per cada un dels ratis molars. Seguidament, se'n va fer un estudi rigorós mitjançant la tècnica (optimitzada ja en el sistema anterior) de EFM dels films dopats, demostrant-ne la correlació entre la segregació de fases, modificada per la incorporació del TTFCOOH, i l'activitat en el transport de càrrega com a material híbrid orgànic.

La microfluídica és una tècnica de micro-fabricació basada en la manipulació de fluids amb la que s'ha demostrat la seva incidència en ocasions en la micro-estructura i auto-assemblatge final dels compostos que s'hi han processat, a través de l'ajust dels valors del cabals hidrodinàmics dels fluxos (efecte de confinament). Com a avantatges que ofereix respecte a treballar en *bulk* (en massa) són una major relació superfície-volum, menor consum de reactius i un millor control dels gradients de concentració. És per això que es va demostrar una millora del contacte intermolecular en la utilització de la tècnica de microfluídica en un sistema de des-dopatge d'un compost simètric C_3 de TTF (C_3-TTF). Aquesta molècula, està composta per tres unitats derivades de TTF unides entre sí a través un anell aromàtic central, i en determinades condicions de *bulk*, es poden obtenir grans fibres helicoïdals com a resultat de la seva agregació. Així doncs, l'objectiu marcat va ser el de promocionar l'auto-assemblatge a través de des-dopatge (utilitzant dissolvents no-coordinants) mitjançant l'efecte de les condicions de microfluídica i, alhora provar que les fibres resultants podien ser dopades mitjançant oxidació i així, obtenir fibres semiconductores basades en TTF. Posteriorment, una nova metodologia de caracterització basada en Microscòpia Atòmica de Força-bimodal (bimodal-AFM) i EFM es va establir per aquest sistema, amb la finalitat de distingir les contribucions electrostàtiques de les mecàniques provinents de les

agregats helicoïdals i així, assegurar-se de que el fenomen de transferència de carrega era realment present.

Per altre banda, els hidrogels han tingut i tenen actualment un paper destacat per la seva biocompatibilitat en, per exemple, aplicacions en l'enginyeria de teixits (*tissue engineering*). És per aquest motiu que, aprofitant els avantatges que la microfluídica ofereix, juntament amb les possibilitats dels hidrogels, es va decidir estudiar les millores, des del punt de vista estructural d'un hidrogel obtingut per coacervació iònica a través de microfluídica a través de l'efecte de confinament. En un pas més enllà, es va marcar també l'objectiu de funcionalitzar aquest hidrogel amb molècules de TTFCOOH en *bulk* i a través de microfluídica i finalment estudiar-ne el seu comportament. Addicionalment, es van provar diverses estratègies amb l'objectiu d'immobilitzar l'hidrogel en superfície a través de la tècnica litogràfica d'impressió per micro-contacte (*micro-contact printing*), podent-se corroborar la seva efectivitat.

Seguint amb l'anàlisi de la química supramolecular dels materials i aprofitant les característiques de segregació de fases del PS-*b*-P4VP, es va aproximar a l'obtenció d'un sistema polimèric coordinat amb un sistema porfirínic. Les porfirines en general, tenen unes propietats òptiques i electròniques inherents excepcionals que les fan adequades per aplicacions relacionades amb cel·les solars. Addicionalment, degut a les seves característiques electroquímiques i fotofísiques, poden ser fàcilment modificades per altres grups funcionals. Les porfirines poden estar lliures o complexades per metalls i ambdós tenen propietats d'auto-assemblatge. En aquesta part del treball es va estudiar la coordinació entre el PS-*b*-P4VP i dues porfirines complexades amb zinc (II) per separat, donant-se la seva coordinació entre els nitrògens de l'anell de piridina i el zinc (II) centrat en l'anell de les porfirines. La principal diferència entre aquestes porfirines era la quiralitat, és a dir una era el compost quiral de l'altre (químicament idèntiques). D'aquesta manera es va voler explorar la implicació de la quiralitat en l'auto-assemblatge dels sistemes PS-*b*-P4VP-porfirina-quiral i -aquiral. En aquest cas, es va voler il·lustrar el rol de diferents dissolvents selectius pel copolímer, obtenint d'aquesta manera sistemes micel·lars PS-*b*-P4VP-

porfirina-quiral i –aquiral. Com a última instància i en un intent de fer una aproximació exploratòria a la utilització de les porfirines com a rotors moleculars, es van provar diferents estratègies d'immobilització superficial mitjançant la tècnica d'impressió per micro-contacte (*micro-contact printing*), amb prèvia funcionalització superficial.

Acknowledgments

Des d'un punt de vista científic, voldria agraïr a tota la gent que m'ha dedicat el seu temps i m'han ajudat a comprendre amb més profunditat què és i què suposa la recerca, a fer-me créixer com a persona i investigadora (si em permeteu auto-etiquetar-m'hi) i a encomanar-me el rigor, la passió i el 'voler saber més' (això últim ja venia una mica de 'sèrie'). Voldria poder recalcar de la importància que ha sigut en la meva vida el fet de fer una tesi doctoral, òbviament per tot el què m'ha aportat a nivell científic, però sense deixar de banda el creixement personal que m'ha suposat, com per exemple en la millora de l'expressió oral i escrita (sobretot en idiomes forans), organització mental de conceptes i la seva planificació o també ser més indulgent en intercanvis d'idees.

Voldria començar els agraïments personals primer de tot mencionant director de la meva tesi, en David per donar-me la oportunitat de formar part del seu grup de recerca i donar-me consells i suggeriments sempre que ho he necessitat.

També voldria donar les gràcies especialment a l'Arantzázu per tot el suport donat des de la vessant científica al principi, i finalment convertint-se en co-directora d'aquest treball i pilar indiscutible en el meu creixement científic. Sempre disposada a escoltar-me i fer un lloc a la seva agenda per resoldre'm qualsevol dubte que m'ha sorgit.

M'agradaria mencionar i donar les gràcies pel suport rebut a través de la Lluïsa, primer acceptant ser la meva tutora i després mostrant-se molt receptiva en els aspectes més burocràtics del treball.

Voldria fer menció especial de tots els companys/es que formen i han format part del grup de recerca com és la Núria, que va agafar les regnes del grup sent-ne ara l'actual coordinadora, que amb el seu caràcter afable i pacient, la seva disponibilitat i les seves suggerències sempre positives m'ha ajudat a veure la química des d'un punt de vista més ampli. També la Cristina (la meva b* preferida) i amb la que he compartit molt bons moments fent cafès, treballant colze a colze (i calculant estequiometries!) i passant juntes tot el període d'escriptura, fent-me sentir motivada i compresa en tot moment. También mi compañera Wenjie, que siempre con su dulce sonrisa hemos compartido momentos divertidos, de

exhaustivas limpiezas de laboratorio y clases improvisadas tanto de conducción como castellano (谢谢). Al Raúl (o Rafa), que encara que estigui la major part del temps a la UB, sempre s'ha mostrat molt receptiu del punt de vista científica i també hem tingut moments molt divertits, sobretot la setmana conviscuda junts durant la conferencia que vam fer a Sitges. Me gustaría mencionar a Ezhil también, que recientemente se ha unido al grupo y que su línea de investigación me impresionó el primer día que la expuso y tuvo una paciencia tremenda en explicarme todos los detalles.

També voldria donar les gràcies als membres que han format part del grup durant tota la meva estança, com ara el Romén (Rominókulos o el canario), per la seva paciència i hores dedicades en ensenyar-me tot el què s'ha de saber de microfluídica, fent petits *breaks* per fer cafès tot rient i salvant el món. No em voldria oblidar del Josep, qui em va iniciar la meva inquietud per la microfluídica i m'ha ajudat i guiat en quasi tots els resultats relacionats amb els TTFs, sempre amb paciència, dedicació i rigurositat. También mi sevillana Angela, ahora ya doctora, por el caluroso recibimiento desde un principio, por transmitirme los conocimientos de la técnica de *printing* en superficies en sala blanca, en tu dedicación por enseñarme SEM y por las conversaciones arreglando el mundo. El noi de Polònia preferit, el Wojciech per regalar-me cada dia el seu somriure i el 'bon rotllo' que el caracteritza. I sense deixar-me a totes les persones que han anat passant pel nostre grup durant aquests anys, com ara Alessandro y sus divertidísimas italianadas (y fotos, oi Cris?), Giuseppe the 'italian-american' *boy*, i demés companys/es que he compartit bons moments.

Gracias a la gente con la que he compartido despacho, por aguantarme y hacerlo todo más ameno, siempre asegurándonos que no nos quedáramos escasos de dulces en los momentos clave, Maria, Laura, Davide, Markus i Magda.

Voldria també agraïr a aquella gent amb la que hem compartit llargues xerrades, riures i debats a l'hora de dinar i cafès a l'ICMAB i fora la 'popi' Laura (gràcies per posar fil musical a tots aquests anys), la Stefania (la 'negra'), l'Ana López (y sus reivindicaciones), el Carlos (sempre amb bon humor i endolcint-nos la vida), la 'bessona' Berta (divertidíssima i desprenent energia per allà on passa). A Justo y Víctor por hacerme reír hasta llorar con sus 'indian issues' i la resta de gent amb la que he estat acompanyada al llarg d'aquest anys la Mar, la Jessica, la Roberta y a

tots/es que formeu part de l'Institut. I també la gent que ja no és per la 'casa' però també hem compartit sobretaules i em van fer sentir de seguida integrada, la Jessica, la Nina, la Nerea, la Regina i altres que segur que em deixo (perdó!).

També voldria mencionar a les persones que han posat el seu gra de sorra perquè tot pogués tirar endavant, la Judith i les nostres eternes sessions de TEM amb mostres ben complicades i sense perdre mai el sentit de l'humor, la Roberta con la que intentamos un montón de cosillas que al final no han podido ser añadidas, Andrés y Maite por su infinita paciencia con mis 'muestrecillas' (y 'curviñas', por no olvidarnos de sus devaneos por el 'Bangladesh'), a Enrique que fue testigo en mis inicios de sala blanca y siempre se mostró disponible y atento. Todos/as aguantándome horas y horas y solventando mis dudas, gracias.

I would like to thank to Prof. Craig Hawker for give me the great opportunity to join his research group at the UCSB and always appears available and comprehensive to solve my doubts. I've learnt a lot also from the people of his group, thank you to everyone and people from Santa Barbara that help me to my scientific and personal growth. I'll never forget you! The Materials Research Laboratory (MRL) shared experimental facilities supported by the MRSEC Program of the NSF under Award No. DMR 1121053; a member of the NSF-funded Materials Research Facilities Network.

Voldria també citar als agraïments al Dr. Ramon Pons i a Jaume Caelles de l'Institut de Química Avançada de Catalunya (IQAC) per la seva col·laboració i ajuda en el desenvolupament, mesura i interpretació de resultats obtinguts per SAXS. També al Dr. Teodor Parella, del Servei de Ressonància Magnètica Nuclear de la UAB, per ajudar-me en l'execució i interpretació dels DOSY.

Gràcies al CSIC he pogut disfrutar de la beca JAE Predoc, emmarcada pel finançament rebut del Ministeri d'Economia i Competitivitat (MINECO) amb el projecte MAT2013-47869-C4-2-P.

Finalment, voldria donar gràcies de tot cor a la meva família per ser allà i donar-me sempre suport i l'energia necessària en els moments més difícils, sempre amb el positivisme que ens caracteritza i amb gran sentit de l'humor. A la Clàudia que és la millor amiga que podria tenir i que juntes hem passat de tot. Al Xavi, per ser la persona amb més paciència

del món i que sempre ha entès i m'ha motivat a lluitar pel què volia fer, sóc molt afortunada. GRÀCIES!

Abbreviations list

AFM – Atomic Force Microscopy

BCP – Block Copolymer

C_3-TTF, C_3-symmetric tris(TTF) - (*N,N',N''*-Tris[3[3'-bis[(S)-2-methylbutylthio]-tetrathiafulvalenyl] formylamino]-2,2'-bipyridyl] – benzene - 1,3,5,-tricarboxamide)

CD – Circular Dichroism

CSIC – Consejo Superior de Investigaciones Científicas

CyD - Cyclodextrin

dC_3-TTF – Doped C_3-TTF

DOSY, DOSY NMR – Diffusion-Ordered Nuclear Magnetic Resonance

EDX, EDAX – Energy-Dispersive X-ray Spectroscopy

EFM – Electrostatic Force Microscopy

EPR – Electron Paramagnetic Resonance

FTIR – Fourier Transform Infrared Spectroscopy

G - Gyroid

GPC – Gel Permeation Chromatography

HEX – Hexagonally Packed Cylinders

HPL – Hexagonally Perforated Layers

HT – High Tension

ICMAB – Institut de Ciència de Materials de Barcelona

IQAC – Institut de Química Avançada de Catalunya

LAM – Lamellar

M_w – Weight average molecular weight

NMR – Nuclear Magnetic Resonance

P4VP – Poly(4-vinyl pyridine)

PDMS – Poly(dimethyl siloxane)

PS – Poly(styrene)

PS-*b*-P4VP – Poly(styrene-*block*-4-vinyl pyridine)

q^* - Primary Reflection, Bragg peak

SAXS – Small-Angle X-ray Scattering

SEM – Scanning Electron Microscopy

SPM – Scanning Electron Microscopy

TEM – Transmission Electron Microscopy

THF - Tetrahydrofuran

TTF – Tetrathiafulvalene

TTFCOOH, acid TTF - 2,3-Bis(dodecylthio)-6-(carboxy)tetrathiafulvalene

UAB – Universitat Autònoma de Barcelona

UB – Universitat de Barcelona

UCSB – University of California Santa Barbara

UV-Vis – Ultra-violet Visible Absorption Spectroscopy

UV-Vis-NIR - Ultra-violet Visible-Near-Infrared Absorption Spectroscopy

Zn-(*R,R,R,R*)-1 – 5,10,15,20-[4-(*R,R,R,R*)-2-*N*-octadecylamideethyloxy-phenyl] zinc porphyrin

Zn(2) – 5,10,15,20-[4-*N*-octadecylacetamido phenoxy] zinc porphyrin

***β*-CD** - *β*-Cyclodextrin

***β*-CDSH** - Per-6-thio-*β*-cyclodextrin

μcP – Micro-contact printing

Preface

Supramolecular chemistry, which allows the assembly of molecules by non-covalent interactions, has become important in the preparation of new macromolecular-based materials to have a control of their structure and incorporation in devices. In this thesis, the functionalization of polymers has been explored by hydrogen-bonding interactions and metal ion coordination to obtain new organic-based materials. Moreover, the combination of supramolecular chemistry and nanofabrication techniques has been explored to have a control of the final microstructure of the polymeric and macromolecular-based materials.

Chapter 1 provides a general introduction to polymers and block copolymers field, together with a literature review of the strategies that have an incidence in their supramolecular chemistry and functionalization.

Chapter 2 describes the preparation of poly(4-vinyl pyridine) (P4VP) thin films obtained after the incorporation of a tetrathiafulvalene-(TTF) derivative. The incorporation of the TTF derivative allows us to study the conductivity and charge transportation of the film upon the oxidation of the TTF derivative with different oxidants agents. Different techniques such as UV-Visible Visible absorption spectroscopy and Electrostatic Force Microscopy (EFM) are used to characterize and study the conductivity of the films.

Chapter 3 continues the idea described in Chapter 2: the same TTF derivative was used to functionalize the amphiphilic block copolymer poly(styrene-*b*-4-vinyl pyridine) (PS-*b*-P4VP) in order to study the influence of the phase segregation of the PS-*b*-P4VP in the final structure and properties of the films. The correlation of the phase segregation of different PS-*b*-P4VP with different ratios of both blocks and the final conductive properties of the films is investigated using Small-Angle X-ray Scattering (SAXs) and Electrostatic Force Microscopy (EFM).

Taking advantage of the interesting possibilities of the combination of supramolecular chemistry and nanofabrication techniques, in Chapter 4, the control of the microstructure and assembly of the disk-shaped C_3-symmetric tris(TTF) macromolecule are studied using microfluidics. Microfluidics or lab-on-a-chip microfabrication devices offer the possibility to improve the contact, *via* hydrodynamic flow focusing, between units of the TTF-based macromolecule and to affect their structural arrangement. Moreover in this Chapter, the electrostatic and mechanical responses of the material upon oxidation are studied by the combination of EFM with bimodal-AFM results.

In the same way, Chapter 5 is focused on the demonstration of the implication of the hydrodynamic flow focusing parameter using microfluidics in the final microstructure of a TTF functionalized ionically-driven coacervated ABA triblock copolymer hydrogel. The improvement of the preparation and microstructure of the TTF-based hydrogel is studied comparing the hydrogel obtained in bulk and in the chip. Additionally, the immobilization of this hydrogel on functionalized surfaces using micro-contact printing is also presented.

Chapter 6 contains the study of the coordination between the amphiphilic block copolymer PS-*b*-P4VP and an achiral- and a chiral-zinc (II) metalloporphyrin. The incorporation of the chiral Zn-porphyrin and the influence of its chirality to the superstructures formed are investigated by Transmission Electron Microscopy (TEM). This Chapter also contains a preliminary experiment for the preparation of molecular rotors through the immobilization on surfaces of the coordinated polymeric system by different strategies.

Finally, in Chapter 7 a brief description of the characterization techniques and the equipment details used in this work is described. Chapter 8 contains a summary of the conclusions extracted from the others Chapters.

CHAPTER 1

General Introduction

1.1. POLYMERS AND COPOLYMERS: GENERAL CONCEPTS

Polymers are present in our daily life under the name of commodity plastics and find a wide range of applications such as packaging, clothing and a variety of household products (European enterprises of plastics and rubbers generated a turnover of almost EUR 300 billion in 2006).[1] Nowadays, researchers are making many efforts in order to constantly develop and improve their efficiency, life cycle and to find new pathways to synthesize and make them more eco-friendly.

Etymologically, the word *polymer* comes from the union of the Greek words *poly-* (= many) and *–mer* (= part)[2] and is defined as a substance consisting of large molecules made from many smaller and simpler molecules[3] (monomeric units) covalently bonded.

Polymers have been widely used materials in several areas due to their lightness, transparency, stability, consistency, reproducibility and malleability among other general properties. Natural and synthetic biocompatible polymers have been widely used in medicine, for instance in tissue regeneration processes.[4] From a general point of view, the word *scaffold* might have a broad meaning in which it could be included the use of polymers as hosting matrixes.[5] In this context, many strategies could be successfully applied such as either during the polymerization process (organic chemistry) or afterwards (commonly known as 'click chemistry') to introduce different functionalities in a polymeric matrix.[6, 7]

Block copolymers have been the focus of many research studies due to their ability to self-assemble at nanometer length scales,[8, 9] making them suitable for a wide number of nanotechnological applications such as nanotemplating,[10, 11] membranes[12-14] and organic optoelectronics[15] among others. The final properties of polymers and copolymers (behavior and characteristics) are treated and introduced into devices, i.e. bulk, thin film or in solution.[16-19]

Furthermore, 'intelligent' polymer-based materials with responsive properties are desirable to have a control of their structure and properties. This is the case, for instance, of UV- or pH-responsive polymeric-based materials bearing responsive guests (Fig. 1.1).[20-23] Employing molecular recognition, superstructures can also be achieved with self-assembled systems.[8, 24, 25]
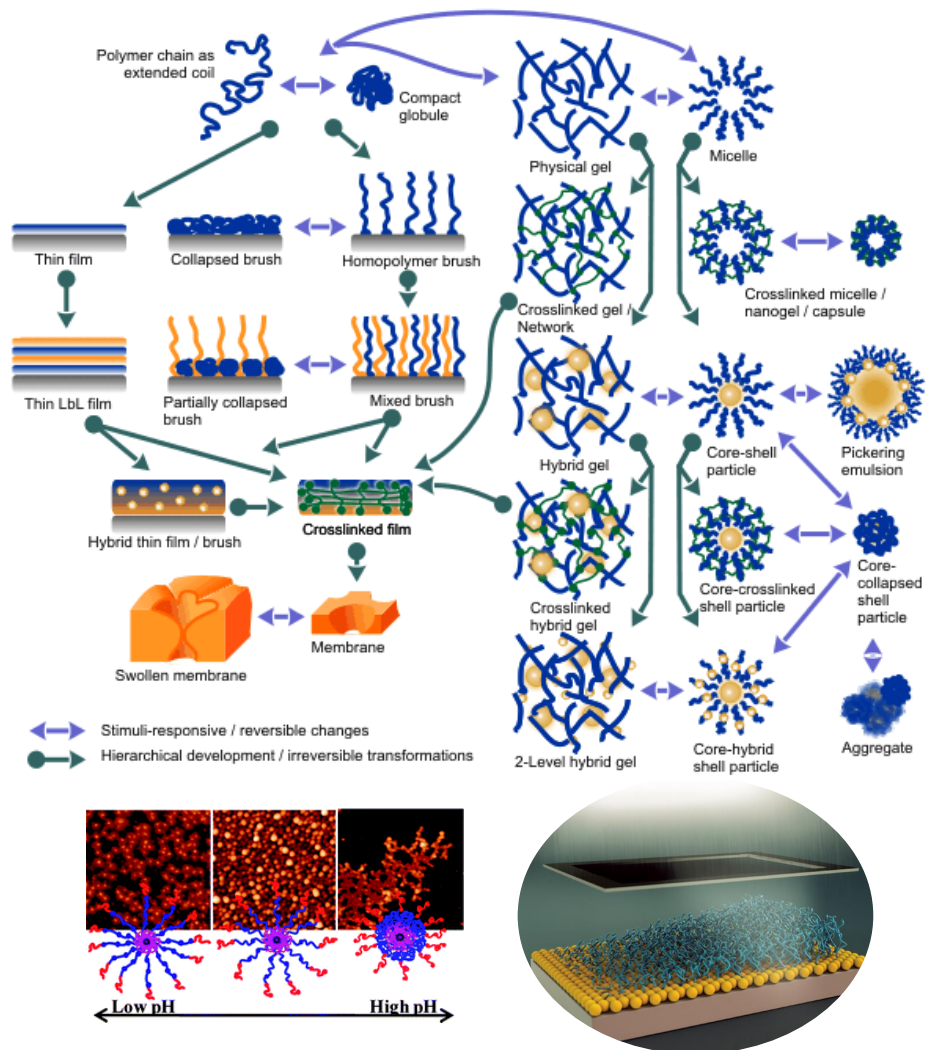
Fig. 1.1 *Polymer-based assembled conformations adopted (micelles, brushes, etc.) upon different stimuli, like pH or UV-light.[20, 23]*

The principle which stimuli-responsive polymers are based on, consists in the recognition, the evaluation of the magnitude and the

generation of a response to an external signal. Stimuli can be either physical (e.g. temperature[26], electric/magnetic field,[27] mechanical stress,[28] etc.) or chemical (e.g. pH[29], addition of chemical agents, changes in ionic strength, etc.).[30] It is relatively easy to imagine these effects in solution as is the case of micelles or vesicles based on block copolymers for biological applications (e.g. drug delivery[31]). Blanazs *et al.*[32] reviewed those polymers that are environmentally responsive/reactive, emphasizing the ones in solution. Another interesting approach is the preparation of stimuli-responsive copolymers in solid state, concretely thin films, for their incorporation in devices.[30, 33] Numerous studies have been reported in this field and their bases are explained in this chapter. First, an introduction of the general concepts of polymer chemistry and their preparation in solution, solid and thin film is presented.

Polymers are macromolecules that can be classified diversely, although the first way is based on the source from where they are obtained, differencing between (i) natural polymers, that are those who can be found directly in the nature, (ii) derived polymers, including those that derived from the natural polymers but suffered some chemical modification and, (iii) synthetic polymers, which have been entirely synthetized artificially. Polymers can also be classified accordingly to their thermal properties as (i) thermoplastics, those that can be reversibly melted or dissolved in a suitable solvent, (ii) thermosets, which can neither be melted nor dissolved and exhibit a glassy and brittle behavior due to their three dimensional (3-D) network (with short crosslinked chains) that provides their characteristic stiffness, and, (iii) elastomers, those which possess 3-D crosslinked network with long and flexible chains, although they cannot be melted (Fig. 1.2).[34] On the other hand, whether the classification is based on their structure or degree of crosslinking, it is possible to find (i) linear polymers, which comprises the chain-like structures and, (ii) branched polymers also called dendrimers, which have a chain-like structure with branch junctions between chains.

thermoplastics   **thermosets**   **elastomers**
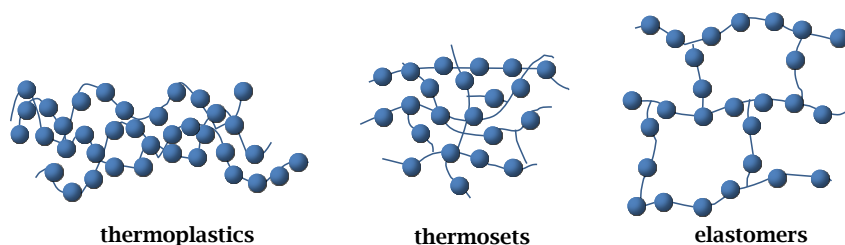
Fig. 1.2 *Illustration of different types of polymers according to thermal properties.*

Another important parameter to take into account is the stereochemistry (or tacticity) of polymers, because small variations in the spatial arrangement results in differentiated materials and final properties. There are three distinct configurational arrangements, (i) isotactic in which the pendant groups of the main chain are placed on the same side of the chain, (ii) syndiotactic where the pendant groups are alternatively disposed with respect to the main chain and, (iii) atactic which the pendant side groups are randomly arranged with respect to the main macromolecular chain (Fig. 1.3).[34]

isotactic

syndiotactic
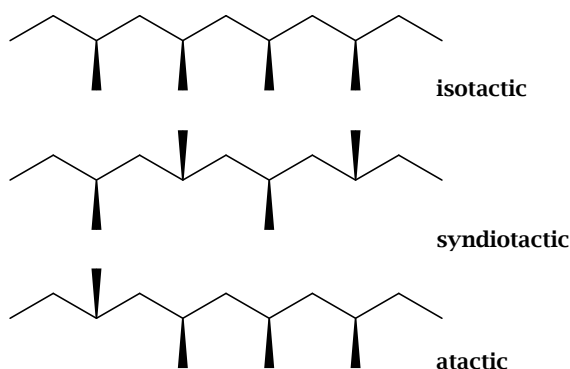
atactic

Fig. 1.3 *Stereochemistry (or tacticity) of polymers.*

The general way to denote polymers is by indicating the monomer (M) and, the number of repetitive units of monomer (n):

$$n \cdot M \rightarrow [P]_n \, \{n\} \in \{1, 2, \dots \infty\}$$

where P is the resulting polymer with an n degree of polymerization.

One can also draw a distinction based on the repeating monomeric units present in the macromolecular structure, (i) homopolymers, are those composed by a single repeating monomeric unit (one monomer) and, (ii) copolymers, which consist on at least two different repeating units (more than one monomer) (Fig. 1.4).[35]
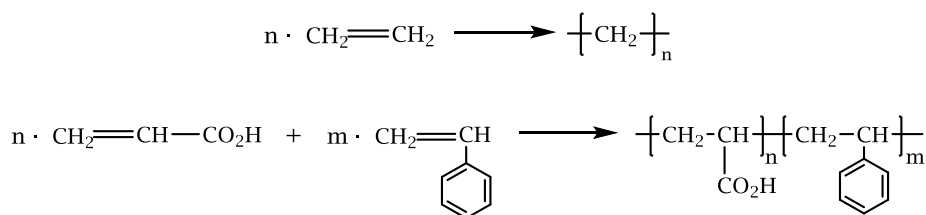
Fig. 1.4 *Examples of a homopolymer (poly(ethylene), top) and a copolymer (poly(acrylic acid-b-styrene), bottom).*

Copolymers can, also be subdivided, depending on the periodicity and disposition of the monomers that compose them: (i) alternating copolymers, the ones where a unit of each monomer is alternately repeated, (ii) random or statistical, monomeric units from those are randomly disposed, (iii) periodic, composed by blocks of arranged units of each monomer, (iv) block copolymers, composed by a bunch of repeating units of one monomer linked with a bunch of repeating units of the other monomer and, (v) grafted copolymers, the ones that have lateral chains of repeating units of one monomer bonded to the main polymeric main chain (Table 1.1).

Table 1.1   *Copolymers classification.*

Alternating	A - B - A - B - A - B - A - B
Random or statistical	A - B - B - B - A - B - A - A
Periodic	$\{A-B-B\}_n B\{A-B-A\}_m$
Block	$\{A\}_n\{B\}_m$
Grafted	- A - A - A - A - A - A - A - A - -B - B - B B - B - B-

The synthesis of polymers is also indistinctly named as polymerization, which according to the IUPAC definition is 'the process of converting a monomer or a mixture of monomers into a polymer'.[36] Other small molecules or ions such as initiators or chain transfer agents may be involved in polymerizations without significantly altering the resultant polymer. It is possible to gather polymerization reactions into three main groups, (i) chain polymerizations, (ii) polycondensations and, (iii) polyadditions. Chain polymerizations are based on the reaction only between monomers, resulting in the growing of the chain of the polymer. This chain will grow through a reactive-site at the end of it and by the incorporation of new units of the unreacted/free monomer. According to the IUPAC, the growing process can be expressed as:

$$P_x + M \rightarrow P_{x+1} \; (+L) \; \{x\} \in \{1, 2, \dots \infty\}$$
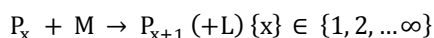
where P_x represents the growing chain with a degree of polymerization x, M is the monomer and L a by-product with a low-molar mass in condensative chain polymerizations context.[36] Polycondensation reactions involve condensation reactions during the growth of the polymer chain. The growth steps can be expressed by:

$$P_x + P_y \rightarrow P_{x+y} + L \; \{x\} \in \{1, 2, \dots \infty\}; \; \{y\} \in \{1, 2, \dots \infty\}$$
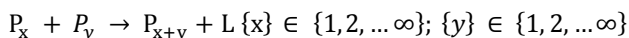
in where P_x and P_y are polymer chains with a degree of polymerization x and y, respectively and, L a by-product with low-molar mass.[36] In polyaddition polymerizations the reaction proceeds by additional reactions between molecules of all degrees of polymerization. The growing process can be written:

$$P_x + P_y \rightarrow P_{x+y} \; \{x\} \in \{1, 2, \dots \infty\}; \; \{y\} \in \{1, 2, \dots \infty\}$$
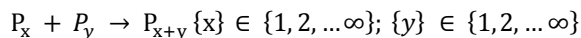
where P_x and P_y are chains with a degree of polymerization x and y, respectively.[36]

Polymers and copolymers are considered macromolecules due to their usual heavy (high molecular weight) and large (depending on the structure and composition of the basic repetitive unit and the degree of polymerization) nature. During the polymerization processes, undesired

side-reactions can take place, resulting on low-molecular weight by-products that can alter significantly the properties of the polymer or broadening out the number and size distribution (polydispersity). The degree of polymerization essentially, could not give always the sufficient information to know the molecular distribution of the polymer. Thus, forced to figure out complementary information about them, it is very common and useful write down the average molecular weight and specify the polydispersity. Because the possible different size and weight distributions can be obtained from the same polymerization, general notations can be defined: (i) number average molecular weight ($\bar{M}_n$), (ii) weight average molecular weight ($\bar{M}_w$), (iii) Z-average molecular weight ($\bar{M}_z$) and, (iv) polydispersity ($\bar{P}$). $\bar{M}_n$ can be defined as the statistical average molecular weight of all the polymer chains present in the sample:

$$\bar{M}_n = \frac{\sum_{i=1}^{N} N_i \cdot M_i}{\sum_{i=1}^{N} N_i}$$

in where N_i denotes the number of molecules and M_i the molecular weight. On the other hand, $\bar{M}_w$ takes into account that the larger molecules have a higher contribution in the averaged molecular weight and can be described as:

$$\bar{M}_w = \frac{\sum_{i=1}^{N} N_i \cdot M_i^{2}}{\sum_{i=1}^{N} N_i \cdot M_i}$$

$\bar{M}_z$ is the third power average molecular weight and is defined[35]:

$$\bar{M}_z = \frac{\sum_{i=1}^{N} N_i \cdot M_i^{3}}{\sum_{i=1}^{N} N_i \cdot M_i^{2}}$$

Finally, $\bar{P}$ is the way to identify how accurate is the size distribution of the synthesized polymer. It can be denoted as the ratio $\bar{M}_w/\bar{M}_n$ and values close to 1 will mean that a uniform polymer was obtained, with low spread of weights.[37] $\bar{M}_n$, $\bar{M}_w$, $\bar{M}_z$ and $\bar{P}$ can be easily deducted by the characterization technique of Gel Permeation Chromatography (GPC) or also called Size-Exclusion Chromatography (SEC).

Another important parameter related with the morphology of polymers is the thermal transitions. Polymer chains can arrange in lateral or longitudinal order or contain regions with a certain regularity of arrangement. Here, the terms degree of superstructural regularity or crystallinity are used to define the ordering degree of the polymer.[35] Polymers are considered to be either amorphous or crystalline even though they might not be entirely one or the other. Generally, in polymers the term crystalline is barely used as they are not perfect materials and so, the concept semi-crystalline is commonly used.[34] These concepts are closely related with the transition temperatures of the polymers. In a temperature cycle of a regular polymer (implying a heating up and cooling down), it is possible to observe three temperature transitions: (i) glass transition temperature (T_g), in where enough energy is applied to the polymer to allow a slight and relative movement of the macromolecular chains of them, inducing a relaxation of the chains in the lowest energy level conformation, (ii) crystallization temperature (T_c), in some cases, after the T_g is possible to induce a certain organization by a continuous application of energy and, (iii) melting temperature (T_m), which is the necessary temperature to melt the polymer and change completely its macromolecular structure and state. Concretely in the case of amorphous polymers, they are in fact non-crystalline but are crystallizable.[34] Generally, after their obtaining they can be cooled down quickly without any variation of their structured conformation or even relaxation of the macromolecular chains, and a kind of a frozen-like structure is obtained. Totally amorphous polymers only possess a thermal transition, the T_g, above which the material becomes rubbery and can be easily deformed. However, semi-crystalline polymers exhibit T_g and T_m as thermal transitions because they are provided with crystalline and amorphous parts. Crystalline polymers have a single thermal transition, which is the T_m. In these, the degree of crystallinity is so high that even one increases the temperature, there will be not an intermediate rubbery state and consequently the polymer will be directly melted. There are several characterization techniques that allow the observation of these thermal transitions, for instance Differential Scanning Calorimetry (DSC) or Thermo-Gravimetric Analysis (TGA).

1.1.1. Block copolymers

Block copolymers are included in the category of soft materials and they have the capacity to self-assemble into nanostructures.[9, 38] As was described previously, a block copolymer is a material composed of, at least, two chemically distinct polymer blocks covalently bonded. Systems that are most interesting are those with inherent immiscibility of the blocks at certain temperatures or solvents, which is the case for instance of amphiphilic block copolymers. Some amphiphilic block copolymer systems can provide a wide range of final properties (optical and mechanical) only by varying parameters such as the relative volume fraction (f) of each block, or the degree of polymerization (N) of each block, resulting in different microphase segregated areas where the interphase is the union between the blocks.[9]

1.1.1.1. Phase segregation

Due to the mentioned immiscibility, the thermodynamic incompatibility between blocks A and B in an AB type block copolymer, the system self-arranges at interphases[38] into the two states, molten and solid and in aqueous solutions.[9] The resulting morphology of this self-arrangement is directly related with the packing parameter, $p = v/a_0 l_c$, where v is the volume of the hydrophobic segment, a_0 is the contact area of the head group and, l_c is the length of the hydrophobic segment (Fig. 1.5).[39]
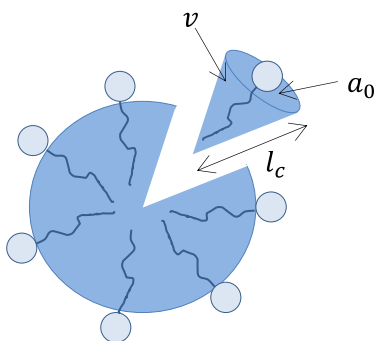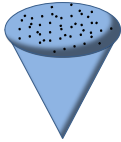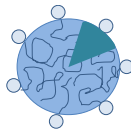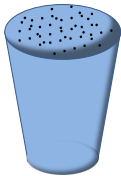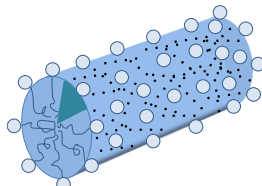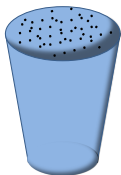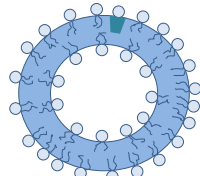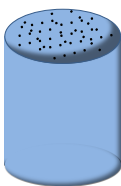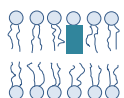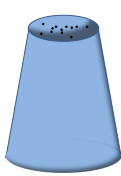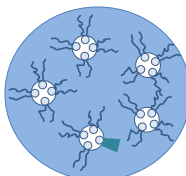
Fig. 1.5 *Micelles parameters that influence in the packing factor,* p.[40]

Depending on the values of the p parameter (Fig. 1.5, Table 1.2), different expected resulting arrangements can be formed: spheres for $p < 1/3$, cylinders for $1/3 < p < 1/2$, lamellae or vesicles for $1/2 < p < 1$, planar lamellae when the value is $p = 1$ and, when the values are $p > 1$ inverted structures could be appreciated.[8, 41]

Table 1.2   *Relationship between the packing parameter,* p*, and the expected structures.*[40]

Packing parameter , *p*	Packing shape	Structure
<1/3	Cone	Spherical micelles
1/3 - 1/2	*Truncated cone*	Cylindrical micelles
1/2 - 1	Truncated cone	Flexible bilayers, vesicles
~1	Cylinder	Planar bilayers
>1	Inverted truncated cone or wedge	Inverted micelles

Similar morphologies can be obtained either in bulk or in solution, although the mechanisms involved in their formation are different. Because of this, the different routes towards the promotion of the segregation in block copolymers have been separated in subsections. Techniques commonly used to characterize phase segregation conformations are: Scanning Electron Microscopy (SEM), Transmission Electron Microscopy (TEM), Atomic Force Microscopy (AFM) and Small-Angle X-ray Scattering (SAXS).

1.1.1.2. Block copolymers in bulk

Focusing the attention in AB diblock copolymers, the microphase separation between A and B can result in a great variety of morphologies such as spheres, cylinders, bicontinuous, gyroids, lamellae, etc., depending on the f (volume fraction) of each block ($f_A + f_B = 1$) (Fig. 1.6).[9]
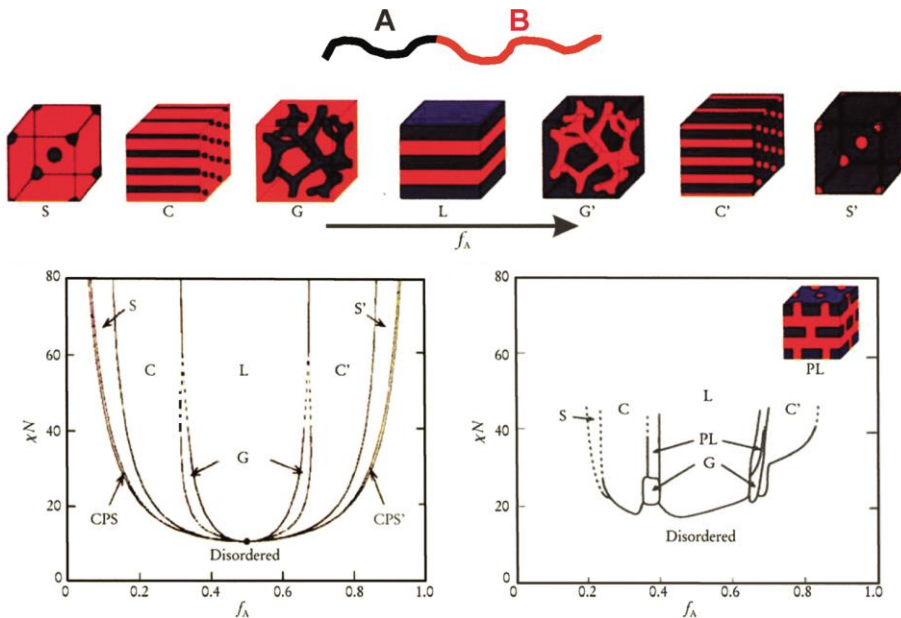
Fig. 1.6 *On the top, several equilibrium morphologies of AB block copolymers in bulk by adjusting the f_A value, S and S' = body-centered-cubic spheres, C and C' = hexagonally packed cylinders, G and G' = bicontinuous gyroids and, L = lamellae. On the bottom-left, predicted phase segregation diagram for AB diblock copolymers based on the Flory-Huggins theory, where CPS and CPS' = closely packed spheres. On*

the bottom-right, experimental phase diagram of poly(isoprene-b-styrene) in which A block is poly(isoprene) and PL = perforated lamellae.[9]

Among the previously mentioned parameters that the microphase separation depends on (f and N), the Flory-Huggins parameter, χ_{AB}, quantifies the degree of incompatibility between A and B blocks. Flory-Huggins theory considers that the free energy of mixing a pure polymer with a pure solvent has two contributions, the enthalpy and the entropy of mixing. The last one is determined by the f of the solvent and polymer, whereas the enthalpy of mixing is determined by the dimensionless interaction parameter $\chi \cdot \chi kT$ (where χ is the Flory-Huggins parameter, k the Boltzmann constant and T the absolute temperature).[42] The degree of microphase separation is given by the product $\chi \cdot N$. However, the temperature plays an important role here, because above certain critical value the structured microdomain in the polymeric interphase disappears to give rise to an homogenous and disordered state. This phenomenon is known as order-to-disorder transition (ODT) and the critical temperature is where the order-to-disorder temperature (T_{ODT}) takes place.[9, 43, 44] At low values of χN the AB block copolymer comprises a single disordered phase with unperturbed dimension of its chains.[43] The microphase separation is predicted at $\chi N \approx 10$, also known as the weak segregation limit, WSL, in which ordered structures are formed up to $\chi N \gg 10$, the strong segregation limit (SSL) in which the microphase is essentially pure A or pure B.[43]

When the microphase separation occurs, the two blocks separate from each other with the aim to minimize the interfacial area to decrease the total interfacial energy.[41] This explains why in the case when the blocks are highly asymmetric, the block with low volume fraction, for example A, will prefer to aggregate into spherical microdomains while B will be surrounding the spheres, like a matrix. At a fixed temperature, as f_A increases the relative volume fraction f_B, decreases, polymer chains adopt new arrangements to reduce the internal stretching, giving a morphological transition to cylinders. If f_A continues increasing, the successively transitions that one could observe will be gyroid and lamellae. Afterwards, when f_A values are above f_B the inverse patterned

structures will be observed.[9, 41] This permits to tune the conformation adopted at the interphase.[45]

More complex systems are obtained in the case of multiblock copolymers, for instance in the case of triblock copolymers, ABC. ABC copolymer is composed by three different blocks A, B and C and its phase behavior depends on χ_{AB}, χ_{AC} and χ_{BC}, the total degree of polymerization (N), the volume fractions f_A, f_B and f_c ($f_A + f_B + f_C = 1$), and the sequences of the segments (ABC, BCA or CAB) (Fig. 1.7).[46] As higher is the number of blocks in a block copolymer system, higher is the complexity of the behavior of the phase segregation.
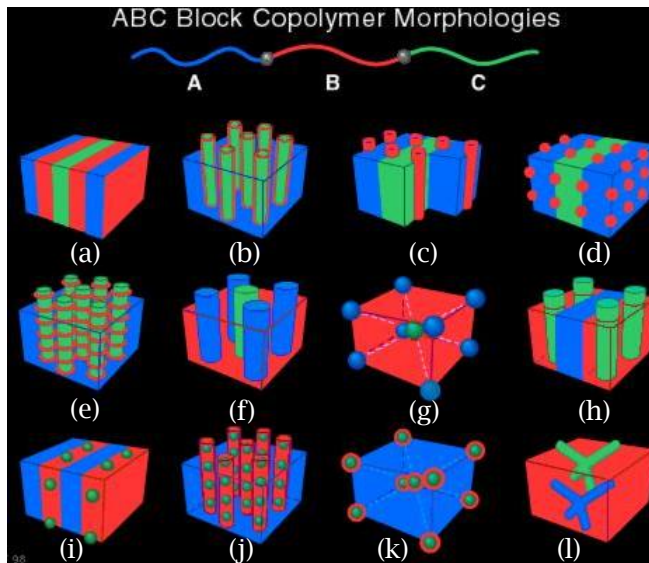
Fig. 1.7 *Microphase separation morphologies for ABC triblock copolymers. (a) Lamellar phase, (b) coaxial cylinder phase, (c) lamella-cylinder phase, (d) lamella-sphere phase, (e) cylinder-ring.phase, (f) cylindrical domains in a square lattice structure, (g) spherical domains in the CsCl-type structure, (h) lamella-cylinder-II, (i) lamella-sphere-II, (j) cylinder-sphere, (k) concentric spherical domain in the bbc structure, (l) gyroid in a square lattice.[46]*

1.1.1.3. Block copolymers in solution

When a solvent is involved in the self-assembly of a block copolymer, the complexity of the behavior of the phase separation

increases, compared with the behavior in bulk without solvent. In solution the different solubility of the blocks has to be considered. Since water is a common used solvent, one can classify block copolymers depending on their solubility in water like amphiphilic,[43] double hydrophilic or double hydrophobic systems.[41] The selectivity of the solvent is a very valuable parameter, and also it will help to determine the final phase separation morphology. As been mentioned before, amphiphilic block copolymers can arrange in many of different ordered structures that can be transformed from one to another when the solution conditions, such as pH, temperature or electrolyte concentrations change.[8] For instance, Klinger and coworkers explored the possible conformations that the micellar/vesicular system poly(styrene-*b*-2-vinyl pyridine) (PS-*b*-P2VP) offers under different solvent-exchange and pH treatment with different bearing molecules (Fig. 1.8).[47, 48]
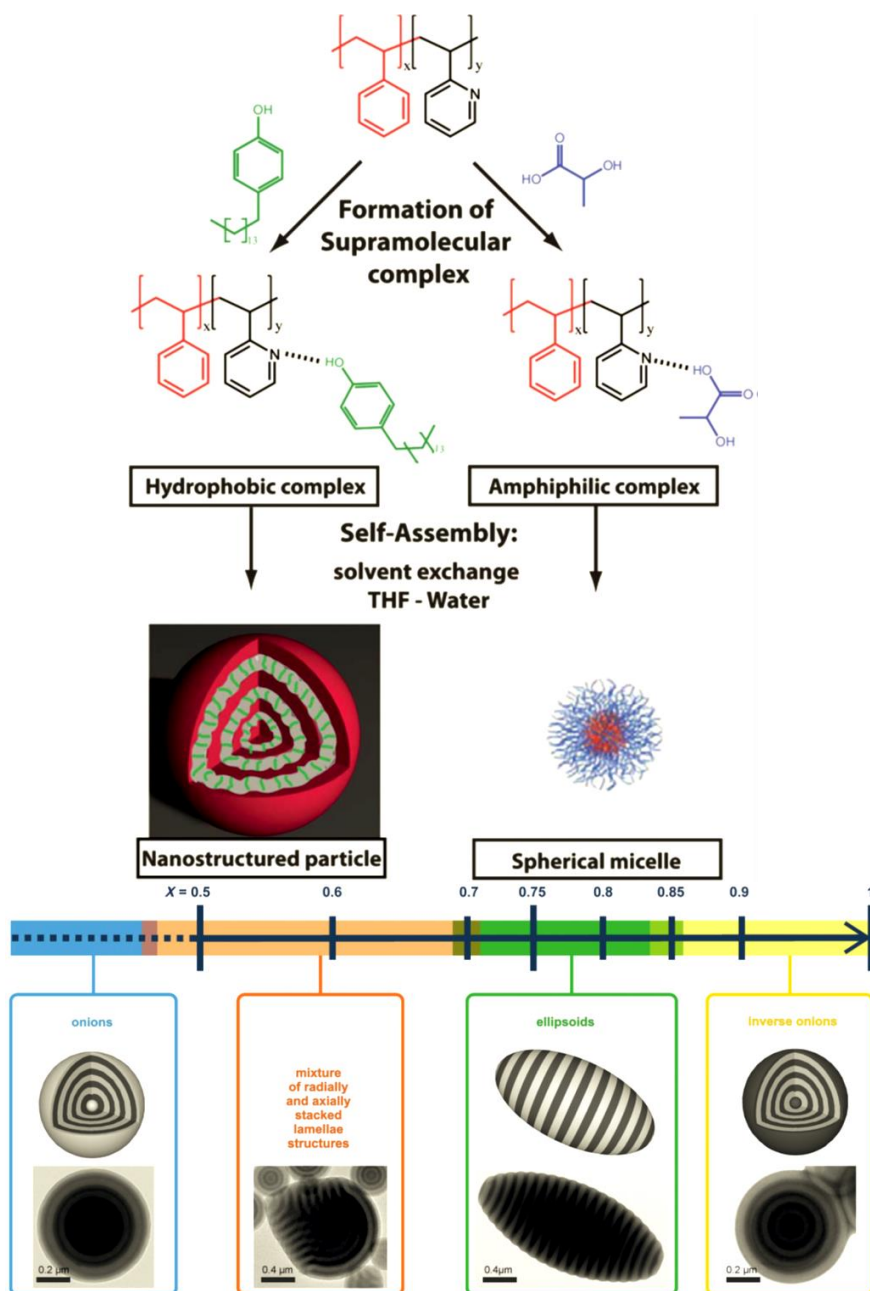
Fig. 1.8 *Representation of the self-assembled morphologies of PS-b-P2VP containing different guests conducted by solvent-exchange and pH treatments.*[47, 48]

Similarly, Jeon *et al.* obtained emulsified complex colloidal spheres of poly(styrene-*b*-butadiene) (PS-*b*-PB) blended with polystyrene

homopolymer (*h*PS) in aqueous solution, showing different internal arrangements.[49]

1.1.1.4.   Block copolymer thin films

The entropy of a system and, consequently the resulting properties, is a parameter closely related with the matter confinement of it.[19] The confinement and the entropic effects depend mainly on the degrees of freedom and how packed is the system[19], for example in the case of polymers, the dynamics and glass transition of a polymer layer of few nm of thickness may differ from the bulk, considering the different entanglement of the macromolecular chain.[19, 50] In general, block copolymers confined by copolymer-substrate and copolymer-air interphases; undergo both surface relaxation and surface reconstruction due to periodicity changes induced by interfacial forces of one of the blocks. Thin films can be prepared by the techniques of drop-casting, spin-coating, atomic layer deposition, layer-by-layer approaches, chemical/physical vapor deposition, lithographic techniques, and molecular beam epitaxy among others, or through bottom-up-like techniques as directly growth on surface. The choice of the manufacture technique will be restricted with regard to the final characteristics of the thin layer one wants to achieve.[51] Li and Han reported an interesting study in where they created different phase-segregated poly(styrene-*b*-4-vinyl pyridine) (PS-*b*-P4VP) thin films by what they called non-solvent-induced treatment. The resulting thin films demonstrated optical activity, due to the arrangement of the different domains.[52] Another interesting approach was performed by Kuila *et al.* They functionalized a copolymer of PS-*b*-P4VP with a fluorescent probe molecule of pyrenebutyric acid (PBA) by hydrogen bonding with what they built thin films (Fig. 1.9). They presented results obtained through different techniques, such as AFM, SAXS, UV-Visible absorption spectroscopy and photoluminescence to demonstrate the directed-conformations of the phase segregation of the polymeric film by solvent-annealing treatment.[53]
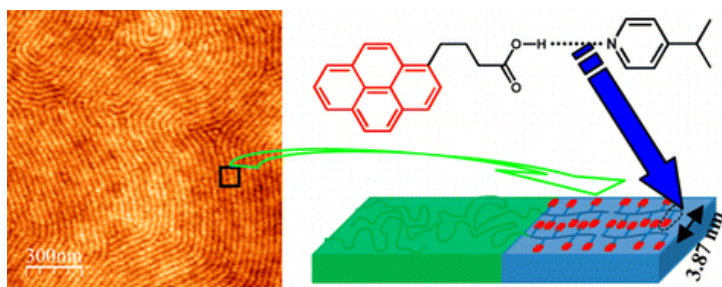
Fig. 1.9 *Supramolecular assembly driven by hydrogen bonding between PBA and P4VP units from PS-b-P4VP block copolymer thin films, and the resulting stoichiometric ratio dependent domains.[53]*

Going over the wide range of possibilities that systems based on block copolymers offer, it easy comes out that, from the a great portion of research studies involving them, the majority are based on amphiphilic polymeric compounds. The reasons have been indirectly exposed along the present section; regardless in the next section a view more focused on amphiphilic block copolymers is presented.

1.2.   BLOCK COPOLYMERS SELF-ASSEMBLY

Supramolecular chemistry is widespread and omnipresent in nature. A frequently-cited example is the DNA that forms a double helix structure by non-covalent bonding of two biopolymer strands coiled around each other. For its, a priori, simplicity, researchers have put many efforts in mimicking natural processes such as enzymatic catalysis,[54] molecular recognition[55, 56] or controlled material transportation.[55, 57] It was in 1953 when Hermann Staudinger received the Nobel Prize in Chemistry 'for his discoveries in the field of macromolecular chemistry'.[58] Later, in 1988, J.-M. Lehn suggested that supramolecular chemistry may be defined as 'chemistry beyond the molecule, bearing on the organized entities of two or more chemical species held together by intermolecular forces'.[56]

Extending these basic concepts to the polymers field, it becomes obvious why industries, with the help of researchers, have focused many resources and efforts in developing new routes in improving supramolecular structure or assembly of polymers. In this section, some bottom-up and top-down strategies and their role in the self-assembly of copolymers are going to be reviewed. These strategies comprise a brief introduction to amphiphilic block copolymers and a general view of the possibilities of arrangement, chiral recognition-conducted self-assembly, passing through a brief vision of the lithographic technologies available, also microfluidics as a platform for tuning self-assembled conformations of organic systems. Finally, π-electron- and ionic-based polymeric systems and their implication in the resultant packing of structures in the microphase are also reviewed due to the importance for this thesis.

1.2.1.   Amphiphilic block copolymers

Recalling the concept of self-assembly, which is the spontaneous agglomeration of molecules or objects into stable and well-defined structures by non-covalent forces,[56] the controlling of the chemistry of the elements involved is the main issue. Nevertheless there are systems whose self-assembly can be tuned by external factors, such as solvents and temperature. This is the case of amphiphilic block copolymer systems.

An amphiphilic molecule contains both, hydrophilic and hydrophobic groups and some examples are surfactants, some copolymers and proteins. The intermolecular and/or electrostatic interactions between the hydrophobic tail groups and the hydrophilic head groups will determine the properties of these molecules.[8] Concretely, block copolymers have had a significant role in the field of functional materials due to the possibility to be tailor-made designed just by the combination of different monomers. In this way, amphiphilic block copolymers have focused the attention of many studies because the opposite solubility characteristics of the constituent blocks, which can permit the 'tunability' of the material. Amphiphilic systems are constituted by both hydrophobic and hydrophilic parts allowing for a

same given material, a resulting system with uneven properties only by playing with the polarity of the solvents they are immersed in, acting like surfactants (Fig. 1.10).[43] The simplest example is the case of the AB amphiphilic diblock copolymers (comprising two blocks) that have the contributions of the hydrophobic and the hydrophilic blocks. In this situation, in aqueous solutions, the amphiphile orientates itself removing the hydrophobic part from the aqueous media, achieving the minimum free energy state and forming micelles. This, in common with small molecule surfactants, is only accomplished at a narrow range of concentration values of the amphiphile in the solution, around the critical micelle concentration (CMC). When the concentration of the amphiphile remains above the CMC, the formed micelles are thermodynamically stable, although when the degree of dilution is raised below the CMC, micelles tend to be disassembled.[59]

(a) = hydrophilic head
(b) = hydrophobic tail

non-polar solvent
polar solvent
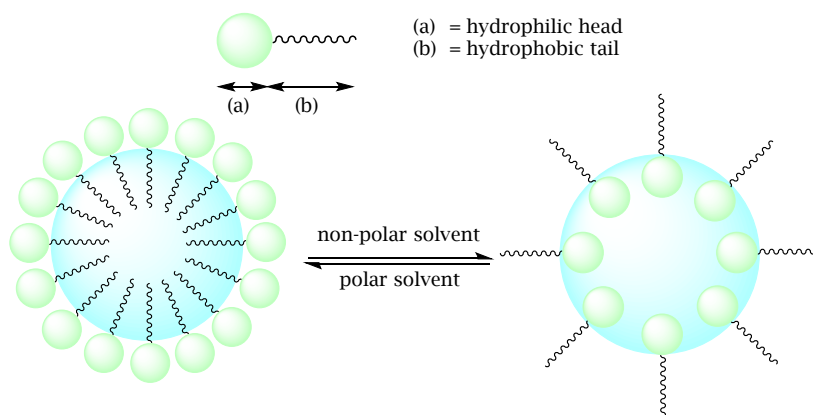
Fig. 1.10 *Self-aggregation behavior of an amphiphile in a polar or non-polar media.*

The morphology of this self-packing can differ from the shape of a perfect sphere because of the dependence on the volume and the length of the hydrophobic tails as well as the area of the hydrophilic heads. Varying the different parameters, differentiated shapes like spherical micelles, cylindrical micelles and vesicles could be achieved.[32, 60] Even more complex structures can be obtained by changing the media or the conditions of the system.[61] All these characteristic properties of amphiphilic copolymers are well-known in drug-delivery systems, in which a drug has to be transported and released when is needed. The

mechanisms of drug-releasing are based on biocompatible and biodegradable polymers and on the hydrophobic-hydrophilic interactions between the hydrophobic drug-carrier and the aqueous environment.[59, 60, 62] As examples of biocompatible and biodegradable hydrophobic blocks there are polyesters and poly(amino acids)[59] that are covalently bonded to biocompatible and hydrophilic blocks such as typically poly(ethylene glycol) or poly(lactic acid).[60, 63, 64] Amphiphilic block copolymers are also present in biocatalytic applications since the structure-function of soluble enzymes that act at lipid-water interfaces.[65]

Interestingly, an amphiphilic block copolymer that has been in the scientific spotlight is poly(styrene-*b*-vinyl pyridine) (PS-*b*-P4VP). This block copolymer allows having an easy control of the segregation of each block thanks to the opposite behavior of the forming polymers. Indeed, there is large literature already reported of studies based on PS-*b*-P4VP, as a result of the promising perspectives still unexplored of this system. For instance, in a recent work reported by Cummins *et al.* the self-assembly possibilities that this block copolymer offers were applied to a multi-step strategy to conduct the alignment of semiconductive silicon nanofins.[66] Concurrently, Poggi and coworkers prepared PS-*b*-P4VP thin films aiming the cylindrical packing arrangement of P4VP fraction to use it as template for polymeric Janus nanoparticles (Fig. 1.11).[67]
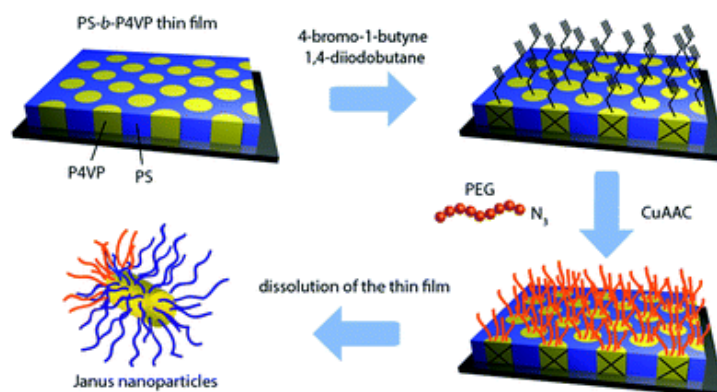
Fig. 1.11 *Formation of Janus nanoparticles by grafting a homopolymer of poly(ethylene glycol) (PEG) onto a PS-b-P4VP thin film.*[67]

Another recent work by Minsoo *et al.* showed the creation of self-assembled gold-decorated block copolymer micelles and deposited on surface to obtain porous nanostructures.[68] There are other amphiphilic block copolymers that have been deeply explored so far. For instance, Yu *et al.* reported a new approach to obtain porous membranes through a blending of poly(styrene-*b*-acrylic acid) (PS-*b*-PAA) and PS-*b*-P4VP.[69] Bellettini and coworkers also used PS-*b*-PAA to perform amphiphilic poly(ethylene imine) decorated nanovesicles with the aim to improve their biocompatibility.[70] On the other hand, Zhang studied the assembly behavior of PS-*b*-PAA micelles on substrates from the point of view of block lengths and interaction forces.[71] Recently, Manners and Winnik reported the interesting hierarchical self-assembled structures of amphiphilic cylindrical block copolymers based them on poly(ferrocenyldimethylsilane-*b*-2-vinyl pyridine) (PFS-*b*-P2VP) and poly(ferocenyldimethylsilane-*b*-dimethyl siloxane) (PFS-*b*-PDMS) for obtaining one-dimensional (1D) or 3D superlattices that persist in both solution and the solid state with a wide variety of superstructures.[72]

1.2.2.   Chiral recognition

Interestingly, the concept of chirality is frequently an inherent part of the supramolecular chemistry and it is manifested in most of biological materials (DNA included). Chirality is based on the concept of asymmetry, so a system is chiral whether it is distinguishable from its mirror image (enantiomer), and thus cannot be superposed onto it (Fig. 1.12). Two enantiomers of a chemically identical molecule can have totally different properties, such as smell, flavor and, as pharmaceuticals perfectly know, different activity and selectivity when they are incorporated in drugs.[73]
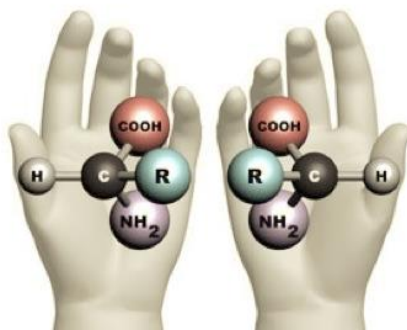
Fig. 1.12*Enantiomers of chemically identical chiral amino acid molecule.*

In polymer-based chiral systems, the influence in the aggregation behavior of the block copolymers such as poly(ethylene glycol-*b*-L-lysine) meditated by a chiral porphyrin have been studied, resulting in chiral J- and H-aggregated porphyrin arrays.[74] On the other hand, Qing and Sun reported a chiral-triggered smart chiral-responsive copolymer films for future applications in chiral separation, chiral medicine, smart microfluidic devices or bio-devices.[75] Going further, conductive chiral materials are remarkably important because of the possibilities that offer to observe chiral electron motion[73] and even electrical conductivity can be amplified.[76] Electrochemical chiral sensing or asymmetric synthesis are some of the possible applications, for example.[76] The functionalization of polymers with conductive organic pendants have explored for the preparation of *n-* or *p*-type organic semiconductors. One important is the developed by Wallis and Griffiths. They synthesized chiral tetrathiafulvelene (TTF) derivatives (TTFs can form stacks through interactions sulfur-sulfur with neighboring units), resulting in π-electron donor polymorphs and opening new pathways of exploration with combination with block copolymers.[77, 78]

Beyond the spontaneous supramolecular self-assembly conducted with solvents or chirality, there are some strategies that might promote higher contact between molecules. Nanofabrication techniques have opened new approaches for the control of the polymer assembly. From these, soft lithography and microfluidics have attracted more interest to modify the inherent self-assembly of block copolymers. Microfluidic techniques have been used as platform to control the reaction kinetics

and matter-transportation tuning the hydrodynamic flow focusing parameter.[79]

1.2.3.   Lithography and soft lithography

Since the invention of transistors in 1947 and the later apparition of microelectronics, the increasing demand of integrated devices requirements, such as low consumptions, fast operation, miniaturization and high effectiveness, have involved the improvement of microfabrication.[80-83]

Lithographic techniques generally are those relying in the fabrication or replicating structures molds or photomasks to immobilize compounds on solid substrates. Some advantages that these methodologies comprise are low cost of production, fast operation and high performance results.[84] Because the interactions between compounds occur at sub-nanometer ranges, the object of interest here will be developments enclosing nanolithographic techniques. Photolithography (also termed optical lithography) for instance, uses patterned photomasks as filter to get engraved substrates by light exposition at the nanoscale (photopatterning). This approach has been widely used in the circuitry of modern microelectronic devices.[85] Advanced lithographic techniques include extreme UV (EUV) lithography, soft X-ray lithography, electron-beam and nanoimprint lithography that are, among much others, variations and tailor-made lithographic techniques that have covered another desired requirements.[86, 87]

On the other hand, soft-lithography for micro- and nanofabrication include, according to Xia and Whitesides, micro-contact printing (µcP), replica molding (REM) micro-transfer molding (µTM) micro-molding in capillaries (MIMIC) and solvent-assisted micro-molding (SAMIM).[84] They are designated as 'soft' because elastomeric stamps or molds are needed to transfer the pattern to the substrate and broadly used for the preparation of patterned self-assembled monolayers (SAMs), especially for flexible organic molecules.

SAMs are thin molecular layers on a surface that provide functionality and because of that, the understanding of surface chemistry becomes important. Different strategies for the functionalization of the surfaces have been reported and they include surface-molecule recognition and μcP. There are several works based on surface-molecule recognition, for instance thiol-end meditated 'click-chemistry' is a commonly recurred pathway to immobilize thiolated compounds on gold surfaces.[88-90] Other well-developed approach is the use of host-guest interactions between functionalized surfaces and the molecule to immobilize.[91] This strategy has been followed by Reinhoudt and Huskens who prepared β-cyclodextrin SAMs, also called molecular printboards.[92, 93] Thanks to the host-guest interactions between cyclodextrins and different guest molecules, such as ferrocene and adamantly, the printboards have been used for a controllable immobilization of dendrimers,[94, 95] particles[96] and biomolecules.[97]

On the other hand, from all the soft-lithographic techniques, μcP is one of the most used and developed strategy to create patterns of molecules on all type of surfaces.[98] Concretely, μcP developed an important role in this field due to is an efficient 2-D fabrication technique method for pattern transfer by conformal contact between an elastomeric stamp (carrying desired molecules to immobilize) and the substrate or surface (place in where molecules will be fixed on).[84] In general, poly(dimethyl siloxane) (PDMS) is the elastomer used to build the stamps, obtained at the same time, by replica molding procedures with a patterned master wafer (usually of silicon), allowing in this way to create patterned SAMs on surface (Fig. 1.13). One of the main limitations of this technique is the narrow compatibility between PDMS and organic solvents to dissolve compound to imprint, becoming one of the key factors for a successful process.[99]
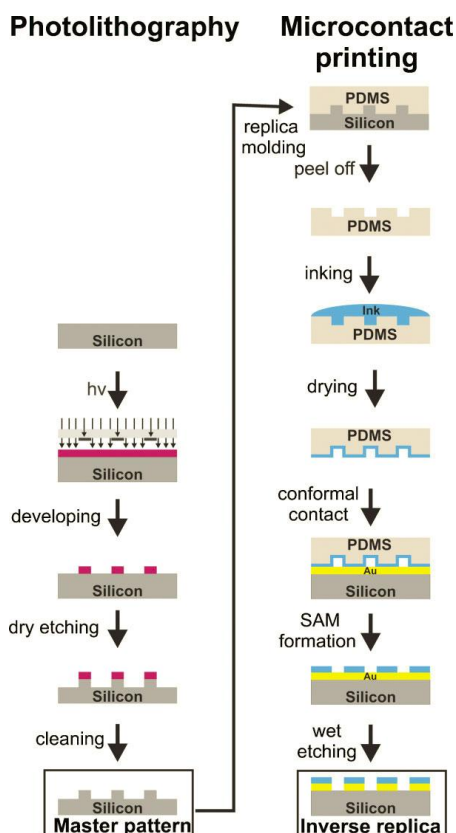
Fig. 1.13 *Scheme of the general process of μcP, from the PDMS replica molding to molecule immobilization on surface.[98]*

The immobilization of polymers on surfaces is an important field for their integration in devices and to tailor the surface properties. For this reason, one strategy is the directed polymerization of the corresponding homopolymer grafted on a surface, obtaining the called polymer brushes. They are classically prepared from block copolymers or end-grafted polymers where the functional block is exposed at the surface, thus serving as a brush layer. Polymerization methods developed to this purpose include cationic, anionic, ring-opening, free-radical and living anionic polymerizations.[100] For the preparation of patterned surfaces with polymer brushes photolithography and μcP methods have been reported.[101, 102] Hawker and coworkers reported a recent study in where 3-D graded polymer brushes of poly(methyl methacrylate-*b*-methacrylic acid) (PMMA-*b*-PMAA) grown using a photomask by light-meditated radical polymerization.[20] Another interesting approach was

performed by Roling *et al.* in where with a combination of polymer brushes growth and µcP methodologies achieved the immobilization of poly(styrene) and poly(acrylate) on glass.[103] Kong *et al.* grown amphiphilic polymer brushes of poly(methyl methacrylate-*b*-acrylamide) (PMMA-*b*-PAAM) grafted on silicon surface.[104] Moffitt explored the controllable self-organization of inorganic particles provided with polymer brushes on their surface (Fig. 1.14).[105] One of the advantages that represent having patterned surfaces is the major control and selectivity of the different functionalities given to a system. Thus, a new generation of advanced materials selectively-active or –responsive for complex applications such as biomedical or engineering, will be achieved.
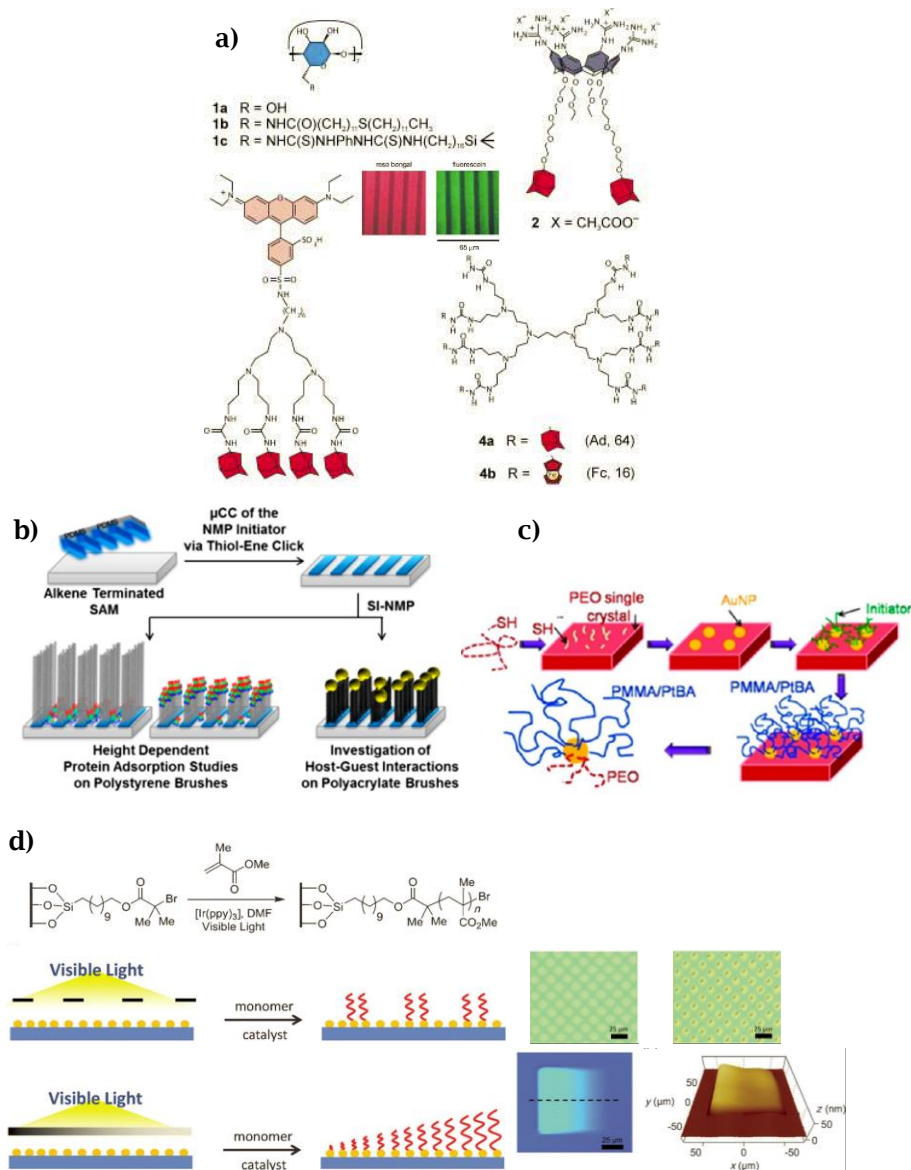
Fig. 1.14a) β-cyclodextrin and β-cyclodextrin adsorbates for the attachment of dendrimeric structures onto gold and silicon oxide surfaces using μcP as molecular printboards.[92] b) Strategy based on the immobilization of nitroxide-meditated polymerization initiators via μcP for the growing of poly(styrene) and poly(acrylate) brushes on different substrates.[103] c) Synthesis of polymer functionalized Janus gold nanoparticles combining 'solid-state grafting-to' and 'grafting from' methods.[105, 106] d) Patterning of polymer brushes from substrates uniformly functionalized with UV-responsive initiators, using a photomasks to grow selectively located polymer brushes and polymer brushes with a gradient of heights.[20]

29

Another strategy to immobilize polymers on surfaces is the preparation of Langmuir-Blodgett films, which consist on the adsorption of one or more monolayers of molecules with accurate thickness values. The basis of their preparation is by the immersion or emersion of a solid substrate into or from a liquid-containing the organic compound to immobilize. The monolayers are assembled vertically and usually are composed by amphiphilic molecules adhere on the surface due to interactions air-liquid-surface.[107] Martín-García and Velázquez demonstrated that it was possible to tune the morphology of CdSe quantum dots poly(styrene-*co*-maleic anhydride) partial 2 buthoxy ethyl ester cumene terminated (PS-MA-BEE) Langmuir-Blodgett films by modifying the polymer composition.[108] Bazuin and coworkers reported the different conformations of the phase segregation adopted with poly(styrene-*b*-4-vinyl pyridine) (PS-*b*-PVP) Langmuir-Blodgett thin films.[109] Recently, Destri *et al.* published an exhaustive characterization study of the amphiphilic block copolymer poly(styrene-*b*-methyl methacrylate) (PS-*b*-PMMA) Langmuir-Blodgett films and its self-assembled conformation correlation with the spreading parameter.[110]

1.2.4.   Microfluidics platform: lab-on-a-chip

Microfluidics techniques are based on the manipulation of fluids in sub-millimeter dimensions, with all the implications that suppose the miniaturization of reactions down to the microscale.[111] This lab-on-a-chip technique emerged as a novel and promising tool for micro- and nano-fabrication of devices. Moreover, it offers the possibility to be used for reactions at the microscale due to the lower consumption volumes, larger surface-to-volume ratios and the better control of the concentration gradients[112, 113] compared with systems in bulk.[79] Since then, many studies on the field have been focused on the application of the microchips for microengineering,[114] micro- and nano-crystallization[79, 115, 116] and biological approaches[112, 117] among others. Several parameters like flow velocity, diffusion degree, residence time and concentration of the reagents, can easily be controlled, making microfluidics a remarkable robust technique. This platform operates using little reactors or chips in where the

reactions/mixings take place (lab-on-a-chip). There are infinite chip layouts because they are usually unique and self-made pieces covering specific necessities. Marre and Jensen listed some of the most highlighting layouts specifically designed for uneven applications.[118] Nevertheless, depending on the performance and set up of the experiment, one possible limitation to handle with is the stability of the material of the microchip, especially in the case of the elastomer poly(dimethyl siloxane) (PDMS), one of the most commonly used due to its low cost, easy manipulation and accessibility.[79, 99] The PDMS-based microchips are fabricated using soft-lithography moulding techniques, previously described (Fig. 1.13). Currently, the research to improve the stability and fabrication of the microchips is focused in finding other polymers with higher chemical resistance. Thus, thermoset polymers such as SU-8, or polymers like poly(methyl methacrylate) (PMMA), poly(carbonate) (PC) and poly(tetrafluoroethylene) (Teflon®) are nowadays used.[119]

One of the most straightforward characteristics of the microfluidics technology is that operates under laminar regime and lateral mixing of the fluids does not take place, diffusion in the interface plays this role. The fluid dynamics relies in the Reynolds number:

$$R_n = \frac{\rho v L}{\mu}$$

in where ρ is the density of the fluid, v is the velocity of the fluid, L is the length or distance that the fluid travels and, μ is the dynamic viscosity of the fluid. Situations in which the Reynolds number is small are called slow viscous flows because viscous forces arising from shearing motions of the fluid predominate over inertial forces associated with acceleration for deceleration of fluid particles.[120] Working with low Reynolds number values (laminar regime, $R_n \ll 1$) eliminates the uncertainty in chemical reaction predictions and low reproducibility that happens in bulk (mostly turbulent flows). If one extrapolates the idea of laminar flow regime to a fluid travelling inside a small and straight pipe represented by parallel layers in the direction of the flow, appears the

Stokes law[*]. The Stokes law determines that the velocity of a fluid flowing in the vicinities of the wall of a pipe, can be considered practically zero. Consequently, if one considers a particle inside the described pipe travelling with the flow direction can be easily deducted that the particle will be located in the middle of the pipe, where the friction exercised by the walls will tend to zero (the place furthest away from the walls) and at the same time and for the same reason, is the region in where the fluid acquires major velocity (Fig. 1.15).
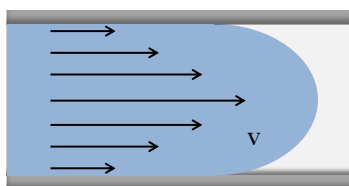
Fig. 1.15 *Representation of a fluid flowing inside a straight pipe. The arrows indicate the direction of the flow and their lengths represent the advancing velocity.*

Several biological applications implying chiral recognition, such as enantiomeric separation have been devised.[121] The majority of reactions developed in this lab-on-a-chip devices arise from the diffusion between reagents due to the laminar flow working conditions. Therefore, an easy-to-handle parameter that has notable implications is the hydrodynamic flow focusing. Puigmartí-Luis and researchers exemplified that with TTF-based fibers, correlating flow-rate ratio of reactants in solution with the conformational assembly of the final product.[122] As it will be described in detail in next chapters, TTFs are molecules with the capacity to self-assemble through the disulfur rings forming ordered stacks in bulk and interestingly, they could tune the shape of the section of these solid stacks obtaining fascinating morphologies.

---

[*] An incompressible, Newtonian fluid motion can be described by the Navier-Stokes equation when it is assumed that the viscous stresses on a fluid element are proportional to the element strain rates and the coefficient of viscosity. S.K. Mitra and S. Chakraborty, *Microfluidics and Nanofluidics Handbook*, CRC Press, 2011.

1.2.5. Semiconductive polymers: electron and ion transportation-based systems

Semiconductive polymers are considered organic semiconductors with an electrical conductivity between a conductive and insulating material. Since their origin in the 1970s,[123] semiconductive and hybrid polymers have experimented an emergent interest due to the wide possible applications.

The conduction of the current in a semiconductor occurs by the movement of free electrons and holes, also known as charge carriers. Introducing intentionally impurities into a pure semiconductor (an action known as 'doping') one can increase the number of charge carriers and increase the electrons motion. There are two types of doped semiconductors, *p*-type are those which contain free holes (or cation radicals), and *n*-type, which mostly contain free electrons (or anion radicals) and therefore, its donor density is greater than its acceptor density (Fig. 1.16). A single semiconductor can have many *p*- and *n*-type regions in where the *p-n* junctions between these regions relies the electronic behavior. The semiconductors used in electronic devices have been mainly inorganic materials precisely doped with *p*- and *n*-type dopants. Some examples of elements having semiconducting properties are silicon, germanium and certain elements in the group XIV of the periodic table, binary compounds between elements in groups III and V (e.g. gallium arsenide), groups II and VI, groups IV and VI (e.g. silicon carbide), certain ternary compounds, oxides and alloys and, of course, organic semiconductors made of organic compounds.[124] However, nowadays an important field of research is the development of organic-based semiconductive devices using small molecules or oligomers.[125-127]
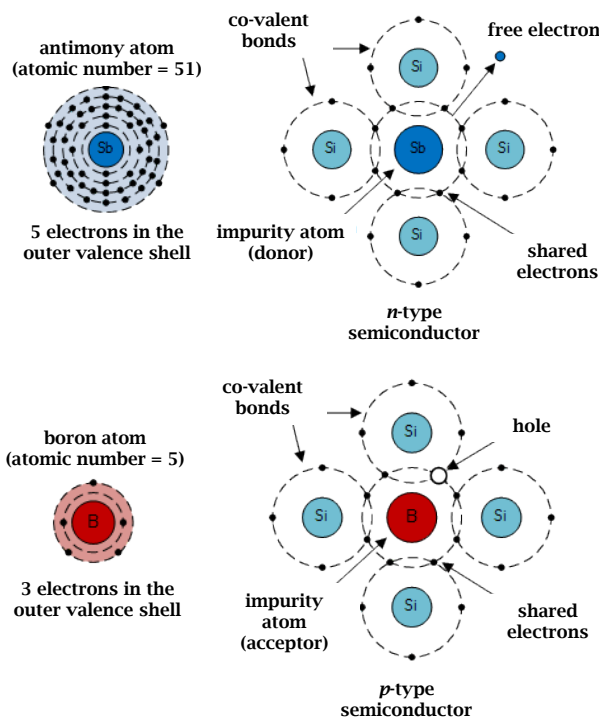
Fig. 1.16 Examples of n-type and p-type semiconductors.[124]

Polymers and block copolymers, thanks to their ability to self-assembly in periodic domains at the microphase in a range from 5 to 50 nm, have attracted the interest of the semiconductor industry for fabrication of integrated circuits.[45] In this way, polymeric conductors such as poly(pyrrole) (PPy), poly(aniline) (PANI), poly(3,4-ethylenedioxythiophene) (PEDT, PEDOT) or poly(acetylene) (PAc), among others, have been explored due to their ability to conduct charge, their great electrical and optical properties, as well as their flexibility in processing and ease of synthesis. The phenomenon of doping is essential for the conductivity of these type of polymers towards the gain of higher conductivity values.[128] Shi *et al.* reviewed different synthetic strategies of a variety of nanostructured conductive polymers for energy storage applications, highlighting also that the resultant conductivity of these materials depends on the dopants used.[129] Ramaswamy and coworkers investigated the combination of metal organic frameworks (MOFs) and coordination polymers as possible candidates for proton-conducting

applications.[130] Additionally, liquid crystal polymeric structures have had an important role in the research of new conductive materials.[131-133]

Researchers have been focused their efforts in the improving of already known semiconductive materials and exploring new synthesize paths with the aim to find balanced materials that combine properties, such as efficient conductivity with long stability. For instance Bao and coworkers had carried out numerous studies in high-performance polymer-based semiconductors, establishing correlations between the processing methodologies from the solution to thin film and their final properties.[134-138] Conjugated systems[139-141] are well-established in this field because they comprise properties such as low-cost, light weight, possibility to obtain flexible and large-area electronic devices and for their application in organic photovoltaics.[142] Polymers for this kind of applications are designed to have a narrow bandgap to promote the charge transportation.[142] One of the most studied conjugated polymers for its potential application in solar cells is the poly(3-hexylthiophene) (P3HT). P3HT can become conducting upon doping conditions due to the delocalization of electrons along the polymer backbone. Moreover, P3HT is an stimuli-responsive material, supposing a serious alternative to traditional semiconductor components for a range of applications.[143-146] Azo dyes and poly(3,4.ethylenedioxythiophene) (PEDOT) are also appreciated due to their light-sensitivity properties. Other existing applications for conjugated polymers are for instance photopolymerization for growing polymer brushes.[20, 147-149]

Another approach for the preparation of semiconductive organic-based devices is the use of small molecules with π-electron donors combined with their supramolecular assembly. Brand-new examples are tetrathiafulvalenes (TTFs), well-known for their reversibility to be oxidized to dication, passing through the intermediate cation-radical mixed valence state upon either doping or reducing processes. TTFs and their derivatives form highly ordered stacks as a result of intermolecular π-π and non-bonded sulfur-sulfur interactions (Fig. 1.17).[150]
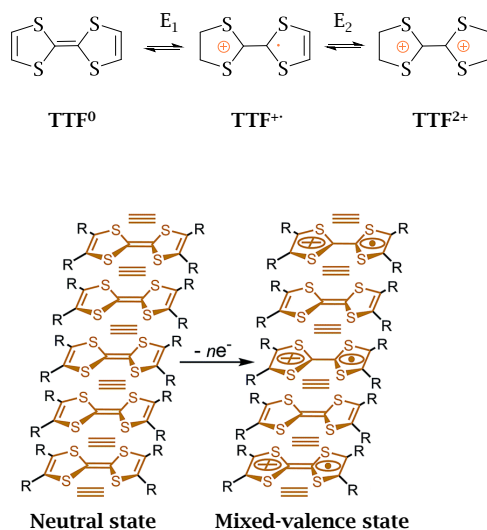
Fig. 1.17 Reversible oxidation states of TTFs, neutral (TTF⁰), cation-radical (TTF⁺·) and dication (TTF²⁺) adjacent to representations of self-assembled stacks of neutral and mixed valence state of TTFs. For unsubstituted TTF, $E_1^{1/2} = +0.34\ V$ and $E_2^{1/2} = +0.78\ V$, vs. Ag/AgCl in acetonitrile.[150]

Ahn *et al.* obtained electrical fibers of a derivative TTF packed in a triple helix conformation.[151] The supramolecular chemistry of TTFs as building blocks was early reviewed by Nielsen and coworkers, showing the numerous possibilities as sensors, molecular switches or catalysts.[152] Its conductivity in polymeric systems has also been demonstrated, for instance, Gomar-Nadal proposed redox-switchable organic systems based on a derivative TTF-tethered system with a chiral polymer.[153, 154] On the other hand, Chujo made exhaustive studies on TTFs and their combination with polymeric systems, describing materials with charge transportation properties.[155] Other studies are based on the charge transportation of conjugated polymers or metal salts. One example is the study elaborated by Yasuda and coworkers, showing the packing structure of π-conjugated copolymers consisting in self-assembled electron-accepting and electron donating units.[156] Another approaches have used doped alkali metal salts in block copolymers as improve the electron transportation capability[157] or semiconductive liquid-crystalline block copolymers.[158, 159]

Finally, from another point of view, ionic transportation have also been demonstrated to be an effective strategy for synthetizing semiconducting polymers, as well as the influence of the polymer electrolytes determining the final assembly of the phase separation. This was the objective of the work performed by McIntosh *et al.* in where they polymerized *via* induction phase separation block copolymer electrolytes, correlating the segregated conformations with the ion-conductivity for membrane applications (Fig. 1.18).[160] In a recent work conducted by Jones, Grubbs and coworkers the synthesis, self-assembly, conductivity and rheological properties of an ABA triblock brush copolymer with grafted PS and poly(ethylene oxide) (PEO) (*g*PS-*g*PEO-*g*PS) was reported. They studied the phase segregation variations by including doped lithium cations demonstrating the narrow correlation between the phase segregation of the polymers and the resulting ionic conductivity of the compounded material (Fig. 1.18).[161] In the same way, Jo *et al.* investigated the improvement of ionic conductivity of a lamellar-segregated poly(ethylene oxide-*b*-dithiooxamide) (PEO-*b*-PDTOA) through the incorporation of PEO-salt electrolytes.[162]
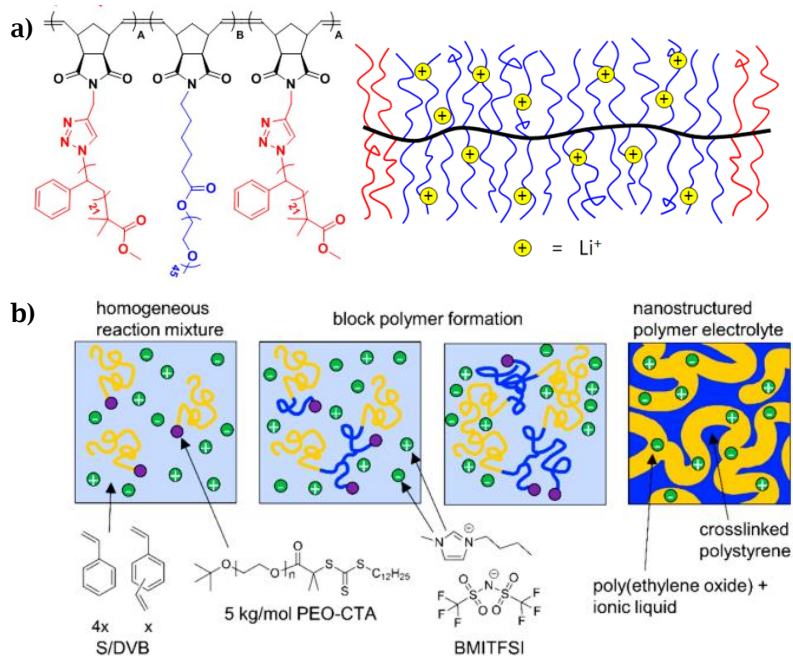
Fig. 1.18 *a) Grafted ABA gPS-gPEO-gPS triblock copolymer to a polynorbornene chain, doped with lithium ions for conductive applications.[161] b) Polymerization-induced phase separation (PIPS) strategy to prepare polymer electrolyte membranes.[160]*

1.3. REFERENCES

1. E. Commission, Eurostat, http://ec.europa.eu/eurostat/web/main/home, (accessed May 2015, 2015).
2. Online Etymology Dictionary, http://www.etymonline.com/, (accessed May 2015, 2015).
3. C. U. Press, Cambridge Dictionaries Online, http://dictionary.cambridge.org/es/, (accessed May 2015, 2015).
4. Y. Y. B. Dhandayuthapani, T. Maekawa, D.S. Kumar, *International Journal of Polymer Science*, 2011, **2011**.
5. J. M. J. Fréchet, *Science*, 1994, **263**, 1710.
6. H. C. Kolb, M. G. Finn and K. B. Sharpless, *Angewandte Chemie International Edition*, 2001, **40**, 2004-2021.
7. D. N. Schulz and O. P. Abhimanyu, in *Functional Polymers*, American Chemical Society, 1998, vol. 704, ch. 1, pp. 1-14.
8. Jin Zhang, Zhon-lin Wang, Jun Liu, Shaowei Chen and G.-y. Liu, *Nanostructure Science and Technology: Self-Assembled Nanostructures*, Kluwer Academic/Plenum Publishers, 2003.
9. F. S. Bates and G. H. Fredrickson, *Physics Today*, 1999, **52**, 32.
10. V. N. Urade, T.-C. Wei, M. P. Tate, J. D. Kowalski and H. W. Hillhouse, *Chemistry of Materials*, 2007, **19**, 768-777.
11. R. Ruiz, H. Kang, F. A. Detcheverry, E. Dobisz, D. S. Kercher, T. R. Albrecht, J. J. de Pablo and P. F. Nealey, *Science*, 2008, **321**, 936-939.
12. T. Thurn-Albrecht, R. Steiner, J. DeRouchey, C. M. Stafford, E. Huang, M. Bal, M. Tuominen, C. J. Hawker and T. P. Russell, *Advanced materials*, 2000, **12**, 787-791.
13. D. A. Olson, L. Chen and M. A. Hillmyer, *Chemistry of Materials*, 2008, **20**, 869-890.
14. W. A. Phillip, B. O'Neill, M. Rodwogin, M. A. Hillmyer and E. L. Cussler, *ACS Applied Materials & Interfaces*, 2010, **2**, 847-853.
15. R. A. Segalman, B. McCulloch, S. Kirmayer and J. J. Urban, *Macromolecules*, 2009, **42**, 9205-9216.
16. I. W. Hamley, *Progress in Polymer Science*, 2009, **34**, 1161-1210.
17. R. K. Krishnaswamy and A. M. Sukhadia, *Polymer*, 2000, **41**, 9205-9217.
18. L. Singh, Georgia Institute of Technology, 2004.
19. S. Perkin and J. Klein, *Soft Matter*, 2013, **9**, 10438-10441.
20. J. E. Poelma, B. P. Fors, G. F. Meyers, J. W. Kramer and C. J. Hawker, *Angewandte Chemie International Edition* 2013, **52**, 6844-6848.
21. J. Yang, G. Yu, D. Xia and F. Huang, *Chemical communications*, 2014, **50**, 3993-3995.
22. G. Yu, K. Jie and F. Huang, *Chemical reviews*, 2015, **115**, 7240-7303.
23. Z. Iatridi, Y. Roiter, N. Stavrouli, S. Minko and C. Tsitsilianis, *Polymer Chemistry*, 2011, **2**, 2037-2044.
24. R. B. Grubbs and Z. Sun, *Chemical Society reviews*, 2013, **42**, 7436-7445.
25. M. A. C. Stuart, W. T. S. Huck, J. Genzer, M. Muller, C. Ober, M. Stamm, G. B. Sukhorukov, I. Szleifer, V. V. Tsukruk, M. Urban, F. Winnik, S. Zauscher, I. Luzinov and S. Minko, *Nature materials*, 2010, **9**, 101-113.
26. D. Roy, W. L. A. Brooks and B. S. Sumerlin, *Chemical Society reviews*, 2013, **42**, 7214-7243.
27. P. W. Majewski, M. Gopinadhan and C. O. Osuji, *Soft Matter*, 2013, **9**, 7106-7116.

28. J. Li, J. K. Park, R. B. Moore and L. A. Madsen, *Nature materials*, 2011, **10**, 507-511.
29. S. Dai, P. Ravi and K. C. Tam, *Soft Matter*, 2008, **4**, 435-449.
30. *Block Copolymers in Nanoscience*, Wiley-VCH Verlag GmbH & Co. KGaA, 2006.
31. K. Huh, H. Kang, Y. Lee and Y. Bae, *Macromol. Res.*, 2012, **20**, 224-233.
32. A. Blanazs, S. P. Armes and A. J. Ryan, *Macromolecular rapid communications*, 2009, **30**, 267-277.
33. I. Tokarev, M. Motornov and S. Minko, *Journal of Materials Chemistry*, 2009, **19**, 6932-6948.
34. D. T. G. L.C. Sawyer, G.F. Meyers, *Polymer Microscopy*, Springer, New York, 3rd Edition edn., 1987.
35. *Journal of Polymer Science*, 1952, **8**, 257-277.
36. *Journal of Polymer Science*, 1996, **68**, 2287-2311.
37. M. H. R.G. Gilbert, A.D. Jenkins, R.G. Jones, P. Kratochvíl, R.F.T. Stepto, *International Union of Pure and Applied Chemistry*, 2009, **81**, 351-353.
38. S. B. Darling, *Progress in Polymer Science*, 2007, **32**, 1152-1204.
39. in *Intermolecular and Surface Forces (Third Edition)*, ed. J. N. Israelachvili, Academic Press, San Diego, 2011, DOI: http://dx.doi.org/10.1016/B978-0-12-375182-9.10025-9.
40. J. N. Israelachvili, *Intermolecular and Surface Forces*, Academic Press, San Diego, 2nd edition edn., 1992.
41. Y. Mai and A. Eisenberg, *Chemical Society reviews*, 2012, **41**, 5969-5985.
42. T. Tadros, in *Encyclopedia of Colloid and Interface Science*, ed. T. Tadros, Springer Berlin Heidelberg, 2013, DOI: 10.1007/978-3-642-20665-8_89, ch. 89, pp. 523-524.
43. P. Alexandridis, *Current Opinion in Colloid & Interface Science*, 1996, **1**, 490-501.
44. C. D. Han, J. Kim and J. K. Kim, *Macromolecules*, 1989, **22**, 383-394.
45. H.-C. Kim, S.-M. Park and W. D. Hinsberg, *Chemical reviews*, 2010, **110**, 146-177.
46. W. Zheng and Z.-G. Wang, *Macromolecules*, 1995, **28**, 7215-7223.
47. D. Klinger, M. J. Robb, J. M. Spruell, N. A. Lynd, C. J. Hawker and L. A. Connal, *Polymer Chemistry*, 2013, **4**, 5038-5042.
48. D. Klinger, C. X. Wang, L. A. Connal, D. J. Audus, S. G. Jang, S. Kraemer, K. L. Killops, G. H. Fredrickson, E. J. Kramer and C. J. Hawker, *Angewandte Chemie International Edition*, 2014, **53**, 7018-7022.
49. S.-J. Jeon, G.-R. Yi, C. M. Koo and S.-M. Yang, *Macromolecules*, 2007, **40**, 8430-8439.
50. T. G. Dane, P. T. Cresswell, G. A. Pilkington, S. Lilliu, J. E. Macdonald, S. W. Prescott, O. Bikondoa, C. F. J. Faul and W. H. Briscoe, *Soft Matter*, 2013, **9**, 10501-10511.
51. K. Seshan, ed. K. Seshan, William Andrew Publishing, Norwich, NY, 2001, DOI: http://dx.doi.org/10.1016/B978-081551442-8.50002-X.
52. X. Li and Y. Han, *Journal of Materials Chemistry*, 2011, **21**, 18024-18033.
53. B. K. Kuila, C. Chakraborty and S. Malik, *Macromolecules*, 2013, **46**, 484-492.
54. J. Meeuwissen and J. N. H. Reek, *Nature chemistry*, 2010, **2**, 615-621.
55. K. Ariga and T. Kunitake, *Supramolecular Chemistry - Fundamentals and Applications: Advanced Textbook*, Springer Berlin Heidelberg, 2006.
56. J.-M. Lehn, *Angewandte Chemie International Edition*, 1988, **27**, 89-112.
57. X. Zhou, G. Liu, K. Yamato, Y. Shen, R. Cheng, X. Wei, W. Bai, Y. Gao, H. Li, Y. Liu, F. Liu, D. M. Czajkowsky, J. Wang, M. J. Dabney, Z. Cai, J. Hu, F. V. Bright, L. He, X. C. Zeng, Z. Shao and B. Gong, *Nature communications*, 2012, **3**, 949.
58. N. P. Organization, http://www.nobelprize.org/, (accessed 2015/09/09).

59. K. Letchford and H. Burt, *European Journal of Pharmaceutics and Biopharmaceutics*, 2007, **65**, 259-269.
60. C. Allen, D. Maysinger and A. Eisenberg, *Colloids and Surfaces B: Biointerfaces*, 1999, **16**, 3-27.
61. C. Fong, T. Le and C. J. Drummond, *Chemical Society reviews*, 2012, **41**, 1297-1322.
62. A. Rösler, G. W. M. Vandermeulen and H.-A. Klok, *Advanced drug delivery reviews*, 2001, **53**, 95-108.
63. H. M. Burt, X. Zhang, P. Toleikis, L. Embree and W. L. Hunter, *Colloids and Surfaces B: Biointerfaces*, 1999, **16**, 161-171.
64. L. Deng, A. Li, C. Yao, D. Sun and A. Dong, *Journal of Applied Polymer Science*, 2005, **98**, 2116-2122.
65. R. Verger and F. Carrière, *Biochimie*, 2000, **82**, 971.
66. C. Cummins, A. Gangnaik, R. A. Kelly, D. Borah, J. O'Connell, N. Petkov, Y. M. Georgiev, J. D. Holmes and M. A. Morris, *Nanoscale*, 2015, **7**, 6712-6721.
67. E. Poggi, J.-P. Bourgeois, B. Ernould and J.-F. Gohy, *RSC Advances*, 2015, **5**, 44218-44221.
68. P. K. Minsoo, K. Hyeong Jun, J. K. Bumjoon and Y. Gi-Ra, *Nanotechnology*, 2015, **26**, 095302.
69. H. Yu, X. Qiu, N. Moreno, Z. Ma, V. M. Calo, S. P. Nunes and K.-V. Peinemann, *Angewandte Chemie International Edition*, 2015, DOI: 10.1002/anie.201505663, n/a-n/a.
70. I. C. Bellettini, M. A. Witt, R. Borsali, E. Minatti, A. F. Rubira and E. C. Muniz, *Journal of Molecular Liquids*, 2015, **210, Part A**, 29-36.
71. Y. Zhang, J. Zhou, Y. Yu and B. Wen, *Colloid and Polymer Science*, 2015, DOI: 10.1007/s00396-015-3761-y, 1-7.
72. H. Qiu, Z. M. Hudson, M. A. Winnik and I. Manners, *Science*, 2015, **347**, 1329-1332.
73. D. Amabilino and J. Veciana, in *Supramolecular Chirality*, eds. M. Crego-Calama and D. Reinhoudt, Springer Berlin Heidelberg, 2006, vol. 265, ch. 34, pp. 253-302.
74. A. Li, L. Zhao, J. Hao, Q. Tao, R. Ma, Z. Zhang, Y. An and L. Shi, *Colloid and Polymer Science*, 2013, **291**, 2975-2984.
75. G. Qing and T. Sun, *Advanced materials*, 2011, **23**, 1615-1620.
76. L. A. P. Kane-Maguire and G. G. Wallace, *Chemical Society reviews*, 2010, **39**, 2545-2576.
77. J. D. Wallis and J.-P. Griffiths, *Journal of Materials Chemistry*, 2005, **15**, 347.
78. J.-P. Griffiths, H. Nie, R. J. Brown, P. Day and J. D. Wallis, *Organic & Biomolecular Chemistry*, 2005, **3**, 2155-2166.
79. J. Puigmarti-Luis, *Chemical Society reviews*, 2014, **43**, 2253-2271.
80. K. Gilleo, *Microelectronics International*, 1996, **13**, 19-22.
81. J. Van der Spiegel, in *Introduction to Nanoscale Science and Technology*, eds. M. Di Ventra, S. Evoy and J. Heflin, Jr., Springer US, 2004, DOI: 10.1007/1-4020-7757-2_10, ch. 10, pp. 217-260.
82. M. Rezazadeh, F. Safaei and M. Moazez, *Microelectronics Journal*, 2015, **46**, 875-892.
83. D. Bucknall, *Nanolithography and Patterning Techniques in Microelectronics*, Elsevier Science, 2005.
84. Y. Xia and G. M. Whitesides, *Angewandte Chemie International Edition*, 1998, **37**, 550-575.
85. C. Mack, *Fundamental Principles of Optical Lithography: The Science of Microfabrication*, Wiley, 2011.
86. S. Seal, *Functional Nanostructures: Processing, Characterization, and Applications*, Springer New York, 2007.

87. A. Erdmann, R. Liang, A. Sezginer and B. Smith, *Appl. Opt.*, 2014, **53**, LI1-LI2.
88. A. B. Lowe, *Polymer Chemistry*, 2010, **1**, 17-36.
89. A. Rezvani-Boroujeni, M. Javanbakht, M. Karimi, C. Shahrjerdi and B. Akbari-adergani, *Industrial & Engineering Chemistry Research*, 2015, **54**, 502-513.
90. N. Gupta, B. F. Lin, L. M. Campos, M. D. Dimitriou, S. T. Hikita, N. D. Treat, M. V. Tirrell, D. O. Clegg, E. J. Kramer and C. J. Hawker, *Nature chemistry*, 2010, **2**, 138-145.
91. B. V. K. J. Schmidt, M. Hetzer, H. Ritter and C. Barner-Kowollik, *Progress in Polymer Science*, 2014, **39**, 235-249.
92. T. Auletta, B. Dordi, A. Mulder, A. Sartori, S. Onclin, C. M. Bruinink, M. Peter, C. A. Nijhuis, H. Beijleveld, H. Schonherr, G. J. Vancso, A. Casnati, R. Ungaro, B. J. Ravoo, J. Huskens and D. N. Reinhoudt, *Angewandte Chemie International Edition*, 2004, **43**, 369-373.
93. O. Crespo-Biel, B. Jan Ravoo, J. Huskens and D. N. Reinhoudt, *Dalton transactions*, 2006, DOI: 10.1039/b517699a, 2737-2741.
94. S. Onclin, J. Huskens, B. J. Ravoo and D. N. Reinhoudt, *Small*, 2005, **1**, 852-857.
95. B. J. Ravoo, *Dalton transactions*, 2008, DOI: 10.1039/B718133G, 1533-1537.
96. M. D. Yilmaz and J. Huskens, *Soft Matter*, 2012, **8**, 11768-11780.
97. P. Neirynck, J. Schimer, P. Jonkheijm, L. G. Milroy, P. Cigler and L. Brunsveld, *Journal of Materials Chemistry B*, 2015, **3**, 539-545.
98. A. Perl, D. N. Reinhoudt and J. Huskens, *Advanced materials*, 2009, **21**, 2257-2268.
99. J. N. Lee, C. Park and G. M. Whitesides, *Analytical Chemistry*, 2013, 6544-6554.
100. W. Senaratne, L. Andruzzi and C. K. Ober, *Biomacromolecules*, 2005, **6**, 2427-2448.
101. S. Edmondson, V. L. Osborne and W. T. S. Huck, *Chemical Society reviews*, 2004, **33**, 14-22.
102. B. Zhao and W. J. Brittain, *Progress in Polymer Science*, 2000, **25**, 677-710.
103. O. Roling, A. Mardyukov, J. A. Krings, A. Studer and B. J. Ravoo, *Macromolecules*, 2014, **47**, 2411-2419.
104. X. Kong, T. Kawai, J. Abe and T. Iyoda, *Macromolecules*, 2001, **34**, 1837-1844.
105. M. G. Moffitt, *The Journal of Physical Chemistry Letters*, 2013, **4**, 3654-3666.
106. B. Wang, B. Li, B. Zhao and C. Y. Li, *Journal of the American Chemical Society*, 2008, **130**, 11594-11595.
107. K. Ariga, T. Nakanishi and T. Michinobu, *Journal of Nanoscience and Nanotechnology*, 2006, **6**, 2278-2301.
108. B. Martín-García and M. M. Velázquez, *Materials Chemistry and Physics*, 2013, **141**, 324-332.
109. Perepichka, II, Q. Lu, A. Badia and C. G. Bazuin, *Langmuir : the ACS journal of surfaces and colloids*, 2013, **29**, 4502-4519.
110. G. Li Destri, A. A. M. Gasperini and O. Konovalov, *Langmuir : the ACS journal of surfaces and colloids*, 2015, **31**, 8856-8864.
111. P. Tabeling and S. Chen, *Introduction to Microfluidics*, OUP Oxford, 2010.
112. A. G. Toh, Z. P. Wang, C. Yang and N.-T. Nguyen, *Microfluid Nanofluid*, 2014, **16**, 1-18.
113. K. Junemo and K. Clement, *Journal of Micromechanics and Microengineering*, 2003, **13**, 568.
114. R. Ameloot, F. Vermoortele, W. Vanhove, M. B. J. Roeffaers, B. F. Sels and D. E. De Vos, *Nature chemistry*, 2011, **3**, 382-387.

115. J. Puigmarti-Luis, M. Paradinas, E. Bailo, R. Rodriguez-Trujillo, R. Pfattner, C. Ocal and D. B. Amabilino, *Chemical Science*, 2015, **6**, 3471-3477.
116. L. Li and R. F. Ismagilov, *Annual Review of Biophysics*, 2010, **39**, 139-158.
117. X. J. Li and Y. Zhou, in *Microfluidic Devices for Biomedical Applications*, eds. X. Li and Y. Zhou, Woodhead Publishing, 2013, DOI: http://dx.doi.org/10.1016/B978-0-85709-697-5.50023-2, pp. xxi-xxiii.
118. S. Marre and K. F. Jensen, *Chemical Society reviews*, 2010, **39**, 1183-1202.
119. K. Ren, J. Zhou and H. Wu, *Accounts of Chemical Research*, 2013, **46**, 2396-2406.
120. S. K. Mitra and S. Chakraborty, *Microfluidics and Nanofluidics Handbook: Chemistry, physics, and life science principles*, CRC Press, 2011.
121. S. Nagl, P. Schulze, S. Ohla, R. Beyreiss, L. Gitlin and D. Belder, *Analytical Chemistry*, 2011, **83**, 3232-3238.
122. J. Puigmartí-Luis, D. Schaffhauser, B. R. Burg and P. S. Dittrich, *Advanced materials*, 2010, **22**, 2255-2259.
123. *Semiconducting polymers [Recurso electrónico] : chemistry, physics and engineering*, Weinheim : Wiley-VCH, Weinheim, 2005.
124. E. Tutorials, http://www.electronics-tutorials.ws/, (accessed 07/06, 2015).
125. I. Salzmann and G. Heimel, *Journal of Electron Spectroscopy and Related Phenomena*, 2015, **204, Part A**, 208-222.
126. A. Mishra and P. Bäuerle, *Angewandte Chemie International Edition*, 2012, **51**, 2020-2067.
127. V. Coropceanu, H. Li, P. Winget, L. Zhu and J.-L. Brédas, *Annual Review of Materials Research*, 2013, **43**, 63-87.
128. R. Balint, N. J. Cassidy and S. H. Cartmell, *Acta Biomaterialia*, 2014, **10**, 2341-2353.
129. Y. Shi, L. Peng, Y. Ding, Y. Zhao and G. Yu, *Chemical Society reviews*, 2015, **44**, 6684-6696.
130. P. Ramaswamy, N. E. Wong and G. K. H. Shimizu, *Chemical Society reviews*, 2014, **43**, 5913-5932.
131. T. Kato, *Science*, 2002, **295**, 2414-2418.
132. J. Lu, F. Yan and J. Texter, *Progress in Polymer Science*, 2009, **34**, 431-448.
133. D. Mecerreyes, *Progress in Polymer Science*, 2011, **36**, 1629-1648.
134. Y. Diao, L. Shaw, Z. Bao and S. C. B. Mannsfeld, *Energy & Environmental Science*, 2014, **7**, 2145-2159.
135. G. Giri, E. Verploegen, S. C. B. Mannsfeld, S. Atahan-Evrenk, D. H. Kim, S. Y. Lee, H. A. Becerril, A. Aspuru-Guzik, M. F. Toney and Z. Bao, *Nature*, 2011, **480**, 504-508.
136. R. Schmidt, J. H. Oh, Y.-S. Sun, M. Deppisch, A.-M. Krause, K. Radacki, H. Braunschweig, M. Könemann, P. Erk, Z. Bao and F. Würthner, *Journal of the American Chemical Society*, 2009, **131**, 6215-6228.
137. S. Liu, W. M. Wang, A. L. Briseno, S. C. B. Mannsfeld and Z. Bao, *Advanced materials*, 2009, **21**, 1217-1232.
138. Y.-L. Loo, T. Someya, K. W. Baldwin, Z. Bao, P. Ho, A. Dodabalapur, H. E. Katz and J. A. Rogers, *Proceedings of the National Academy of Sciences*, 2002, **99**, 10252-10256.
139. J. Jensen, A. L. Dyer, D. E. Shen, F. C. Krebs and J. R. Reynolds, *Advanced Functional Materials*, 2013, **23**, 3728-3737.
140. J. A. Kerszulis, K. E. Johnson, M. Kuepfert, D. Khoshabo, A. L. Dyer and J. R. Reynolds, *Journal of Materials Chemistry C*, 2015, **3**, 3211-3218.
141. J.-F. Chang, M. C. Gwinner, M. Caironi, T. Sakanoue and H. Sirringhaus, *Advanced Functional Materials*, 2010, **20**, 2825-2832.
142. I. Osaka, *Polym J*, 2015, **47**, 18-25.
143. M. T. Dang, L. Hirsch and G. Wantz, *Advanced materials*, 2011, **23**, 3597-3602.

144. B. Dorling, V. Vohra, T. T. Dao, M. Garriga, H. Murata and M. Campoy-Quiles, *Journal of Materials Chemistry C*, 2014, **2**, 3303-3310.

145. G. Lu, J. Blakesley, S. Himmelberger, P. Pingel, J. Frisch, I. Lieberwirth, I. Salzmann, M. Oehzelt, R. Di Pietro, A. Salleo, N. Koch and D. Neher, *Nature communications*, 2013, **4**, 1588.

146. S. Ludwigs, *P3HT Revisited – From Molecular Scale to Solar Cell Devices*, Springer Berlin Heidelberg, 2014.

147. D. Cimen and T. Caykara, *Polymer Chemistry*, 2015, **6**, 6812-6818.

148. M. Dübner, N. D. Spencer and C. Padeste, *Langmuir : the ACS journal of surfaces and colloids*, 2014, **30**, 14971-14981.

149. Z. Bao, M. L. Bruening and G. L. Baker, *Journal of the American Chemical Society*, 2006, **128**, 9056-9060.

150. M. R. Bryce, *Advanced materials*, 1999, **11**, 11-23.

151. S. Ahn, Y. Kim, S. Beak, S. Ishimoto, H. Enozawa, E. Isomura, M. Hasegawa, M. Iyoda and Y. Park, *Journal of Materials Chemistry*, 2010, **20**, 10817-10823.

152. M. B. Nielsen, C. Lomholt and J. Becher, *Chemical Society reviews*, 2000, **29**, 153-164.

153. E. Gomar-Nadal, J. Veciana, C. Rovira and D. B. Amabilino, *Advanced materials*, 2005, **17**, 2095-2098.

154. E. Gomar-Nadal, L. Mugica, J. Vidal-Gancedo, J. Casado, N. J.T.L., J. Veciana, C. Rovira and D. B. Amabilino, *Macromolecules*, 2007, 7521-7531.

155. S. Inagi, K. Naka and Y. Chujo, *Journal of Materials Chemistry*, 2007, **17**, 4122.

156. T. Yasuda, T. Imase, Y. Nakamura and T. Yamamoto, *Macromolecules*, 2005, **38**, 4687-4697.

157. K. Zhang, S. Liu, X. Guan, C. Duan, J. Zhang, C. Zhong, L. Wang, F. Huang and Y. Cao, *Science China Chemistry*, 2012, **55**, 766-771.

158. D. Broer, G. P. Crawford and S. Zumer, *Cross-Linked Liquid Crystalline Systems: From Rigid Polymer Networks to Elastomers*, CRC Press, 2011.

159. I. McCulloch, M. Heeney, C. Bailey, K. Genevicius, I. MacDonald, M. Shkunov, D. Sparrowe, S. Tierney, R. Wagner, W. Zhang, M. L. Chabinyc, R. J. Kline, M. D. McGehee and M. F. Toney, *Nature materials*, 2006, **5**, 328-333.

160. L. D. McIntosh, M. W. Schulze, M. T. Irwin, M. A. Hillmyer and T. P. Lodge, *Macromolecules*, 2015, **48**, 1418-1428.

161. C. M. Bates, A. B. Chang, N. Momčilović, S. C. Jones and R. H. Grubbs, *Macromolecules*, 2015, **48**, 4967-4973.

162. G. Jo, H. Jeon and M. J. Park, *ACS Macro Letters*, 2015, **4**, 225-230.

CHAPTER 2

Functional Supramolecular Tetrathiafulvalene-Based Films with Mixed Valence States[*]

---

[*] Part of this chapter has been submitted in: Riba-Moliner M., Gómez-Rodríguez A., Amabilino D.B., Puigmartí-Luis J., González-Campo A., *Polymer,* submitted.

2.1. INTRODUCTION AND OBJECTIVES

The non-covalent functionalization of polymers via supramolecular chemistry is a potentially efficient route to introduce a particular property with which a new functional molecular material can be originated. Functional polymers can be described as one class of molecular materials where function can be achieved through the incorporation of active side-groups and provide particular properties to the final construct.[1] Interestingly, the incorporation of conjugated structures in polymeric constructs has been already exploited to synthesize new semiconducting materials that have found application in many fields including photovoltaics.[2, 3] Although important advances have been made in this field, the incorporation of π-electron functional units to polymeric backbones with well-controlled arrangement between the donor and acceptor parts is still an area of huge interest for material science. In this regard, the incorporation of hydrogen bond donating or accepting site groups has allowed the formation of new polymeric supramolecular assemblies through hydrogen-bonding interactions. The principles of this kind of approach have been laid for some systems, notably containing pyridine as the hydrogen bond acceptor.[4-6]

On the other hand, polymers have also been used as templates to control the nucleation/crystallization of organic compounds, for the preparation of functional structures with applications in semiconductors or energy conversion.[7-11] The major challenge is the control of the nucleation and growth processes and consequently, can get 'tailor-made' crystals of the desired compound. Bottom-up crystallization strategies enabling the direct growth of nanocrystal assemblies have been established, such as the addition of specific additives.[12-16] Many studies in this way have been performed based them on vapor-grown single crystals due to the better charge carrier mobility of the resulting materials.[9] Nevertheless, important advances in growing crystals of organic semiconductors from thin film solutions have been pursued.[17-20] Therefore, polymers offer the possibility to tune their natural alignment of the macromolecular chains and provide functional groups in where

semiconducting molecules with self-assembly properties can be anchored and growth.

Poly(4-vinyl pyridine) (P4VP) has become a widely used polymer to prepare new functionalized hybrids. Sugiyama and Kamogawa demonstrated that the basic character of the nitrogen atom present in the pyridyl unit can be advantageously used for the formation of charge-transfer complexes quinone and P4VP.[21, 22] P4VP is obtained from the polymerization of the monomer 4-vinyl pyridine (Fig. 2.1) and is commonly used as a copolymer, covalently bonded to other homopolymers such as poly(methyl methacrylate) (PMMA) for photolithography applications, or poly(styrene) for pH responsive materials.[23, 24]
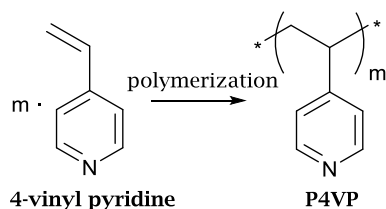
Fig. 2.1 *Preparation of P4VP from its monomer.*

The nitrogen atom in P4VP provides an anchoring point where various compounds can be incorporated with the objective to add functionality to the final polymeric construct. There are many studies in the functionalization of the P4VP driven by hydrogen bonding.[4, 22, 25] Furthermore, this strategy has become important to prepare organic semiconductor-based films with a control of the nanoscopic assembly of the organic molecules and to obtain charge mobility within the film. Slough and co-workers found a variation in the conductivity of donor polymers with the incorporation oligothiophene organic semiconductors to P4VP to obtain an uniform film that can be used as *p*-type semiconductor using solution processing.[26] Very recently, a complex between P4VP and a derivative of the rylenebisimides family (used as an electron accepting component) also permitted the formation of a material with charge transport properties similar to those of the acceptor alone,

proving the promise of this approach for the preparation of n-type organic semiconductors.[27]

In this chapter, the combination of P4VP with an electron donating unit based on a tetrathiafulvalene (TTF) moiety is presented. Tetrathiafulvalenes (TTFs) are excellent π-electron donor units that are widely studied in molecular electronic applications due to their *p*-type character and stable doped states.[28, 29] As electron-donor species, TTFs can be oxidized reversibly under their exposure to an appropriate oxidant. Three oxidization states are present in TTFs, the neutral TTF (TTF⁰), which exists under ambient conditions, the cation-radical (TTF⁺·) and the dication (TTF²⁺) state that are prepared by chemical or electrochemical oxidation of the neutral compounds. The three states can be accessed and controlled sequentially through one electron processes. Furthermore, TTF derivatives can form highly ordered mono- or bi-dimensional stacks through $\pi - \pi$ interactions between the planar core as well as through side-by-side sulfur-sulfur interactions between the neighbouring TTF units (Fig. 2.2).[30, 31]
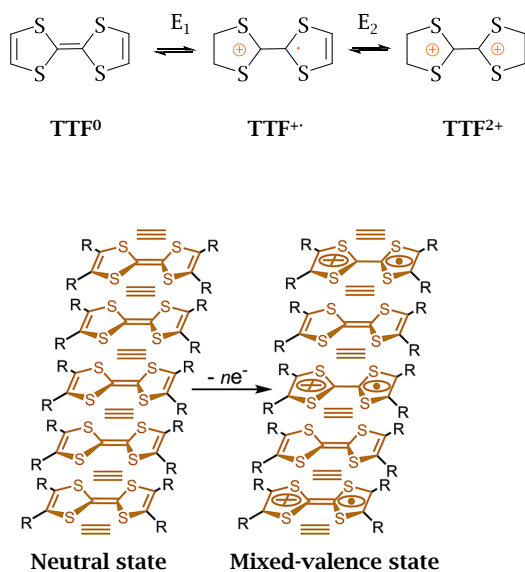
Fig. 2.2 *Reversible oxidation states of TTFs, neutral (TTF⁰), cation-radical (TTF⁺) and dication (TTF²⁺) adjacent to representations of self-assembled stacks of neutral and mixed valence state of TTFs. For unsubstituted TTF, $E_1^{1/2}$ = +0.34 V and $E_2^{1/2}$ = +0.78 V, vs. Ag/AgCl in acetonitrile.[32]*

The intermolecular π-π interactions together with sulfur-sulfur interactions facilitate the stabilization of TTF dimers, ordered stacks or even 2-D sheets.[32] Therefore, combining TTFs or its derivatives with proper acceptors it is possible to prepare an intramolecular charge-transfer system.[32] Among a large family of acceptors, the more used are the ones which include subunits like tetracyano-*p*-quinodimethane, quinones, electron-deficient aryl groups, pyridinium and bipyridinium units, fullerenes, phthalocyanines and mesomerically conjugated carbonyl, thiocarbonyl, ester and related groups.[32] Thus, TTFs and its derivatives have been largely exploited and used as salts with conducting and superconducting properties,[33] ferromagnetic compounds,[34, 35] synthetic intermediates in organic chemistry,[36, 37] as donor moieties in intramolecular donor-acceptor systems for nonlinear optic materials,[38] in liquid crystalline materials,[39-41] Langmuir-Blodgett films[42, 43] and organic semiconductors.[44, 45]

The ability to control the self-assembly of TTF derivatives and to obtain supramolecular assemblies for conductive materials have attracted wide attention in materials field. Cai and coworkers took advantage of the self-assembly through π-π interactions of TTFs to build 2-D covalent organic frameworks (COFs) with conducting properties.[46] For instance, Yokota *et al.*, embedded thiol-terminated TTFs into a *n*-alkanethiol matrix and observed how strong was the influence of the intermolecular electronic coupling of them by applying different bias values.[47] The capacity of TTF derivatives to generate mixed-valence states by UV-irradiation in polymer matrices of PMMA containing a photo-induced acid generator has also been studied by Tanaka *et al.*, showing the regulation of TTF electronic states by photo-reaction in TTF-based polymeric films.[48] Recently, the same authors have also synthesized TTF-tethered polymeric films and demonstrated the conductivity of this material thanks to the formation of a TTF mixed-valence state generated after the oxidation of the TTF units.[49]

The continuous research and the desire to improve the efficiency of the current organic field-effect transistors (OFETs) systems, have also made TTFs and its derivatives simple and interesting compounds to explore in new polymeric organic charge-carrier systems.[50] Chujo *et al.*

implemented TTF-based polymer thin films using conventional polymers such as poly(methyl methacrylate) (PMMA), poly(styrene) (PS) and demonstrated the charge motion comparing them with a referential conductive polymer poly(3,4-ethylenedioxythiophene)-poly(styrene sulfonate) (PEDOT-PSS).[51] Guided in the same way and seizing the TTF capability to form individual fibers by π-stacking, Chujo and their collaborators explored the charge-transfer complexes of TTF fibers grown during film deposition.[52] In a further step, Chujo also could control selectively the different states of oxidation and the self-assembly of TTF contained in PMMA-based thin films.[48] Recently, they claimed a better dispersion of TTF nanofibers and the regulation of conductivity using TTF-tethered pendant-type polymers as supporting platform.[49] Gomar-Nadal *et al.* synthetized multifunctional poly(isocyanide) functionalized with (2,3-bis(dodecylthio)-6-(carboxy)tetrathiafulvalene) (TTFCOOH), which showed charge transfer properties *via* electron transport upon oxidation of TTF moieties.[53] Kobayashi *et al.* also studied the electron conduction of similar compounds and their salts.[54]

Here, the preparation and the study of a new supramolecular polymeric film generated by the incorporation of a TTF derivative (TTFCOOH) to P4VP are presented (Fig. 2.3). The TTFCOOH has been designed with a carboxylic acid group (-COOH), to allow hydrogen bond formation with the pyridyl groups of the P4VP, and with two long alkyl chains to ease solubility. As result of the interaction between TTFCOOH and P4VP, a new material is formed with unique synergistic functionalities and with a control of the TTFCOOH assembly (P4VP-TTFCOOH, Fig. 2.3). Finally, the P4VP has also been explored as 'specific additive' for a controllable TTFCOOH crystallization with the aim of obtaining a crystallized organic semiconducting material.
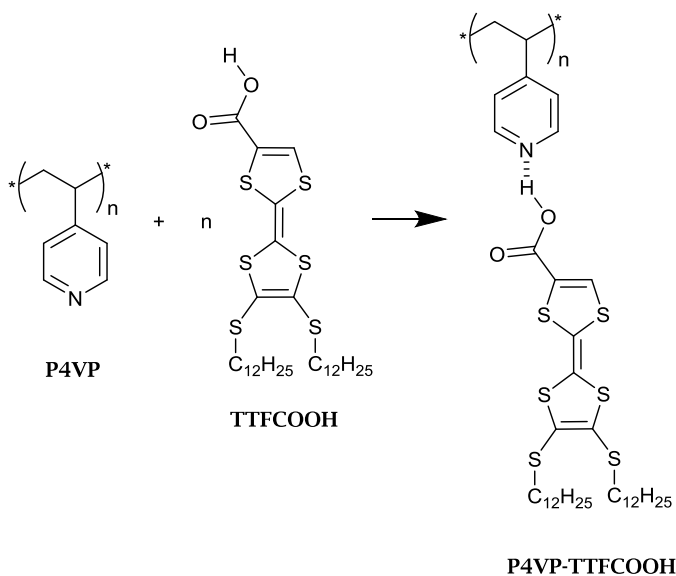
Fig. 2.3 *Formation of the P4VP-TTFCOOH complex through the hydrogen bond formation between P4VP and TTFCOOH.*

The properties of the P4VP-TTFCOOH composite material were studied by UV-Visible-Near-Infrared spectroscopy (UV-Vis-NIR), Fourier-Transform Near-Infrared spectroscopy (FTIR), Transmission Electron Microscopy (TEM), Scanning Electron Microscopy (SEM), Energy Dispersive X-ray (EDX), Electron Paramagnetic Resonance (EPR), and Scanning Probe Microscopy (SPM) techniques such as Electrostatic Force Microscopy (EFM). SPM techniques can provide information about the phase segregation of the constituent compounds present in the sample, the surface potential of the composite polymeric film, and further, can be employed to study the charge transportation in the film.[55] Additionally, the effect of doping the TTFCOOH in the P4VP its crystallization was studied and analyzed by optical microscope and SEM.

2.2.   RESULTS AND DISCUSSION

2.2.1.   Self- assembly of P4VP-TTFCOOH

The complexation between P4VP and TTFCOOH is generated through the hydrogen bond formation between the acid group of the TTFCOOH with the nitrogen atom of the pyridine rings present in the polymeric matrix (Fig. 2.3).[56-58] In order to ensure the complete supramolecular assembly of the TTFCOOH, solubility studies were performed in where chloroform was first identified as the most suitable solvent for the experiments because is an organic and non-polar solvent that dissolved both P4VP and TTFCOOH. In this way, chloroform-based solutions and thin films of the polymer with TTFCOOH were prepared and their properties were analyzed separately. To perform thin films of the polymeric complex, a first approach by drop-casting was carried out, even though spin-coating was the strategy finally followed because the higher homogeneity and reproducibility of the resulting P4VP-TTFCOOH films.

FTIR spectroscopy was first used to trace the formation of the P4VP-TTFCOOH complex following the shift of characteristic bands of the free pyridine ring located at 1596, 1413 and 993 cm^{-1} upon the non-covalent hydrogen bond interaction with TTFCOOH, (Fig. 2.4).[27, 59, 60] The FT-IR spectrum of P4VP-TTFCOOH films revealed a decrease of intensity and a shift of the bands located at 993 and 1596 cm^{-1} bands to 1030 and 1608 cm^{-1}, respectively, confirming the hydrogen bond between P4VP and TTFCOOH. It was not possible to trace the band at 1415 cm^{-1} due to the presence of a band around 1422 cm^{-1} for pure TTFCOOH in the same region. On the other hand, the disappearance of the C=O stretching vibration transmission band at 1663 cm^{-1} and the appearance of a new band at 1694 cm^{-1} was associated to the coordination of TTFCOOH moieties to the nitrogen atoms of the pyridine ring present in the polymer matrix. This change is typically related with systems having hydrogen bonds, providing further evidence that the assembly between the carboxylic acid group of TTFCOOH and the nitrogen atom of the pyridyl unit present in P4VP took place.[51, 59-61] The bands at 2920 and 2848 cm^{-1},

which appeared for TTFCOOH and P4VP, are associated to the v_{as}(C-H) and v_{sym}(C-H) of the alkyl chains of the hydrogen bonded composite film.
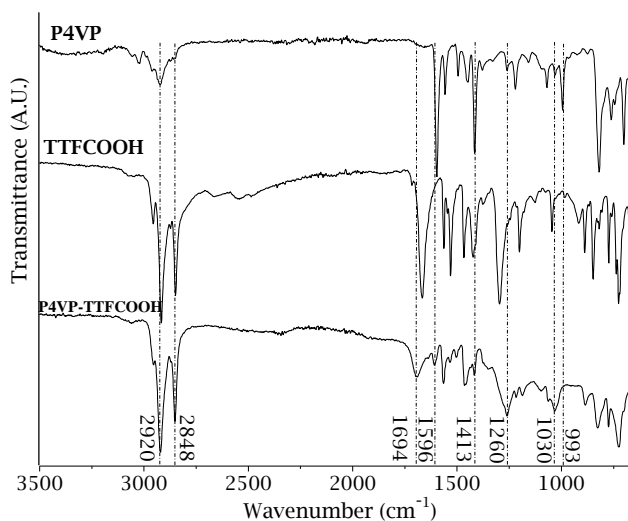
Fig. 2.4 *FT-IR spectra of P4VP, TTFCOOH and P4VP-TTFCOOH film.*

The formation of P4VP-TTFCOOH was also studied comparing the UV-visible absorption spectra obtained from drop-cast solutions of pure TTFCOOH and a mixture of poly(styrene) and TTFCOOH (PS+TTFCOOH) on quartz surfaces. The latest was studied as a control sample; in this case the non-covalent assembly between the carboxylic acid group of TTFCOOH molecules and the polymer matrix is avoided. As shown in Fig. 2.5, the broad peak at 510 nm for pure TTFCOOH and PS+TTFCOOH was associated to free and non-coordinated TTFCOOH moieties. Contrarily, the spectrum of P4VP-TTFCOOH films showed an absorption band at 416 nm, which was assigned to the non-covalent assembly of TTFCOOH molecules with P4VP and to their organization within the film. Another evidence of the non-covalent assembly of TTFCOOH molecules to the pyridyl units of P4VP was the slight shift of the band located at around 306 nm when compared to the pure TTFCOOH and PS+TTFCOOH samples.
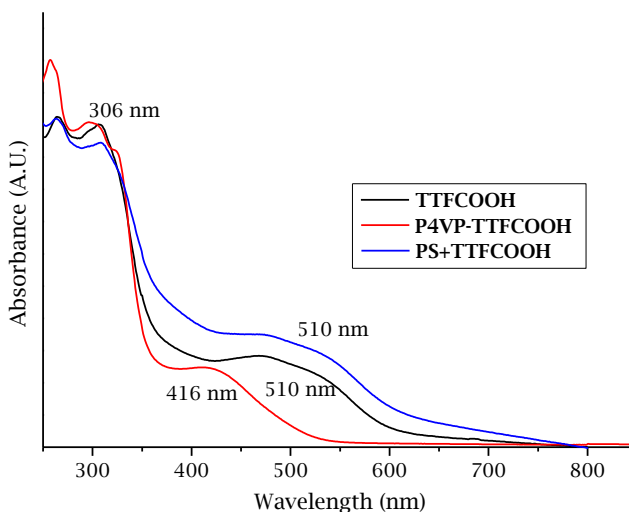
Fig. 2.5 *UV-visible absorption spectra of TTFCOOH, P4VP-TTFCOOH and PS+TTFCOOH drop-casted films. The solvent used to prepare the films was CHCl$_3$ in all the cases.*

The chemical resistance of P4VP-TTFCOOH films was studied at different pH values by UV-visible spectroscopy.[62] After immersing the films in the different solutions and varying the pH value, it could be concluded that the films are stable between $2 \leq pH \leq 10$. However, in strongly basic medium, a shift in the peak at 416 nm evidences a chemical change in the film construct. Concretely, at values above 9, a decrease of the band at 416 nm and an initial red-shift was observed, resulting in two isosbestic points at 349 and 433 nm, which undoubtedly indicated a modification of the film structure probably due to the deprotonation of the carboxyl group of TTFCOOH(Fig. 2.6).
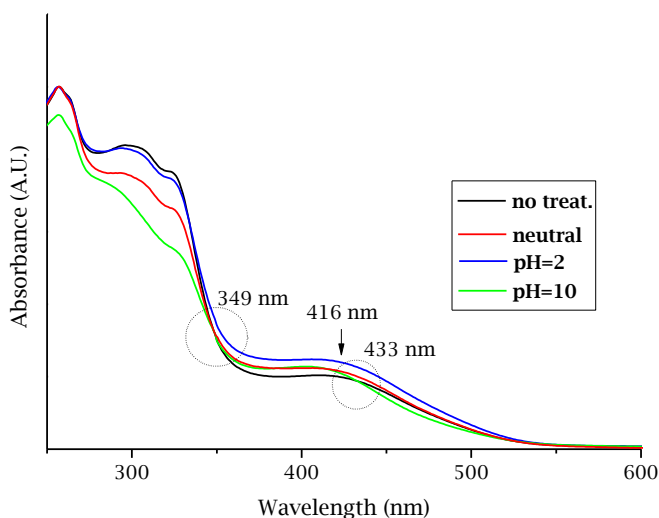
Fig. 2.6 *UV-visible absorption spectra of neat P4VP-TTFCOOH film (as "no treat."), and P4VP-TTFCOOH films after 10 minutes of immersion separately in neutral (pH=7), acid (pH=2) and basic (pH=10) solutions. Films were prepared by drop-casting on quartz surfaces. The direction of the arrow indicates increase/decrease or shift of the signal.*

2.2.2. Doping and film oxidation

Previously, our group has demonstrated that materials based on TTF derivatives can be oxidized (doped) easily under certain conditions.[53, 63] Solutions of different oxidizing agents such as $HAuCl_4$ and $Fe(ClO_4)_3$ in $CHCl_3$ were added to dilute solutions of P4VP-TTFCOOH to study and elucidate the possible effects of oxidation of the TTFCOOH in the chemical and physical properties of the hydrogen bonded composite films.

The doping processes were first studied in solution and followed by UV-Vis-NIR absorption spectroscopy after the successive addition of oxidants (Fig. 2.7). During the oxidation process with $HAuCl_4$ a change in the colour of P4VP-TTFCOOH solutions was observed, which was an indication that the TTFCOOH was oxidized from the neutral state (light orange), passing through the cation-radical (greenish), and to the dication state (intense blue) (Fig. 2.7).[63]
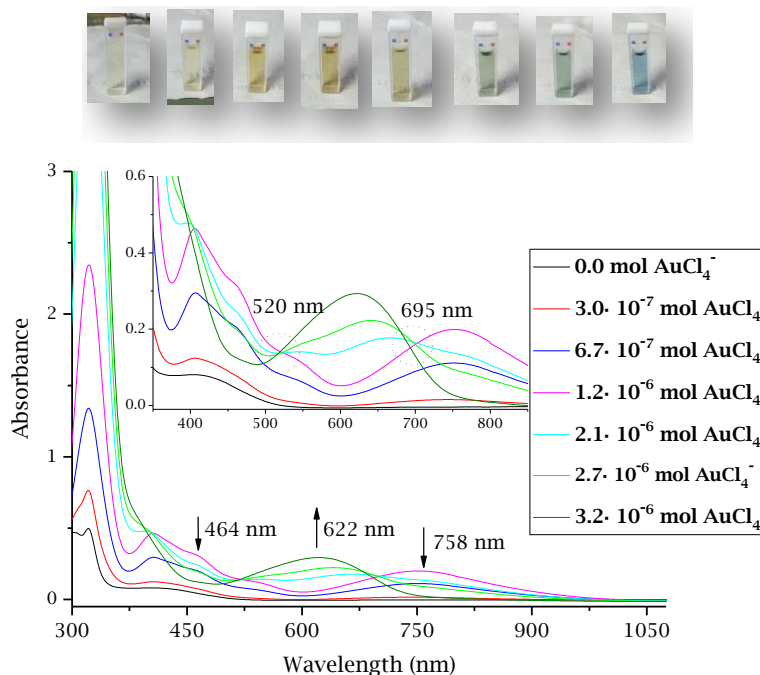
Fig. 2.7 *On the top, colour evolution of P4VP-TTFCOOH solution by adding HAuCl₄. The oxidation states started from P4VP-TTFCOOH⁰, passed through P4VP-TTFCOOH⁺˙ and form P4VP-TTFCOOH²⁺ (from the left to the right). On the bottom, UV-Vis-NIR absorption spectra showing the evolution of the TTFCOOH oxidation as P4VP-TTFCOOH complex in solution with HAuCl₄. The direction of the arrows indicates increase/decrease or shift of the signals.*

UV-Vis-NIR absorption spectra revealed that it is possible to oxidize the TTFCOOH molecules to the dicationic state (TTF^{2+}) in the polymeric composite supramolecular system with both oxidants, $HAuCl_4$ and $Fe(ClO_4)_3$ (Fig. 2.7 and Fig. 2.8). The band at approximately 413-423 nm was attributed to TTF^0, when no doping agent was added. After several additions of $HAuCl_4$, the TTF^0 band progressively decreased due to the formation of $TTF^{+\cdot}$ species until its total vanishing.[53] Then, a shoulder appeared at 464 nm (437 nm in the case of $Fe(ClO_4)_3$ doping), which indicated the formation of free cation radicals ($TTF^{+\cdot}$) reaching its maximum value at $1.2 \cdot 10^{-6}$ mol of doping agent. At the same point of the doping process, the maximum of the peak at 758 nm was reached, attributed to the formation of π-dimers between cation-radical TTFs in solution (744 nm in the case of $Fe(ClO_4)_3$ doping process). This band was subsequently replaced by a band at 622 nm upon further doping, which is

characteristic of the formation of TTF^{2+} during the doping process (with $Fe(ClO_4)_3$ as oxidizing agent a slight shoulder at 546 nm also appeared). Moreover, isosbestic points at 520 and 695 nm were observed, in the absorption spectra resulting from doping with $HAuCl_4$ (618 and 917 nm in the case of $Fe(ClO_4)_3$ doping), which indicated that a clear change in the doped species was produced, *i.e.* TTFs were fully oxidized to TTF^{2+}.[53]
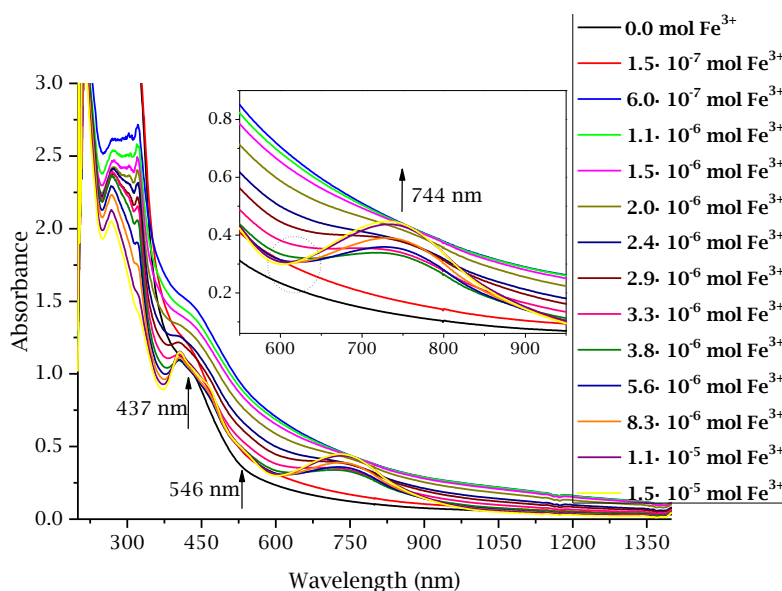
Fig. 2.8 *UV-Vis-NIR absorption spectra of the oxidation process of a P4VP-TTFCOOH solution in $CHCl_3$ with $Fe(ClO_4)_3$ in $CHCl_3$. The direction of the arrows indicates increase/decrease or shift of the signals.*

Once the capacity to oxidize the TTF residues in the P4VP-TTFCOOH solutions was confirmed, same studies in solid state were performed to produce doped polymeric thin films. The oxidation of films was also followed with UV-Vis-NIR absorption spectroscopy using $HAuCl_4$, $Fe(ClO_4)_3$ as well as I_2 vapors as doping and/or oxidizing agents. In this case, the oxidizing agents were dissolved in MilliQ water (except I_2) to ensure the stability of the films. The oxidation process consisted on dipping the films in a solution containing the oxidant in molar ratio of TTFCOOH:oxidizing agent 25:1 for 10 minutes and then rinsing them in a ultrapure water bath for 10 additional minutes. During the oxidation process and because films were not porous (vide infra), co-existence of all

three oxidation states of the TTF units was demonstrated depending on the proximity of TTFCOOH molecules to the oxidant solution or to the substrate. After doping P4VP-TTFCOOH films with $HAuCl_4$ (Fig. 2.9), the absorption band at 423 nm associated to TTF^0 disappeared while another band at 651 nm appeared after the first doping cycle, which is related with the formation of $TTF^{+\cdot}$ in the polymeric film. Moreover, an absorption shoulder was observed between 816 and 1120 nm, which was associated to the formation of a charge transfer band due to the charge mobility between TTF^0 and $TTF^{+\cdot}$ states, as previously reported by our group.[64]
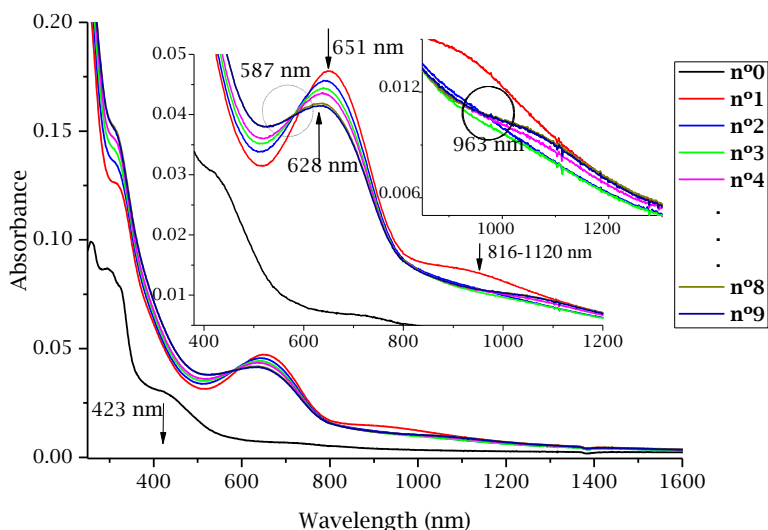
Fig. 2.9 *UV-Vis-NIR absorption spectra of the evolution of the oxidation of the P4VP-TTFCOOH film on quartz after each doping cycle with $HAuCl_4$ (aq). The numbers of the legend correspond to the number of doping cycles, where 0 is the neat film without treatment. The direction of the arrows indicates increase/decrease or shift of the signals.*

Therefore, P4VP-TTFCOOH films can induce the assembly of partially oxidized TTF stacks, thanks to the hydrogen bonding formation.[65] In additional doping cycles, the $TTF^{+\cdot}$ band was shifted slightly to a high energy (absorption maximum at 628 nm) and with slightly less intensity, suggesting the formation of TTF^{2+} species, which absorb in that region. An isosbestic point at 587 nm indicated a change from $TTF^{+\cdot}$ states to TTF^{2+}. However, the completely formation of TTF^{2+} could not be reached fully in the film, even after prolonged exposure to the $HAuCl_4$ doping solution.

Although a weak charge transfer absorption band could be observed (816 and 1120 nm) for the first cycle, a more intense band at 963 nm was observed after the fourth cycle. The appearance of this charge transfer absorption band at lower energy indicated that high charge mobility could be reached between TTF^0-$TTF^{+\cdot}$ units after the first doping cycle. After the fourth cycle (probably because of the presence of intermediate states such as $TTF^{+\cdot}$-TTF^{2+} and other monomers) charge mobility was not favorable. [65, 66] The charge transfer band was observed at 892 and 948 nm when the film was doped with $Fe(ClO_4)_3$ (Fig. 2.10) and I_2 vapors (Fig. 2.11), respectively. Therefore, it was possible to reach the same oxidized state with all the doping agents studied under these conditions.[66]
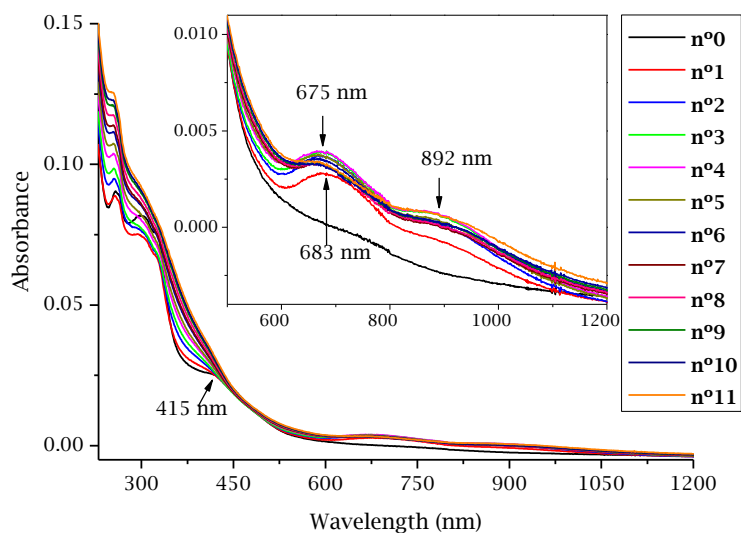
Fig. 2.10 *UV-Vis-NIR absorption spectra of the oxidation cycles of a P4VP-TTFCOOH film generated by its immersion in an aqueous solution of $Fe(ClO_4)_3$ (in the legend, each number after "nº" means the number of immersions). The direction of the arrows indicates increase/decrease or shift of the signals.*
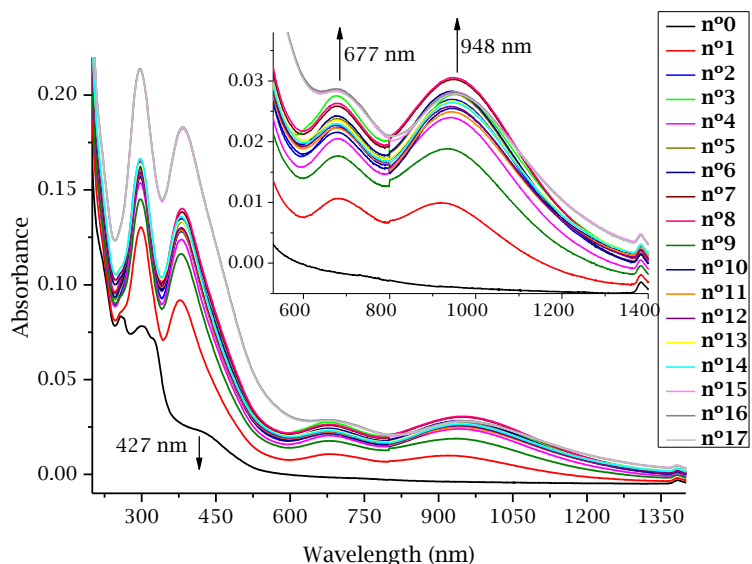
Fig. 2.11 *UV-Vis-NIR absorption spectra of the oxidation cycles of a P4VP-TTFCOOH film generated by its exposure to I_2 vapors (in the legend, each number after "nº" means the number of expositions to I_2 vapors). The direction of the arrows indicates increase/decrease or shift of the signals.*

Once the capacity of the TTF units of the P4VP-TTFCOOH films to be oxidized was proved using different doping agents, the reversibility of the oxidation process for P4VP-TTFCOOH solution and film was also studied. With this aim, firstly a doped TTFCOOH^{2+} solution of P4VP-TTFCOOH with HAuCl$_4$, was reduced. Sequential additions of trimethylamine (TEA) in acetonitrile at stoichiometric concentration to the TTFs present in P4VP-TTFCOOH hybrid state solution were added, in order to reach the completely neutral state TTF^0. The dedoping process evolution followed by UV-Vis-NIR spectroscopy illustrated the decreasing of the absorption signal, at 667 and 902 nm, associated to the mixed valence state TTF$^{+\cdot}$-TTF^{2+} and charge transfer band, respectively (Fig. 2.12). The charge transfer band disappeared practically from cycle nº9 and the mixed valence state still remained indicating that the P4VP-TTFCOOH could be only partially reduced.
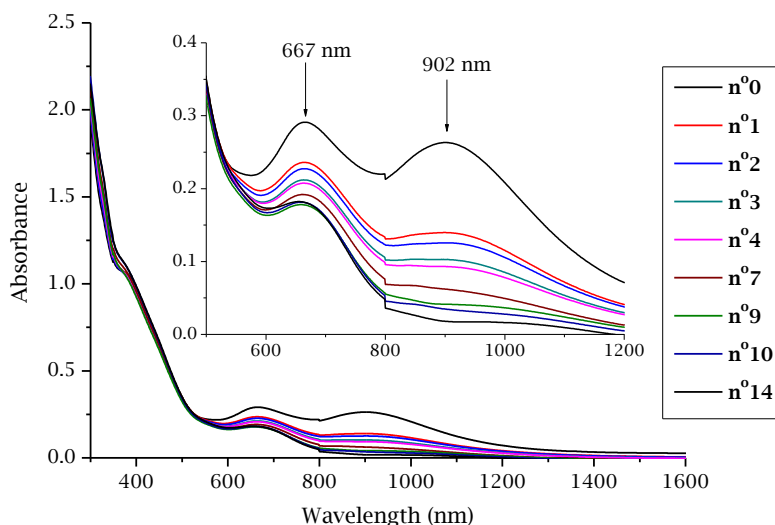
Fig. 2.12 *UV-Vis-NIR absorption spectra of the evolution of the dedoping process performed by immersion P4VP-TTFCOOH in TEA solution (in the legend, each number after "nº" means the number of immersions). The direction of the arrows indicates increase/decrease or shift of the signals.*

Concurrently, dedoping process was also performed for a $HAuCl_4$ doped P4VP-TTFCOOH film by immersions of 10 minutes in a TEA aqueous solution. The TEA concentration was stoichiometrically calculated according to TTF units present in the P4VP-TTFCOOH hybrid film. After each immersion, film was washed in an ultrapure water bath for 10 additional minutes to eliminate the film adsorbates. The evolution of the dedoping process was followed by UV-Vis-NIR absorption spectroscopy (Fig. 2.13), corroborating that the doped P4VP-TTFCOOH film could be reduced from oxidized dication $TTFCOOH^{2+}$ to the mixed valence $TTFCOOH^0$-$TTFCOOH^+$ state. The spectrum of the doped P4VP-TTFCOOH film showed an absorption peak at 619 nm associated to the $TTFCOOH^{2+}$ state, and was established as starting state of the film in the dedoping process. In subsequent immersions of the P4VP-TTFCOOH film in TEA solution, the progressively reduction of the $TTFCOOH^{2+}$ units in the polymeric hybrid was observed by the appearance of the bands at 415 and 440 nm. The appearance of these bands indicated the presence of the $TTFCOOH^{+\cdot}$-$TTFCOOH^{2+}$ and $TTFCOOH^0$-$TTFCOOH^{+\cdot}$, respectively. Then, some neutralized $TTFCOOH^0$ units were obtained, although the

simultaneously absorption signal at 524 nm, suggested that in film, the completely neutral state could not be reached.
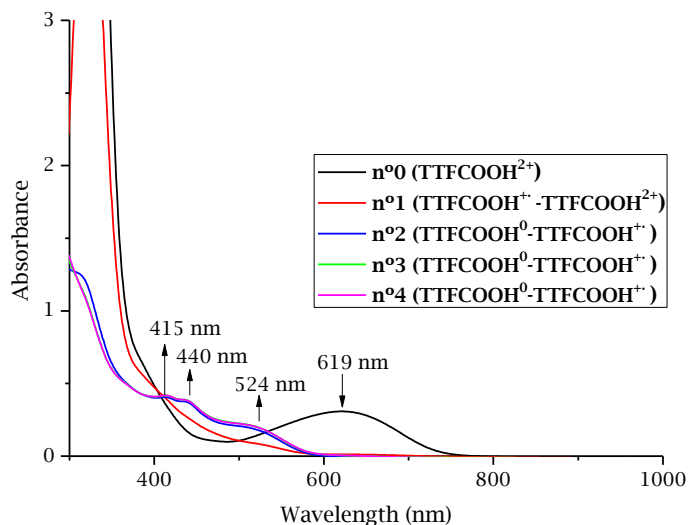
Fig. 2.13 *UV-Vis-NIR absorption spectra of the evolution of the TTFCOOH oxidized states in a P4VP-TTFCOOH film after immersion in TEA solution (in the legend, each number after "nº" means the number of immersions). The direction of the arrows indicates increase/decrease or shift of the signals.*

P4VP-TTFCOOH films doped with $HAuCl_4$, $Fe(ClO_4)_3$, and I_2 vapors were also measured by FT-IR-NIR spectroscopy (Fig. 2.14). A broad charge-transfer band appeared from 5000 to 2000 cm^{-1}, upon oxidation of the film with any of the agents, which was in concordance with previously reported systems.[48] In addition, we also observed a decrease of the transmittance signal that is assigned to the charge transfer between radicals and neutral TTF moieties. It should be noted that these results are in good agreement with the previous charge transfer bands observed by other UV-visible absorption studies.[61, 66-71] Kimura and Cooke *et al.* observed the appearance of a new band at the region 1340-1348 cm^{-1}, that they associated with the coupling of a conduction electron with the vibrational mode of the TTF moiety (electronic-molecular vibration coupling).[69, 72] The C-N stretching bands of the pyridine were observed at 1351 cm^{-1} in the undoped film, at 1336 cm^{-1} in the film doped with $HAuCl_4$, at 1388 cm^{-1} in the film doped with $Fe(ClO_4)_3$ and at 1351 cm^{-1} in the film doped with I_2. These little deviations in the ν(C-N) bands are probably

related with the orientation of the internal macromolecules when the samples were drop-casted on KBr pellets. According to Mulliken, charge-transfer forces could be related with the orientation and symmetry of the atoms, as well as with the compression applied. This phenomenon can also have a relatively important effect when the samples were doped, affecting the doping grade reached and producing non-desired light scatter effects. Moreover, this could explain the deviations observed in FTIR spectra that had slight differences non-related with molecular bond vibrations.[73]
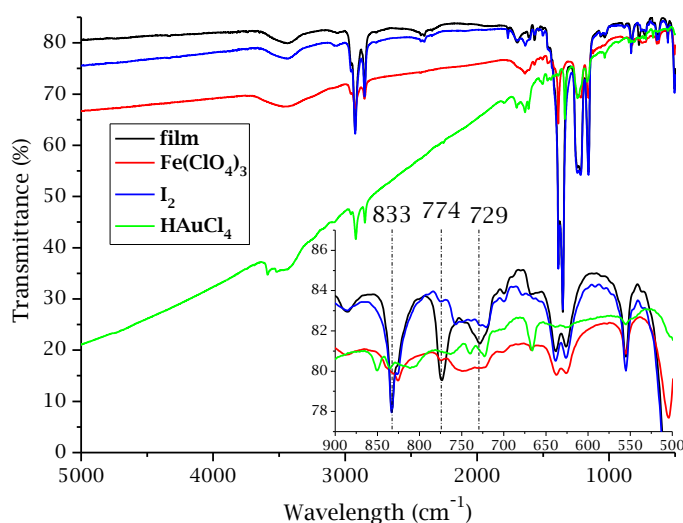
Fig. 2.14 *FT-IR-NIR spectra of P4VP-TTFCOOH films: non-oxidized, and oxidized with Fe(ClO$_4$)$_3$ (aq), I$_2$ vapors and HAuCl$_4$ (aq). Samples were prepared by drop-casting solutions on KBr pellets.*

In the fingerprint region of the FT-IR spectra, the absorption band at 833 cm^{-1} disappeared while the bands at 774 cm^{-1} and 729 cm^{-1} slightly decreased and shifted to 724 cm^{-1}, after the doping process of the film using Fe(ClO$_4$)$_3$ and HAuCl$_4$. According to Bozio *et al.*, this change could be attributed to the changes in the polarization and the symmetry of the TTF moieties.[61] In the case of doping with I$_2$ vapors, only the disappearance of the band present at 774 cm^{-1} was observed, which may imply a partial polarization of those moieties following the same reasoning. Given that the P4VP was not expected to be a rigid skeleton and a non-evident lamellar structure, the charge transfer bands were most likely to arise

from relatively local oligomers in which neutral and cation radical TTF moieties came into close contact. Finally, after all the UV-Vis-NIR and FTIR experiments, in Fig. 2.15 a proposed assembled and the mixed valence P4VP-TTFCOOH⁰-TTFCOOH⁻ are presented. The possibility to reach this intermediated state with different doping agents allowed us to study the charge transfer of this polymeric composite in the form of thin films. It is very important to notice that even though studies have been conducted in solution, feasibility of processing this composite material from the liquid state to a thin solid film is required for further technological applications.
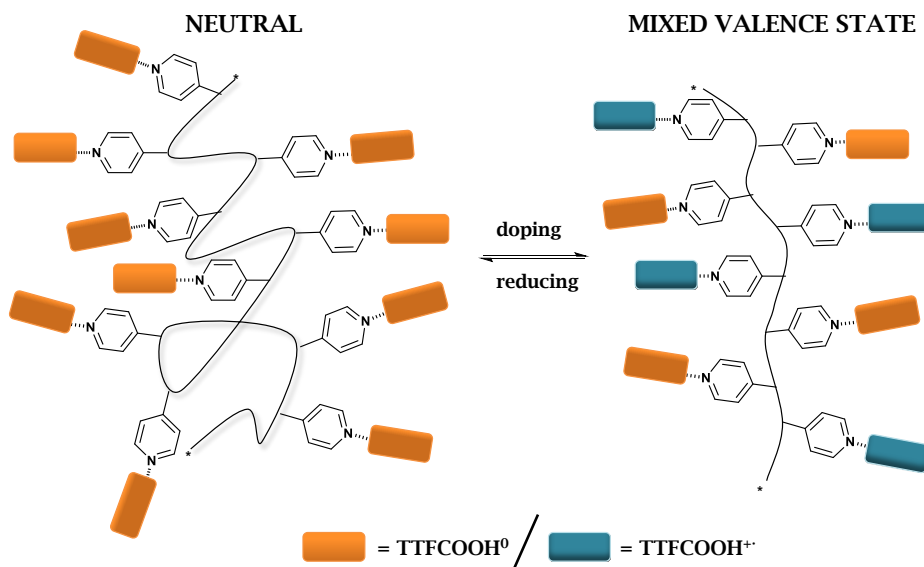
Fig. 2.15 *Representation of P4VP-TTFCOOH⁰-P4VP-TTFCOOH⁻ mixed valence state after the doping process.*

2.2.3. Film characterization

For the consistency in this investigation, an important parameter to be controlled in the preparation of P4VP-TTFCOOH films was the thickness of the samples generated. Indeed, homogeneity and reproducibility of the preparation method were studied in detail employing ellipsometry measurements. Moreover, for Electrostatic Force Microscopy (EFM) experiments a maximum thickness of the film samples was also necessary to avoid artifacts during measurements. The

ellipsometry studies were conducted on different samples: neat spin-coated films, the same films after doping with $HAuCl_4$ (aq), and spin-coated pre-oxidized solutions (the latter to create oxidized films with no need for further treatment). The thickness values were 30.6±0.4, 38.2±0.3 and 35.3±0.4 nm, respectively. Variations in the thickness of the undoped and doped films could be a result of different factors such as the incorporation of chloride ions to compensate the charge of TTF cation radical, the reduction of part of the Au^{3+} to Au^0 and the incorporation of the metal into the film, as well as, due to a slight swelling of P4VP in aqueous media.

The properties of compounds in solution can differ greatly with respect to when they are deposited on a surface due to the influence of the proximity of neighbouring chains and compound-substrate interactions.[74, 75] In the present case and according to the previous results obtained, undoped and doped P4VP-TTFCOOH solutions could have slight differences in the packing of the macromolecular chain and these, might be translated in changes in compound-substrate interactions. Then, order to study the surface tension of undoped and doped P4VP-TTFCOOH mixtures and their adhesion to different surfaces static contact angle (sessile drop) measurements were performed. Solutions of undoped P4VP-TTFCOOH in $CHCl_3$, at the same concentration used in previous UV-Vis-NIR characterization experiments, and $Fe(ClO_4)_3$ doped P4VP-TTFCOOH solutions were prepared and analysed (Table 2.1). The $Fe(ClO_4)_3$ doping agent was taken as reference, as the similar behaviour of the oxidized films observed during doping processes in the UV-Vis-NIR absorption spectra with other oxidants. Additionally, to approach the degree of hydrophobicity of the undoped and doped solutions by compound-surface interactions, quartz and graphite surfaces were used. Due the nature of the quartz and the possibility to be easily activated with piranha solution, the two scenarios of quartz with and without piranha activation (immersion for 45 minutes, sequentially rinsed with ultrapure water and dried with N_2 flow) are presented in Table 2.1. Contact angle values were very variable for undoped P4VP-TTFCOOH solution on quartz depending on whether the surface was activated with piranha. Concretely, the collected values were of 8.55º in front of 17.23º for undoped and doped

P4VP-TTFCOOH, respectively, can be correlated with the increase of the hydrophobicity or less interaction of P4VP-TTFCOOH with the surface due to the activation. The measured angle in the interface polymeric solution-graphite was of 17.33°, a value practically identical to the activated quartz, emphasizing the low interaction with the hydrophobic surface. On the other hand, analysing doped P4VP-TTFCOOH, the obtained values resulting from the angle of the drop at the interface polymeric solution-quartz, did not differed between no activated and activated quartz. The resulting 16.88° in both cases and, at the same time being this very similar to the more hydrophobic situations in the undoped solution, was correlated with the increasing tendency of doped TTF to self-arrange and consequently, the system resulted more packed. In the test on graphite, the tendency of the obtained angles was different respect to the undoped situation, obtaining and angle of 12.87° due to an unexpected higher interaction compound-surface. This might also be related with the conducting nature of the graphite surface and the charge movement between doped TTF units that finally increases their attraction.

	Table 2.1	Static contact angle (sessile drop) results.	
	Quartz		**Graphite**
	No activated	**Activated**	
Undoped	8.55°	17.23°	17.33°
Doped	16.88°	16.88°	12.87°
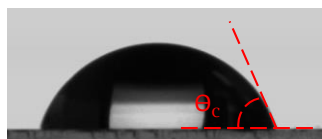
From the contact angle measurements, surface tension and density were also calculated. Surface tension and density results of undoped P4VP-TTFCOOH solution were 17.98 mN/m and 1.19 g/ml respectively, and the values for the doped homologous were 19.93 mN/m and 1.12 g/ml, respectively. Differences in the values were attributed to the oxidation state of TTFCOOH in the P4VP-TTFCOOH hybrid system, since the presence of ions Fe^{3+} in the doped solution and the probably TTFs in

the mixed valence TTFCOOH^0-TTFCOOH$^{+\cdot}$ state that tended to self-assembly in order to enhance the charge transportation along the created gaps. This could explain why undoped P4VP-TTFCOOH solution had lower values of surface tension respect to the doped state. By extension, the slightly lower value of density in the doped system was presumably attributed to the organization that P4VP-TTFCOOH hybrid experienced when was doped, diminishing in this way the 'degree of packing or meshing' given by the nature of the homopolymer by itself.

Towards the study of the homogeneity and the structure of P4VP-TTFCOOH films before and after doping, Transmission Electron Microscopy (TEM) measurements were used. As shown in Fig. 2.16, a uniform film was generated before doping. After doping, some branch-shaped structures grew in the film (Fig. 2.16), attributed to the reduction of Au^{3+} to Au^0.[76]
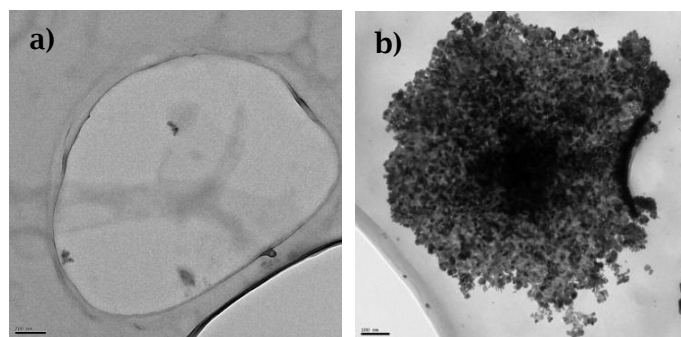
Fig. 2.16 TEM images of a) P4VP-TTFCOOH film; and b) the same film after doping with HAuCl$_4$ (scale bars are 200 and 100 nm, respectively), both on a holey carbon grid.

In order to confirm the nature of these branch-shaped structures, Scanning Electron Microscopy (SEM) and Energy-dispersive X-ray (EDX) spectroscopy studies were conducted on P4VP-TTFCOOH films doped with HAuCl$_4$ (aq). The corresponding SEM images and EDX analysis revealed a mixed composition of carbon, chlorine, nitrogen, oxygen, sulfur and gold, suggesting the formation of TTF-Au hybrid structures upon oxidation of TTFCOOH and the reduction of Au^{3+} (Fig. 2.17). Similar results had been previously reported in the literature; however the authors based their studies in solution and on stand-alone pure TTF molecules that resulted in

the formation of TTF-Au hybrid wires.[77, 78] In the present case, the presence of the polymer conditioned the resulting TTF-Au hybrid structures that self-assembled in a different fashion producing plate-like aggregates.
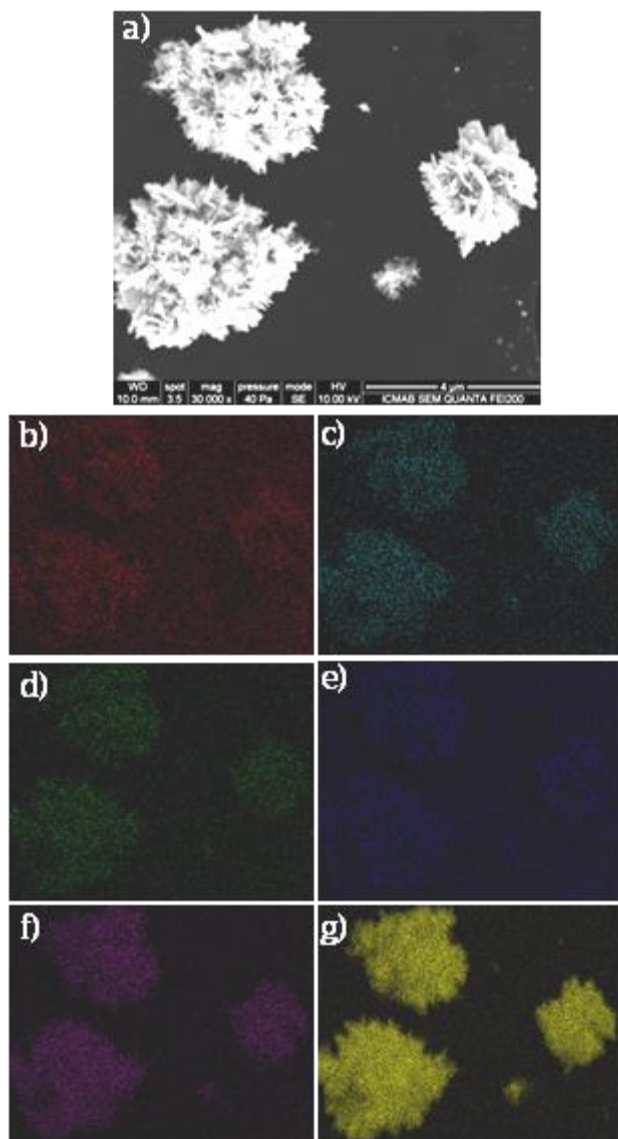
Fig. 2.17 *SEM and EDX analyses: a) SEM image of a P4VP-TTFCOOH film after doping with HAuCl$_4$ (scale bar 4 μm). From b) to g) the corresponding EDX mapping for b) carbon, c) chlorine, d) nitrogen, e) oxygen, f) sufur, and g) gold.*

After the chemical and structural characterization of P4VP-TTFCOOH in solution and solid state, Electrostatic Force Microscopy (EFM)

was used to demonstrate that TTF-based polymeric thin films could be used as charge transfer material upon doping. The EFM measurements were performed with a single-pass scan in which topographic and electrostatic measurements are obtained at the same time through different order modes.[79] With the aim of understanding the effect of the doping process on P4VP-TTFCOOH films, EFM measurements were performed on undoped P4VP-TTFCOOH films deposited onto graphite (HOPG) by spin-coating (Fig. 2.18) as well as HAuCl$_4$ (Fig. 2.20), Fe(ClO$_4$)$_3$ (Fig. 2.22) and I$_2$ doped P4VP-TTFCOOH films (Fig. 2.23). Firstly, EFM measurements were performed in undoped P4VP-TTFCOOH films (as-prepared). The collected images corresponding to the topography (Fig. 2.18a), amplitude (Fig. 2.18b), phase (Fig. 2.18c) and the corresponding absolute height profile for the undoped films (Fig. 2.18d) indicated that the films were homogeneous.
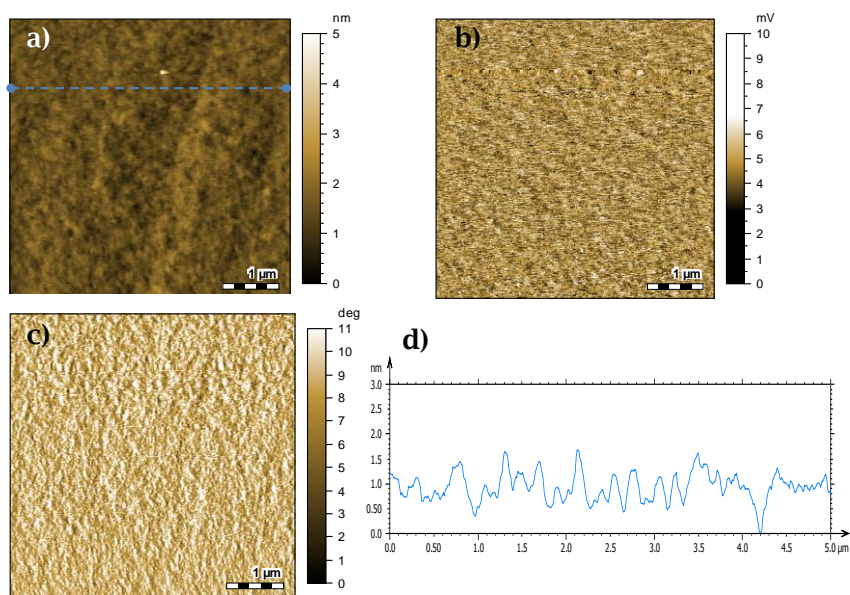
Fig. 2.18 EFM results of an undoped P4VP-TTFCOOH film; a) topography image; b) amplitude image; c) phase image; and d) topography profile.

To discard cross-talking signals as a result of the swelling of P4VP during the oxidation process, control experiments were performed using a spin-coated film of P4VP-TTFCOOH on HOPG. The film was then immersed in pure aqueous solution for 10 minutes, confirming that no changes were

appreciated by EFM, hence ensuring that future observations will result directly from the doped P4VP-TTFCOOH hybrid thin films (Fig. 2.19).
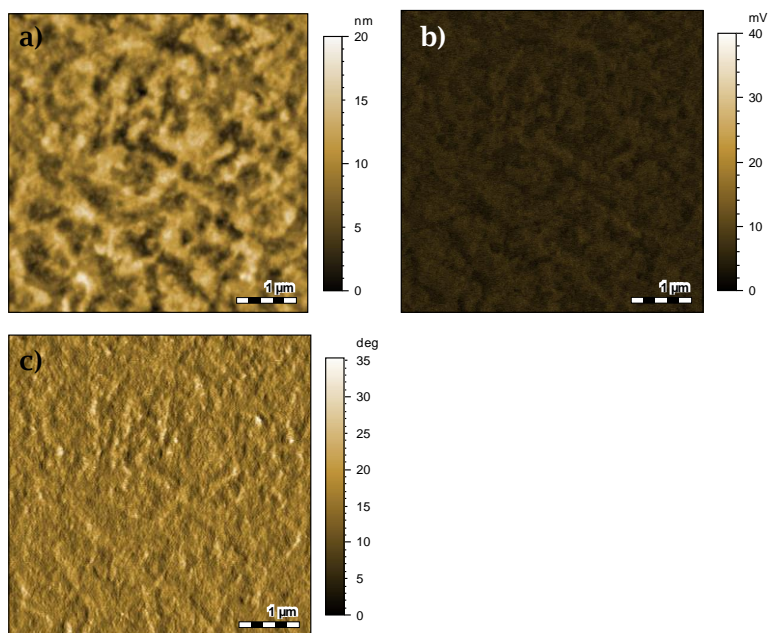
Fig. 2.19 *EFM results of a P4VP-TTFCOOH film after immersing it in an aqueous solution; a) topography image; b) amplitude image and, c) phase image.*

The effect of doping P4VP-TTFCOOH films with $HAuCl_4$ (aq) (Fig. 2.20) resulted in drastic changes of the topography, the phase and the amplitude response. The increase of the roughness that the topography depicted was attributed, on the one hand, to the tendency of TTFCOOH to self-assemble between their neighboring units, and on the other, to the non-negligible effect of the water, which did not affect the polymer by itself (according to EFM results depicted in Fig. 2.19) but did in the complex (Fig. 2.20 a-b).[80] The contribution of the aqueous solvent was palpable, apparently this medium allows the P4VP-TTFCOOH to conduct a redistribution of the forming parts due to both phenomena, on the one hand solvent polarity which had a preferentially interaction with polymeric parts and on the other, the tethered and doped pendant TTFCOOH units with tendency to self-assemble, thus leading this observed readjustment of matter on the thin film. In the amplitude response, the considerable contrast highlighted the self-assemble behavior between TTFCOOH[0] and TTFCOOH[-] units, suggesting a charge transportation

along the film. Under a certain electric field, a tunnel barrier effect was produced as a result of the charge transportation between TTFCOOH^0 and TTFCOOH$^{\cdot-}$ (Fig. 2.20c). Later on, this charge was accumulated, and reversibly tunnelled out when an opposite electric field was applied, recovering initial values. To corroborate that the topographic signal was not due to a result of cross-talking with the amplitude response, the amplitude profile was measured and compared with the topographic homologue (Fig. 2.20d) (the same onset and offset points as the height profile were taken). No correlation between the two profiles could be observed and therefore, no significant cross-talking was produced. A higher contrast was noticed in the first order phase (Fig. 2.20e), emphasizing the new organization of the film and distinguishing the different nature of the hybrid system.

The EFM technique allowed a complementary study of the relationship between tip bias and the amplitude. Plotting the curves of amplitude-tip bias is helpful to analyse qualitatively the amplitude response of the film to an applied voltage. Comparing the amplitude response curve from the HOPG and the undoped film (Fig. 2.20f), a completely different behaviour of the doped film was evident. The slope of the HOPG curve was ~20 times lower than the corresponding to the undoped film, mainly due to the different conductive response. This effect can be explained as result of the reduced conductivity of the surface due to the presence of a dielectric organic film on HOPG. The dark areas from the doped film had a lower slope (~2 times) than the bright areas from the same sample and approximately 10 times lower than the undoped film. Moreover, this slope was at least 2 times higher than that of the HOPG. Taking as a reference the HOPG curve, it could be proved that the dark areas of the doped film could behave as charge carriers when sufficient bias was applied to the sample. A shift in the tip bias values (corresponding to the minimum of amplitude) was also evident. Certainly this hysteresis depends, for instance, on the thickness of the film, on the type of bonding to the surface, on the chemical composition, and on the dielectric constant of the tunnel barrier.[81] However, the different shifts observed in the curves of the bright and dark areas in Fig. 2.20c respect to the centred position and slope of the curve of the undoped film,

suggested a relationship between the charge carrier character of the film under an electric field.[82-84] In the particular case of the curve of the bright area, a deviation of the amplitude at large biases was observed due to a mismatch in the output amplitude channel. Nevertheless, it was the only deviation observed in this sample.

Fig. 2.20 EFM results of a P4VP-TTFCOOH film after doping with HAuCl$_4$ (aq) as oxidant agent; a) topography image; b) height profile; c) amplitude image; (d) amplitude profile; e) phase image; f) amplitude vs. tip bias curves from HOPG, the undoped film and the film doped with HAuCl$_4$ (aq) (value following s is the calculated slope). For the same doped sample, values from the brighter and the darker areas were measured.

With the aim to corroborate the tunnel effect produced due to the charge transport in the dark areas of the doped P4VP-TTFCOOH film; several amplitude-tip bias curves (one after the other) were also collected at intervals of 1 second (Fig. 2.21). Effectively, a shift, an increasing of the

slope, and a progressive sharpening of the curves after the third bias sequentially applied could be observed. This observation implied that charge was accumulated on the surface of the film, induced by the bias applied between the tip and the conductive substrate. When a bias was applied sequentially, the charge was continuously accumulated in the area closest to the tip, until not enough time was given for the tunneling out of this charge or that the inverse voltage applied was not strong enough. After the third curve, no significant additional changes were observed. Comparing the shape and the position of last collected curve with the curves obtained from HOPG and the neat undoped films, we could conclude that the undoped films were clearly much less conductive than HOPG, while $HAuCl_4$ (aq) doped films presented some areas that have charge transportation.
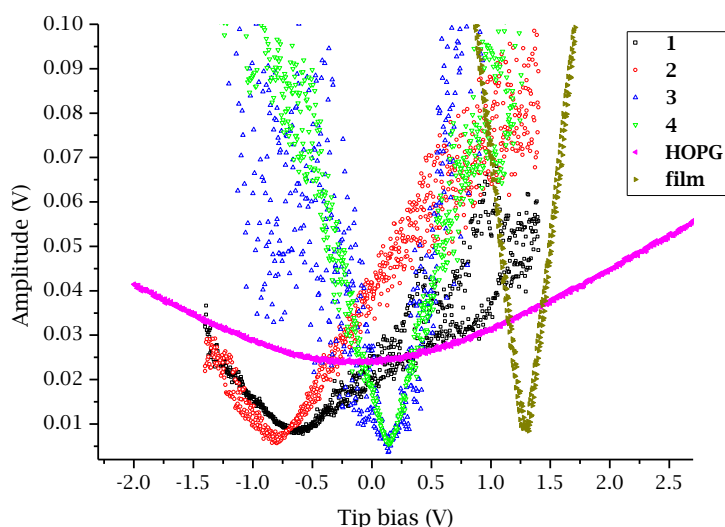
Fig. 2.21 *The tunnel barrier effect produced by the charge transport within a P4VP-TTFCOOH doped film with $HAuCl_4$ (aq).*

The same EFM studies were performed with films doped with the other oxidants, $Fe(ClO_4)_3$ (Fig. 2.22) and I_2 vapors (Fig. 2.23). After doping with $Fe(ClO_4)_3$ (aq), a significant change in the topography (roughness), as well as a dramatic change in the amplitude were observed (Fig. 2.22 a-c). The changes in the topography were related with the self-assembly of the doped pendant TTFCOOH units in order to favor the charge delocalization between $TTFCOOH^0$-$TTFCOOH^+$ pairs. Correlation between the height and

amplitude profiles (Fig. 2.22 b-d) could not be observed, similarly to Au^{3+} doped samples (Fig. 2.20 b-d), indicating as well that no cross-talking was obtained. On the other hand, the phase image agreed with the observed changes in roughness and amplitude. Observing the amplitude vs. tip bias curves for the film doped with $Fe(ClO_4)_3$ (Fig. 2.22f), the same tendency as found for Au^{3+} doped samples was observed but with less differences between the films before and after doping. The amplitude response of undoped films reached its minimum value at 0.105 V, whereas after doping, this value shifted approximately -0.500 V and the hysteresis of the minimum amplitude values between brighter and darker areas was of 0.120 V. These important observations in the hysteresis of the amplitude minimums and slight change of the slope of the curves, which followed the same reasoning process previously discussed for $HAuCl_4$ doped samples, proved that the results obtained were not isolated results and that are not an effect of the influence of the reduction of Au^{3+} to Au^{0}. Thus, certainly doped P4VP-TTFCOOH films can lead to materials with charge transport properties through the formation of packed $TTFCOOH^{0}$-$TTFCOOH^{+ \cdot}$ pairs. For $Fe(ClO_4)_3$ doped P4VP-TTFCOOH films, the absence of Fe^{3+} in the EDX spectra, upon doping of film, suggested that Fe^{3+} is reduced to Fe^{2+}, which stayed in the doping solution.
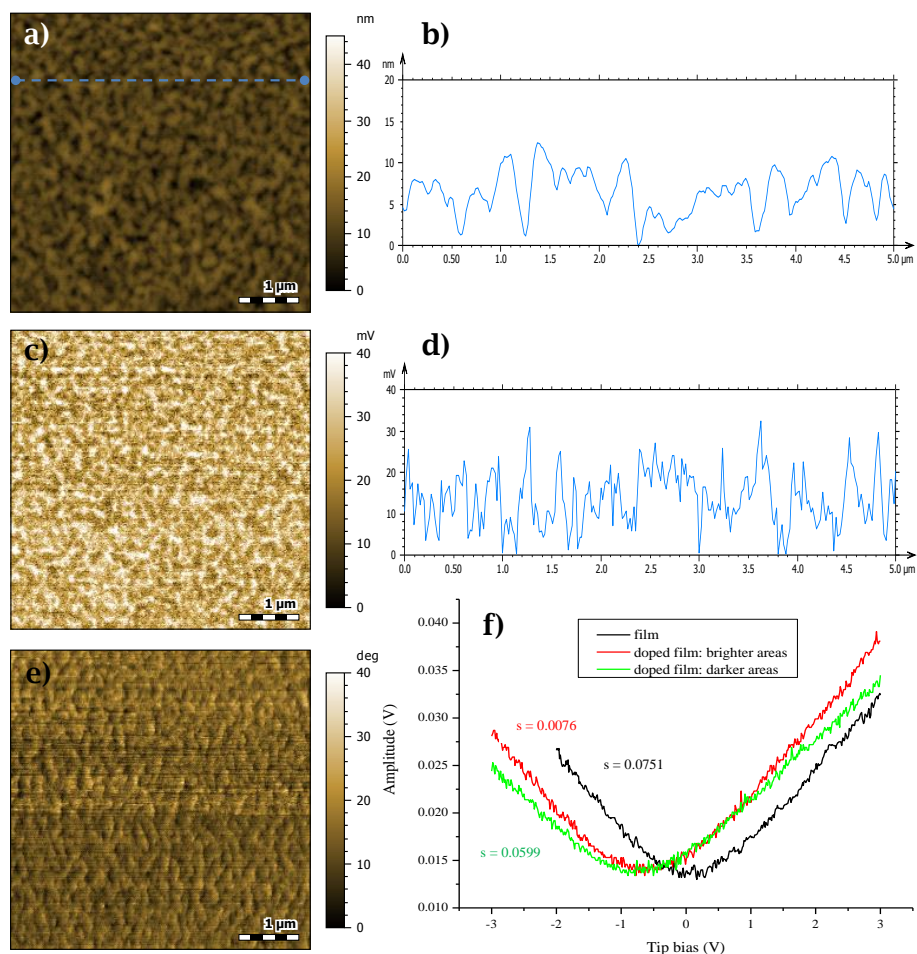
Fig. 2.22 *EFM results of a P4VP-TTFCOOH film after doping with Fe(ClO₄)₃; a) topography image; b) height profile; c) amplitude image; d) amplitude profile; e) phase image; f) amplitude vs. tip bias curves (value following* s *is the calculated slope).*

It has been shown that under appropriate conditions P4VP-TTFCOOH films could be doped to TTFCOOH⁰-TTFCOOH⁺ ˙ when $HAuCl_4$ and $Fe(ClO_4)_3$ were used as oxidants. In contrast, it was not possible to observe a similar effect after doping with I_2 vapors (Fig. 2.23). The amplitude vs. bias curves before and after doping were only slightly shifted (in the same sense as the other doped films) accompanied by a slight increase in the surface roughness. This suggested that a less effective doping of the film was achieved when the oxidation was conducted with I_2 vapors. Therefore, the dependence of the oxidizing level to the oxidation medium, indicated that a better arrangement of the

polymer near the surface occurred during the immersion process and, consequently, a better diffusion of the oxidant.
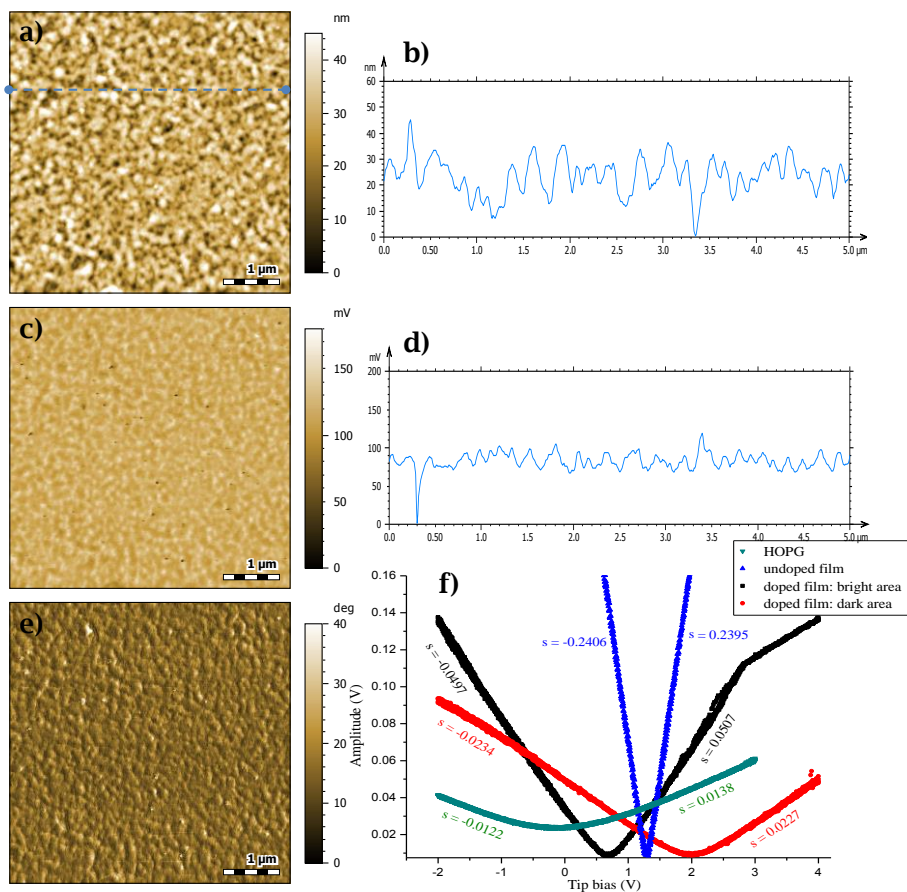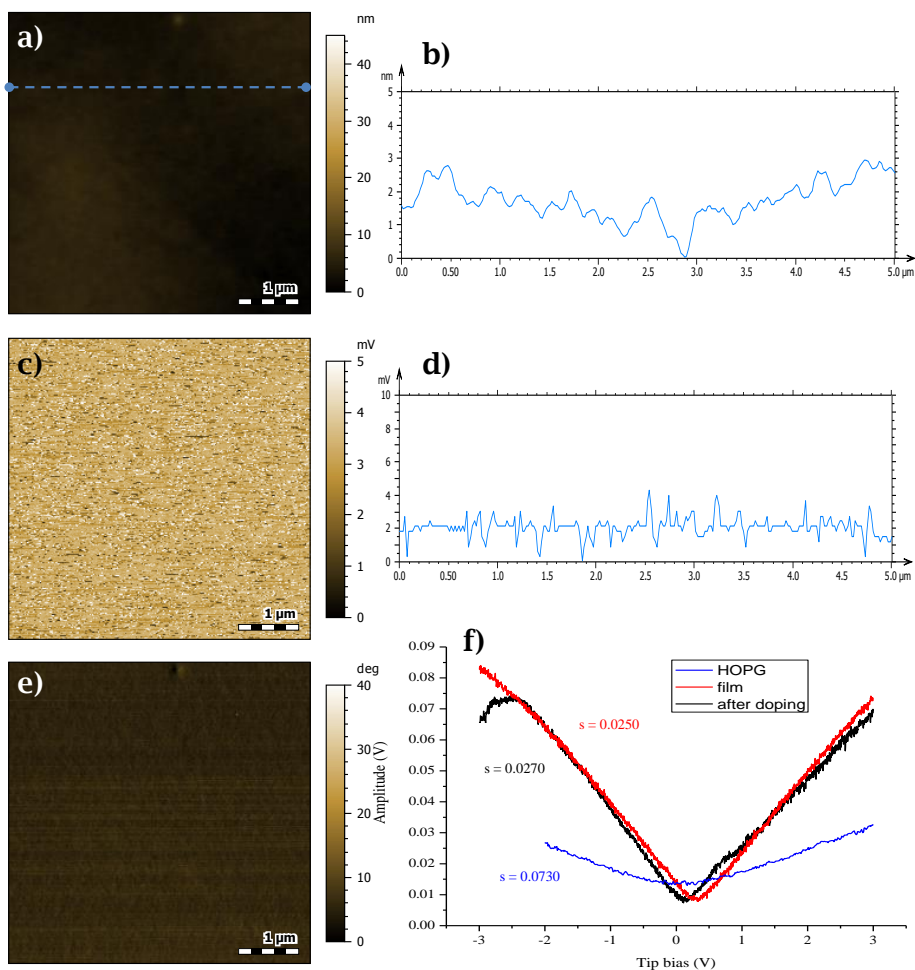

Fig. 2.23 *EFM results of a P4VP-TTFCOOH film after doping with I$_2$ as oxidizing agent; a) topography image; b) height profile; c) amplitude image; d) amplitude profile; e) phase image; f) amplitude vs. tip bias curves (value following* s *is the calculated slope).*

Finally, Electron Paramagnetic Resonance (EPR) was used as complementary technique to measure the unpaired electrons of doped TTFCOOH moieties in the film. EPR signals of undoped films and films doped with HAuCl$_4$, Fe(ClO$_4$)$_3$ and I$_2$ vapors are shown in Fig. 2.24. The EPR spectrum corresponding to undoped films showed a very low intensity signal that had an average g value of 2.007 (composed of 2.011, 2.008, and 2.003) and a band width (ΔHpp) of 16 G. A signal and a splitting in the

energy intensity of the bands were observed although in principle the compound was neutral. A possible explanation for this phenomenon is that P4VP-TTFCOOH in solution or in film state has suffered a slight oxidation, due to the presence of O_2 (manipulation of the samples was made in air). On the other hand, $HAuCl_4$, $Fe(ClO_4)_3$ and I_2 doped films had averaged g and ΔHpp values of 2.007 and 11.9 G, 2.007 and 16 G, and 2.007 and 11.9 G, respectively. As it is shown in the EPR spectra (Fig. 2.24), when the films were oxidized with the different oxidizing agents the intensity of the EPR signals increased dramatically when compared with the as-deposited film and undoped P4VP-TTFCOOH films. This increment in the free electron signal was a clear result of the formation of TTF$^{+\cdot}$ species.[85]
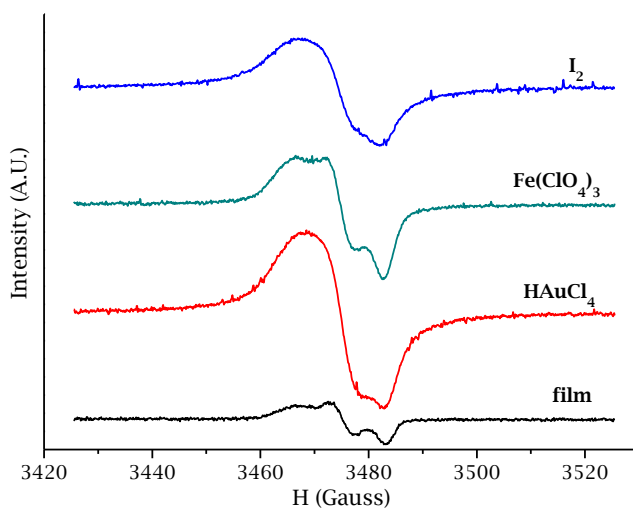
Fig. 2.24 *EPR spectra of P4VP-TTFCOOH film, and films doped with I_2, $Fe(ClO_4)_3$ and $HAuCl_4$ on glass slides.*

Comparing all the EPR spectra for the different doping agents used, it was confirmed that $HAuCl_4$ provided a more efficient doping. The EPR spectrum of the film oxidized with $HAuCl_4$ presented a greater area of peaks, which is related with the number of the cation-radicals in the sample. The higher presence of cation-radicals favored a more significant concentration of areas with a high magnetic interaction between the species.[53, 61, 70, 86, 87] Moreover, the line shape suggested a similar packing between TTFCOOH-TTFCOOH$^{+\cdot}$ units regardless of the doping agent used,

with the exception of iodine, in line with the results obtained from EFM measurements.

2.2.4. Semiconducting crystals of TTFCOOH grown from P4VP-TTFCOOH film

Due to the promising results obtained with P4VP-TTFCOOH film, the possibility to have a controlled crystallization of the TTFCOOH units within the P4VP matrix was also explored. Therefore, in this section the formation of TTF-metal frameworks using P4VP as template to control their assembly has been studied. The little mobility of the P4VP matrix observed during the doping process in water was not sufficient to promote the crystal growing of the TTFCOOH. For this reason, another solvent was considered to promote a rearrangement of P4VP-TTFCOOH hybrid and get the desired charge-carrier crystals in P4VP-TTFCOOH films. Acetonitrile is a polar aprotic organic solvent that dissolves a wide range of ionic and nonpolar compounds, it is miscible in water and, because its relatively high dielectric constant ($\sim$36)[88] it is commonly used in battery applications.[89, 90] Thus, acetonitrile was considered as good solvent for the crystallization studies.

Firstly the solubility of $HAuCl_4$ in acetonitrile as well as the stability of drop-casted P4VP-TTFCOOH film in acetonitrile was checked. Indeed $HAuCl_4$ was soluble in acetonitrile and the film was also resistant. Apart from the solution of $HAuCl_4$ in pure acetonitrile, a mixture water:acetonitrile 1:1 v/v was also tested to compare with the results obtained in pure water. P4VP-TTFCOOH drop-casted films on glass were independently immersed in 7.1 mM $HAuCl_4$ solutions of pure water, pure acetonitrile and water/acetonitrile for 1 minute (Fig. 2.25).
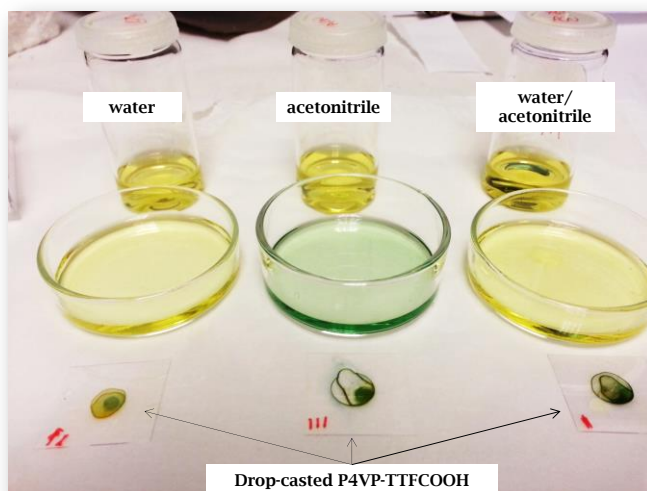
Fig. 2.25 *Picture of drop-cast P4VP-TTFCOOH films on glass surfaces after doping with solutions of HAuCl$_4$ in water (Milli-Q grade), acetonitrile and a mixture water/acetonitrile 1:1 v/v. Glass surfaces were previously cleaned with soap and sequentially rinsed with deionized and ultrapure water.*

Observing the oxidizing solutions after the films immersions, a change in the color was obtained. This change of color suggested that in acetonitrile a re-arrangement of the P4VP-TTFCOOH film occurred and free TTFCOOH was re-dissolved. The observation of the films after doping by bare eye and optical microscope showed up differences that were attributed to a different grade and control of the oxidizing process, Fig. 2.25 and Fig. 2.26, respectively. Therefore, when pure water was used as solvent, the film acquired a pale-green color in the center, due to the presence of high concentrated material, and a faded yellow in the surroundings. This indicated that in water, a more controlled and slower oxidizing process occurred and, hence different mixed valence states were obtained at the same time, which was in concordance with the previous discussed experiments. On the other hand, when acetonitrile was used, pure or mixed with water, the films became directly green, indicating the formation of the TTFCOOH$^{+\cdot}$-TTFCOOH^{2+} intermediate and a faster and uncontrollable oxidation process. Furthermore, some crystalline structures were also obtained. The crystals looked blue-turquoise under the polarized light, indicating the presence of doped TTFCOOH crystals (Fig. 2.27 a-d). The corresponding SEM images of the crystals showed the

presence of planar fibers together with wires (Fig. 2.27 d-e), which were attributed to the formation of TTF-Au hybrid structures. Previously, Puigmartí-Luis *et al.* reported the formation of similar conductive TTF-Au hollow hybrid wires using microfluidic approach.[78] In the present case, the P4VP matrix can play the role of template-assistant towards the assembly of the hybrid fibers.
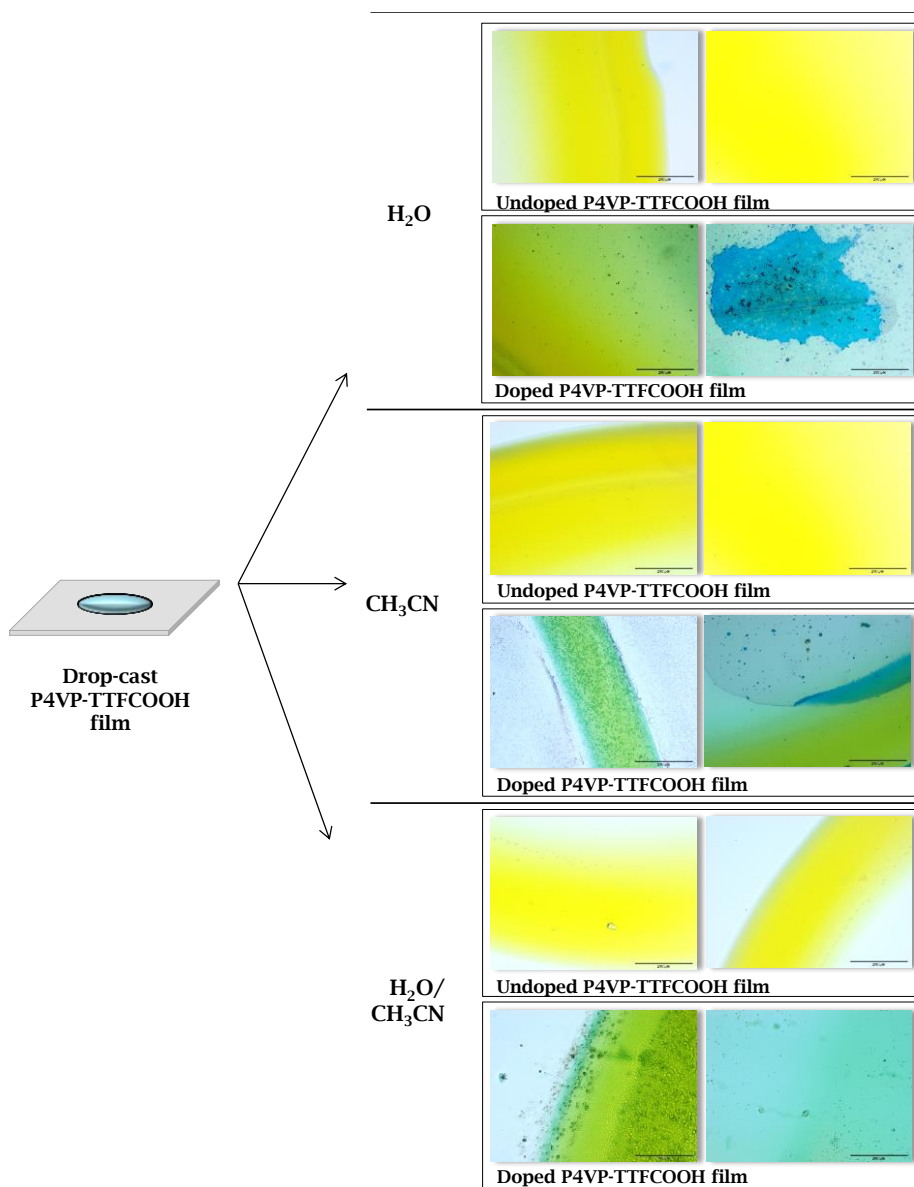
Fig. 2.26 *Images of drop-cast P4VP-TTFCOOH films on glass, undoped and doped with different HAuCl$_4$ solutions in water (H$_2$O), acetonitrile (CH$_3$CN) and a mixture water/acetonitrile 1:1 v/v (H$_2$O/CH$_3$CN). Scale bars represent 200 μm.*
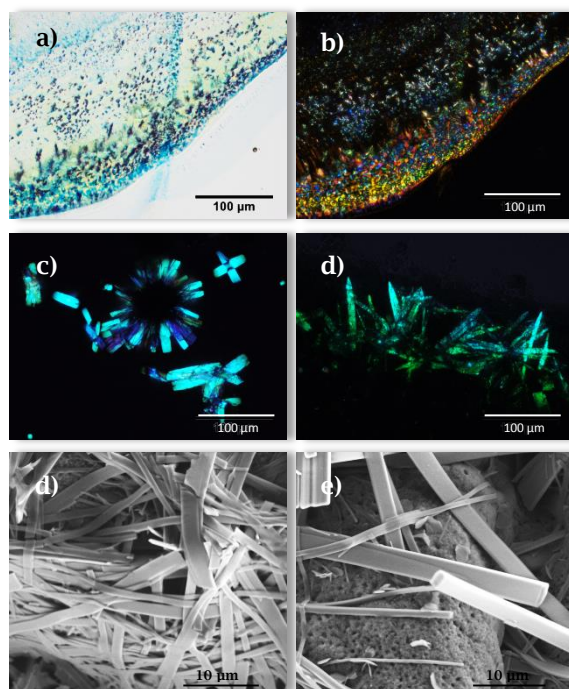
Fig. 2.27 *a) to d) Images of different regions of the drop-casted P4VP-TTFCOOH film on glass doped with HAuCl4 in acetonitrile taken from optical microscope (white light) and polarized light (scale bars 100 µm). d) and e) Corresponding SEM images of the sample (scale bars 10 µm).*

2.3.   CONCLUSIONS AND OUTLOOK

It has been demonstrated that the supramolecular functionalization of P4VP polymer with a TTF derivative through complementary hydrogen bonding components is a viable strategy for the preparation of solutions and stable films which incorporate redox active components. The homogeneity and the achieving of stable thin films with a range of thickness values comprised between 30 to 40 nm was reached by spin-coating. Both as a film and in solution, TTF moieties retained their ability to form the corresponding valence states in the doped P4VP-TTFCOOH hybrid material. In doped P4VP-TTFCOOH films, mixed valence states such as TTFCOOH^0-TTFCOOH$^+$ and TTFCOOH$^+$-TTFCOOH^{2+} were

confirmed by the appearance of the charge transfer bands in UV-Vis-NIR absorption spectroscopy, however these states could not be observed in P4VP-TTFCOOH doped solutions. This difference between solid state and solution was attributed to a major mobility of the polymeric structure in the latest, which promoted an uncontrolled and fast doping effect. Contrarily, P4VP-TTFCOOH films reduced the velocity of the oxidation process due to the limited access of the doping agents to all TTFCOOH units, providing a certain control of the different valences of TTFs reached, and thus, permitting the observation of charge transfer bands. UV-Vis-NIR spectroscopy also demonstrated that drop-casted P4VP-TTFCOOH films could be indistinctly doped by sequential cycles of immersion into aqueous salts of Au^{3+}, Fe^{3+} and by exposition to I_2 vapors.

EFM studies of spin-coated P4VP-TTFCOOH thin films indicated that a reorganisation at the surface of the films took place. This phenomenon was correlated to the self-assembly tendency of TTFs in the mixed valence state which facilities charge motion. Moreover, the electrostatic measurements acquired with the EFM technique also demonstrated that superficial charge inhomogeneities in doped P4VP-TTFCOOH thin films could be associated to a charge-transport phenomenon directly derived from the oxidation process. After analysing the results obtained with UV-Vis-NIR spectra, EPR and EFM results, $HAuCl_4$ and $Fe(ClO_4)_3$ were concluded to be the most effective doping agents to achieve TTFCOOH mixed valence states due to their indistinctly effectiveness in drop-casted and spin-coated films.

On the other hand, the possibility to obtain TTF-based crystals grown from a P4VP polymer matrix has also been demonstrated. This approach confirmed that P4VP can be used as support or template for organic conductive materials, opening numerous potential applications of the P4VP-TTFCOOH hybrid.

2.4.   EXPERIMENTAL PART

PS and P4VP were synthetized using living anionic polymerization based on the procedure that Varshney *et al.*[91] described.

Materials: styrene ≥99%, 4-vinyl pyridine (containing 100 ppm hydroquinone as inhibitor), α-methylstyrene 99% (containing 15 ppm *p*-tert-butylcatechol as inhibitor), the initiator *sec*-butyllithium (1.4 M in cyclohexane), $HAuCl_4$ (gold (III) chloride trihydrate ≥99.9% trace metal basis), $Fe(ClO_4)_3$ (iron (III) perchlorate hydrate crystalline), I_2 (≥99.99% trace metals basis) and methanol (anhydrous, 99.8%) were purchased from Sigma-Aldrich. THF was HPLC degree from Teknokroma. TTFCOOH was synthetized in a previous work following the literature procedure.[91]

Synthesis of PS: styrene was distilled and tetrahydrofuran (THF) was dried with sodium/benzophenone before used. α-methylstyrene was previously dried by distillation over calcium hydride. A solution of 1.5 mmols of α-methylstyrene in THF was prepared. Then, *sec*-butyllithium was added dropwise to the mixture using a stainless steel syringe until the color of the solution persisted. The color of the solution was given by the formation of the α-methylstyryllithium (α-MS-Li$^+$) as a product of the reaction of α-methystyrene and *sec*-butyllithium. Then, the reaction was cooled down to -78ºC and 32 mmol of styrene was added slowly, observing a sudden change of the color of the initiator (from red to light yellow). The polymerization was ended by adding methanol and, the precipitation of the polymer $(C_8H_8)_n$ occurred. Afterwards, the polymer was recovered by precipitation in hexane and it was thoroughly dried under vacuum (Fig. 2.28). ^{1}H NMR $(C_8H_8)_n$ (CDCl$_3$, 300 MHz), δ_H (ppm): 1.29-1.53 (m, 1H), 1.74-2.20 (m, 2H),6.25-6.87 (m, 2H), 6.87-7.25 (m, 3H). M_w (GPC) $(C_8H_8)_n$: 137908 g/mol.
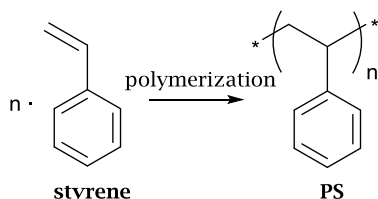
Fig. 2.28 *Formation of the PS from its monomer.*

Synthesis of P4VP: 4-vinyl pyridine was distilled and tetrahydrofuran (THF) was dried with sodium/benzophenone before used. α-methylstyrene was previously dried by distillation over calcium hydride. A solution of 1.5 mmols of α-methylstyrene in THF was prepared. Then, *sec*-butyllithium was added dropwise to the mixture using a stainless steel syringe until the color of the solution persisted. The color of the solution was given by the formation of the α-methylstyryllithium (α-MS-Li$^+$) as a product of the reaction of α-methystyrene and *sec*-butyllithium. Then, the reaction was cooled down to -78ºC and 32 mmol of 4-vinyl pyridine was added slowly, observing a sudden change of the color of the initiator (from red to light yellow). The polymerization was ended by adding methanol and, the precipitation of the polymer $(C_7H_7N)_n$ occurred. Afterwards, the polymer was recovered by precipitation in hexane and it was thoroughly dried under vacuum. ^{1}H NMR $(C_7H_7N)_n$ (CDCl$_3$, 300 MHz), δ_H (ppm): 1.27-1.79 (br, 3H), 6.22-6.56 (m, 2H), 8.15-8.58 (m, 2H). M_w (GPC) $(C_7H_7N)_n$: 358 g/mol.

Molecular weight determination (GPC): molecular weights (M_w) of both homopolymers specified in Table 2.2, were determined by gel permeation chromatography (GPC). The chromatographer was calibrated by using standardized samples of PS (from Supelco Inc., PS Standard Kit). The column used was TSK-GEL G3000H 7.8 mm ID x 30.0 cm L with a pore size of 6 µm (from Tosoh Bioscience). THF (HPLC degree) was the eluent, the flow rate was fixed at 1 µl/min, the volume of sample injected in each experiment was 20 µl and the lamp wavelength was set at 254 nm. Injected solutions were concentrated at 2 mg/ml.

Homo-/co-polymer	PS:P4VP molar ratio	initiator amount (mmol)	styrene amount (mmol)	4-vinyl pyridine amount (mmol)	M_w (GPC) (g/mol)
PS	-	34	32	-	137908
P4VP	-	24	-	32	358

Table 2.2   *Data from polymerizations of PS and P4VP.*

Self-assembly of P4VP-TTFCOOH and film formation: A solution of P4VP and TTFCOOH (10 mM, 1:1 molar ratio) in chloroform was prepared and vigorously stirred. Films were obtained by spin-coating 170 µl of the as-prepared solution on a surface and allowing the evaporation of the solvent. The conditions used for film sample formation were: 4000 rpm, 5500 rpm·s^{-2} and 30 seconds of rotation. In the case of drop casted films, samples were prepared by depositing a droplet of the P4VP-TTFCOOH solution on the surface and letting it to evaporate at room temperature.

Solution oxidation: A solution of P4VP and TTFCOOH (10 mM, 1:1 molar ratio) in chloroform was prepared. An aliquot of 10 µl was taken, diluted in 3 ml of acetonitrile and transferred into a 10.00 mm path quartz cuvette. Meanwhile, a $HAuCl_4$ 0.015 M and a $Fe(ClO_4)_3$ 0.0150 M solutions in chloroform were prepared separately. To follow the oxidation of P4VP-TTFCOOH in solution, the progressively addition of the oxidizing solution of each doping agent to the cuvette was conducted.

Film oxidation: The oxidation process consisted of doping cycles by immersing a film on quartz support in an aqueous solution (Milli-Q grade) of an oxidizing agent for 1 minute. Then, the film was dried with N_2 flow, washed also by immersion in H_2O (Milli-Q grade) for 1 minute, and dried with a flow of nitrogen gas. The molar ratio TTFCOOH:oxidizing agent was 25:1 for the $HAuCl_4$, as well was for the $Fe(ClO_4)_3$. In the case of I_2 vapors, the films were doped by exposing them to the I_2 vapors for 3 seconds, without further washing (Fig. 2.29).
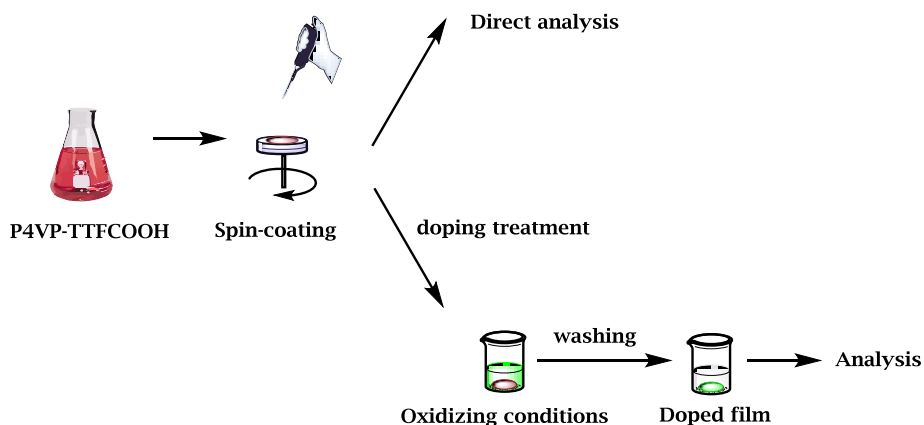
Fig. 2.29 *Representation of the film formation and doping process.*

Contact angle: The volume to create a sessile drop on surface was of 4 or 5 µl. The surface tension of the liquids was calculated by the angle created of a pendant drop of the studied solution.

SEM/EDX imaging: The samples were measured at high and low vacuum conditions where the electron beam acceleration voltage was set between 10 kV and 20 kV.

EFM measurements: All measurements were made with Nano World Pointprobe silicon SPM sensor tips, provided with a force constant of 2.8 N/m, a coating tip side of Pt/Ir, and a coating detector side of Pt/Ir. The measurements were conducted under controlled atmospheric conditions by flowing compressed air and N_2, to reach 3.5-5.0% of relative humidity. Set-point values of 2.47 and 1.9 V were fixed to image areas of 2x2 and 5x5 µm respectively. Previously, set-point voltage values were calibrated and referenced to the height between the sample surface and the tip (1V~ 30 nm). Films were prepared and doped following the methodologies previously detailed. HOPG pieces (Bruker ZYB grade 12x12x2 mm and, NT-MDT Co., ZYB grade mosaic spread 0.8-1.2 degree and thickness dispersion ± 0.2 mm) were used as conductive substrates. After numerous previous trials for EFM the most reliable results were found in samples with calculated molar ratio of TTFCOOH:$HAuCl_4$ of 10:1. The amplitude-tip bias curves were an average of the at least 100 curves from different points of the studied area. Bias swept to take each curve were made from -2 to 4 V in 7.48 s and from 4 to -2 V in 7.48 s, taking 400

measurements in each swept, and a pausing time after each curve of 20 s. The first resonance mode of the cantilever depicts the topography of the film, while the second order mode quantifies the electrostatic interactions of tip with the scanned sample area. The EFM data was acquired biasing the tip with 2 V AC at 440kz and biasing the sample with -2 V DC, while maintaining constant the tip-sample distance. Slope values of amplitude-tip bias curves were calculated by fitting to lineal equations ($y = a \cdot x + b$) taking the minimum as reference in each side of the "V" shaped graphics.

TEM imaging: For TEM sample preparation of the P4VP-TTFCOOH film, a drop of a diluted solution of P4VP and TTFCOOH in chloroform was used (5 mM). This solution was drop-casted on a holey carbon coated copper TEM grid (200 lines/inch). Doped samples were produced by the immersion of the as-prepared TEM grid into a solution of $HAuCl_4$ (aq) (0.007 M) for 1 minute.

EPR measurements: Two measurements of four scans for each sample were taken. P4VP-TTFCOOH solutions were drop-cast on glass slides to obtain the polymeric films under study. Doping of the polymeric films was achieved by their immersion into an aqueous solution of doping agent under study. Previous to the sample measurement, a cleaned slide was measured to obtain the background signal, and hence, to ensure the absence of spurious signals.

Ellipsometry (film thickness): All the experiments were made by measuring spin-coated films on silicon surfaces. Results are the mean of a pair of samples for each measurement where 60º, 65º, 70º and 75º were the angles used in the detector for all the measurements performed. The doping agent used to dope P4VP-TTFCOOH films was the $HAuCl_4$ (aq).

2.5. REFERENCES

1. J. Frechet, *Science*, 1994, **263**, 1710-1715.
2. J.-T. Chen and C.-S. Hsu, *Polymer Chemistry*, 2011, **2**, 2707-2722.

3. D. C. Coffey and D. S. Ginger, *Nature materials*, 2006, **5**, 735-740.
4. J. Ruokolainen, G. ten Brinke, O. Ikkala, M. Torkkeli and R. Serimaa, *Macromolecules*, 1996, **29**, 3409-3415.
5. B. J. Rancatore, C. E. Mauldin, S.-H. Tung, C. Wang, A. Hexemer, J. Strzalka, J. M. J. Fréchet and T. Xu, *ACS Nano*, 2010, **4**, 2721-2729.
6. C.-H. Yu, Y.-H. Chuang and S.-H. Tung, *Polymer*, 2011, **52**, 3994-4000.
7. T. Wang, A.-W. Xu and H. Cölfen, *Angewandte Chemie International Edition*, 2006, **45**, 4451-4455.
8. S. Ibe, R. Ise, Y. Oaki and H. Imai, *Crystal Engineering Communications*, 2012, **14**, 7444-7449.
9. Y. Diao, L. Shaw, Z. Bao and S. C. B. Mannsfeld, *Energy & Environmental Science*, 2014, **7**, 2145-2159.
10. M.-C. Lin, B. Nandan and H.-L. Chen, *Soft Matter*, 2012, **8**, 7306-7322.
11. R. Saberi Moghaddam, S. Huettner, Y. Vaynzof, C. Ducati, G. Divitini, R. H. Lohwasser, K. P. Musselman, A. Sepe, M. R. J. Scherer, M. Thelakkat, U. Steiner and R. H. Friend, *Nano letters*, 2013, **13**, 4499-4504.
12. N. S. Trasi and L. S. Taylor, *Crystal Growth & Design*, 2012, **12**, 3221-3230.
13. G. A. Ilevbare, H. Liu, K. J. Edgar and L. S. Taylor, *Crystal Growth & Design*, 2012, **12**, 3133-3143.
14. H. Konno and L. S. Taylor, *Journal of Pharmaceutical Sciences*, 2006, **95**, 2692-2705.
15. P. V. Dhanaraj, G. Bhagavannarayana and N. P. Rajesh, *Materials Chemistry and Physics*, 2008, **112**, 490-495.
16. M. Van der Leeden, D. Kashchiev and G. Van Rosmalen, *Journal of crystal growth*, 1993, **130**, 221-232.
17. Y. Diao, B. C. K. Tee, G. Giri, J. Xu, D. H. Kim, H. A. Becerril, R. M. Stoltenberg, T. H. Lee, G. Xue, S. C. B. Mannsfeld and Z. Bao, *Nature materials*, 2013, **12**, 665-671.
18. N. N. Nguyen, S. B. Jo, S. K. Lee, D. H. Sin, B. Kang, H. H. Kim, H. Lee and K. Cho, *Nano letters*, 2015, **15**, 2474-2484.
19. B. Wang, T. Zhu, L. Huang, T. L. D. Tam, Z. Cui, J. Ding and L. Chi, *Organic Electronics*, 2015, **24**, 170-175.
20. L. Bu, T. J. Dawson and R. C. Hayward, *ACS Nano*, 2015, **9**, 1878-1885.
21. H. Sugiyama and H. Kamogawa, *Journal of Polymer Science Part A-1: Polymer Chemistry*, 1966, **4**, 2281-2288.
22. J. M. J. Fréchet and M. V. de Meftahi, *British Polymer Journal*, 1984, **16**, 193-198.
23. R. Abargues, P. J. Rodríguez-Cantó, R. García-Calzada and J. Martínez-Pastor, *The Journal of Physical Chemistry C*, 2012, **116**, 17547-17553.
24. S. Rangou, K. Buhr, V. Filiz, J. I. Clodt, B. Lademann, J. Hahn, A. Jung and V. Abetz, *Journal of Membrane Science*, 2014, **451**, 266-275.
25. X. Liu, X. Chen, J. Wang, G. Chen and H. Zhang, *Macromolecules*, 2014, **47**, 3917-3925.
26. W. Slough, *Transactions of the Faraday Society*, 1962, **58**, 2360-2369.
27. R. Narayan, P. Kumar, K. S. Narayan and S. K. Asha, *Journal of Materials Chemistry C*, 2014, **2**, 6511.
28. M. Sallé, D. Canevet, J.-Y. Balandier, J. Lyskawa, G. Trippé, S. Goeb and F. Le Derf, *Phosphorus, Sulfur, and Silicon and the Related Elements*, 2011, **186**, 1153-1168.
29. Y. Mina, M. Yoshiyuki and S. Matthias, *New Journal of Physics*, 2011, **13**, 073039.
30. H. A. J. Govers and C. G. de Kruif, *Acta Crystallographica Section A*, 1980, **36**, 428-432.
31. J. B. Torrance, B. A. Scott, B. Welber, F. B. Kaufman and P. E. Seiden, *Physical Review B*, 1979, **19**, 730-741.
32. M. R. Bryce, *Advanced materials*, 1999, **11**, 11-23.

33. D. Jérome, A. Mazaud, M. Ribault and K. Bechgaard, *Journal Physique Letters*, 1980, **41**, 95-98.

34. F. Pointillart, J. Jung, R. Berraud-Pache, B. Le Guennic, V. Dorcet, S. Golhen, O. Cador, O. Maury, Y. Guyot, S. Decurtins, S.-X. Liu and L. Ouahab, *Inorganic chemistry*, 2015, **54**, 5384-5397.

35. F. Pointillart, S. Golhen, O. Cador and L. Ouahab, *European Journal of Inorganic Chemistry*, 2014, **2014**, 4558-4563.

36. J. Becher, J. Lau, P. Leriche, P. Mork and N. Svenstrup, *Journal of the Chemical Society, Chemical Communications*, 1994, DOI: 10.1039/C3940002715, 2715-2716.

37. M. B. Nielsen, C. Lomholt and J. Becher, *Chemical Society reviews*, 2000, **29**, 153-164.

38. S. Chopin, Z. Gan, J. Cousseau, Y. Araki and O. Ito, *Journal of Materials Chemistry*, 2005, **15**, 2288-2296.

39. L. Wang, H. Cho, S.-H. Lee, C. Lee, K.-U. Jeong and M.-H. Lee, *Journal of Materials Chemistry*, 2011, **21**, 60-64.

40. L. Wang, S.-Y. Park, S.-M. Kim, S. Yoon, S.-H. Lee, E. Lee, K.-U. Jeong and M.-H. Lee, *Liquid Crystals*, 2012, **39**, 795-801.

41. J. Martínez-Perdiguero, I. Alonso, J. Ortega, C. L. Folcia, J. Etxebarria, I. Pintre, M. B. Ros and D. B. Amabilino, *Physical Review E*, 2008, **77**, 020701.

42. M. Vandevyver, M. Roulliay, J. P. Bourgoin, A. Barraud, V. Gionis, V. C. Kakoussis, G. A. Mousdis, J. P. Morand and O. Noel, *The Journal of Physical Chemistry*, 1991, **95**, 246-251.

43. C. Dourthe, M. Izumi, C. Garrigou-Lagrange, T. Buffeteau, B. Desbat and P. Delhaes, *The Journal of Physical Chemistry*, 1992, **96**, 2812-2820.

44. M. Shatruk and L. Ray, *Dalton transactions*, 2010, **39**, 11105-11121.

45. J. L. Segura and N. Martín, *Angewandte Chemie International Edition*, 2001, 1372-1409.

46. S.-L. Cai, Y.-B. Zhang, A. B. Pun, B. He, J. Yang, F. M. Toma, I. D. Sharp, O. M. Yaghi, J. Fan, S.-R. Zheng, W.-G. Zhang and Y. Liu, *Chemical Science*, 2014, **5**, 4693-4700.

47. Y. Yokota, K.-i. Fukui, T. Enoki and M. Hara, *Journal of the American Chemical Society*, 2007, **129**, 6571-6575.

48. K. Tanaka, F. Ishiguro and Y. Chujo, *Langmuir : the ACS journal of surfaces and colloids*, 2010, **26**, 10254-10258.

49. K. Tanaka, T. Matsumoto and Y. Chujo, *Synthetic Metals*, 2013, **163**, 13-18.

50. S. Inagi, K. Naka and Y. Chujo, *Journal of Materials Chemistry*, 2007, **17**, 4122.

51. K. Tanaka, F. Ishiguro, T. Kunita and Y. Chujo, *Journal of Polymer Science Part A: Polymer Chemistry*, 2009, **47**, 6441-6450.

52. K. Tanaka, T. Kunita, F. Ishiguro, K. Naka and Y. Chujo, *Langmuir : the ACS journal of surfaces and colloids*, 2009, **25**, 6929-6933.

53. E. Gomar-Nadal, L. Mugica, J. Vidal-Gancedo, J. Casado, N. J.T.L., J. Veciana, C. Rovira and D. B. Amabilino, *Macromolecules*, 2007, 7521-7531.

54. Y. Kobayashi, M. Yoshioka, K. Saigo, D. Hashizume and T. Ogura, *Journal of the American Chemical Society*, 2009, **131**, 9995-10002.

55. M. Fujihira, *Annual Review of Materials Science*, 1999, **29**, 353-380.

56. T. Kato and J. M. J. Frechet, *Macromolecules*, 1989, **22**, 3818-3819.

57. T. Kato, H. Kihara, U. Kumar, T. Uryu and J. M. J. Fréchet, *Angewandte Chemie International Edition in English*, 1994, **33**, 1644-1645.

58. S. Malik, P. K. Dhal and R. A. Mashelkar, *Macromolecules*, 1995, **28**, 2159-2164.

59. F. A. Brandys and C. G. Bazuin, *Chemistry of Materials*, 1996, **8**, 83-92.

60. A. Laforgue, C. G. Bazuin and R. E. Prud'homme, *Macromolecules*, 2006, **39**, 6473-6482.
61. R. Bozio, I. Zanon, A. Girlando and C. Pecile, *The Journal of Chemical Physics*, 1979, **71**, 2282-2293.
62. B. Yameen, M. Ali, R. Neumann, W. Ensinger, W. Knoll and O. Azzaroni, *Nano letters*, 2009, **9**, 2788-2793.
63. E. Gomar-Nadal, J. Veciana, C. Rovira and D. B. Amabilino, *Advanced materials*, 2005, **17**, 2095-2098.
64. J. Puigmarti-Luis, V. Laukhin, A. Perez del Pino, J. Vidal-Gancedo, C. Rovira, E. Laukhina and D. B. Amabilino, *Angewandte Chemie International Edition English*, 2007, **46**, 238-241.
65. M. S.A. Abdou and S. Holdcroft, *Synthetic Metals*, 1993, **60**, 93-96.
66. L. M. Goldenberg, V. Y. Khodorkovsky, J. Y. Becker, M. R. Bryce and M. C. Petty, *Journal of Materials Chemistry*, 1995, **5**, 191-192.
67. R. S. Mulliken, *The Journal of Physical Chemistry*, 1952, **56**, 801-822.
68. V. Khodorkovsky, L. Shapiro, P. Krief, A. Shames, G. Mabon, A. Gorgues and M. Giffard, *Chemical communications*, 2001, 2736-2737.
69. T. Kitamura, S. Nakaso, N. Mizoshita, Y. Tochigi, T. Shimomura, M. Moriyama, K. Ito and T. Kato, *Journal of the American Chemical Society*, 2005, **127**, 14769-14775.
70. C.-K. Jeong and Y.-I. Kim, *Bulletin Korean Chemical Society*, 1999, **20**, 1509-1512.
71. M. B. Inoue, M. Inoue, Q. Fernando and K. W. Nebesny, *Inorganic chemistry*, 1986, **25**, 3976-3980.
72. G. Cooke, A. S. Dhindsa, Y. P. Song, G. Williams, A. S. Batsanov, M. R. Bryce, J. A. K. Howard, M. C. Petty and J. Yarwood, *Synthetic Metals*, 1993, **57**, 3871-3878.
73. R. S. Mulliken, *Journal of the American Chemical Society*, 1952, **74**, 811-824.
74. S. D. Evans, R. Sharma and A. Ulman, *Langmuir : the ACS journal of surfaces and colloids*, 1991, **7**, 156-161.
75. H. J. Butt, K. Graf and M. Kappl, *Physics and Chemistry of Interfaces*, Wiley, 2006.
76. X. Wang, K. Naka, H. Itoh, S. Park and Y. Chujo, *Chemical communications*, 2002, DOI: 10.1039/b203185j, 1300-1301.
77. K. Naka, D. Ando, X. Wang and Y. Chujo, *Langmuir : the ACS journal of surfaces and colloids*, 2007, **23**, 3450-3454.
78. J. Puigmartí-Luis, D. Schaffhauser, B. R. Burg and P. S. Dittrich, *Advanced materials*, 2010, **22**, 2255-2259.
79. M. J. Cadena, R. Misiego, K. C. Smith, A. Avila, B. Pipes, R. Reifenberger and A. Raman, *Nanotechnology*, 2013, **24**, 135706.
80. M. M. S. Abdel-Mottaleb, E. Gomar-Nadal, M. Surin, H. Uji-i, W. Mamdouh, J. Veciana, V. Lemaur, C. Rovira, J. Cornil, R. Lazzaroni, D. B. Amabilino, S. De Feyter and F. C. De Schryver, *Journal of Materials Chemistry*, 2005, **15**, 4601-4615.
81. A. Roy-Gobeil, Y. Miyahara and P. Grutter, *Nano letters*, 2015, **15**, 2324-2328.
82. R. Dianoux, F. Martins, F. Marchi, C. Alandi, F. Comin and J. Chevrier, *Physical Review B*, 2003, **68**, 045403.
83. I. H. Campbell, J. D. Kress, R. L. Martin, D. L. Smith, N. N. Barashkov and J. P. Ferraris, *Applied Physics Letters*, 1997, **71**, 3528.
84. L. Collins, M. B. Okatan, Q. Li, Kravenchenko, II, N. V. Lavrik, S. V. Kalinin, B. J. Rodriguez and S. Jesse, *Nanotechnology*, 2015, **26**, 175707.
85. L. Ćavara, F. Gerson, D. O. Cowan and K. Lerstrup, *Helvetica Chimica Acta*, 1986, **69**, 141-151.

86. Y. Harima, Y. Kunugi, H. Tang, K. Yamashita, M. Shiotani, J. Ohshita and A. Kunai, *Synthetic Metals*, 2000, **113**, 173-183.

87. C. Rovira, J. Veciana, N. Santalo, J. Tarres, J. Cirujeda, E. Molins, J. Llorca and E. Espinosa, *The Journal of Organic Chemistry*, 1994, **59**, 3307-3313.

88. G. Ritzoulis, N. Papadopoulos and D. Jannakoudakis, *Journal of Chemical & Engineering Data*, 1986, **31**, 146-148.

89. Y. Yamada, K. Furukawa, K. Sodeyama, K. Kikuchi, M. Yaegashi, Y. Tateyama and A. Yamada, *Journal of the American Chemical Society*, 2014, **136**, 5039-5046.

90. N. Mozhzhukhina, M. P. Longinotti, H. R. Corti and E. J. Calvo, *Electrochimica Acta*, 2015, **154**, 456-461.

91. S. K. Varshney, X. F. Zhong and A. Eisenberg, *Macromolecules*, 1993, **26**, 701-706.

CHAPTER 3

Electrostatic Response Dependence on Tetrathiafulvalene-Based Block Copolymer Thin Films

3.1. INTRODUCTION AND OBJECTIVES

Organic thin films based on amphiphilic block copolymers (BCP) had been deeply studied due to the tunability of the different self-assembled conformations adopted between the immiscible blocks at the interfase.[1-4] Volume fraction of each block and the solvent used to dissolve/disperse them are the key factors to control the different conformations.[5-8] These parameters were early studied by Bates and coworkers demonstrating their dependence to the resulting segregated structures.[9] Poly(styrene-*b*-4-vinyl pyridine) (PS-*b*-P4VP) is an amphiphilic block copolymer that, thanks to the different nature of the poly(styrene) (PS) and poly(4-vinyl pyridine) (P4VP) blocks covalently bonded, its malleability, pH-responsiveness and reactivity of the P4VP block combined with the stiffness of the PS part, make this BCP a desirable material with interesting properties. The variety of conformations that can be achieved such as membranes, micelles and thin films, among others with totally different final properties[10-14], together with the use of the pyridine ring as anchoring point have made this BCP to be used for a wide range of applications.

The commonly known and easiest pathway to synthetize PS-*b*-P4VP (also valid for PS[15] and P4VP[16] homopolymers) is by 'living' anionic polymerization (Fig. 3.1). This type of polymerization provides well-defined homo- and copolymers with the possibility to control a wide range of molecular weights, molecular weight distributions, stereochemistry and high structural and compositional homogeneity.[17, 18] From a general point of view, 'living' polymerizations can be classified in the chain-growth polymerizations group, as the reaction proceeds by sequential monomer addition.[18] The polymerization of PS-*b*-P4VP starts with the polymerization of the PS block, due to the higher stability of the conjugated acid of the carbanion of the chain end form[18] (when PS block is growing, so it is still 'living') followed by the polymerization of P4VP. The relative stability of the carbanionic forms depends on the pK_a values of the mentioned conjugated acids.[18] The ending process usually proceeds by the addition of a counter-ion that neutralizes the 'living' ending of the macromolecular

chain, then the polymerization stops and the polymer is collected by precipitation.
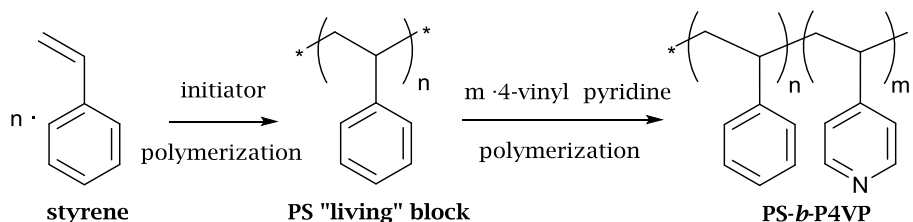
Fig. 3.1 Synthesis of PS-b-P4VP via living anionic polymerization.

PS-*b*-P4VP combines the properties of each block that compound it. P4VP block is selectively solubilized by polar protic solvents, except in water, in where it swells.[19] Oppositely, PS block is selectively soluble in non-polar solvents. There are some non-selective solvents that dissolve entirely the PS-*b*-P4VP like chloroform and tetrahydrofuran and the corresponding solvent polar-non-polar solvent mixtures. These 'solubility rules' are not invariables and can differ in function of the molar fraction of each block and consequently, of the degree of polymerization. Moreover, the amphiphilic character of the BCP allows a good phase separation that can be adjusted and, at some point, induced by controlling the molar fraction and the solvent in which it is partially or totally solubilized. The combination of the characterization techniques Transmission Electron Microscopy (TEM) and Small-Angle X-ray Scattering (SAXS) are commonly used to depict and measure, respectively, the phase segregation of BCP systems at the interface. Rangou *et al.*[20] used of the solvent selectivity to perform PS-*b*-P4VP dynamically pore-sized membranes based on the swelling-deflating and protonation-deprotonation of the P4VP units when water flowed through the porous system. In a further step, Clodt *et al.*[13] demonstrated the possibility to create thermo-sensitive pNIPAM-functionalized PS-*b*-P4VP membranes. Tailor-made phase-segregated PS-*b*-P4VP thin films can also be obtained by, for example, spin-coating and a consequent treating with selective solvent vapours and/or temperature.[5, 6, 21-23]

Besides the solvent or temperature, another important strategy to modify and tune the phase-segregation of the PS-*b*-P4VP is the

introduction of a pendant group through the P4VP block. Thus, the supramolecular chemistry of the PS-*b*-P4VP through the reactive nitrogen of pyridine group of P4VP units has been also reported for mainly obtaining different self-assembled nanostructures, films and porous materials with uneven properties.[24-31] Precisely due to the reactivity of P4VP and the possibility to obtain consistent thin films with different phase segregation, organic semiconductors based on PS-*b*-P4VP thin films could be approached.[32] Yoo and researchers created highly porous membranes of PS-*b*-P4VP functionalized by nucleophilic substitution with an energy modifier agent that was proposed as alternative separator material for high power lithium-ion batteries.[33] Another interesting approach was made by Chen and coworkers, in where they built electrically switchable memory devices based on self-assembled thin films of PS-*b*-P4VP with fullerene derivatives.[34] In the same way, Laforgue *et al.* presented PS-*b*-P4VP thin films with the P4VP units complexed via hydrogen bonding with a naphthalene derivative.[35] Another example was reported by del Barrio and coworkers, in where they functionalized PS-*b*-P4VP BCP through hydrogen bonding interactions with a derivate of an azo chromophore, obtaining in this way homogeneous liquid crystalline systems dependent on the molar fraction of the blocks of the BCP.[36] Leidel and coworkers investigated the kinetics of the alignment of BCP-nanoparticle thin films composed by poly(styrene-*b*-2-vinyl pyridine)-gold under an electric field using in-situ SAXS technique. They could tune and measure the segregated conformations and calculate the kinetics of the processes by varying nanoparticle content and solvent vapor annealing process.[37]

The hydrogen bonding between the P4VP homopolymer and the derivative TTF (2,3-bis(dodecyl thio)-6-(carboxy) tetrathiafulvalene) (TTFCOOH), furthermore to the capacity of the hybrid polymer P4VP-TTFCOOH to be doped upon oxidizing conditions in film state, was already demonstrated in Chapter 2. In a further step, in this chapter thin films of TTFCOOH-functionalized PS-*b*-P4VP (PS-*b*-P4VP-TTFCOOH) capable to transport charges along their surfaces upon oxidation will be explored (Fig. 3.2). For this, firstly the phase-segregation conformation dependence of spin-coated PS-*b*-P4VP-TTFCOOH films with different molar

ratios of the blocks PS:P4VP (concretely 1:1, 4:1 and 1:4) with the subsequent content of TTFCOOH according to P4VP ratio will be studied. The capacity to tune these PS-*b*-P4VP film arrangements at the interfaces by the introduction of the TTFCOOH in P4VP:TTFCOOH proportion of 1:1 will be explored by TEM and SAXS. In this way, a study performed by Kuila and coworkers demonstrated the synergic cooperation of volume fraction and the phase-segregate conformations adopted of hydrogen-bonding-functionalized PS-*b*-P4VP with pyrenebutyric acid (PBA) with π-π stacking properties.[38] Moreover, Kuila and collaborators reported the use of different segregated conformations of 2-(4'-hydroxybenzeneazo) benzoic acid- (HABA) functionalized PS-*b*-P4VP films as nanotemplates for the fabrication of nanomaterials.[39] Finally, the electrostatic response upon doping process of each PS-*b*-P4VP-TTFCOOH film with different molar ratio of PS:P4VP will be conducted by Electrostatic Force Microscopy (EFM). In this way, a correlation between the phase-segregation of the doped PS-*b*-P4VP-TTFCOOH hybrid films and their charge-transportation behaviour will be established.

PS-*b*-P4VP

TTFCOOH
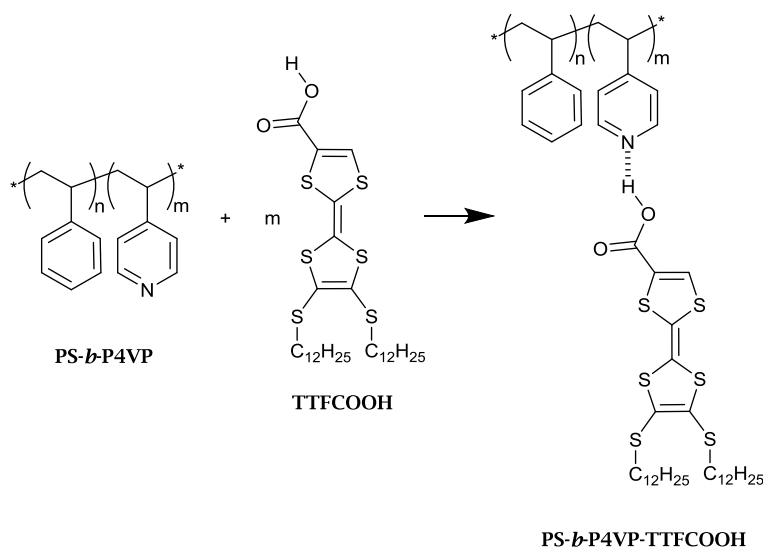
PS-*b*-P4VP-TTFCOOH

Fig. 3.2 *Formation of the PS-b-P4VP-TTFCOOH complex through hydrogen bonding between P4VP and TTFCOOH.*

According to the observations in Chapter 2, EFM is an useful tool to obtain a quick approach in the determination of the electrostatic activity of organic thin films. There are several studies reported using EFM

and/or the equivalent technique Kelvin Probe Microscopy (KPFM)[40, 41] in the characterization of BCP-based semiconductive systems, although they are not the regularly used and still is a field to be explored. For instance, Sowwan *et al.* reported an study of the polarizability of doped DNA-based nanoparticles conducted by EFM and their later use as nanoelectronic and sensing applications.[42] Polymer-blend bulk heterojunctions were characterized by KPFM in a study conducted by Maturová *et al.*[43] Similarly, Spadafora and coworkers used KPFM technique to characterize charge-carrier blends of phase segregated poly(3-hexylthiophene) (P3HT) and [6,6]-phenyl C61 butyric acid methyl ester, allowing the direct visualization of the carrier generation at the donor-acceptor interfaces.[44] On the other hand, Peponi *et al.* with the mapping of a system based on carbon nanotubes (CNT) embedded in a triblock copolymer of poly(styrene-*b*-isoprene-*b*-styrene), characterized the CNT-rich phases using EFM, obtaining a functional self-assembled polymeric and conductive material.[45]

Here, the influence in the arrangement of the phase-segregation driven by the introduction of TTFCOOH units as pendant groups into the PS-*b*-P4VP is presented. For this, TEM and SAXS studies of PS-*b*-P4VP-TTFCOOH with molar ratios PS:P4VP of 4:1, 1:1 and 1:4 are shown. Moreover, the obtained results are correlated with the electrostatic response of the corresponding doped thin films by EFM, permitting to determine which system is the more promising for organic charge-transportation applications (Fig. 3.3).
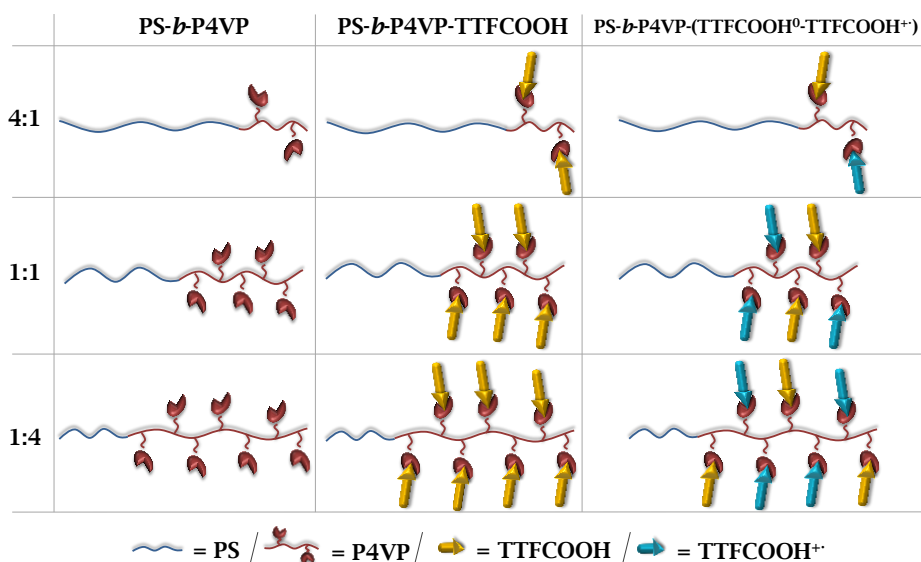
Fig. 3.3 *Resume of studied PS-b-P4VP BCPs, expected PS-b-P4VP-TTFCOOH hybrids and expected mixed valence PS-b-P4VP-(TTFCOOH⁰-TTFCOOH⁺˙) hybrids after doping process.*

3.2.   RESULTS AND DISCUSSION

3.2.1   Phase segregation of PS-*b*-P4VP-TTFCOOH

With the aim of elucidating the influence of the phase segregation of the new PS-*b*-P4VP-TTFCOOH hybrids to their conductive properties, three different PS-*b*-P4VP BCP with different PS:P4VP molar ratios were prepared.[9] For this, the PS:P4VP ratios used were 1:1, 4:1 and 1:4, respectively. The corresponding PS-*b*-P4VP-TTFCOOH hybrids were prepared in chloroform with molar ratio 1:1 of P4VP:TTFCOOH. To determine the conformation of the different phase segregations of the PS-*b*-P4VP 1:1, PS-*b*-P4VP 4:1 and PS-*b*-P4VP 1:4 BCPs and the corresponding PS-*b*-P4VP-TTFCOOH 1:1, PS-*b*-P4VP-TTFCOOH 4:1 and PS-*b*-P4VP-TTFCOOH 1:4 films, SAXS and TEM were used.[46-48]

It is worth mentioning to mention that for TEM characterization and, in order to have an enhance in the contrast between the PS and the P4VP blocks the microtomed samples were stained with iodine (I_2) vapours to have P4VP domains darker from the PS, as a result of the interaction between the I_2 and the P4VP. For the SAXS measurements, a drop of each pure BCP PS-*b*-P4VP 1:1, 4:1 and 1:4 dissolved in chloroform was drop-cast on different silicon surfaces. The same procedure was followed for the corresponding PS-*b*-P4VP-TTFCOOH 1:1, 1:4 and 4:1 hybrid compounds.

The phase segregation of the PS-*b*-P4VP 4:1 BCP observed by TEM (Fig. 3.4a) exhibited a disordered structure with different phase segregation depending on the area. Similarly to what it was observed in the equimolar fraction of BCP, SAXS pattern for the pure compound did not show a concretely packing (Fig. 3.7). In general for all pure BCP samples, poorly ordered or weakly segregated conformations were observed. Moreover, Bragg peaks (q^*) were not able to be assigned, presumably either due to form disordered conformations at the interface or due to the absence of a previous treatment of annealing, which altered and promoted the ordering of the raw phase segregation of the BCPs. Contrastingly, the PS-*b*-P4VP-TTFCOOH 4:1 hybrid material displayed a remarkable change in the self-assembly structure (Fig. 3.4b). The incorporation of the TTFCOOH involved a change of the initial packing structure to a hexagonally packed cylinder (HEX) structure for the new hybrid. The obtaining of a more ordered structure, confirmed the functionalization of the BCP with the TTFCOOH and the tuning of the BCP morphology. The change of the PS-*b*-P4VP structure was also confirmed by SAXS (Fig. 3.7). The PS-*b*-P4VP-TTFCOOH 4:1 hybrid exhibited a domain coexistence between dominant lamellar (LAM) and HEX morphologies due to the appearance of reflections at $2q^*$, $3q^*$ and $4q^*$; and $\sqrt{4q^*}$ and $\sqrt{9q^*}$, respectively. Structure factor extinctions $\sqrt{3q^*}$ and $\sqrt{7q^*}$ for the HEX morphology were also observed indicating a lack of perfect order.[49] Moreover, the domain spacing distance of 4.52 nm and, a scattering pattern similar previously[50] described for hexagonally perforated layers (HPL) arrangement or catenoid-lamellar phase[51], agreed with the TEM results. HPL conformations are given in a narrow range of volume fractions and segregations, between the LAM and cylindrical

morphologies, so probably the BCP-TTFCOOH prepared from the bulk was in an order-to-order LAM-to-HEX transition.[50-53] The orientation of the sample is also a key factor in the SAXS measurements because the scattering signal is given from the different planes. Therefore, after the TEM and SAXS experiments the proposed structure for the PS-*b*-P4VP-TTFCOOH 4:1 consists on the confinement of the TTFCOOH pendant into the P4VP oblique cylinders. At the same time, the TTFCOOH pendants and the P4VP are contained within the PS matrix (Fig. 3.4b).[51]

Fig. 3.4 *TEM images of the phase segregation of a) PS-b-P4VP and, b) PS-b-P4VP-TTFCOOH with PS:P4VP molar ratios of 4:1. Scale bars = 100 nm.*

When the P4VP block was increased, the BCP TEM images of pure PS-*b*-P4VP 1:1 (Fig. 3.5a) showed a LAM arrangement between the PS and P4VP blocks. However, the SAXS presented a noisy signal that could be only correlated with a disordered packing (Fig. 3.7). This was attributed to the large surface analyzed, that probably allowed locally ordered domains in coexistence with disordered, being more prominent the last phase. A similar packing was depicted by TEM for the corresponding PS-*b*-P4VP-TTFCOOH 1:1, even though bigger P4VP domains (in dark) than for the pure BCP could be appreciated due to the presence of the TTFCOOH-pendant moieties in the system (Fig. 3.5b). The SAXS pattern of the PS-*b*-P4VP-TTFCOOH 1:1 (Fig. 3.7) showed a domain spacing distance of 4.67 nm found, larger than the one found for the PS-*b*-P4VP-TTFCOOH 4:1, probably due to a major immiscibility of the PS and P4VP blocks because the larger content P4VP fraction. On the other hand, the phases

corresponding to LAM morphology were identified by the presence of the peaks spaced at reciprocal space position ratios of $2q^*$, $3q^*$ and $4q^*$, which were in concordance with TEM images of the hybrid. Moreover, the incipient scattering peak spaced at $\sqrt{3q^*}$, combined with $\sqrt{4q^*}$ (which matched also with $2q^*$), with a very weak signal at $\sqrt{7q^*}$ and with the broad at $\sqrt{9q^*}$ (which matched also with $3q^*$) suggested the possibility of a coexistence of a HEX phase with a poorly defined scattering signal at $\sqrt{(4/3)q^*}$, together with a relatively intense peak at $\sqrt{(7/3)q^*}$, typically from a gyroid (G) conformation were also spotted. Therefore, these signals suggested that the arrangement of this hybrid was a combined HPL morphology with G domains.[50, 51]
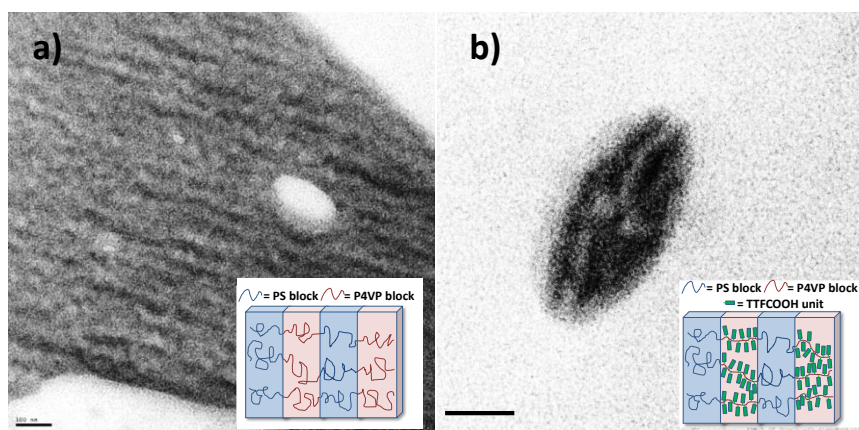
Fig. 3.5 *TEM images of the phase segregation of a) PS-b-P4VP and, b) PS-b-P4VP-TTFCOOH with PS:P4VP molar ratios of 1:1. Scale bars = 100 nm.*

Finally, PS-*b*-P4VP 1:4 BCP TEM images (Fig. 3.6a) showed a phase segregation of G in coexistence with a disordered phase, as it was expected, due to a major predominance of the P4VP domains (dark). Weak scattering signals appeared in the SAXS profile that could be attributed to a poorly ordered (G) phase. Then, an increase in the molar ratio of P4VP block resulted in alteration of the conformation respect to the lower P4VP-content BCPs, culminating in a disorder-to-'low-order' phase transition observation (Fig. 3.7). For the PS-*b*-P4VP-TTFCOOH 1:4 hybrid material, an increasing of the darker domains (corresponded to the major content of P4VP-TTFCOOH bonded units respect to previous samples) were also observed, together with a drastic change in the structure to an HEX

packing (Fig. 3.6b). This was attributed to the introduction of the TTFCOOH pendants and their tendency to self-assemble. SAXS scattering profile (Fig. 3.7) showed a shorter domain spacing with distance (long period), of 4.39 nm, which was related with the major hydrogen bonded TTFCOOH content due to the increase of P4VP molar fraction (larger volume occupied), shortening the spatial distance of the different planes. From the 2-D scattering profile a peak very close to the spatial position of the designated as primary reflection peak for this hybrid, q^*, at approximately $\sqrt{(4/3)\,q^*}$ could be seen, consequently indicating that perhaps a G phase conformation have also been constituted.[54-56] G phase was also identified by the presence of spaced poorly intense peak positions at $\sqrt{(11/3)\,q^*}$ and $\sqrt{(13/3)\,q^*}$ with the corresponding intermediate extinct factors. A phase transition from order-to-order G-to-HEX was the suggested crossing results with the TEM image and, moreover, the appearance weak and broad scattering signals near $\sqrt{3q^*}$ and $\sqrt{4q^*}$ confirmed the proposed arrangement.
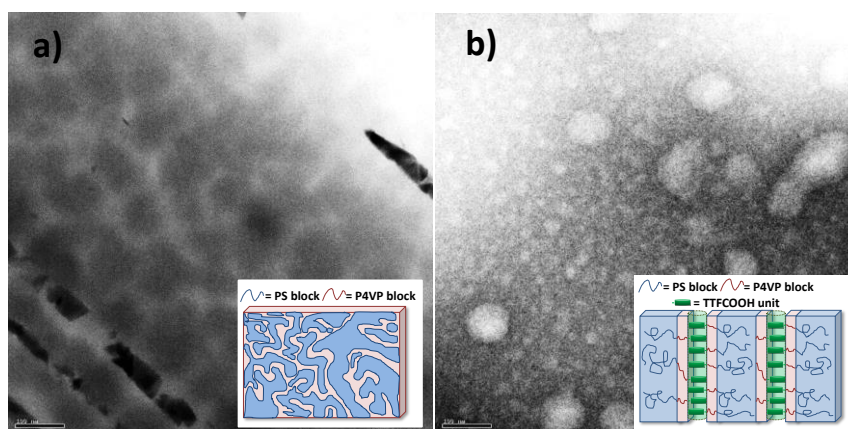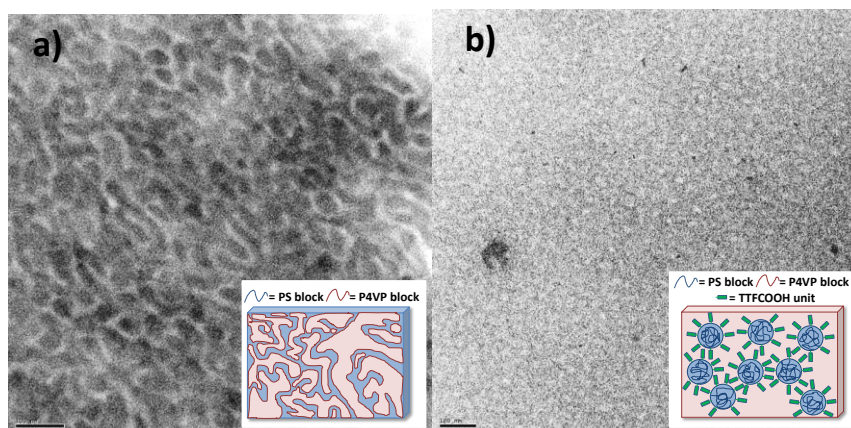

Fig. 3.6 *TEM images of the phase segregation of a) PS-b-P4VP and, b) PS-b-P4VP-TTFCOOH with PS:P4VP molar ratios of 1:4. Scale bars = 100 nm.*
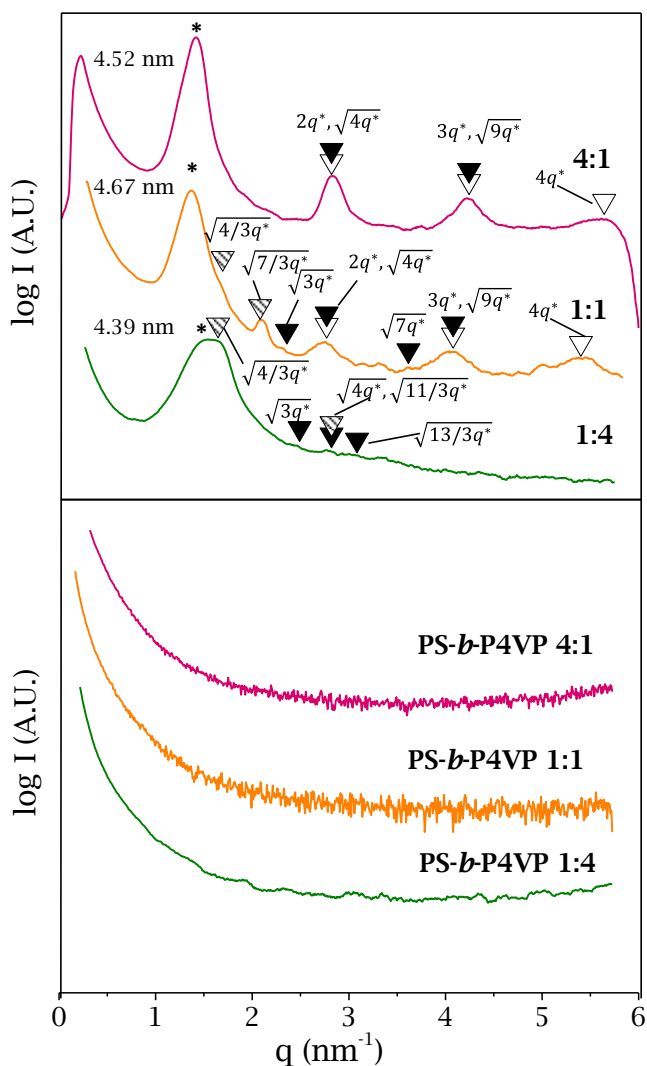
Fig. 3.7 *SAXS profiles of: (on the top) polymer-based hybrids and (on the bottom) neat block copolymers. 4:1 = PS-b-P4VP-TTFCOOH 4:1, 1:1 = PS-b-P4VP-TTFCOOH 1:1 and, 1:4 = PS-b-P4VP-TTFCOOH 1:4. ▽ = gyroid (Ia3d – G), ▼ = hexagonally packed cylinders (HEX), ▽ = lamellae (LAM). * indicates the primary reflection (Bragg peak, q^*). Domain spacing distances (d) were calculated from: $d = 2\pi / q^*$.*

From the TEM and SAXS experiments it could be concluded that untreated PS-b-P4VP BCP and PS-b-P4VP-TTFCOOH drop-cast hybrid samples in different molar ratios, resulted mainly in BCP-based films with a self-arrangement state of non-equilibrium, in coexistence with other segregated conformations. However, the introduction of the TTFCOOH

allows a better identification of the phases and an increase of the ordering and definition of the segregation between the blocks of the BCPs at the interfaces (Fig. 3.8).
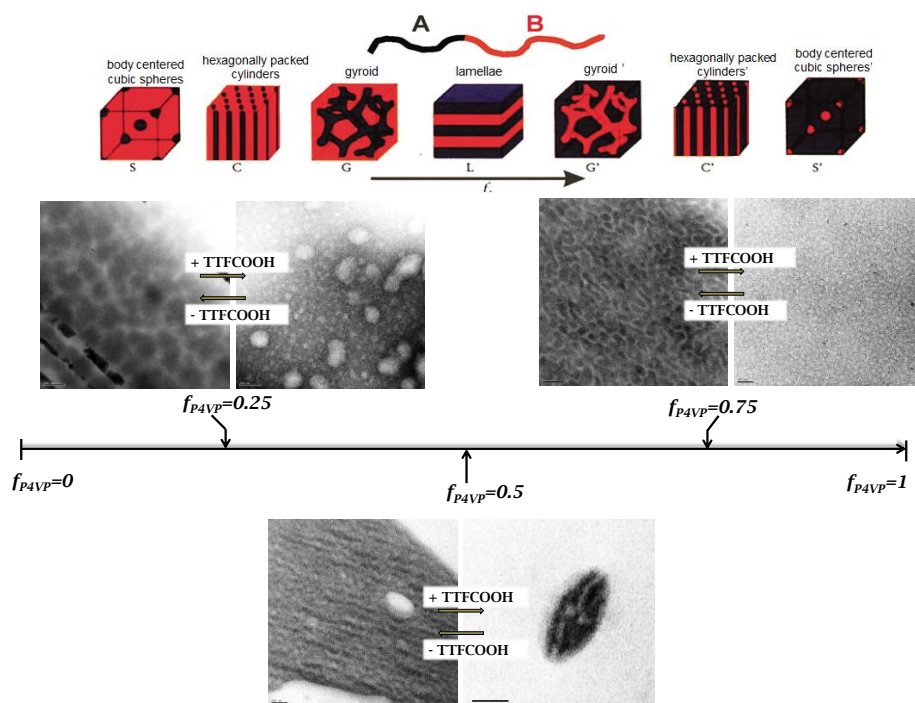
Fig. 3.8 *Diagram of the evolution of the phase segregation conformations observed by TEM of pure PS-b-P4VP BCPs and PS-b-P4VP-TTFCOOH hybrids according to Bates and Fredrickson's theory.[9] f correspond to the P4VP molar fraction ($f_{P4VP}+f_{PS}$ = 1). Scale bars = 100 nm.*

3.2.2 Electrostatic response of doped PS-*b*-P4VP-TTFCOOH thin films

Towards the purpose to obtain a semi-oxidized state of the TTFCOOH pendants of the PS-*b*-P4VP-TTFCOOH, which would allow charge transportation along the self-packed TTFCOOH^0-TTFCOOH$^{+ \cdot}$ (neutral-cation-radical), films of this hybrid material were prepared. For this, different solutions of PS-*b*-P4VP-TTFCOOH at PS:P4VP ratios of 4:1, 1:1 and 1:4 in chloroform were spin-coated on HOPG (Highly Ordered Pyrolytic Graphite), doped using an aqueous solution of iron (III) perchlorate ($Fe(ClO_4)_3$) and analysed by EFM. In parallel and

complementary to this study, an amplitude-voltage statistic study was performed to support that electrostatic changes occurred. First, as a control experiment and in extension of Chapter 2, a film of pure PS-*b*-P4VP-TTFCOOH 1:4 was prepared, immersed in an aqueous solution and analysed by EFM, resulting in non-observable changes before and after immersion, as it was expected. So with this, any change observed in the PS-*b*-P4VP-TTFCOOH by EFM could be attributed to the assembly of the TTFCOOHpendants and their oxidation producing semiconducting films.

In the EFM studies of the undoped PS-*b*-P4VP-TTFCOOH 4:1 film (Fig. 3.9a and Fig. 3.11a), the self-assembled organization of the film in the topography and in the phase images, suggesting an HPL conformation, was also possible to be distinguished, according to the SAXS studies (Fig. 3.7). No significant response in the amplitude could be observed indicating the no existence of electrostatic responsive domains. After doping, a modest change in the topography could be noticed whereas only smooth changes in the phase and in the amplitude were observed (Fig. 3.10a), probably due to the lower content in P4VP and TTFCOOH than the 1:1 film (Fig. 3.11a). Regardless, segregated domains of the doped sample seemed spatially thicker with respect to the undoped, as a direct effect of the doping process. Weak-contrasted amplitude image was spotted, suggesting a lower charge-carrier thin film behaviour respect to the PS-*b*-P4VP-TTFCOOH 1:1 doped film (Fig. 3.11b).
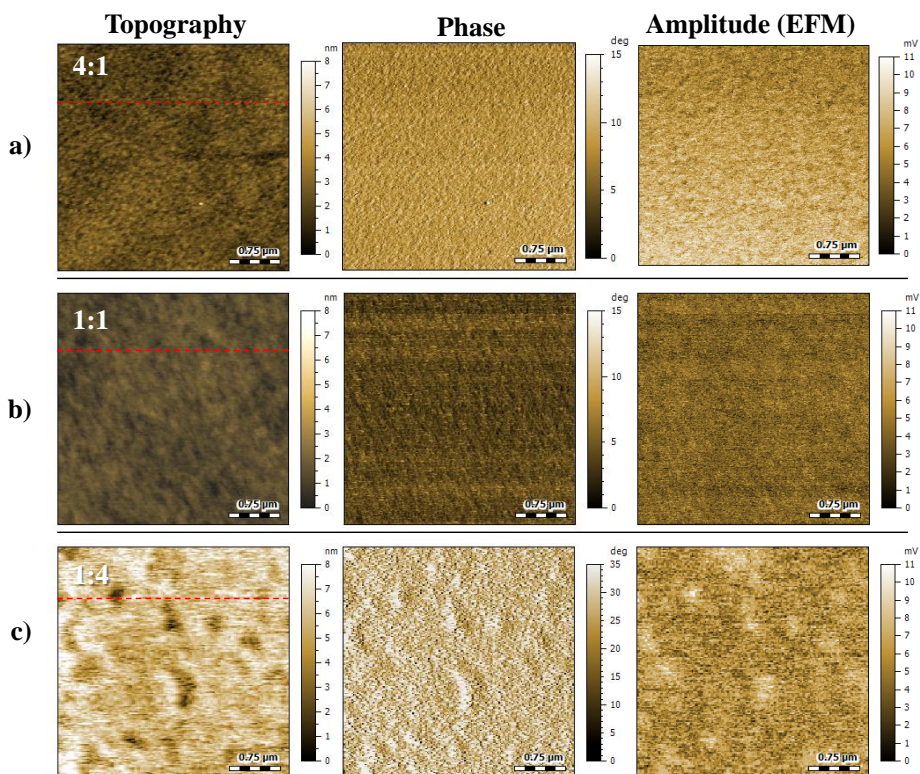
Fig. 3.9 *EFM images of undoped PS-b-P4VP-TTFCOOH films. a) PS-b-P4VP-TTFCOOH 1:1, b) PS-b-P4VP-TTFCOOH 4:1, c) PS-b-P4VP-TTFCOOH 1:4. Dashed lines correspond where the topographic profiles were taken from. Scale bars = 0.75 µm.*

In the case of the undoped PS-*b*-P4VP-TTFCOOH 1:1 film, the topography and the phase images slightly revealed a self-assembly between the blocks of the polymer (Fig. 3.9b), which were in concordance with TEM observations (Fig. 3.5). In the amplitude response in the second mode a practically homogeneous image was recorded, indicating that no electrostatic inhomogeneities on the film surface were obtained, as it was expected. The same film was doped and notable changes in the topography, in the phase and in the amplitude were observed (Fig. 3.10b) with an increase of the relative roughness from few nanometres up to ~15 nanometres (Fig. 3.11b). This phenomena might be as a result of the π-stacking of the disulfur rings between TTFCOOH^0-TTFCOOH$^+$ units, favouring the movement of delocalized charges along the pendant moieties.[57] Moreover, the consistency of the film, given by the amphiphilic

copolymer which had inherent differences in the solubility between each block by nature, prompted the re-assembling during the immersion in the polar medium. The combination of those effects resulted in a charge carrier film as demonstrated the amplitude response in the EFM mode (Fig. 3.10b). Darker zones appeared in correspondence with the protruding structures appeared in the topography, which were attributed to the P4VP-TTFCOOH. This effect was related with the preferential solubility of the P4VP into the aqueous medium during the doping process together with the electrostatically activated self-packing of the TTFCOOH^0-TTFCOOH$^+$ units.
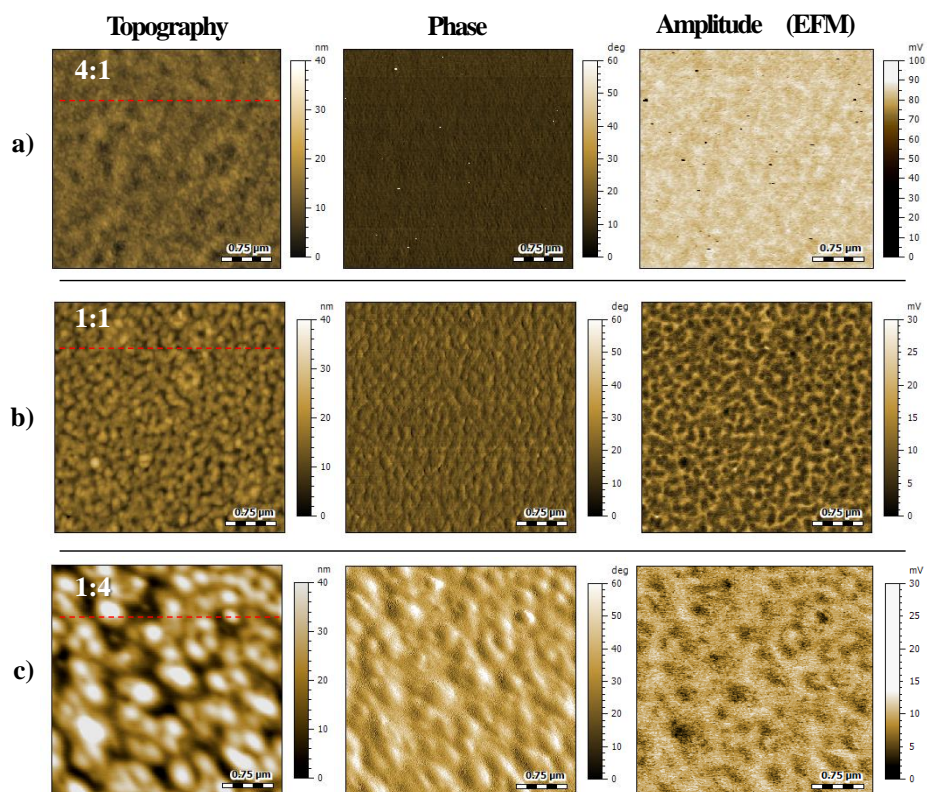
Fig. 3.10 *EFM images of PS-b-P4VP-TTFCOOH films upon Fe(ClO$_4$)$_3$ doping treatment. a) PS-b-P4VP-TTFCOOH 4:1, b) PS-b-P4VP-TTFCOOH 1:1, c) PS-b-P4VP-TTFCOOH 1:4. Dashed lines correspond where the topographic profiles were taken from. Scale bars = 0.75 μm.*

For undoped PS-*b*-P4VP-TTFCOOH 1:4 film (Fig. 3.9c), in the topography and in the phase, low contrasted images were acquired.

Agreed to the topography and the phase to SAXS profile (Fig. 3.7), some domains could be spotted. Unexpectedly, in the image of amplitude response, bright domains appeared smoothly. This observation could be related with two factors: first, by the direct consequence of the composition of the BCP, from the fact that PS phase was in lower proportion than P4VP-TTFCOOH phase and so, slight electrostatic inhomogenities more probably related with the composition were detected; or second, due to the thickness of the film (not perfectly homogeneous) that revealed the conductive HOPG surface that was behind. Once the PS-*b*-P4VP-TTFCOOH 1:4 film was doped, the roughness of the surface drastically changed (Fig. 3.10c and Fig. 3.11c). Spheric-like structures, presumable swollen from the doped film, were observed, resulting in an increase of the relative height of ~30 nm (Fig. 3.11c). This observation was in concordance with the results obtained with PS-*b*-P4VP-TTFCOOH 1:1, although with higher differences between undoped and doped films in this case, due to the higher P4VP ratio respect to the PS. As a result of that, a highly-contrasted image in the amplitude response was acquired (Fig. 3.10c), confirming an electrostatic response when a bias was applied.[47]
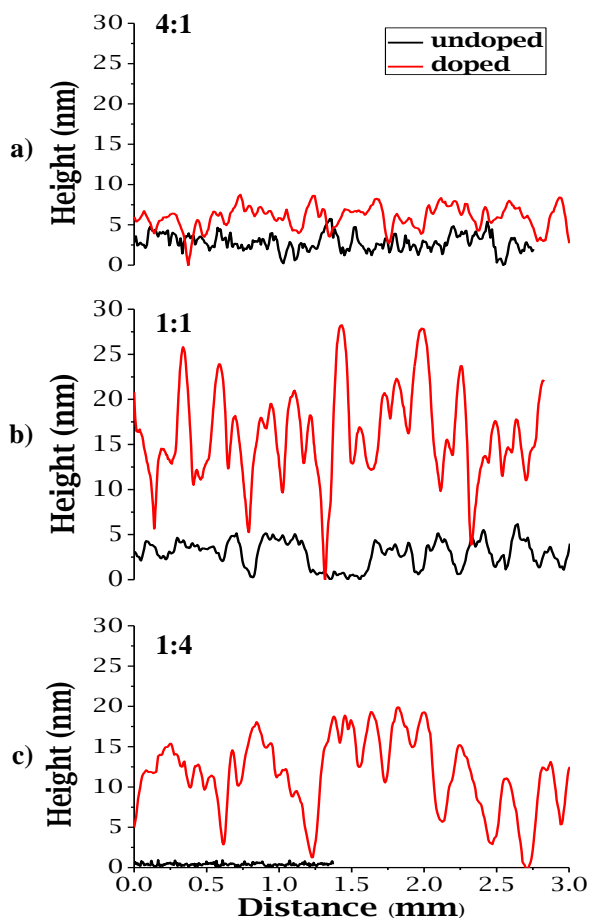
Fig. 3.11 *Height profiles of undoped and doped a) PS-b-P4VP-TTFCOOH 4:1, b) 1:1 and c) 1:4 films.*

Concurrently, to support the previous obtained results, an additional experiment was performed by correlating the hysteresis experienced in the minimum values of the amplitude response between the undoped and doped samples[58]. Plotting this amplitude response vs. the tip bias is possible to obtain curves "V"-shaped that give information about the electrostatic response.[59] As Campbell *et al.*[60] claimed, movement of the charges along the surface of a material could be correlated with the hysteresis of the minimums of the "V"-shaped curves. For this, a control measurement of a P4VP-TTFCOOH (molar ratio P4VP:TTFCOOH of 1:1) thin film which was prepared under the same conditions and analysed before and after doping was performed. Contrary to expectations, the registered shift for P4VP-TTFCOOH homopolymer film was only of 0.006,

taking in account that was the sample with higher TTFCOOH content (Table 3.1). The hysteresis experienced in the amplitude response in PS-*b*-P4VP-TTFCOOH 4:1 was 0.241, while in the case of PS-*b*-P4VP-TTFCOOH 1:1 film, an effective and noticeable shift of 0.454 in the minimum of the amplitude response between the undoped and doped sample was observed. This hysteresis was also related with the dielectric constant of the tunnel barrier effect of the sample,[61] in concordance with the previously obtained results (Table 3.1). However, for the PS-*b*-P4VP-TTFCOOH 1:4 film, a surprisingly hysteresis of 0.176 was obtained, lower than for the PS-*b*-P4VP-TTFCOOH 1:1 film, even the content in TTFCOOH was higher (Table 3.1). This may indicate that the more favourable system to the charge transportation would be the doped PS-*b*-P4VP-TTFCOOH 1:1. A higher mobility of mixed valence charges of TTFCOOH as a result of an advantageous segregated conformation in the BCP-TTFCOOH 1:1 took place, probably induced by the coexistence between the phases HPL and G that promoted a more effective assembly of the TTFCOOH pendant units.

Table 3.1 *Hysteresis of the minimum values of the amplitude response vs. tip bias plots in the EFM mode of the sample.*

Sample	Undoped (V)	Doped (V)	Hysteresis ($|\Delta|_{amplitude}$)
P4VP	0.007±0.004	0.013±0.0002	0.006
PS:P4VP 4:1	1.486±0.101	1.727±0.132	0.241
PS:P4VP 1:1	0.545±0.074	0.081±0.059	0.454
PS:P4VP 1:4	0.184±0.068	0.360±0.104	0.176

3.3. CONCLUSIONS AND OUTLOOK

The adopted self-packing configuration dependence on the molar fraction of the blocks compounding the PS-*b*-P4VP amphiphilic BCP has been demonstrated. Direct analyses performed by TEM and SAXS of these BCPs in different molar ratios obtained from the solid residue remained after solvent evaporation, resulted mainly in disordered domains. The incorporation of TTFCOOH units through the pyridine groups to the PS-*b*-P4VP BCPs, derived in more defined self-arrangements at the non-equilibrium state compared to the pure BCPs, and the coexistence of more than one conformation or phase were presented. It could be concluded that the introduction of a pendant group like the TTFCOOH promoted the re-distribution of the amphiphilic blocks of PS and P4VP at the interface of the BCPs.

On the other hand, consistent thin films of PS-*b*-P4VP BCP, as well as PS-*b*-P4VP-TTFCOOH hybrid in different molar ratios could be achieved by spin-coating. The successfully demonstration of the charge-transfer doped PS-*b*-P4VP-TTFCOOH hybrid thin films was performed by EFM. After doping process, a superficial re-arrangement could be observed in all hybrid thin films and was attributed to the tendency of the doped TTFCOOH$^{\rho}$-TTFCOOH^{-} units to self-assemble in order to enhance the charge transportation along of the generated gaps. These re-arrangements were dependent on the P4VP content and extensively to the TTFCOOH too, more pronounced in the PS-*b*-P4VP-TTFCOOH thin film with molar ratio of 1:1 than the rest. Surprisingly, the organic system with more electrostatic response and more promising perspectives in optoelectronic applications was concluded to be the PS-*b*-P4VP-TTFCOOH hybrid thin film with the molar ratio of 1:1, due to the most favourable adopted phase segregation after the doping process.

3.4. EXPERIMENTAL PART

Living anionic polymerizations of the BCPs were based on the procedure that Varshney *et al.*[62] described.

Materials: styrene ≥99%, 4-vinyl pyridine (containing 100 ppm hydroquinone as inhibitor), *α*-methystyrene 99% (containing 15 ppm *p-tert*-butylcatechol as inhibitor), the initiator *sec*-butyllithium (1.4 M in cyclohexane) and methanol (anhydrous, 99.8%) were purchased to Sigma-Aldrich. THF was HPLC degree from Teknokroma. TTFCOOH was synthesized following the literature procedure.[62]

Synthesis of P4VP: tetrahydrofuran (THF) was dried by refluxing it over metallic sodium with benzophenone for several hours under argon atmosphere. *α*-methystyrene was previously dried by distillation over calcium hydride. 100 ml of THF was transferred to a three-necked round-bottom flask and 1.5 mmols of *α*-methystyrene was incorporated. Later, *sec*-butyllithium was added dropwise to the reaction using a stainless steel syringe until the color of the solution persisted. The color of the solution was given by the formation of the *α*-methylstyryllithium (α-MS-Li$^+$) as a product of the reaction of *α*-methystyrene and *sec*-butyllithium. Then, the reaction was cooled down to -78ºC and the required amount of the 4-vinyl pyridine was added slowly and a sudden change of the color of the initiator was noticed (from red to light yellow). The polymerization was terminated by adding methanol and, a milky and dense solution was obtained. Afterwards, the polymer was recovered by precipitation in hexane and it was thoroughly dried under vacuum (Table 3.2). ^{1}H NMR $(C_7H_7N)_n$ (CDCl$_3$, 300 MHz), δ_H (ppm): 1.27-1.79 (br, 3H), 6.22-6.56 (m, 2H), 8.15-8.58 (m, 2H). M$_w$ (GPC) $(C_7H_7N)_n$: 358 g/mol.

Synthesis of PS-*b*-P4VP: tetrahydrofuran (THF) was dried by refluxing it over metallic sodium with benzophenone for several hours under argon atmosphere. *α*-methystyrene was previously dried by distillation over calcium hydride. 100 ml of THF was transferred to a three-necked round-bottom flask and 1.5 mmols of *α*-methystyrene was incorporated. Later, *sec*-butyllithium was added dropwise to the reaction

using a stainless steel syringe until the color of the solution persisted. The color of the solution was given by the formation of the α-methylstyryllithium (α-MS-Li$^+$) as a product of the reaction of α-methystyrene and *sec*-butyllithium. Then, the reaction was cooled down to -78ºC and the required amount of the styrene was added slowly and a sudden change of the color of the initiator was noticed (from red to light yellow). When the solution turned to intense red again, the polymerization of the P4VP by the addition of the 4-vinyl pyridine started. The polymerization was terminated by adding methanol and a milky solution was obtained. Afterwards, the block copolymer was recovered by precipitation in hexane and it was thoroughly dried under vacuum (Table 3.2). ^{1}H NMR [$(C_8H_8)_n(C_7H_7N)_m$] (CDCl$_3$, 300 MHz), δ_H (ppm): 1.30-1.72 (br, 2H), 1.72-2.30 (m, 4H), 6.17-6.86 (m, 5H), 6.86-7.23 (br, 2H), 8.13-8.63 (m, 2H). M_w (GPC) [$(C_8H_8)_n(C_7H_7N)_m$]: (Table 3.2).

Table 3.2   *Data from polymerizations of P4VP and PS-b-P4VP.*

Homo-/co-polymer	PS:P4VP molar ratio	initiator amount (mmol)	styrene amount (mmol)	4-vinyl pyridine amount (mmol)	M_w (GPC) (g/mol)
P4VP	-	24	-	32	358
PS-*b*-P4VP	1:1	61	40	40	114,664
PS-*b*-P4VP	1:4	36	17	63	42,540
PS-*b*-P4VP	4:1	36	64	16	163,289

Molecular weight determination: molecular weights (M_w) of both homo- and copolymers were determined by gel permeation chromatography (GPC). The chromatographer was calibrated by using standardized samples of PS (from Supelco Inc., PS Standard Kit). The column used was TSK-GEL G3000H 7.8 mm ID x 30.0 cm L with a pore size of 6 µm (from Tosoh Bioscience). THF (HPLC degree) was the eluent, the flow rate was fixed at 1 µl/min, the volume of sample injected in each experiment was 20 µl and the lamp wavelength was set at 254 nm.

Self-assembly of PS-*b*-P4VP-TTFCOOH: solutions of PS-*b*-P4VP 1:1, 4:1 and 1:4 with the corresponding amount of TTFCOOH (10 mM, P4VP:TTFCOOH 1:1 molar ratio) in $CHCl_3$ were separately prepared and vigorously stirred.

Transmission Electron Microscopy (TEM): TEM images were acquired at 120 KV. For sample preparation, solutions of block copolymers with PS:P4VP molar ratio of 1:1, 4:1 and 1:4, and their TTFCOOH-functionalized homologous in $CHCl_3$, were let evaporate in open air until the obtaining of a solid. The solids of each sample were mixed with an epoxy resin and cured for 2 days at 60ºC. Thin slices of 70-100 nm of thickness were cut using a microtome and placed on holey carbon coated copper TEM grids (200 lines/inch). Previously to the TEM analyses, each sample was selectively stained with I_2 vapours in a sealed container for 0.5-1 h to enhance phase segregation contrast.

Film formation of PS-*b*-P4VP-TTFCOOH: from the self-assembled PS-b-P4VP-TTFCOOH 1:1, 4:1 and 1:4 solutions, 170 µl of the prepared solutions were spin-coated on HOPG (Highly Oriented Pyrolytic Graphite, Bruker ZYB grade 12x12x2 mm) surfaces and the free evaporation of the solvent was allowed. The conditions used for film samples formation were: 4000 rpm, 5500 rpm·s^{-2} and 30 seconds of rotation.

SAXS measurements: samples were prepared by drop-casting on silicon surfaces dissolved BCPs in chloroform and evaporation of the solvent in open air. Films were placed in a holder that allowed its free rotation. SAXS measurements were performed at the Institut the Química Avançada de Catalunya (IQAC-CSIC) in collaboration with Dr. Ramon Pons Pons.

PS-*b*-P4VP-TTFCOOH thin film doping process: oxidizing solutions of $Fe(ClO_4)_3$ were freshly prepared prior doping. The molecular ratio of TTFCOOH:doping agent (10:1) Milli-Q water solutions were transferred to different recipients. Films with different molar ratios were immersed in the oxidizing solution for 1 minute, dried with nitrogen flow, cleaned by immersion in Milli-Q water for 1 minute and dried again with nitrogen flow.

Electrostatic Force Microscopy measurements (EFM): all the measurements were made with Nano World Pointprobe silicon SPM sensor tips, provided with a force constant of 2.8 N/m, a coating tip side of Pt/Ir and a coating detector side of Pt/Ir. The measurement atmosphere was controlled by flowing compressed air and N_2, reaching 3.5-5.0% RH. Setpoint values of 2.47 V and 1.9 V were fixed to imaging areas of 2.5x2.5 μm, prior setpoint voltage values were calibrated to reference them to the tip height respect to the sample surface, and the relation was 1 V ~ 30 nm. For the statistic study of the amplitude response vs. the tip bias, voltages from -3 to 3 V in each pixel of the area of the taken image were applied.

3.5.   REFERENCES

1.   J. K. Kim, S. Y. Yang, Y. Lee and Y. Kim, *Progress in Polymer Science*, 2010, **35**, 1325-1349.
2.   J. Heier, E. J. Kramer, S. Walheim and G. Krausch, *Macromolecules*, 1997, **30**, 6610-6614.
3.   J. N. L. Albert and T. H. Epps III, *Materials Today*, 2010, **13**, 24-33.
4.   I. W. Hamley, *Progress in Polymer Science*, 2009, **34**, 1161-1210.
5.   E. B. Gowd, T. Koga, M. K. Endoh, K. Kumar and M. Stamm, *Soft Matter*, 2014, **10**, 7753-7761.
6.   E. B. Gowd, M. Böhme and M. Stamm, *IOP Conference Series: Materials Science and Engineering*, 2010, **14**, 012015.
7.   C. Sinturel, M. Vayer, M. Morris and M. A. Hillmyer, *Macromolecules*, 2013, **46**, 5399-5415.
8.   J. Kao, K. Thorkelsson, P. Bai, B. J. Rancatore and T. Xu, *Chemical Society reviews*, 2013, **42**, 2654-2678.
9.   F. S. Bates and G. H. Fredrickson, *Physics Today*, 1999, **52**, 32.
10.   K. Letchford and H. Burt, *European Journal of Pharmaceutics and Biopharmaceutics*, 2007, **65**, 259-269.
11.   X. Li and Y. Han, *Journal of Materials Chemistry*, 2011, **21**, 18024-18033.
12.   M. Radjabian, J. Koll, K. Buhr, U. A. Handge and V. Abetz, *Polymer*, 2013, **54**, 1803-1812.
13.   J. I. Clodt, V. Filiz, S. Rangou, K. Buhr, C. Abetz, D. Höche, J. Hahn, A. Jung and V. Abetz, *Advanced Functional Materials*, 2013, **23**, 731-738.
14.   D. Klinger, C. X. Wang, L. A. Connal, D. J. Audus, S. G. Jang, S. Kraemer, K. L. Killops, G. H. Fredrickson, E. J. Kramer and C. J. Hawker, *Angewandte Chemie International Edition*, 2014, **53**, 7018-7022.
15.   D. J. Worsfold and S. Bywater, *Canadian Journal of Chemistry*, 1960, **38**, 1891-1900.
16.   C. L. Lee, J. Smid and M. Szwarc, *Transactions of the Faraday Society*, 1963, **59**, 1192-1200.

17. N. Hadjichristidis, H. Iatrou, M. Pitsikalis and J. Mays, *Progress in Polymer Science*, 2006, **31**, 1068-1132.
18. H. L. Hsieh and R. P. Quirk, *Anionic Polymerization: Principles and Practical Applications*, Marcel Dekker, Inc., New York, 1996.
19. A. D'Aprano and R. M. Fuoss, *Journal of Polymer Science*, 1969, **7**, 1101-1109.
20. S. Rangou, K. Buhr, V. Filiz, J. I. Clodt, B. Lademann, J. Hahn, A. Jung and V. Abetz, *Journal of Membrane Science*, 2014, **451**, 266-275.
21. S. Park, B. Kim, J. Y. Wang and T. P. Russell, *Advanced materials*, 2008, **20**, 681-685.
22. R. A. Farrell, T. G. Fitzgerald, D. Borah, J. D. Holmes and M. A. Morris, *International journal of molecular sciences*, 2009, **10**, 3671-3712.
23. W. van Zoelen, E. Polushkin and G. ten Brinke, *Macromolecules*, 2008, **41**, 8807-8814.
24. S.-H. Tung, N. C. Kalarickal, J. W. Mays and T. Xu, *Macromolecules*, 2008, **41**, 6453-6462.
25. C. G. Bazuin and F. A. Brandys, *Chemistry of Materials*, 1992, **4**, 970-972.
26. A. Laforgue, C. G. Bazuin and R. E. Prud'homme, *Macromolecules*, 2006, **39**, 6473-6482.
27. S. Krishnamoorthy, C. Hinderling and H. Heinzelmann, *Materials Today*, 2006, **9**, 40-47.
28. J. Zhu and W. Jiang, *Materials Chemistry and Physics*, 2007, **101**, 56-62.
29. J. Pal, S. Sanwaria, R. Srivastava, B. Nandan, A. Horechyy, M. Stamm and H.-L. Chen, *Journal of Materials Chemistry*, 2012, **22**, 25102.
30. M. P. Kim and G.-R. Yi, *Frontiers in Materials*, 2015, **2**.
31. W. van Zoelen and G. ten Brinke, *Soft Matter*, 2009, **5**, 1568-1582.
32. C.-P. Li, K.-H. Wei and J. Y. Huang, *Angewandte Chemie*, 2006, **118**, 1477-1481.
33. S. Yoo, J.-H. Kim, M. Shin, H. Park, J.-H. Kim, S.-Y. Lee and S. Park, *Science Advances*, 2015, **1**.
34. J.-C. Chen, C.-L. Liu, Y.-S. Sun, S.-H. Tung and W.-C. Chen, *Soft Matter*, 2012, **8**, 526-535.
35. A. Laforgue, C. G. Bazuin and R. E. Prud'homme, *Macromolecules*, 2006, **39**, 6473-6482.
36. J. del Barrio, E. Blasco, L. Oriol, R. Alcalá and C. Sánchez-Somolinos, *Journal of Polymer Science Part A: Polymer Chemistry*, 2013, **51**, 1716-1725.
37. C. Liedel, C. W. Pester, M. Ruppel, C. Lewin, M. J. Pavan, V. S. Urban, R. Shenhar, P. Bösecke and A. Böker, *ACS Macro Letters*, 2013, **2**, 53-58.
38. B. K. Kuila, C. Chakraborty and S. Malik, *Macromolecules*, 2013, **46**, 484-492.
39. B. Nandan, B. K. Kuila and M. Stamm, *European Polymer Journal*, 2011, **47**, 584-599.
40. K. Puntambekar, J. Dong, G. Haugstad and C. D. Frisbie, *Advanced Functional Materials*, 2006, **16**, 879-884.
41. S. Howell, D. Kuila, B. Kasibhatla, C. P. Kubiak, D. Janes and R. Reifenberger, *Langmuir : the ACS journal of surfaces and colloids*, 2002, **18**, 5120-5125.
42. M. Sowwan, M. Faroun, E. Mentovich, I. Ibrahim, S. Haboush, F. E. Alemdaroglu, M. Kwak, S. Richter and A. Herrmann, *Macromolecular rapid communications*, 2010, **31**, 1242-1246.
43. K. Maturová, M. Kemerink, M. M. Wienk, D. S. H. Charrier and R. A. J. Janssen, *Advanced Functional Materials*, 2009, **19**, 1379-1386.
44. E. J. Spadafora, R. Demadrille, B. Ratier and B. Grévin, *Nano letters*, 2010, **10**, 3337-3342.

45. L. Peponi, A. Tercjak, J. Gutierrez, M. Cardinali, I. Mondragon, L. Valentini and J. M. Kenny, *Carbon*, 2010, **48**, 2590-2595.
46. S. Gupta, O. A. Williams and E. Bohannan, *Journal of Materials Research*, 2011, **22**, 3014-3028.
47. B. N. Reddy and M. Deepa, *Electrochimica Acta*, 2012, **70**, 228-240.
48. B. Chu and B. S. Hsiao, *Chemical reviews*, 2001, **101**, 1727-1762.
49. Q. Lan and U. o. Minnesota, *Nanoparticle Dispersions in Polymers: Homopolymer Versus Block Copolymer*, University of Minnesota, 2007.
50. D. A. Hajduk, H. Takenouchi, M. A. Hillmyer, F. S. Bates, M. E. Vigild and K. Almdal, *Macromolecules*, 1997, **30**, 3788-3795.
51. M. M. Disko, K. S. Liang, S. K. Behal, R. J. Roe and K. J. Jeon, *Macromolecules*, 1993, **26**, 2983-2986.
52. R. J. Spontak, S. D. Smith and A. Ashraf, *Macromolecules*, 1993, **26**, 956-962.
53. I. W. Hamley, K. A. Koppi, J. H. Rosedale, F. S. Bates, K. Almdal and K. Mortensen, *Macromolecules*, 1993, **26**, 5959-5970.
54. G. Floudas, R. Ulrich, U. Wiesner and B. Chu, *Europhysics Letters*, 2000, **50**, 182-188.
55. M. W. Matsen, *Physical Review Letters*, 1998, **80**, 4470-4473.
56. K. Yamada and S. Komura, *Journal of Physics: Condensed Matter*, 2008, **20**, 155107.
57. T. Kitamura, S. Nakaso, N. Mizoshita, Y. Tochigi, T. Shimomura, M. Moriyama, K. Ito and T. Kato, *Journal of the American Chemical Society*, 2005, **127**, 14769-14775.
58. R. Dianoux, F. Martins, F. Marchi, C. Alandi, F. Comin and J. Chevrier, *Physical Review B*, 2003, **68**, 045403.
59. J. C. Goeltz and C. P. Kubiak, *The Journal of Physical Chemistry C*, 2008, **112**, 8114-8116.
60. I. H. Campbell, J. D. Kress, R. L. Martin, D. L. Smith, N. N. Barashkov and J. P. Ferraris, *Applied Physics Letters*, 1997, **71**, 3528.
61. A. Roy-Gobeil, Y. Miyahara and P. Grutter, *Nano letters*, 2015, **15**, 2324-2328.
62. S. K. Varshney, X. F. Zhong and A. Eisenberg, *Macromolecules*, 1993, **26**, 701-706.

CHAPTER 4

Electrostatic Responsiveness of a Hierarchically Self-Assembled C_3-Symmetric Tetrathiafulvalene

4.1. INTRODUCTION AND OBJECTIVES

In this Chapter, the preparation of mixed valence molecular materials obtained *via* de-doping process under microfluidic flow and their characterization using a novel method will be studied. Due to the different nature of the studies enclosed in this chapter, the introduction has been divided in several parts for the better understanding of them.

4.1.1. Supramolecular chemistry in electronically relevant molecular materials

The emergence of the supramolecular chemistry[1] has led to different types, sizes and shapes of molecule-based superstructures by spontaneous assembly through non-covalent interactions such as hydrogen bonding,[2, 3] dipole-dipole,[4, 5] charge transfer,[6] van der Waals[7] or π-π stacking.[8] There are countless publications and reviews on this field.[9-12]

Introducing the chirality to supramolecular systems opened new strategies of preparing optically active and hierarchal self-assembled organic compounds, as presented in Chapter 1.[10, 12-14] For example, Danila *et al.*, created organic fibers from a C_3-symmetric tris(TTF) (*N,N',N''*-tris[3[3'-bis [(*S*)-2-methylbutylthio]-tetrathiafulvanelyl]formylamino]-2,2'-bipyridyl]–benzene–1,3,5-tricarboxamide) (C_3-symmetric tris(TTF)) taking advantage of the inherent π-π stacking of the sulfur units of TTFs and intramolecular hydrogen bonding of the component paddle-type moieties (Fig. 4.1).[15]
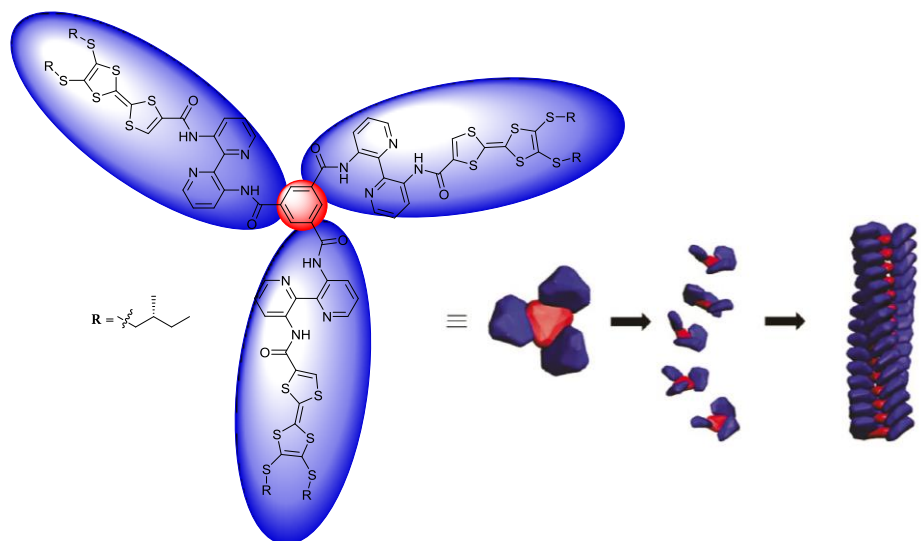
Fig. 4.1 *Model of the self-assembly of the studied C_3-symmetric tris(TTF). Adapted from Danila et al.[15]*

With this approach, they obtained coiled superhelices forming fibers and, at the same time they were able to observe different twisting directions of the (*R*) or (*S*) enantiomers forming a racemic fiber.[15] Moreover, the introduction of the TTFs units allows the preparation of conductive fibers upon a doping process. However, the doping with $Fe(ClO_4)_3$ as oxidizing agent, has not afforded a conductive material. Pursuing the objective to obtain conductive C_3-symmetric tris(TTF)-based materials an alternative is presented in this Chapter. The strategy developed in this Chapter consists on the preparation of conductive fibers by a controlled de-doping process (reverse doping strategy).

Among the techniques that base their principles of actuation on the supramolecular chemistry of compounds to obtain assembled materials, microfluidics has been established as a powerful tool (Fig. 4.2).[16-18] As it has been seen in Chapter 1, microfluidics techniques are based on the manipulation of fluids in sub-millimeter dimensions confined in a closed channel and the manipulable regime of internal fluid dynamics.[19, 20] In this way, Nagl *et al.* used microfluidic chips for chirality screening based on the chemical enantioselectivity of chiral molecules.[21] On the other hand, Stoffelen *et al.* demonstrated microfluidic assisted formation of size-tunable supramolecular nanoparticle clusters driven by

host-guest interactions with cucurbit[8]uril molecules.[22] Furthermore, the potential applications of microfluidics are also widely known in the biological and, concretely in the tissue engineering field.[23-27] In all these applications, the main microfluidics parameter to work with is the internal focusing or hydrodynamic flow focusing of the reactants (fluid dynamics) inside the reaction channel to achieve ordered/aligned or gradient-concentrated materials, among other high-performance properties.[20] Due to the interesting advantages and the potential applications of this technique, the exploration of the influence of microfluidics on the assembly and de-doping process of the C_3-symmetric tris(TTF) is studied in the present Chapter.
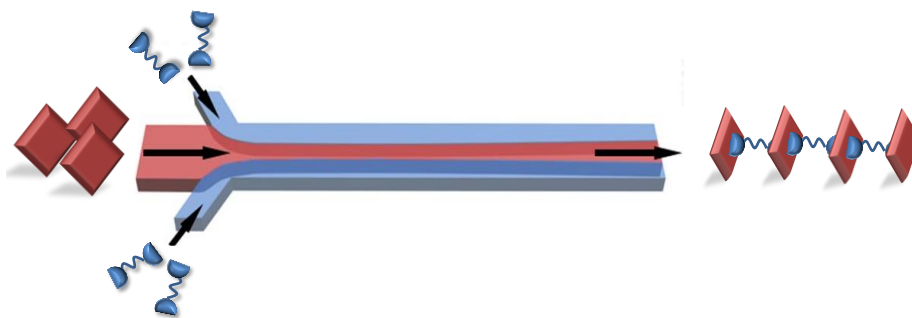
Fig. 4.2 *Representation of the assembly of a compound driven by microfluidics.*

4.1.2. Bimodal AFM

Since the invention of the Scanning Tunnelling Microscopy (STM) by H. Rohrer and G. Binning at IBM's Zurich Research Laboratory in 1982 (for which they were awarded the Nobel Prize for Physics in 1986), there have been many advances in the imaging and probe local properties of materials at the nanoscale.[28] STM operates through detecting the tunnelling current flow generated by an applied external voltage that travels from a small sharp probe (tip) situated above the sample (few angstroms) to a conductive surface (the conductive surface can be the sample or an external piece where the sample is grounded).[29]

On the other hand, Atomic Force Microscopy (AFM) allows obtaining high-resolution images (few nanometers of spatial resolution) of

the surface of not necessarily conductive materials. AFM is a very versatile technique because it can provide information related with the roughness, and hardness of the sample and even is possible to perform atomic manipulation.[30] According to the tip motion, AFM can work in three operational modes: (i) contact mode, in where the deflection of the cantilever is measured while the tip is dragged across the surface of the sample (the cantilever is kept at a constant height respect to the sample), and (ii) non-contact mode, dynamic or amplitude-modulation AFM, is that where the tip is kept close to the surface (contactless) enough the detect the short-range forces (van der Waals forces, dipole-dipole interactions, electrostatic forces, etc.) of the sample (the cantilever oscillates at its resonance frequency tries to keep it constant).[31]

In dynamic AFM, the deflection of the tip is measured in a specific frequency nevertheless the motion of the cantilever is highly non-linear, causing other frequencies encoded in that deflection to be possibly lost.[32, 33] To overcome this limitation, Multifrequency Force Microscopy (MFM) was established, which works using two or more frequencies for the deflection and/or excitation.[32, 34] One of the approaches included in MFM is Bimodal AFM (bimodal-AFM) in where two driving forces are used to drive the vibration of the cantilever.[32, 35] Bimodal-AFM works in two frequency modes, the first mode recalls information either from the amplitude or the frequency shift to provide an image of the topography of the surface of the sample and, in the second mode the amplitude and/or the phase shift are recorded to measure mechanical[36, 37], magnetic[38] or electric[39, 40] changes of the sample surface.[34]

On the other hand, single-pass Electrostatic Force Microscopy (EFM) has been postulated as one of the most advanced techniques in terms of spatial resolution and fastness in data acquisition for the study of electrostatic phenomena at the nanoscale. EFM and Kelvin Probe Force Microscopy (KPFM) techniques have become widely and commonly used in surface characterization of organic semiconductive thin films because they are considered easy and non-destructive methods, as mentioned in previous Chapters.[41-44] Concretely, EFM provides the feasibility of studying electrostatic properties such as dielectric permittivity of insulating materials, surface charge distribution, oxidizing and reduction processes

as well as allowing the distinction between conducting and insulating areas in hybrid materials.[43, 45-51] The EFM technique can be implemented using two different setups: the dual-pass and the single-pass EFM modes. In the dual-pass mode, a conductive tip is used to scan the surface, acquiring in this way the topography in a first scan or pass. Sequentially, the sample is re-scanned (second pass) in non-contact mode biasing the tip, applying AC and DC voltages, in order to collect amplitude and phase variations as a result of tip-sample electrostatic interactions. Because electrostatic interactions strongly depend on the tip-sample distance; the Z-piezo of the equipment is fed with the topographic signal during the second pass, maintaining constant the tip-sample distance.[52] The main drawbacks of the dual-pass EFM are the long time of data acquisition compared with the single-pass setup and the necessity to reduce the drift-effect especially in the Z-axis, with consequent loss of lateral resolution of the electrostatic signal acquired. For these reasons, single-pass EFM has been proposed as an alternative to overcome this scenario. In this setup, a conductive tip is used to obtain the topography using dynamic mode. Concurrently, a combination of AC and DC voltages is applied to the tip, acquiring in this way the topographic and the electrical signals simultaneously. The setup of single-pass EFM provides two output signals at different frequencies, one from the topographic variations and the other from the electrostatic interactions. This approach arises as a faster method for data acquisition, with better lateral resolution and with a better control of tip-sample distance compared with the dual-pass EFM setup.

On the other hand, the frequency chosen for the applied AC voltage to the tip is of great interest in single-pass EFM. Moreover, is considered a key-factor for improving the signal-to-noise ratio and to decrease the topography cross-talk into the electrostatic signal. Because of this, the second resonance frequency of the cantilever is, in terms of signal quality, the more convenient election to be set as frequency value for AC voltage.[53] In the second resonance mode of the cantilever, the signal-to-noise ratio is amplified by the Q-factor of the same cantilever, facilitating the measurement of forces in the order of magnitude of pN, a similar range that electrostatic forces comprise.[54] However, it has to be

remarked that the second resonance mode is, at the same time, influenced by the mechanical properties of the sample; misleading the interpretation of results due to cross-talking with artifacts from the sample. Nonetheless, it has to be considered that cross-talking phenomenon between electrical and topographic signals always occurs due to the nature of the movement of the cantilever and, because of this, its minimization has been an issue of great interest for scientific community.[55-57]

Therefore, the cross-talking anomaly, in which mechanical interactions become indiscernible from tip-sample electrostatic forces, is still a major issue to overcome, specifically in soft and biological samples.[58] In this Chapter a novel method based on bimodal-AFM with the aim to distinguish mechanical from electrostatic interactions in order to reduce cross-talking in the resulting images is then proposed as an alternative to EFM measurements.

In this study, a novel application of bimodal-AFM is presented to draw a distinction between electrical and mechanical contributions by the use of the second resonance mode of the cantilever, i.e. Dual Resonance Electrostatic Force Microscopy (DREFM).[29] The performed study is divided in two main subsections; the first corresponding to the setup of the equipment and the verification that bimodal-AFM can be compared to DREFM. The second part corresponds to experimental tests using a doped organic sample with charge transportation properties, to verify the proposed methodology.

4.1.3.   Objectives

In this Chapter, the behaviour of disk-shaped C_3-symmetric tris(TTF) (*N,N',N''*-tris[3[3'-bis[(*S*)-2-methylbutylthio]-tetrathiafulvalenyl] formylamino]-2,2'-bipyridyl] – benzene - 1,3,5-tricarboxamide) (C_3-symmetric tris(TTF)) (Fig. 4.1), previously synthesized and characterized by Danila *et al.*[15] has been studied. The main objective is to use microfluidic processing to de-dope the C_3-symmetric tris(TTF) structures and thus prepare a mixed valence material that might conduct electricity

with a control at the same time of their assembly. To achieve the main objective, different secondary goals have been proposed:

· The hydrodynamic flow focusing parameter is a powerful tool for enhancing the microstructure of aggregates and it may also affect the self-assembly of the C_3-compound. Therefore, different flow rates and solvents were explored in the microchip, taking as starting point the study performed by Danila et al.[15] in for the neutral molecule. The possibility of controlling and affecting the self-assembly of these neutral helical fibers through the use of microfluidics technology was to be established.

· With the neutral assembly characteristics established, it was planned to obtain mixed valence TTF^0-TTF$^{+·}$ complexes of the C_3-symmetric tris(TTF) fibers with semiconductive properties and demonstrate their electrostatic response by Electrostatic Force Microscopy (EFM), as it was shown in previous Chapters with TTF-based systems.

· Concomitantly with EFM measurements, it was planned to evaluate the effect of the mechanical contributions of the soft material to the electrostatic ones by combining EFM with bimodal-AFM results.

4.2.   RESULTS AND DISCUSSION

4.2.1.   Microfluidics: influence   of hydrodynamic flow focusing on the C_3-symmetric tris(TTF) self-assembly

4.2.1.1. Bulk conditions

The starting point was to reproduce the results obtained in the previous study of Danila et al.[15] In this study, large and twisted fibers of C_3-symmetric tris(TTF) were formed as a result of its self-packing. These superhelical fibers were achieved by precipitation, after cooling down a

hot solution of the C_3-symmetric tris(TTF) ($1 \cdot 10^{-3}$ M) in 1,4-dioxane. The precipitate was deposited on gold surfaces and the Scanning Electron Microscopy (SEM) pictures confirmed the formation of the fibers. In order to study the assembly in microfluidics, an exhaustive study of different bulk conditions and deposition of the aggregates on different surfaces was first performed. In this direction, the influence of the surface on where the fibers were placed,[59, 60] the temperature of the bulk solution[61, 62] and the solvent used were the different parameters studied. For this, the solution of tris(TTF) was prepared in the same conditions with and without applying heat by the use of a heat gun and the results were compared by SEM (Fig. 4.3a-b). In the first two cases fibers were obtained and the helicity could be observed so, it could be concluded that the effect of heating was not a parameter with remarkable impact under these conditions. Nonetheless, after 10 minutes the solution was cooled down without stirring and the resulting aggregates were also analyzed on gold and on glass with coating, in order to observe any influence of the time and the surface (Fig. 4.3c-d). A more contrasted helicity was observed apart from larger and continuous fibers. Moreover, similar assembly showed up in both on gold and glass surfaces. This indicates, on the one hand, that longer times can influence slightly in the consolidation of these supramolecular structures by promoting more encounters between free units and, on the other, the nature of the studied surfaces did not influence neither in the spatial disposition nor in the self-assembly. This observation confirmed the hypothesis that the fibers were formed from the bulk of the solution and not at interfaces.
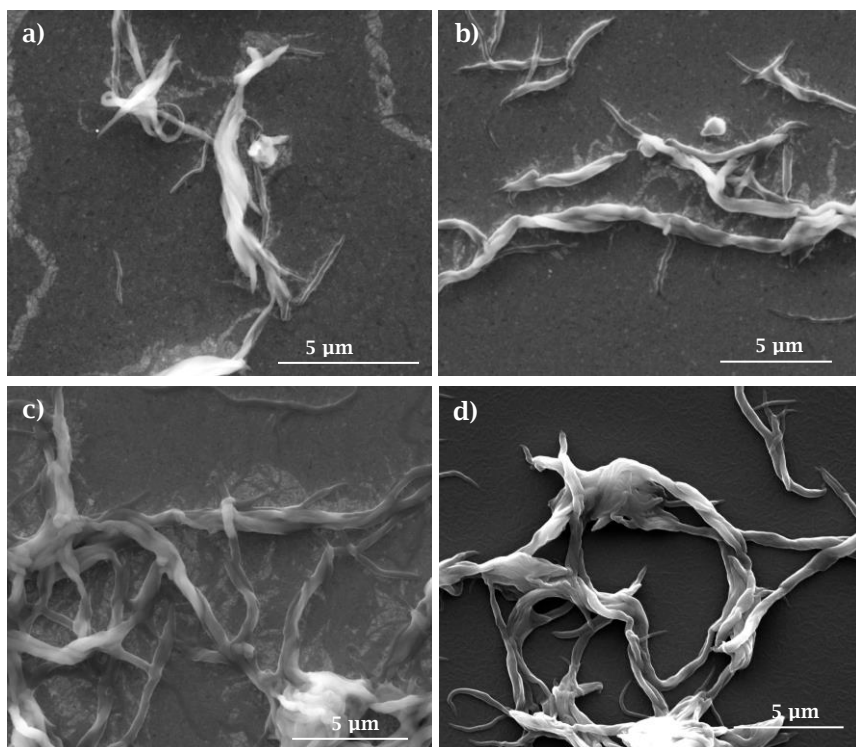
Fig. 4.3 *SEM images of solutions of C_3-symmetric tris(TTF) in 1,4-dioxane drop-cast on gold and glass surfaces: a) without treatment, b) after heating and cooling down, c) 10 minutes after b) and, d) same as c) on glass surface with coating.*

With the objective to obtain similar fibers to the ones observed above with charge-transfer properties by oxidizing TTFs moieties, a doping solution 3.7 mM of iron (III) perchlorate ($Fe(ClO_4)_3$) in ultrapure water (miscible with the 1,4-dioxane) was prepared. Then, the necessary amount of doping solution was added to a heated and cooled down solution of C_3-symmetric tris(TTF) (~0.15 ml) until the TTF^0-$TTF^{+\cdot}$ mixed valence state was reached. Afterwards, taking advantage of the reversibility of the redox character of the TTFs, we prepared a solution 0.36 mM of trimethylamine (TEA) and added the necessary amount to neutralize the charges (~ 0.15 ml). TEA acted as a reducer and the objective was to achieve again the neutral state and check the influence of it in the self-assembly of the system. A drop of each oxidized and reduced states was taken and cast separately on gold surfaces for further analysis with SEM (Fig. 4.4a-b). In the mixed valence TTF^0-$TTF^{+\cdot}$ state similar coiled

fibers were observed (Fig. 4.4a). However, it seemed that some of them were disaggregated, forming narrow and short fibrils. This behavior could mean that the self-assembled structure lost some of its consistency probably due to a higher solubility of it in the intermediate doped state medium. When the fibers were reduced with the TEA and reached again the TTF^0 (neutral) state, they appeared thinner but keeping the π-stacking arrangement characteristic of TTFs (Fig. 4.4b). It is worth mentioning that the reduced fibers appeared very similar to the TTF^0-$TTF^{+\cdot}$ mixed valence state fibers. Therefore, it can be concluded that the fibers of C_3-symmetric tris(TTF) can be reversibly oxidized and reduced without losing their superhelical self-aggregation property.

Dioxane is known in supramolecular chemistry for its natural capacity of acting as a linking agent through the two oxygen atoms placed on the edges of the molecule and even is widely used in metal-organic frameworks (MOFs), in where usually develops linking agent roles.[64-66] With this premise, another solvent was also used to verify the role of 1,4-dioxane in the observed superstructures. Therefore, acetonitrile was selected due to its characteristics: (i) while it can coordinate metal ions, it does not have linking properties, (ii) it solubilizes the doping agent $Fe(ClO_4)_3$ and, (iii) it can be used in microfluidics because it does not swell or degrade the PDMS[67, 68] of the microfluidic chis. Apart from the properties of the acetonitrile, the C_3-symmetric tris(TTF) in its neutral state is insoluble in acetonitrile (even upon heating), whereas it is completely soluble for the $TTF^{+\cdot}$ and the TTF^{2+} oxidized states. This property could act as a visual indicator to easily determine in which state the TTF units of the C_3-symmetric tris(TTF) are.

Ensuring that either the TTF^0-$TTF^{+\cdot}$ or TTF^0 states could also be formed reliably in acetonitrile, a control experiment following the evolution of the different oxidized states with a solution of 0.2 mM of C_3-symmetric tris (TTF) in acetonitrile and adding $Fe(ClO_4)_3$ was followed by UV-Visible absorption spectroscopy (Fig. 4.4c). The appearance and growth of the bands at 701 and 914 nm by the progressively addition of the oxidizing agent certainly indicated the formation of a mixed valence complex.[63] Additional UV-Vis absorption measurements in 1,4-dioxane of the solutions used to take SEM images of Fig. 4.4a-b were performed to

confirm the TTF^0-$TTF^{+\cdot}$ and TTF^0 states (Fig. 4.4d). It was observed that unquestionably the absorption bands were shifted due to the nature of the solvent. However, the incipient signal at 384 nm and the broad band 430-600 nm after being reduced, suggested that not every TTF moiety was totally reduced to the neutral state.
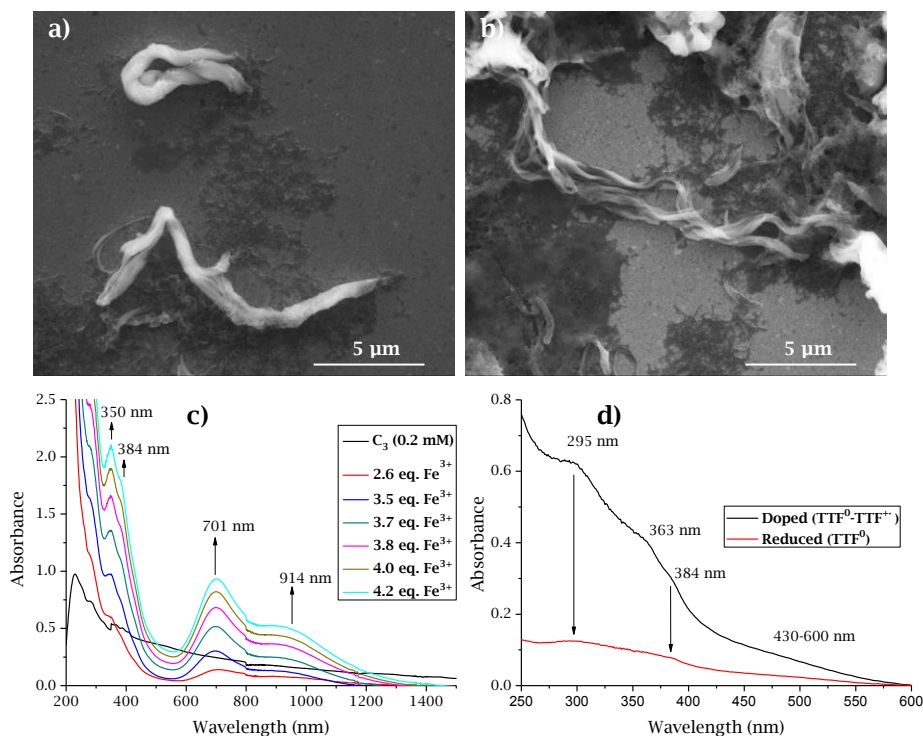
Fig. 4.4 *SEM images of solutions of C_3-symmetric tris(TTF) in 1,4-dioxane drop-cast on gold surfaces: a) doped with $Fe(ClO_4)_3$ and, b) reduced with TEA. UV-Vis spectra of: c) evolution of the oxidized states of C_3-symmetric tris(TTF) in acetonitrile and, d) doped and reduced C_3-symmetric tris(TTF) in 1,4-dioxane solutions used to image samples a) and b), respectively.*

Once it was corroborated that using acetonitrile the TTF^0-$TTF^{+\cdot}$ or TTF^0 states were also reached, the type of the aggregates obtained in this solvent were also analyzed. First, the aggregates obtained for the neutral state were studied. The analyses were made reproducing the same conditions as for 1,4-dioxane and comparing as well the effect of gold and glass surfaces in the arrangement of the derivative TTF molecule. The samples were imaged by SEM (Fig. 4.5).
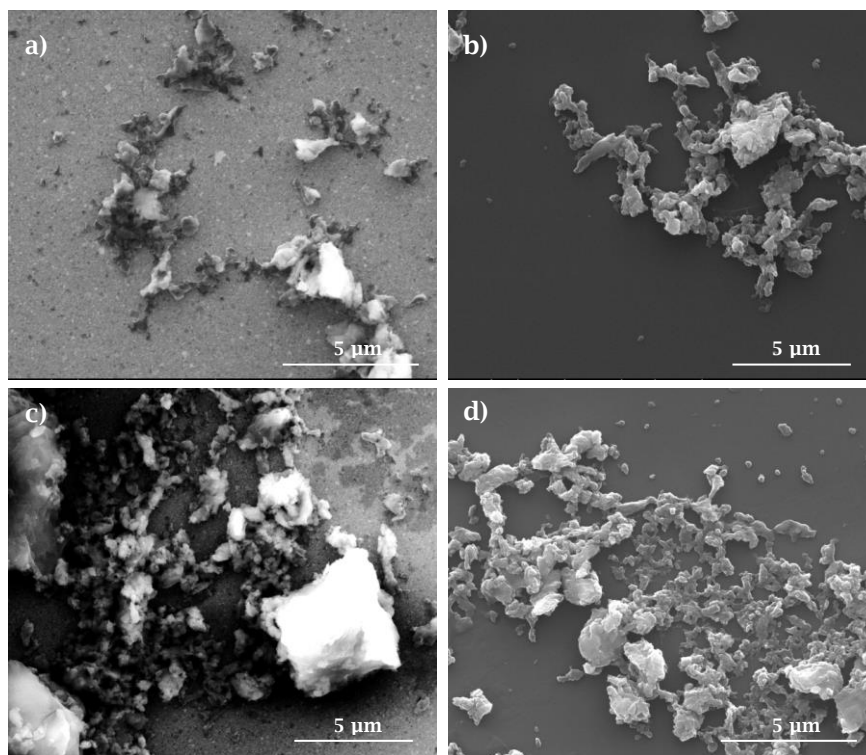
Fig. 4.5 *SEM images of solutions of C_3-symmetric tris(TTF) in acetonitrile drop-cast on gold and glass surfaces: a) hot solution on gold, b) hot solution on glass, c) after cooling down the solution on gold and, d) same as c) on glass surface.*

SEM images showed that no fibrous structures were formed when acetonitrile was used as solvent. This phenomena meant that in the latter case, the solvent 1,4-dioxane played a crucial role in the constitution of consistent coiled fibers of C_3-symmetric tris(TTF). As it was mentioned above, the TTF derivative was totally insoluble in acetonitrile in the neutral state, so the hot solution was directly analyzed (the case when the phenomena of aggregation is less favorable) on gold and on glass (Fig. 4.5a-b, respectively). Rough flakes were observed in both cases, even though a slight tendency of keeping aggregated was appreciated. Similar results were obtained when the solution was cooled down (Fig. 4.5c-d). Temperature did not have a remarkable effect as well as the nature of the surfaces used. The same study was performed upon the doped process using $Fe(ClO_4)_3$ in acetonitrile and a drop of the doped solution was cast

on a glass surface and analyzed by SEM and by Atomic Force Microscopy (AFM) (Fig. 4.6).
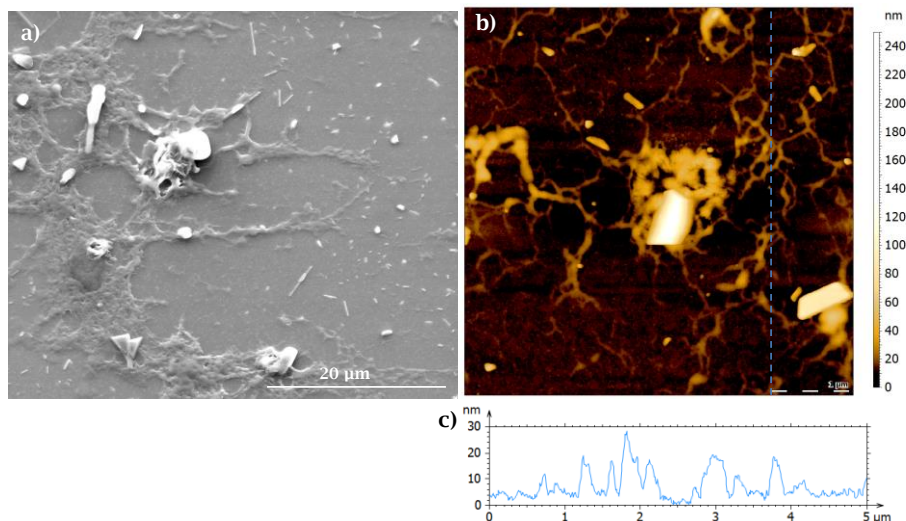
Fig. 4.6 *A drop of C_3-symmetric tris (TTF) in acetonitrile doped solution using Fe(ClO$_4$)$_3$ cast on glass surface. a) SEM image, b) AFM image of the topography (dashed blue line indicates were the height profile was measured) (scale bar 1 µm) and, c) height profile of b).*

A SEM image of the oxidized C_3-symmetric tris(TTF) (Fig. 4.6a) revealed fewer and smaller aggregates as a consequence of the higher solubility of the TTF^0-$TTF^{+\cdot}$ state in acetonitrile (to avoid rough aggregates, the analyzed drop was previously filtered through a filter with a pore size of 0.2 µm). Some tiny and fibrous structures appeared, having a kind of tendency to be aggregated and because of that, the sample was imaged by AFM (Fig. 4.6b). Indeed, the AFM measurements confirmed the presence of fibrous structures. The height profile (Fig. 4.6c) showed that these fibrous structures had a diameter between 19 and 27 nm (supposing cylindrical fibers). The next step was the use of Electrostatic Force Microscopy (EFM) to check the electrostatic response of the fibrous mesh of the doped C_3-symmetric tris(TTF) (Fig. 4.7).
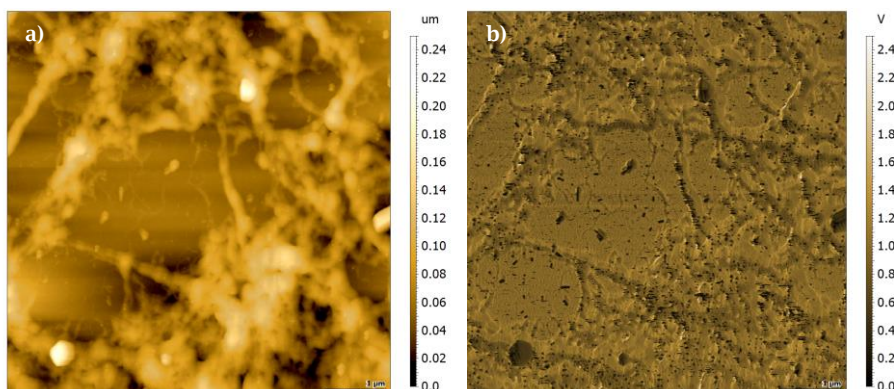
Fig. 4.7 *EFM images of a drop of C_3-symmetric tris(TTF) in acetonitrile doped
solution with Fe(ClO$_4$)$_3$ cast on glass. a) Topography (scale bar 1 μm) and b)
amplitude in the second mode of resonance (scale bar 1 μm).*

In the topography EFM image (Fig. 4.7a) similar fibrous structures
as in the AFM measurements were observed. In the electrostatic response
depicted in the amplitude image (Fig. 4.7b) a higher contrast was revealed.
This might evidence that certainly the fibrous mesh had some kind of
electrostatic response, favored through the gaps generated in the doping
process by the TTF^0-TTF$^{+\cdot}$ charges moving along the self-assembled
microstructure.[50, 69, 70]

Revising the obtained results with both solvents used, the
influence of the microfluidics to the assembly of the C_3-symmetric
tris(TTF) was explored only in the case of acetonitrile. Therefore, the idea
was to study the influence of the hydrodynamic flow focusing through the
manipulation of the flow rates of the microfluidics chips, towards the
formation of fibers when acetonitrile was used, comparing with the bulk
results as well.

4.2.1.2. Microfluidics conditions

The main objective of this part was to establish whether it was
possible to modify the nature of the structuration in the self-assembly of
the neutral C_3-symmetric tris(TTF) obtained in acetonitrile. It has been
shown that the neutral C_3-symmetric tris(TTF) is not soluble in this solvent
and formed rough flakes. However, when TTF units were oxidized and the

doped TTF^0-$TTF^{+\cdot}$ mixed valence state was achieved, fibrous meshes in which charge transportation were obtained.

The different solubility of the C_3-symmetric tris(TTF) molecule when the TTF units are neutral or oxidized was used to design the microfluidics experiments. For the microfluidics experiment the compound must be totally soluble in the feed solutions when they are injected to ensure a reliable precipitation. Then, the designed experiment involved the injection of a solution of the oxidized C_3-symmetric tris(TTF) in acetonitrile and carried out a controlled reduction inside the chip, inducing the precipitation/self-assembly of the neutral C_3-symmetric tris(TTF).

The material used to make the microfluidics chip was poly(dimethyl siloxane) (PDMS) covalently bound to a glass substrate. The chip was built with four inlets arranged symmetrically that they converged into a main channel in which the feeding streams would be mixed by diffusion (the reaction chamber) and flowed into a single outlet (Fig. 4.8).

250 µm
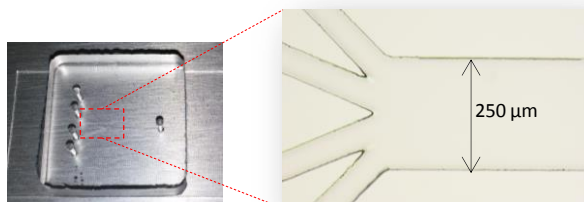
Fig. 4.8 *Images of the chip used in the microfluidics experiments. Size of the main channel (length x width x height): 1 x 0.25 x 0.05 cm.*

In Fig. 4.9 a schematic representation of the experiment is depicted. In one channel a solution of the doped C_3-symmetric tris(TTF) (dC_3-TTF) in acetonitrile was introduced and in the closest channel a solution of TEA was also introduced to have the reaction by diffusion between the doped molecule and the reductant. At the same time, the two other channels were filled with pure acetonitrile to control the lateral flows.
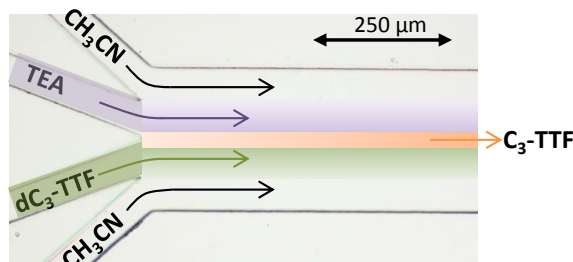
Fig. 4.9 *Layout of the microfluidics experiments.* CH_3CN = *acetonitrile*, TEA = *triethylamine*, d-C_3-TTF = *doped state of C_3-symmetric tris(TTF)*, C_3-TTF = *neutral state of C_3-symmetric tris(TTF).*

The doped C_3-symmetric tris(TTF) mixed valence TTF^0-$TTF^{+\cdot}$ (dC_3-TTF) feed solution was prepared from a stock solution of 0.2 mM of C_3-symmetric tris(TTF) in acetonitrile to which a solution of $Fe(ClO_4)_3$ in the same solvent at a concentration of 0.6 mM was added until the desired oxidized state was reached (~0.94 ml). As the molecule contains three TTF units to be reduced, a solution 0.1 mM of TEA in acetonitrile was prepared. To avoid possible remaining aggregates in dC_3-TTF solution, this was filtered prior its use (0.2 µm pore size). Four experiments were prepared from the basis of TEA:TTF ratios modifying the flow rate of each one and keeping the rest of the parameters invariable, to ensure the total neutralization of the compound (Table 4.1).

Table 4.1 *Detailed summary of the parameters of the different experiments performed in microfluidics.*

TEA:TTF ratio	Flow rates (µl/min)			
	CH_3CN (each)	TEA	dC_3-TTF	TOTAL
0.5:1	100	20	175	400
1:1	100	50	150	400
2:1	100	80	120	400
3:1	100	100	100	100

For each experiment, the reduction processes were followed by optical microscopy in real time and the outgoing suspensions were started

being collected in vials after the stabilization of the system (~ eight s) for three minutes. Additionally, the suspensions collected were analyzed by UV-Visible absorption spectroscopy fifteen minutes after the experiments (Fig. 4.10) and a drop of each one was separately cast on glass surfaces for further analysis by SEM (Fig. 4.11). Firstly, following the evolution of the reduction reaction of the systems through the optical microscope, it was observed that the progressively reduced C_3-TTF was precipitating by diffusion and structures from the precipitate grown from the dC_3-TTF to the TEA stream. This phenomenon occurred because dC_3-TTF was progressively consuming the TEA to reach the neutral state and at the same time it was propagating and growing invading more and more of the reductant stream throughout the main channel of the chip.
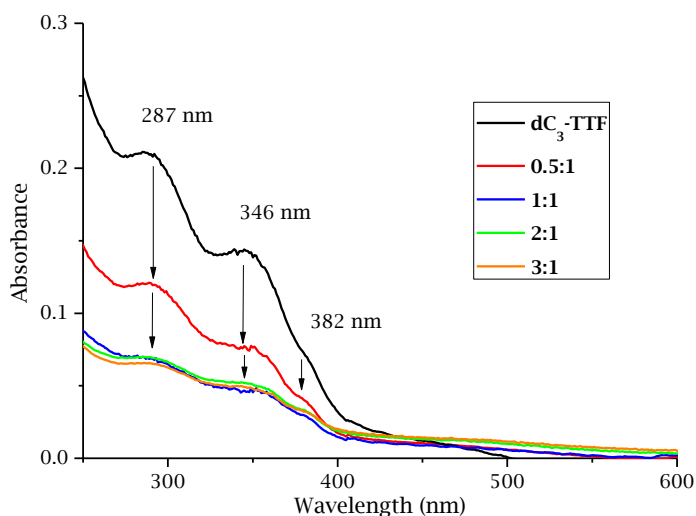
Fig. 4.10 *UV-Visible absorption spectra of the doped feeding solution dC_3-TTF and the solutions collected after microfluidics experiments with ratio TEA:TTF 0.5:1, 1:1, 2:1 and 3:1.*

In the respective UV-Visible absorption spectra of the different outgoing flows from the microfluidics experiments (Fig. 4.10), a relation between the flow rates of the reductant and the degree of oxidation of TTF units could be established. Then, when the flow rate of TEA increased, the degree of oxidation of TTF decreased until the molar ratio TEA:TTF 1:1, in which the degree of oxidation practically kept invariable even if an excess of TEA was added. Absorption signals at 287, 346 and 382 nm were

detected, in concordance with the experiments in bulk with 1,4-dioxane (Fig. 4.4d).
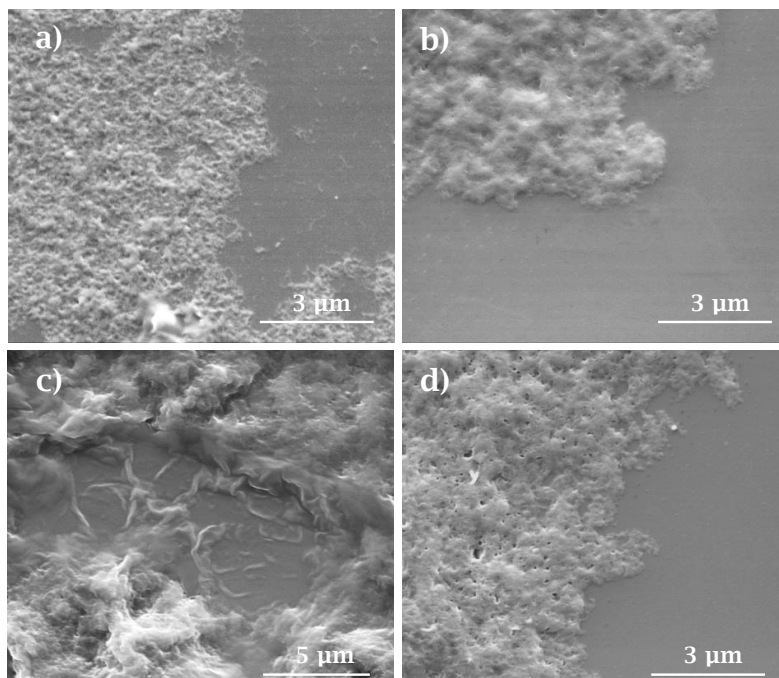
Fig. 4.11 SEM images from outgoing C_3-TTF solutions from the microfluidics experiments TEA:TTF ratios: a) 0.5:1, b)1:1, c) 2:1 and d) 3:1. A drop of each solution was cast on a glass surface (previously cleaned with soap and deionized water) and sputter-coated with gold.

SEM images of the different outgoing C_3-TTF solutions (Fig. 4.11) showed islands of soft matter in all cases. In the 0.5:1 experiment (Fig. 4.11a) a similar aggregation to the one observed in bulk in doped state (Fig. 4.6) was obtained, which is in concordance with the UV-Visible absorption spectrum showed above. Thereby, as the outgoing C_3-TTF solution from the 0.5:1 experiment possessed characteristic absorption signals from the mixed valence state, the aggregation developed in the same way. The 1:1 case (Fig. 4.11b) appeared with undefined and blurred meshed matter, probably due to a major accumulation of the compound in the areas that were imaged. However, in the case of 2:1 (Fig. 4.11c), a fibrous structure could be spotted, indicating that microfluidics had a certainly incidence in the self-assembly of the C_3-TTF compound. The SEM

image from 3:1 experiment (Fig. 4.11d) showed a more fibrous mesh, although it was not possible to distinguish clearly.

On the other hand, the stability of the C_3-TTF outgoing solutions after performing microfluidics experiments was also investigated. The C_3-TTF solutions from experiments TEA:TTF 2:1 and 3:1 as control samples were selected to determine the evolution of the remaining TTF^0-$TTF^{+\cdot}$ signals previously observed by UV-Visible absorption spectroscopy. The absorption spectra of each sample were recorded 1, 24 and 48 hours after each experiment (Fig. 4.12).
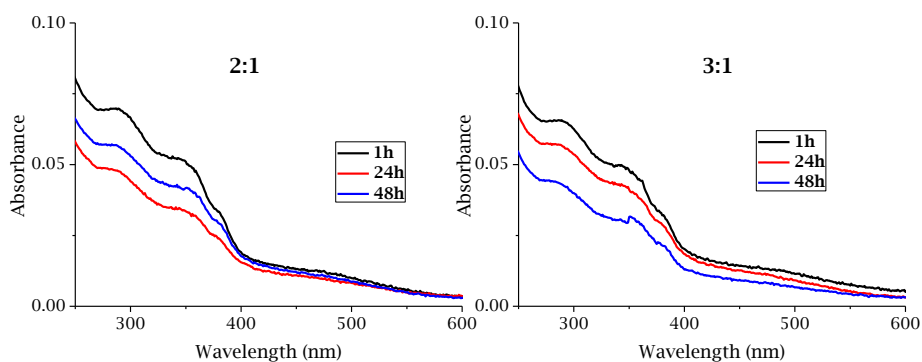
Fig. 4.12 *UV-Visible absorption spectra of the evolution of 2:1 and 3:1 C_3-TTF outgoing solutions from microfluidics experiments after 1, 24 and 48 hours.*

The evolution of the 2:1 and 3:1 solutions (Fig. 4.12) showed a general tendency to decrease slightly the intensity of the remaining TTF^0-$TTF^{+\cdot}$ signals with the time. This could be explained due to the presence of TTF units that were not neutralized and they were progressively reduced by some residual TEA (even the precipitation of the material after the de-doping process was evident). The time of residence for a unit of derivative TTF inside the chip was very short (~ 8 seconds, estimated), so just some of TTF units can be totally reduced inside the micro-device, the rest evolved in the collected solutions from the chip. Unexpectedly, in the 2:1 sample evolution, the signal after 24 hours is less intense rather than 48 hours, for reasons that are not clear at present.

4.2.2. Bimodal-AFM *vs.* EFM: mechanical contributions to electrostatic measurements

This section it is divided in two subsections. The first subsection contains the setup of the equipment and the corresponding verifications for the novel method, in order to demonstrate that bimodal-EFM results could be comparable to DREFM results. In the second subsection, an experimentally applied test of an organic sample, concretely the dC_3-TTF using the novel methodology described is presented.

4.2.2.1. Setup of the equipment

The setup of the equipment for the DREFM approach is shown in Fig. 4.13a, in which an AC voltage signal drive was connected to the piezo-shaker cantilever with a frequency that matched the first resonance frequency of the cantilever (w_1). The amplitude (A_1) was used to depict the topography through the use of a constant amplitude feedback. A second AC voltage was directly rooted to the tip; meanwhile a DC voltage was summed to the AC voltage in order to increase the tip-sample electrostatic interactions. The frequency of the second AC voltage was set to match the second resonance mode of the cantilever (w_2) while changes in the amplitude (A_2) provided information of the electrostatic properties. In the setup for the bimodal-AFM mode (Fig. 4.13b), two AC voltage generators were connected to the piezo-shaker, which forced the vibration of the cantilever at the frequencies w_1 and w_2, the first and second resonant modes of cantilever. Thus, the first mode of resonance, with amplitude A_1, was used to reveal the topography using a constant amplitude feedback and the second mode, with amplitude A_2, provided information of dissimilar mechanical properties of the surface. It is important to remark that, because of the way the equipment was configured, the change from DREFM to bimodal-AFM mode only implied the disconnection of the AC generator from the tip and the subsequent connection of it to the piezo-shaker.
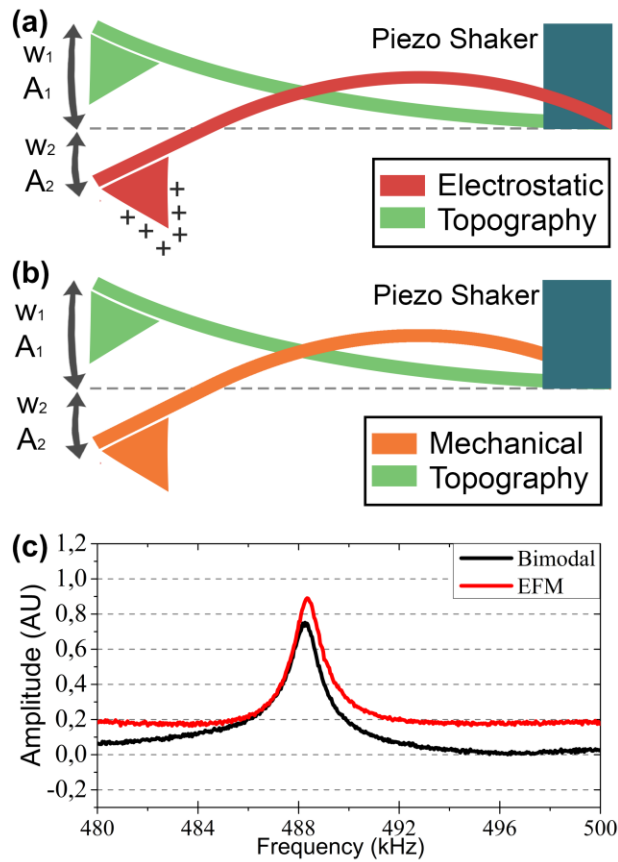
Fig. 4.13 *a) and b) Representations of the vibrational movements of electrostatically-driven and piezo-shaker-driven cantilever. c) Frequency swept of the cantilever acquired in EFM and bimodal-AFM modes.*

Sumali and Epp demonstrated that an electrostatically-driven cantilever can be equivalent to a piezo-shaker-driven cantilever, the cantilever movement being independent of the position (at the base or at the edge of the cantilever) of the applied driving force. [71] Thus, in order to demonstrate that bimodal-AFM could be comparable to DREFM results, a study of an electrostatically-driven and a piezo-shaker-driven cantilever was performed. In this way, with the same cantilever, tip-sample distance and laser position, two frequency sweeps were performed, one in bimodal-AFM and the other in EFM mode. This, resulted in very similar resonance amplitudes in both modes, supporting the assertion that the dynamics of the cantilever were very similar in both modes and consequently, results would be comparable (Fig. 4.13c). Additional information could be

extracted from this analysis, for instance the Q-factors, resonance frequencies and amplitude of the cantilever for both modes, all gathered in Table 4.2. The fact that the resonance frequencies (seen in Fig. 4.13c) and the Q-factors were extremely similar for both cases, validated again that the values resulted from electrostatically- and piezo-shaker-driven cantilever could be comparable and extensively, bimodal-AFM with EFM images could be too.

Table 4.2 *Summary of values for an electrostatically-driven and piezo-shaker-driven cantilever. See experimental part for the calculations of Q-factors.*

	Electrostatic	**Piezo-shaker**
Q-factor	451.26	451.18
Resonance frequency (kHz)	488.34	488.26
Amplitude (mV)	891	751

On the other hand, with the objective to ensure that the setpoint established for the distance tip-sample was comprised within the range of influence of the sample, the correlation between the free amplitude of the tip at the first mode of resonance with the distance tip-sample was performed (Fig. 4.14). For this reason, the free amplitude of resonance of the cantilever was taken as a reference value (2.4 V, in dynamic mode). Then, the tip was progressively approached to a pure gold surface until its free amplitude of resonance became affected due to the proximity to the surface, until both were in contact (Fig. 4.14, point A). With the linear fitting of the region of the curve corresponding to the tip-surface interaction, allowed on first term, knowing the force exerted by the tip to the sample and second, the possibility of working with an amplitude reduction of 25-35%, establishing and standard value of setpoint for the distance tip-sample of 40-60 nm, diminishing in this way, the noise and amplifying the signal.

Fig. 4.14 *Curve of the amplitude* vs. *distance of the cantilever to quantify and calibrate the free amplitude in the first mode of resonance of the cantilever. Linear fit was performed based on $y = a \cdot x + b$.*

The amplitude in the second mode of resonance had to be calibrated as well, also though the plotting of an amplitude *versus* distance curve (Fig. 4.15). In this case, the amplitude of vibration of the cantilever was amplified by a factor of x16 to ensure a good signal-to-noise ratio. Fitting the region of the curve that comprised the tip-surface interaction zone (Fig. 4.15, below point A), the specific setpoint for the second mode of vibration could be ranged between 0.2-1 nm, depending on the specific properties of the sample.
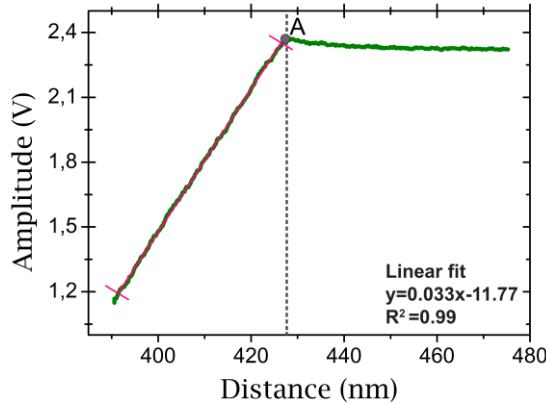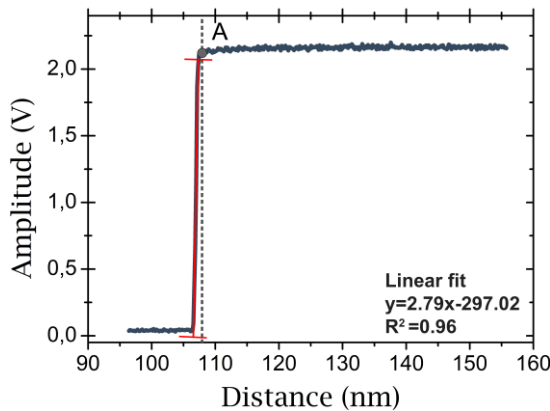

Fig. 4.15 *Curve of the amplitude* vs. *distance of the cantilever to quantify and calibrate the free amplitude in the second mode of resonance of the cantilever. Linear fit was performed based on $y = a \cdot x + b$.*

4.2.2.2. Applied example: dC_3-TTF

The objective with the proposed setup is to discern the electrostatic from mechanic contribution of organic samples by the use of an electrostatically-driven cantilever. Usually, as the force exerted by the cantilever is dependent on the electrostatic properties present on the sample and, at the same time, the cantilever movement can be dependent on the different mechanical properties, the electrostatic outgoing signal can mislead the interpretation of results.

Nevertheless, before applying the methodology described to analyze an electrostatically active organic compound, some previous tests were firstly performed to corroborate the comparability of the DREFM with bimodal-AFM mode signals. Firstly, a reference substrate with dissimilar electrical properties of silicon containing a gold strip of 100 µm of width and 50 nm of height was tested. With this composite substrate a scan on the edge of the gold stripe in DREFM mode was performed, recording in this way the amplitude of vibration in the second mode of resonance. Once the image was finished, the working mode of the microscope was changed to bimodal-AFM. The AC voltage used to drive the piezo-shaker at the second frequency of resonance of the cantilever was adjusted, so that the value of the amplitude of vibration in bimodal-AFM mode was as much alike to the amplitude vibration value in DREFM mode. Moreover, the amplitude of vibration of the cantilever in the first mode and the setpoint were maintained constant in both bimodal-AFM and DREFM modes. The topography (Fig. 4.16a) showed a clear difference in the silicon and gold parts of the substrate due to the difference in height between them. In the image corresponding to the amplitude in the second mode acquired in DREFM (Fig. 4.16b), the conductive part corresponding to the gold and the part corresponding to the silicon could be clearly identified. However, in the amplitude image of the bimodal-AFM mode (Fig. 4.16c) almost no contrast between the two materials could be spotted, confirming in this way that the mechanical properties of both parts were similar, as expected. With this, it could be concluded that contrasted images acquired by DREFM mode depended only on the electrostatic properties of the sample.
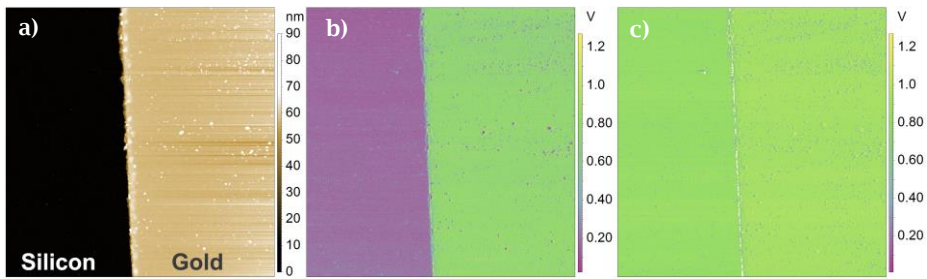
Fig. 4.16Images of 20x20 µm of the reference substrate at the same area. a) Image of the topography from the first pass or scan, b) image of the amplitude acquired simultaneously with the topography in DREFM and, c) the corresponding image of the amplitude acquired in bimodal-AFM.

Additionally, another control experiment to compare the difference between working in and out of resonance in terms of signal-to-noise ratio of the electrostatic signal acquired was performed. This control experiment was also used to demonstrate the dependence of the electrostatic signal with the voltage used. With these objectives, the reference substrate was analyzed in single-pass EFM mode and, during the scanning, amplitude and frequency values were selectively changed (Fig. 4.17). Working in resonance increased dramatically the electrostatic signal respect to working out of it, the increase of the signal being more than 400% (Fig. 4.17a-c). This evidence would enable a further decrease of the tip voltage, resulting in a gain of electrical lateral resolution, as the electrostatic field distribution under the tip has a circular distribution.[72] From the profile depicted in Fig. 4.17b, the differentiation of the electrostatic response of the materials composing the substrate of reference could be clearly observed by using the second resonance frequency of the cantilever. The dependence of the amplitude of vibration of the cantilever with the AC voltage could be also concluded, as was expected due to the conductive nature of the tip, together with the increasing independently of the signal of the driving voltage using the second frequency of the resonance. The amplitude signal recorded for the gold part was obviously more intense due to its metallic nature.
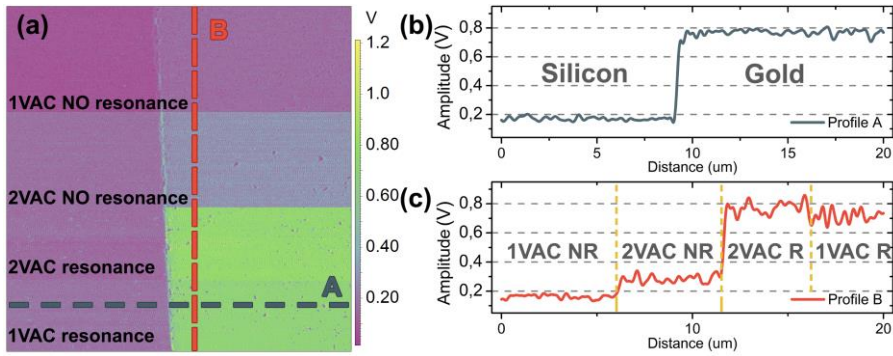
Fig. 4.17 *a) Amplitude image of the reference substrate (20x20 µm) acquired by changing selectively the AC voltage and the frequency of resonance at 1 V and 10 kHz, 2 V and 10 kHz, 2 v and 471.58 kHz and 1 V and 471.58 kHz, from the top to the bottom. b) The amplitude* vs. *distance profile on the X-axis and, c) the amplitude* vs. *distance profile on the Y-axis. The DC voltage was kept constant during the scan at -2 V tip bias.*

Another control experiment using the reference substrate was performed with the objective to demonstrate the bi-directionality of the effect of cross-talking in both, DREFM and bimodal-AFM. For this reason, measurements in DREFM mode were performed in first term and then, in bimodal-AFM. Consequently, the surface was scanned biasing the tip at 2V in AC voltage and working in resonance, while the voltage in DC was changed progressively from 2, 0 and to -2 V. Moreover, the amplitude of resonance *vs.* the bias of the sample in DC voltage was plotted in and out of resonance with the aim to corroborate the gain in sensitivity (Fig. 4.18). When the sample bias was increased, the electrostatic force also increased and, the cantilever vibrated to a given amplitude according to its sensitivity (Fig. 4.18a). The sensitivity of the cantilever in and out of resonance to the DC forces could be compared by extracting the slope of the curves using a linear fit, concluding that working in resonance improved the sensitivity by a factor of a 4.8. On the other hand, a decrease of the electrostatic amplitude within the 0 V region could be spotted in Fig. 4.18b, while increased in the areas corresponding to 2 and -2 V. The electrostatic signal acquired in the phase image (Fig. 4.18c) changed in almost 180º when the voltage changed from -2 to 2 V in DC. This change was in concordance with the fact of changing from attractive to repulsive

forces when the voltage changed, so it could be concluded that electrostatic signal was acquired.
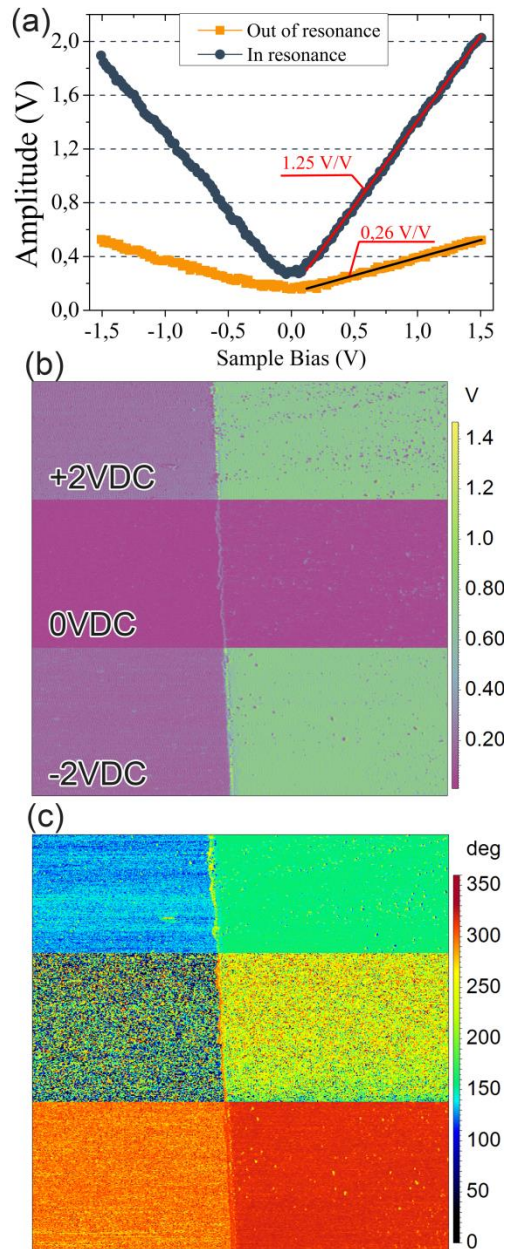
Fig. 4.18 a) Amplitude vs. sample bias obtained from a tip bias of 2 V in AC (the second frequency of resonance of the cantilever, 471.58 kHz) voltage and then changing to a DC voltage on the substrate on the gold of the substrate of reference. b) Amplitude response and c) phase images (20x20 µm) from

*the substrate of reference acquired in DREFM mode with a fixed tip bias of 2
V in AC and working in resonance.*

Afterwards, a similar experiment was performed in bimodal-AFM
mode to prove the bi-directionality of the cross-talking effect. To perform
this, the substrate of reference was scanned in bimodal-AFM mode on the
part of containing the strip of gold, while the sample bias was sequentially
changed from -5 to 5 V in DC at a rate of 20 V/s (Fig. 4.19a). Generally, the
phase is related with the mechanical interactions tip-sample,[73] and the
amplitude response in the second mode of resonance related with the
electrostatic interactions,[56] suggesting in the present case that the
phenomenon of cross-talking was present, due to the narrow correlation
of the signals acquired (Fig. 4.19a). On the other hand, different
electrostatic responses for silicon and gold form the substrate of
reference could be recorded when the DC voltage was sequentially
changed (Fig. 4.19b) thus, revealing also cross-talk from the electrostatic
interactions in the bimodal-AFM mode. So, the cross-talking phenomena
from mechanical and electrostatic interactions in DREFM and bimodal-
AFM modes, respectively, could be corroborated and, the bi-directionality
of the effect could also be demonstrated.
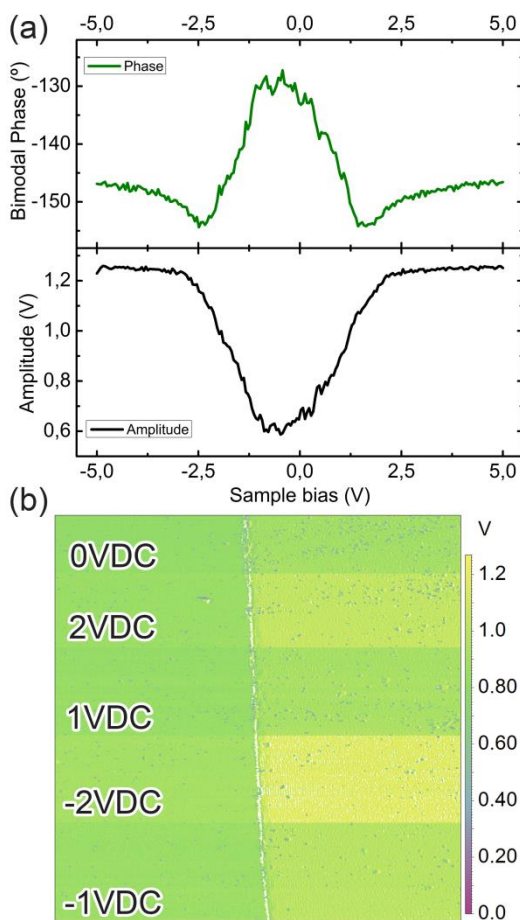
Fig. 4.19 *a) Phase and amplitude response* vs. *sample bias plots in bimodal-AFM acquired from the gold strip of the substrate of reference, the AC voltage was fixed at the second frequency of resonance of the cantilever (471.58 kHz). b) Amplitude image (20x20 μm) of the substrate of reference acquired by changing sequentially the voltage values in DC.*

Once the method was demonstrated and calibrated using the reference substrate, its application on an organic and electrostatically active organic compound was performed. For this reason, as it have been shown in previous sections of the present chapter, the TTF parts of a C_3-symmetric tris(TTF) solution in 1,4-dioxane drop-cast on gold surface could be doped using a solution of $Fe(ClO_4)_3$ (Fig. 4.4). On the other hand and extensively to what it have been demonstrated in chapter 2, where in a derivative TTF was oxidized to the mixed valence state using I_2 vapors as doping agent, here the coiled fibers of C_3-symmetric tris(TTF) obtained in

bulk from 1,4-dioxane solution drop-cast on gold were doped by I_2 vapors exposure. In this way, the doped TTF parts of the C_3-symmetric tris(TTF) fibers (dC$_3$-TTF) were expected to have electrostatic properties that could be analyzed by the novel methodology described.

From the dC$_3$-TTF sample, different regions were chosen with the aim to apply the method. For this reason, each one of the selected areas was firstly scanned using the DREFM mode and subsequently, when the image was already obtained, the working mode was changed to bimodal-AFM in order to acquire the corresponding image for this mode in the same area. In the first area scanned (Fig. 4.20a), hardly any differences could be appreciated in the acquired images corresponding to the amplitude responses when bimodal-AFM (Fig. 4.20b) and DREFM (Fig. 4.20c) modes were compared. In order to clarify whether in this case the mechanical response could be overlapped to the electrostatic, deviations in the amplitude profiles in both modes were compared (Fig. 4.20d). The peaks corresponding to the two larger fibers were coincident or, in other words, could be overlapped, indicating that no further differences between mechanical and electrostatic contributions were displayed and consequently, pointing to cross-talk phenomenon in the DREFM image. The background of the sample showed slight differences in amplitude response, suggesting that the cross-talking phenomenon was less pronounced compared with the large fibers. Even so, it was also thought the possibility that, because the background was proximal to the conductive gold surface while large observed fibers not, the bimodal-AFM results would be influenced by the chemical interaction dC$_3$-TTF-gold, affecting in this way the mechanical contributions and increasing the resulting amplitude contrast.

Fig. 4.20 *Images of the dC$_3$-TTF of 2x2 μm corresponding to a) topography, amplitude response of b) bimodal-AFM mode and c) DREFM mode and, d) height and amplitude profiles obtained from bimodal-AFM and DREFM modes. Blue-dashed line in a) indicates where the profiles depicted in d) were acquired from.*

In another area scanned (Fig. 4.21a), the amplitude image on the fiber showed differentiated regions for bimodal-AFM mode (Fig. 4.21b), indicating that it possessed inhomogeneous mechanical properties, while in the image corresponding to the DRFEM mode (Fig. 4.21c) a practically uniform contrast was observed. Amplitude profiles (Fig. 4.21d) were used to demonstrate that these regions on the fiber could not be overlapped, interpreting the data as a mixture of mechanical and electrical responses, in comparison to the first area analyzed. Although the cross-talk was diminished, the influence of the mechanical contributions to the electrostatic response of the dC$_3$-TTF could not be ensured with these results.
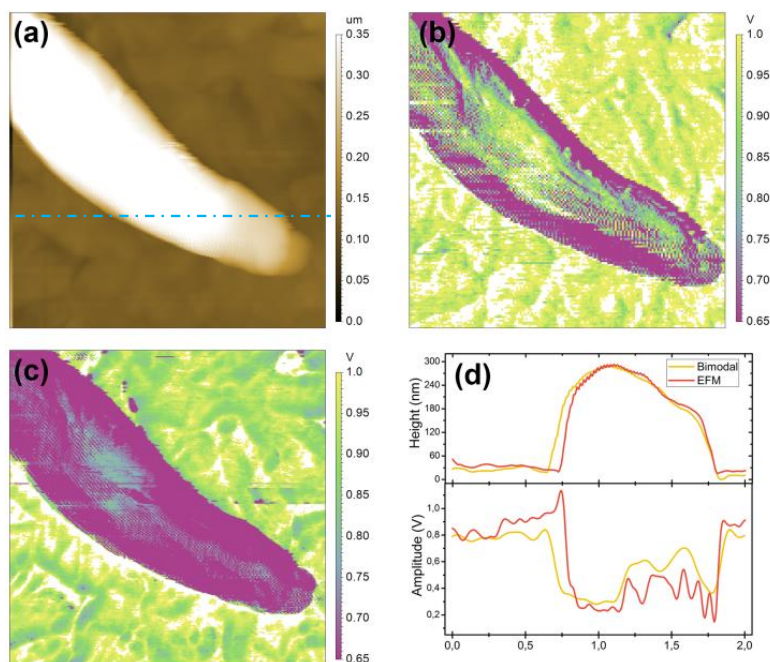
Fig. 4.21 *Images of the dC$_3$-TTF of 2x2 µm corresponding to a) topography, amplitude response of b) bimodal-AFM mode and c) DREFM mode and, d) height and amplitude profiles obtained from bimodal-AFM and DREFM modes. Blue-dashed line in a) indicates where the profiles depicted in d) were acquired from.*

A third area studied (Fig. 4.22a) showed notable differences in the amplitude response images when bimodal-AFM (Fig. 4.22b) and DREFM (Fig. 4.22c) modes were compared. The amplitude image obtained from bimodal-AFM (Fig. 4.22b) revealed a relatively high uniformity, in terms of mechanical contributions (compared with the other analyzed areas), probably as a result of an also very homogeneous distribution of the material on surface. When the working mode was changed to DREFM (Fig. 4.22c), a locally differentiated electrostatic response was evidenced, indicating a non-homogeneous electrostatically-charged sample thus suggesting charge-transportation between the self-assembled doped TTF units of the dC$_3$-TTF compound. Moreover, the differences observed in the contrast of the amplitude DREFM image respect to uniformity in the bimodal-AFM mode (differences of mechanical to electrostatic contributions), confirmed that almost no cross-talking was obtained after using this methodology and real electrostatic response was recorded. This

experiment validated the described methodology in the way of reducing the cross-talk phenomenon between electrostatic and mechanical contributions in an organic sample, together with the demonstration of the charge transportation properties of the dC_3-TTF compound.
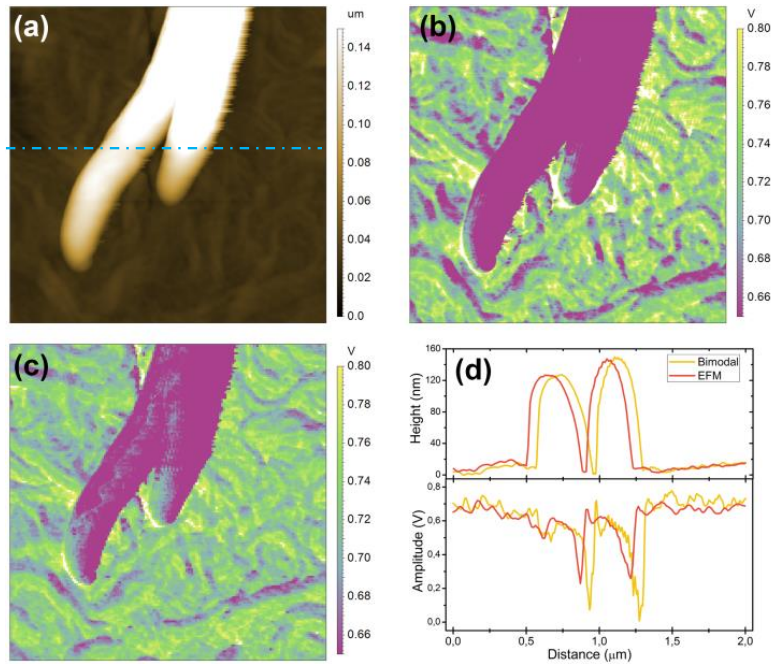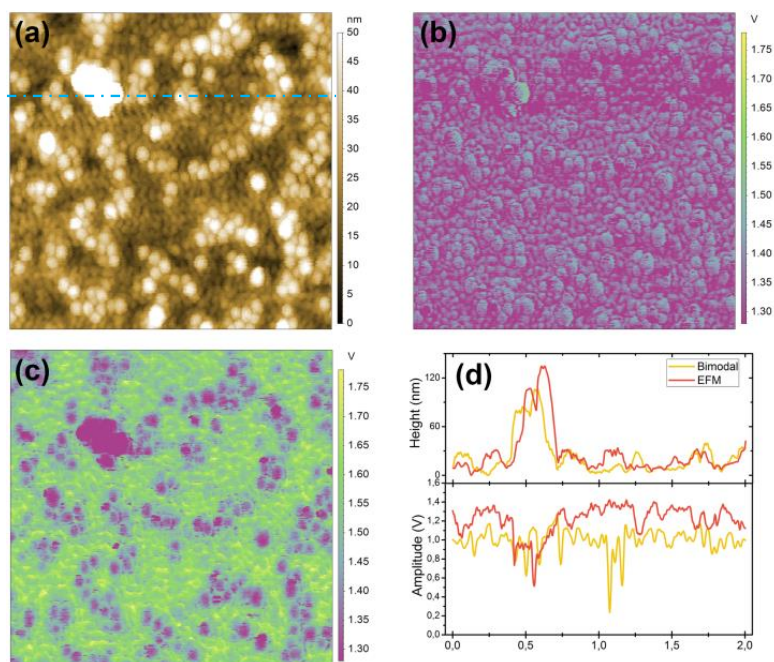

Fig. 4.22 *Images of dC_3-TTF of 2x2 μm corresponding to a) topography, amplitude response of b) bimodal-AFM mode and c) DREFM mode and, d) height and amplitude profiles obtained from bimodal-AFM and DREFM modes. Blue-dashed line in a) indicates where the profiles depicted in d) were acquired from.*

4.3 CONCLUSIONS AND OUTLOOK

In this Chapter it has been demonstrated that redox-responsive coiled C_3-symmetric tris(TTF) fibers can be obtained in 1,4-dioxane, which could play a role of coordinating solvent, either on glass and on gold surfaces. The mixed valence state TTF^0-$TTF^{+\cdot}$ of the self-assembled complex could be achieved upon treatment with a solution of $Fe(ClO_4)_3$

and the reverse process (reduction) by triethylamine. Acetonitrile was another solvent explored due to its particular properties and the different solubility of the doped and neutral C_3-TTF compound, providing completely different flake-like aggregates with some fibrillate regions. Hydrodynamic flow focusing has been demonstrated as a valuable technique in the enhancing of microstructures, improving partially the aggregation of the C_3-symmetric tris(TTF), providing more pronounced fibrils than in bulk in acetonitrile. These fibrous aggregates demonstrated to be still electrostatically active after microfluidics even though the portion of reductant was three times up to the equimolar relation. The activity of the TTF remaining charges in the C_3-symmetric tris(TTF) system was demonstrated to be stable 48 hours after of the experiment.

Moreover, a new method based on Dual-Resonance Electrostatic Force Microscopy (DREFM) mode has been proposed with the objective to draw a distinction between mechanical and electrostatic interactions by the use of single equipment without major changes, such as cantilever or changing the conditions of the measurements. The existence of a cross-talk effect in bimodal-AFM and in DREFM (bi-directionality) has been demonstrated by using a substrate of reference composed of silicon and gold (disparate conductivities but similar mechanical characteristics). Furthermore, the phenomenon associated with cross-talking, which is always observed in EFM and in bimodal-AFM measurements of electrostatically active organic and inorganic samples with uneven mechanical properties, has been diminished and corroborated by testing on a doped dC_3-TTF organic compound with self-assembly and charge-transportation properties, confirming at the same time, the mixed valence state of the TTF parts of the molecule. The proposed study has established as an easy one-step methodology applicable to characterize electrostatically active organic compounds with cross-talking levels below respect to the regular EFM and bimodal-AFM analyses.

4.4 EXPERIMENTAL PART

Bulk experiments: All the surfaces were rinsed with ethanol and dried previously their use. $1 \cdot 10^{-3}$ M of C_3-symmetric tris(TTF) solution in 1,4-dioxane was sonicated and a drop was directly cast on a gold surface (Sense bv type SPR 1.25x12.5x1 mm). The solvent was evaporated freely at room temperature. Then, the same concentration was heated and immediately cooled down using an ice bath. A drop of this solution and was equally taken and cast on another gold surface or glass and the solvent was freely evaporated. For the experiments in acetonitrile, the same procedures and concentrations were used, although the solvent used in the doping solutions was acetonitrile instead of ultrapure water.

SEM: In the case of glass surfaces, samples were sputter-coated with gold to enhance the SEM resolution of the organic compound. The samples were measured at high vacuum conditions where the electron beam acceleration voltage was set between 10 kV and 20 kV.

UV-Visible absorption spectroscopy: Normalized quartz cuvettes with an optical path length of 1 mm were used.

EFM analysis: As samples on glass were previously sputter-coated with gold, for EFM measurements of those samples were simply grounded using conductive silver paint from SPI Supplies. All measurements were made with Nano World Pointprobe silicon SPM sensor tips, provided with a force constant of 2.8 N/m, a coating tip side of Pt/Ir, and a coating detector side of Pt/Ir. The measurements were conducted under controlled atmospheric conditions by flowing compressed air and N_2, to reach 3.5-5.0% of relative humidity.

Microfabrication of the chips: The microfluidics chips were obtained by replica molding technique (soft lithography).[74, 75] The microchannels were fabricated by transferring the complementary structure of a silicon wafer master to poly(dimethyl siloxane) (PDMS) (curing on a hot plate at 150ºC for 10 minutes) and bonding the latter to glass. The silicon wafer master had previously been fabricated by

standard photolithography of SU-8 epoxy resist on top of a silicon substrate (Fig. 4.23).

Microfluidics experimental details: Fluids were introduced to the chip by flexible Teflon® tubing system, including an extra short piece of tube connected to the outlet to facilitate sample collection. Flow rates were controlled using separate syringe pumps for each fluid.

Light

Mask
Photo resist
Si

Photolithography

Master

Pouring and curing PDMS

Peeling-off cured PDMS

Plasma treatment for bonding on glass
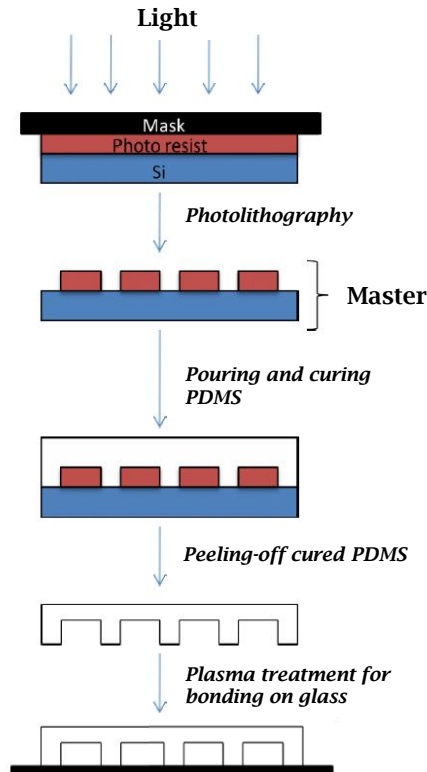
Fig. 4.23 *Scheme of the microfabrication of PDMS chips used in microfluidics experiments.*

Bimodal-AFM and DREFM measurements: This part of the Chapter was elaborated in collaboration with Andrés Gómez-Rodríguez from Institut de Ciència de Materials de Barcelona (ICMAB-CSIC). Bimodal-AFM and DREFM measurements were performed in the same equipment used in EFM measurements of previous chapters. The relative humidity was controlled by a mixture of compressed air and nitrogen streams to reach a HR of 3.5-5.0%. The tips used for those measurements were the

same used in EFM. The reference substrate possessed a Young's modulus of 80 GPa for gold and 150 GPa for silicon and was cleaned by immersion in piranha solution (H_2SO_4/H_2O_2 (30%); 3:1v/v) for 10 s and rinsing thoroughly with ultrapure water before its use. The Q-factor values for the electrostatically-driven and piezo-shaker-driven cantilever showed in Table 4.2, were calculated following Q-factor = $(|f_{-0.7} - f_{+0.7}|)/f_c$, where f_c corresponded to the half of the bandwidth of the curve, $f_{-0.7}$ and $f_{+0.7}$ were the values of the frequencies corresponding to $f_c \pm 0.707$. dC_3-TTF sample preparation procedure consisted firstly on follow the methodology described for bulk experiments in 1,4-dioxane to obtain C_3-symmetric tris(TTF), cast on gold surface. For doping C_3-TTF coiled fibers to obtain dC_3-TTF, the sample was exposed to I_2 ($\geq$99.99% trace metals basis, Sigma-Aldrich) vapours in a sealed container for 30 min.

4.5 REFERENCES

1. S. I. Stupp and L. C. Palmer, *Chemistry of Materials*, 2014, **26**, 507-518.
2. M. Tadokoro, H. Kanno, T. Kitajima, H. Shimada-Umemoto, N. Nakanishi, K. Isobe and K. Nakasuji, *Proceedings of the National Academy of Sciences of the United States of America*, 2002, **99**, 4950-4955.
3. N. A. Wasio, R. C. Quardokus, R. P. Forrest, C. S. Lent, S. A. Corcelli, J. A. Christie, K. W. Henderson and S. A. Kandel, *Nature*, 2014, **507**, 86-89.
4. Z. Mu, Q. Shao, J. Ye, Z. Zeng, Y. Zhao, H. H. Hng, F. Y. C. Boey, J. Wu and X. Chen, *Langmuir : the ACS journal of surfaces and colloids*, 2011, **27**, 1314-1318.
5. T. K. Shimizu, J. Jung, H. Imada and Y. Kim, *Angewandte Chemie International Edition*, 2014, **53**, 13729-13733.
6. W. Zhu, R. Zheng, X. Fu, H. Fu, Q. Shi, Y. Zhen, H. Dong and W. Hu, *Angewandte Chemie International Edition*, 2015, **54**, 6785-6789.
7. D. G. Reuven, K. Suggs, M. D. Williams and X.-Q. Wang, *ACS Nano*, 2012, **6**, 1011-1017.
8. M. Nishijima, H. Tanaka, C. Yang, G. Fukuhara, T. Mori, V. Babenko, W. Dzwolak and Y. Inoue, *Chemical communications*, 2013, **49**, 8916-8918.
9. J. L. Atwood and J. W. Steed, *Encyclopedia of supramolecular chemistry*, CRC Press, 2004.
10. J.-M. Lehn, *Angewandte Chemie International Edition*, 1988, **27**, 89-112.
11. J. P. Sauvage and P. Gaspard, *From Non-Covalent Assemblies to Molecular Machines*, Wiley, 2011.
12. C. Rest, R. Kandanelli and G. Fernandez, *Chemical Society reviews*, 2015, **44**, 2543-2572.

13. K. Bauri, A. Narayanan, U. Haldar and P. De, *Polymer Chemistry*, 2015, **6**, 6152-6162.
14. N. Berova, P. L. Polavarapu, K. Nakanishi and R. W. Woody, *Comprehensive Chiroptical Spectroscopy, Applications in Stereochemical Analysis of Synthetic Compounds, Natural Products, and Biomolecules*, Wiley, 2012.
15. I. Danila, F. Riobe, F. Piron, J. Puigmarti-Luis, J. D. Wallis, M. Linares, H. Agren, D. Beljonne, D. B. Amabilino and N. Avarvari, *Journal of the American Chemical Society*, 2011, **133**, 8344-8353.
16. P. Tabeling, *Current Opinion in Biotechnology*, 2014, **25**, 129-134.
17. M. A. Daniele, D. A. Boyd, A. A. Adams and F. S. Ligler, *Advanced Healthcare Materials*, 2015, **4**, 2-2.
18. B. Shen, J. Ricouvier, M. Reyssat, F. Malloggi and P. Tabeling, *arXiv preprint arXiv:1409.4009*, 2014.
19. P. Tabeling and S. Chen, *Introduction to Microfluidics*, OUP Oxford, 2010.
20. J. M. Martel and M. Toner, *Annual Review of Biomedical Engineering*, 2014, **16**, 371-396.
21. S. Nagl, P. Schulze, S. Ohla, R. Beyreiss, L. Gitlin and D. Belder, *Analytical Chemistry*, 2011, **83**, 3232-3238.
22. C. Stoffelen, R. Munirathinam, W. Verboom and J. Huskens, *Materials Horizons*, 2014, **1**, 595-601.
23. H. Andersson and A. v. d. Berg, *Lab on a Chip*, 2004, **4**, 98-103.
24. M. A. Daniele, D. A. Boyd, A. A. Adams and F. S. Ligler, *Advanced healthcare materials*, 2015, **4**, 11-28.
25. S. A. Castleberry, W. Li, D. Deng, S. Mayner and P. T. Hammond, *ACS Nano*, 2014, **8**, 6580-6589.
26. S. Bai, S. Debnath, K. Gibson, B. Schlicht, L. Bayne, M. Zagnoni and R. V. Ulijn, *Small*, 2014, **10**, 285-293.
27. N. K. Inamdar and J. T. Borenstein, *Current Opinion in Biotechnology*, 2011, **22**, 681-689.
28. J. Wood, *Materials Today*, 2008, **11**, 40-45.
29. R. García, *Amplitude Modulation Atomic Force Microscopy*, 2010.
30. O. Custance, R. Perez and S. Morita, *Nat Nano*, 2009, **4**, 803-810.
31. F. J. Giessibl, *Reviews of Modern Physics*, 2003, **75**, 949-983.
32. R. Garcia and E. T. Herruzo, *Nature nanotechnology*, 2012, **7**, 217-226.
33. J. R. Lozano and R. Garcia, *Physical Review B*, 2009, **79**, 014110.
34. N. F. Martinez, S. Patil, J. R. Lozano and R. Garcia, *Applied Physics Letters*, 2006, **89**, 153115.
35. E. T. Herruzo and R. Garcia, *Beilstein journal of nanotechnology*, 2012, **3**, 198-206.
36. A. X. Cartagena-Rivera, W. H. Wang, R. L. Geahlen and A. Raman, *Scientific reports*, 2015, **5**, 11692.
37. E. T. Herruzo, A. P. Perrino and R. Garcia, *Nature communications*, 2014, **5**, 3126.
38. J. W. Li, J. P. Cleveland and R. Proksch, *Applied Physics Letters*, 2009, **94**, 163118.
39. R. W. Stark, N. Naujoks and A. Stemmer, *Nanotechnology*, 2007, **18**, 065502.
40. U. Bostanci, M. K. Abak, O. Aktas, and A. Dâna, *Applied Physics Letters*, 2008, **92**, 093108.
41. K. Puntambekar, J. Dong, G. Haugstad and C. D. Frisbie, *Advanced Functional Materials*, 2006, **16**, 879-884.
42. S. Howell, D. Kuila, B. Kasibhatla, C. P. Kubiak, D. Janes and R. Reifenberger, *Langmuir : the ACS journal of surfaces and colloids*, 2002, **18**, 5120-5125.
43. F. M. McFarland, B. Brickson and S. Guo, *Macromolecules*, 2015, **48**, 3049-3056.

44. W. Melitz, J. Shen, A. C. Kummel and S. Lee, *Surface Science Reports*, 2011, **66**, 1-27.
45. G. Paul, *Nanotechnology*, 2001, **12**, 485.
46. M. Zdrojek, T. Mélin, H. Diesinger, D. Stiévenard, W. Gebicki and L. Adamowicz, *Physical Review Letters*, 2006, **96**, 039703.
47. E. Escasain, E. Lopez-Elvira, A. M. Baro, J. Colchero and E. Palacios-Lidon, *Nanotechnology*, 2011, **22**, 375704.
48. G. Gramse, I. Casuso, J. Toset, L. Fumagalli and G. Gomila, *Nanotechnology*, 2009, **20**, 395702.
49. Y. Jiang, Q. Qi, R. Wang, J. Zhang, Q. Xue, C. Wang, C. Jiang and X. Qiu, *ACS Nano*, 2011, **5**, 6195-6201.
50. K. L. Sorokina and A. L. Tolstikhina, *Crystallogr. Rep.*, 2004, **49**, 476-499.
51. J. M. Pelto, S. P. Haimi, A. S. Siljander, S. S. Miettinen, K. M. Tappura, M. J. Higgins and G. G. Wallace, *Langmuir : the ACS journal of surfaces and colloids*, 2013, **29**, 6099-6108.
52. M. W. Fairbairn, S. O. R. Moheimani and A. J. Fleming, *Microelectromechanical Systems, Journal of*, 2011, **20**, 1372-1381.
53. H.-J. Butt, B. Cappella and M. Kappl, *Surface Science Reports*, 2005, **59**, 1-152.
54. C. Riedel, A. Alegría, G. A. Schwartz, R. Arinero, J. Colmenero and J. J. Sáenz, *Applied Physics Letters*, 2011, **99**, 023101.
55. S. Sadewasser and T. Glatzel, *Kelvin Probe Force Microscopy: Measuring and Compensating Electrostatic Forces*, Springer Berlin Heidelberg, 2011.
56. S. Magonov and J. Alexander, *Application Note, Agilent Technologies, Inc*, 2008.
57. Naumov I.I., Bellaiche L.M., Prosandeev S.A., Ponomareva I.V., Kornev I.A., Ferroelectric nanostructure having switchable multi-stable vortex states, Patent US7593250, 2008.
58. E. Castellano-Hernández, F. B. Rodríguez, E. Serrano, P. Varona and G. M. Sacha, *Nanoscale Research Letters*, 2012, **7**, 250-250.
59. J. C. Love, L. A. Estroff, J. K. Kriebel, R. G. Nuzzo and G. M. Whitesides, *Chemical reviews*, 2005, **105**, 1103-1170.
60. F. Tao, *Pure and Applied Chemistry*, 2008, **80**, 45-57.
61. Q. H. Wang and M. C. Hersam, *Nature chemistry*, 2009, **1**, 206-211.
62. K. D. Sattler, *Handbook of Nanophysics: Nanoelectronics and Nanophotonics*, CRC Press, 2010.
63. E. Gomar-Nadal, L. Mugica, J. Vidal-Gancedo, J. Casado, N. J.T.L., J. Veciana, C. Rovira and D. B. Amabilino, *Macromolecules*, 2007, 7521-7531.
64. C.-P. Li and M. Du, *Chemical communications*, 2011, **47**, 5958-5972.
65. J. Kua, R. C. Daly, K. M. Tomlin, A. C. T. v. Duin, T. B. Brill, R. W. Beal and A. L. Rheingold, *The Journal of Physical Chemistry A*, 2009, **113**, 11443-11453.
66. T. Hasell, J. L. Culshaw, S. Y. Chong, M. Schmidtmann, M. A. Little, K. E. Jelfs, E. O. Pyzer-Knapp, H. Shepherd, D. J. Adams, G. M. Day and A. I. Cooper, *Journal of the American Chemical Society*, 2014, **136**, 1438-1448.
67. J. N. Lee, C. Park and G. M. Whitesides, *Analytical Chemistry*, 2013, 6544-6554.
68. K. Ren, J. Zhou and H. Wu, *Accounts of Chemical Research*, 2013, **46**, 2396-2406.
69. M. J. Cadena, R. Misiego, K. C. Smith, A. Avila, B. Pipes, R. Reifenberger and A. Raman, *Nanotechnology*, 2013, **24**, 135706.
70. D. D. Kulkarni, S. Kim, M. Chyasnavichyus, K. Hu, A. G. Fedorov and V. V. Tsukruk, *Journal of the American Chemical Society*, 2014, **136**, 6546-6549.
71. H. Sumali and D. S. Epp, SEM International Modal Analysis Conference XXIV, St. Louis, MO, 2006.

72. A. Kumar, T. M. Arruda, A. Tselev, I. N. Ivanov, J. S. Lawton, T. A. Zawodzinski, O. Butyaev, S. Zayats, S. Jesse and S. V. Kalinin, *Scientific reports*, 2013, **3**, 1621.

73. W. W. Scott and B. Bhushan, *Ultramicroscopy*, 2003, **97**, 151-169.

74. A. Jahn, S. M. Stavis, J. S. Hong, W. N. Vreeland, D. L. DeVoe and M. Gaitan, *ACS Nano*, 2010, **4**, 2077-2087.

75. S. Marre and K. F. Jensen, *Chemical Society reviews*, 2010, **39**, 1183-1202.

CHAPTER 5

Microfluidics as a Platform to Design Tetrathiafulvalene-Based Ionically-Driven Coacervated Hydrogels and to Enhance their Microstructure[*]

5.1.   INTRODUCTION AND OBJECTIVES

The synthesis and obtaining of ordered and/or aligned compounds have been a targeting issue for many researchers due to the continuous pursuit of improving materials.[1-5] Highly-ordered polymers can be obtained either, by synthetizing them with functional catalysts[6-8] or by post-modification techniques.[9, 10] The goal in this field is mainly focused on enhancing the properties such as charge transportation[11], chirality transfer[12] or optical properties[13, 14] through the alignment of the microstructure of the compounds. The microstructure of block copolymers (BCPs) can be tuned by, for instance changing experimental conditions[15-17], molecular structure[18], electric field[19, 20], inclusion of other compounds such as ionic liquids[21] or nanoparticles[22, 23], among other pathways.[24] Furthermore, there are also some specific synthetic techniques that could influence in the BCPs in a similar way. This is the case of microfluidics, which is an interesting tool for micro- and nano-fabrication that generally takes advantage of the reactants under conditions of laminar flow to obtain aligned and ordered compounds or products, controllable by the hydrodynamic flow rates.[25-27] Micro- and nanofabrication techniques, supposed a remarkably breakthrough platform in tissue engineering approaches, constructing comprising microfibers, microparticles and hydrogel building blocks as the extensive literature reported.[28-33] In this way, microfluidics emerged as a novel and promising tool for micro- and nano-fabrication of devices as it has been reviewed in Chapter 1 and experimentally observed in Chapter 4.

On the other hand, hydrogels played a decisive role in the polymers field due to their solubility in water that makes them suitable for biological applications.[34, 35] According to Chung and coworkers, microfibers from hydrogels obtained by laminar flow-based multiple phase coaxial flowing systems in microfluidic devices, results in suitable gels for tissue scaffolds.[30] One of the most important and biocompatible hydrogels are the poly(ethylene glycol) (PEG) -based hydrogels, which provides good biocompatibility and the hydroxyl ending groups offer the possibility to be reacted with other monomers towards the building of

complexes 3D-copolymer networks.[36-40] Hunt *et al.* synthetized an ABA PEG-based triblock copolymer poly(allyl glycidyl ether-*b*-ethylene glycol-*b*-allyl glycidyl ether) (P(AGE-*b*-EG-*b*-AGE)) as groundwork to further addition of ionic functionalities through the AGE blocks. The different functionalities were introduced *via* post-polymerization by coupling independently guanidinium hydrochloride- (*Guan*) and sulfonate- (*Sulf*) as ending groups in the main P(AGE-*b*-EG-*b*-AGE) copolymer. In this way, they were able to develop the role of polyelectrolytes, when they were dissolved in water and to achieve the gelation by ionic coacervation[†] (Fig. 5.1).[41] They designed modular, self-organized and well-defined ABA triblock copolyelectrolytes for robust, highly tunable, dynamic and responsive materials.[42]

[†] Ionic coacervation is the spontaneous process in which two molecules oppositely charged in solution (polyelectrolytes) form a neutral and dense phase, usually a gel, as a result of their cross-linking.
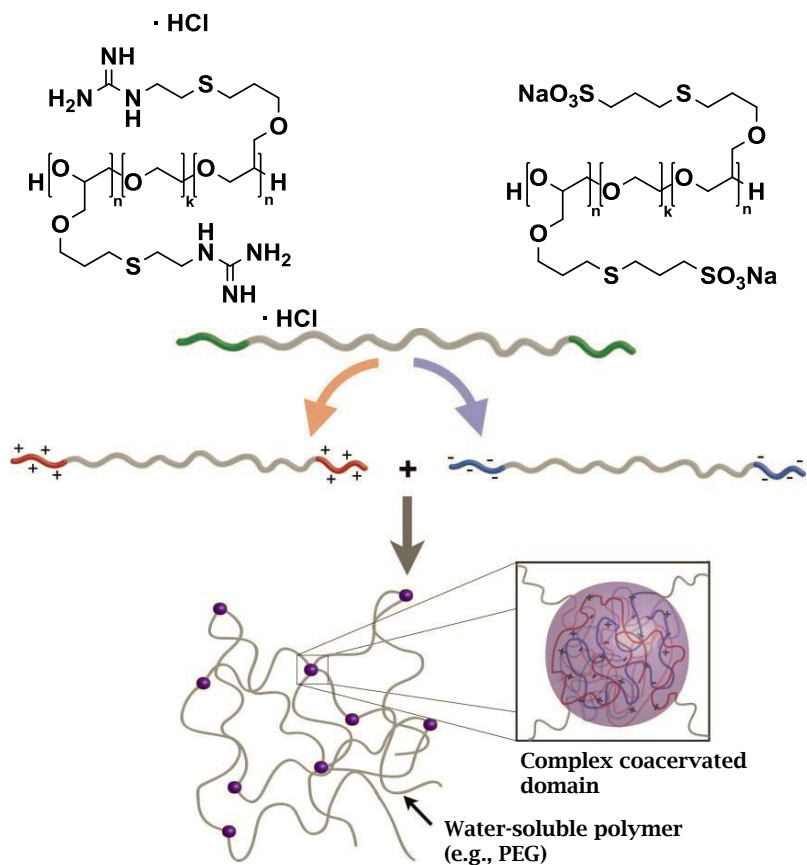
Fig. 5.1 *Representation of the gelation of* Guan- *and* Sulf-*based triblock P(AGE-*
b-EG-b-AGE) copolymer polyelectrolytes driven by ionic coacervation (degree
of polymerization n = 3.5k and k = 10k).[42]

Due to the high solubility in water and good properties of the
P(AGE-*b*-EG-*b*-AGE) triblock copolymer, it resulted very appropriate
candidate for its manipulation using microfluidics. First, the influence of
microfluidic-based synthesis to the improvement of its internal
microstructure was studied. Secondly, due to the fact that *Guan*
functional copolymer offered available reactive sites (amine groups), the
introduction of an acid derivative tetrathiafulvalene (TTF), concretely the
2,3-bis (dodecylthio)-6-(carboxy) tetrathiafulvalene (TTFCOOH)[43], was also
explored in order to obtain hydrogels with charge transportation
properties, with a high control of the structure. Previously, our group
studied the selectivity of the different phases of TTF-based xerogels by
controlling the temperature while doping, resulting in conductive gels.[44, 45]

Similarly, a study developed by Kitamura and coworkers explored electroactive doped TTF-based organogelators. They obtained fibrous gels based on the crosslinking *via* hydrogen bonding of TTF-functionalized amino acids.[46]

Micro- and nanofabrication techniques have been used for the immobilization of hydrogels for several applications, being the development of biomaterials the most studied.[47-49] From all the micro- and nanofabrication techniques, soft lithography and, concretely micro-contact printing (μcP), has emerged as the most used.[50] μcP offers the possibility to control specifically deposition/bonding of molecules on surface by a direct/intimate contact molecule-surface. There are several studies reporting the immobilization of polymers on surface applying μcP.[51-56] Different type of hydrogels such as acrylamide[57], PEG-based[58] and gelatin[59] have been functionalized on surfaces for the study of the cell adhesion and growth. Extending these examples to the P(AGE-*b*-EG-*b*-AGE) triblock system, the micro-patterning of the ionically-driven coacervated hydrogel on surface was explored, involving different immobilization routes and μcP steps. Moreover, the inclusion of the supported hydrogels was also studied.

5.2. RESULTS AND DISCUSSION

5.2.1. Enhancement of the microstructure of ionically-driven coacervated hydrogels by hydrodynamic flow focusing

In this section, first the study of the pure ionically-driven coacervated hydrogel based on P(AGE-*b*-EG-*b*-AGE) obtained from the bulk-based synthesis method and from the microfluidics-based one are presented. Secondly, the introduction of the TTFCOOH to get TTFCOOH-functionalized hydrogels prepared from the bulk and from microfluidics method is also described.

5.2.1.1. Hydrogel system

The synthesis and characterization of the hydrogel obtained by ionic coacervation of *Guan* an *Sulf* triblock copolymers was previously reported by Hunt and coworkers.[42] In that study, they determined the minimum concentration and mixture in aqueous solutions of the *Guan* and *Sulf* copolyelectrolyte precursors to obtain a consistent hydrogel, being $10\%_w$ and 1:1v/v, respectively. Due to the lack of a study of the microstructure of this hydrogel, Scanning Electron Microscopy (SEM) analyses were first performed. For that, after mixing the solutions of the copolyelectrolytes and obtain the pure hydrogel in a vial (bulk), some sample was taken with a spatula, deposited on a carbon tape fixed at a SEM holder and imaged. The solvent was removed using a gentle nitrogen flow stream (Fig. 5.2).
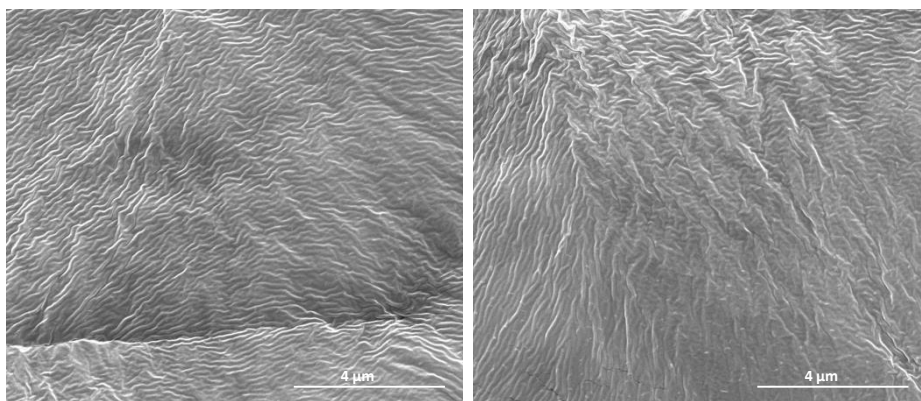
Fig. 5.2 *SEM images of the P(AGE-b-EG-b-AGE) hydrogel obtained in bulk conditions at a concentration of $10\%_w$.[42]*

SEM images of the pure hydrogel revealed locally-aligned fibers in the microstructure, so the crosslinking proceed by ionic coacervation resulted in isotropic ordered domains (without a preferential direction).

Consecutively, experiments involving flow focusing by using microfluidics platform were designed for the control and improvement of the microstructure of the hydrogel. Furthermore, the reduction of the concentration of the copolyelectrolyte precursors at the $1\%_w$ was also explored, as one of the benefits of microfluidics is an increase of the surface-to-volume ratio between species. For this, the initial

concentrations of *Guan* and *Sulf* precursor solutions were diminished down to $1\%_w$ (values 10 times below respect to the previous reported). To conduct an accurate emulation of the microfluidics conditions in the bulk for further comparisons, solutions of polyelectrolytes at $1\%_w$ were first quickly put in contact together and instantaneously later, the necessary amount of ultrapure water was added to reproduce the dilution effect practised by the lateral flows in the microchip. The resulting mixture presented small cloudy aggregates, which were analysed by SEM. For this, cloudy aggregates were transferred with pipette to a SEM holder and the excess of solvent was removed under a gentle nitrogen flow stream (Fig. 5.3). The SEM images of the cloudy aggregates (Fig. 5.3) depicted similar domains than the observed for the hydrogel at higher concentration (Fig. 5.2) at the microscale, suggesting that the dispersed matter suspended in the coacervated final solution (cloudy aggregates) was hydrogel, although it could not be seen by bare eye at the macroscale.
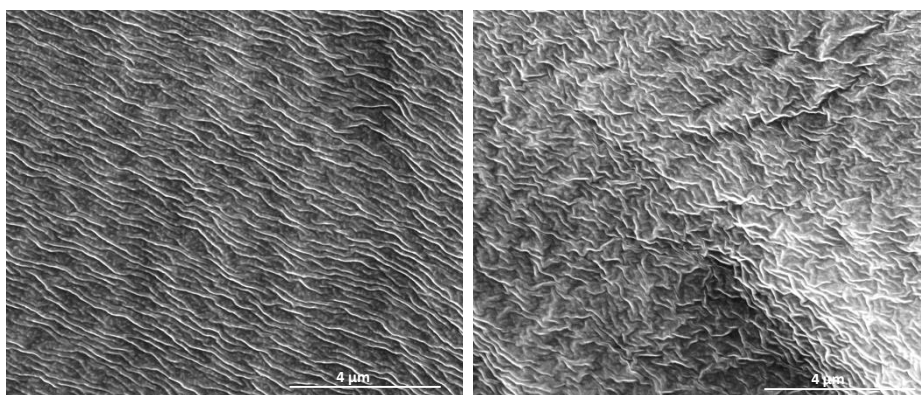
Fig. 5.3 *SEM images of the P(AGE-b-EG-b-AGE) hydrogel obtained in bulk conditions at a concentration of $1\%_w$.*

After this initial test in bulk, microfluidics experiments were designed. In all of them, self-manufactured chips with four symmetric inlets converged in a main channel in where the feeding streams will be mixed by diffusion (reaction chamber) and flowed until one single outlet (Fig. 5.4).
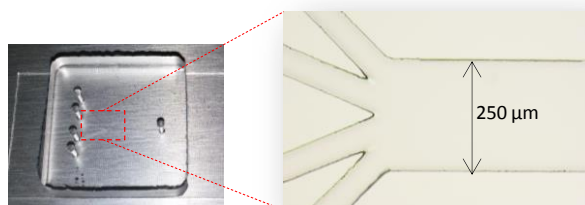
Fig. 5.4 *Images of the chip used in microfluidics experiments. Size of the main channel (length x width x height): 1 x 0.25 x 0.05 cm.*

The design, common to all experiments, is detailed in Fig. 5.5. Lateral solvent streams of ultrapure water were used to avoid contact of the reactant with the walls and promoting the encountering between *Guan* and *Sulf* in conditions of laminar flow. The gelation took place at the copolyelectrolyte precursors interface and extended by diffusion.
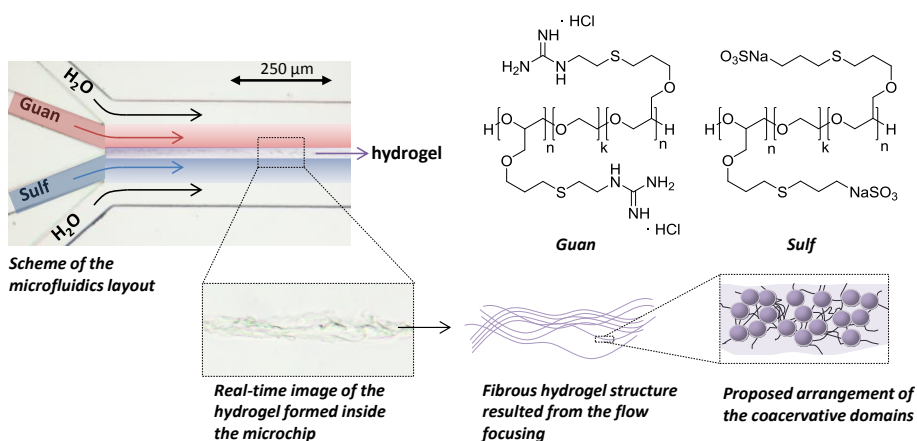
Fig. 5.5 *(From the left to the right counter clockwise) Image acquired by optical microscope in real-time of one of the microfluidics experiments conducted in where each stream was colour-edited to facilitate the comprehension of the layout scheme. On the bottom, a magnified image of the main channel in where the formation of the hydrogel was depicted. On the right, proposed arrangement of the coacervated partially aligned domains[31, 60] of the formed hydrogel under the flow focusing influence, based on Hunt et al. observations.[42] On the upper part, chemical structures of Guan- and Sulf-functional P(AGE-b-EG-b-AGE) triblock copolymers (degree of polymerization: n=3.5k and k=10k).*

168

In this way and according to the experiments already conducted in bulk, two experiments using microfluidics platform were designed to correlate with the laminar flow speed at the microscale. For those high (400 µl/min) and low (40 µl/min) flow rates were fixed that correspond to high and low flow speed, respectively (Table 5.1) following the layout depicted in Fig. 5.5. Then, the outgoing hydrogels from both experiments were analysed by SEM.

Table 5.1	*Flow rate values used in microfluidics experiments.*			
	Flow rates (µl/min)			
Designation	*Guan*	*Sulf*	H_2O **(each)**	**TOTAL**
1 (high rate)	100	100	100	400
2 (low rate)	10	10	10	40

The resulting hydrogel from the high flow rate (experiment 1), showed a remarkable increase in width of the fibrous domains (Fig. 5.6). This effect suggested that the microfluidics platform enhanced the encountering between the precursors *via* flow focusing and seeded the formation of wider, high-aligned and defined fibers compared to same conditions in bulk. An overlapping and alignment of the fibers were observed. They were rotated respect to the underneath, resulting in a kind of knitted pattern ('houndstooth pattern'). 'Houndstooth pattern' could be spotted poorly-defined in bulk conditions (Fig. 5.6), indicating that thanks to the microfluidics, larger and highly-defined microstructure could be provided.
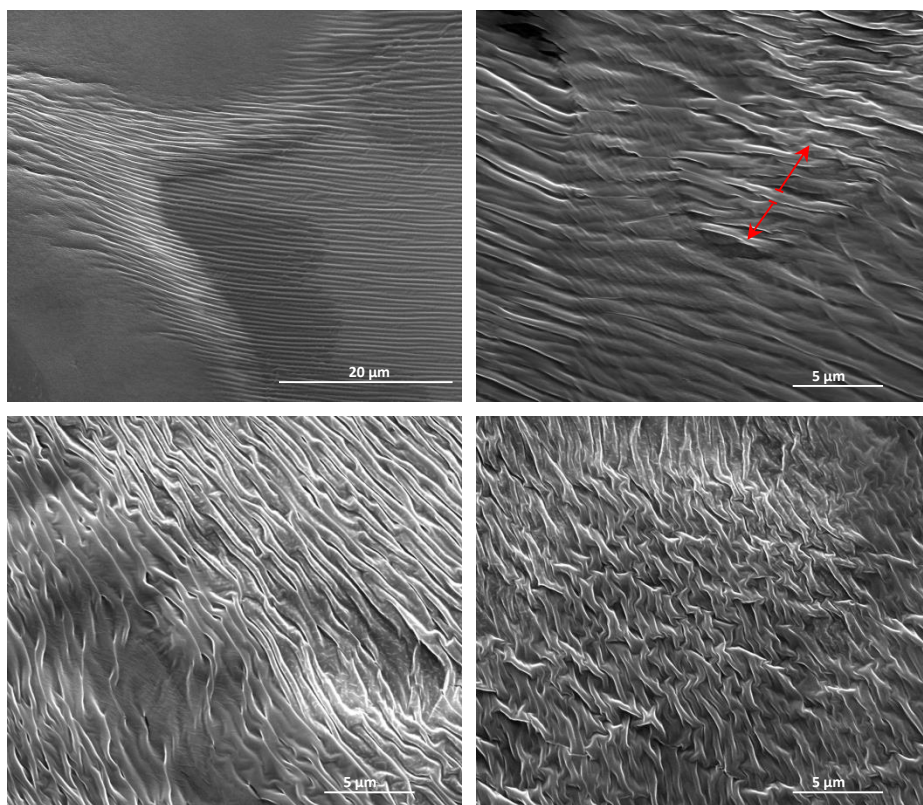
Fig. 5.6 SEM images of hydrogel obtained under microfluidic conditions at a total flow rate of 400 µl/min. Red arrows were drawn to emphasize the increase in width of fibres.

Generally in microfluidics, the interaction between reacting molecules takes place in a more controlled and ordered way, resulting in more organized structures. Differences observed between experiment 1 and 2 rely on the speed of the flows[61] and consequently, in the time of residence of the hydrogel in formation inside the chip. In the case of experiment 2 (total flow of 40 µl/min), the time of residence was 10 times greater rather than in the case of experiment 1 (total flow of 400 µl/min), being also longer the time that the hydrogel was confined under laminar flow conditions. In this way, a more ordered microstructure was expected for the low rate experiment, as it could be confirmed by SEM (Fig. 5.7). Indeed SEM images revealed a microstructure formed by bigger fibers for experiment 2 (~ 5 µm) respect to experiment 1 and also, in some regions big fibers composed of nanofibrils were also spotted. The reason because some other regions of the sample from experiment 2 looked similar to the

sample of bulk conditions, was attributed to a partial precipitation of the hydrogel in formation inside the chip at the reaction zone. This phenomenon implied that at certain point, the reagents could not react due to a physic barrier of precipitated matter (formed hydrogel) that avoided their encountering and consequently, the reaction between them took place outside the chip, similar to bulk conditions.
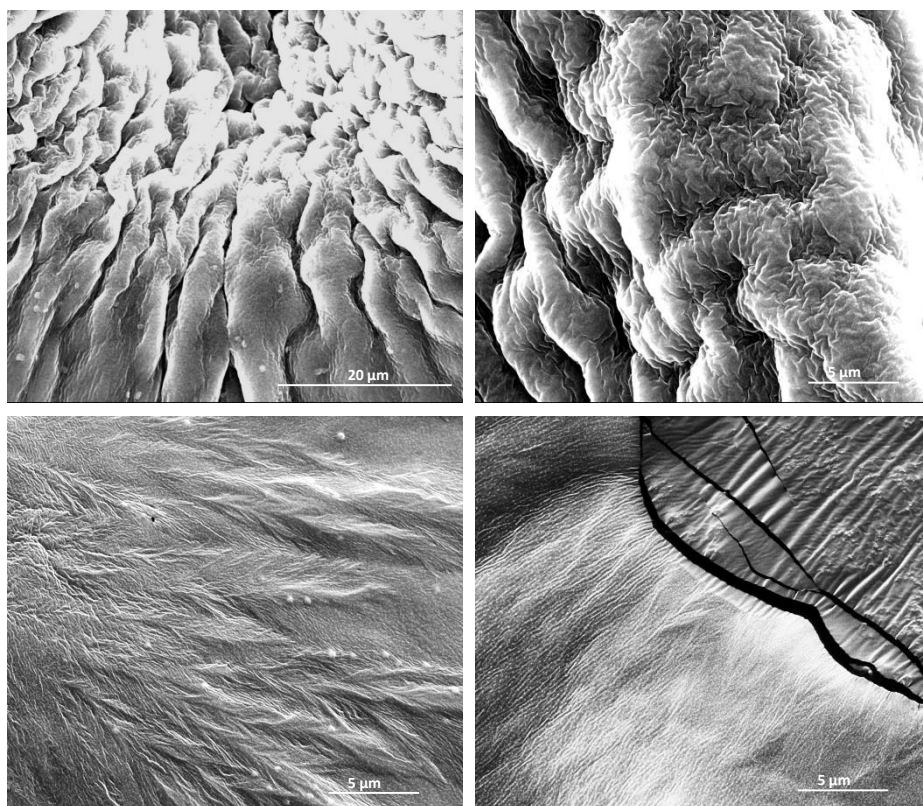
Fig. 5.7   *SEM images of the hydrogel obtained under microfluidic conditions at a
total flow of 40 μl/min.*

5.2.1.2. Hydrogel-TTFCOOH system

After being demonstrated the controllable and powerful focusing effect of microfluidics to the microstructure of the P(AGE-*b*-EG-*b*-AGE), it was extensively thought the possibility to equally enhance the microstructure of a charge-carrier hydrogel by the previous incorporation of TTFCOOH to the *Guan* part (*Guan*-TTFCOOH). The introduction of the TTFCOOH was first studied in bulk, at a concentration of 10%$_w$. To have a

control of the functionalization of the *Guan* groups with the TTFCOOH, together with the objective of avoiding their total functionalization for the later gelation of free *Guan* with the *Sulf* polyelectrolyte, different ratios *Guan*:TTFCOOH were tested. For this, different ratios *Guan*:TTFCOOH ratio per functional group units were mixed with *Sulf* ionic block copolymer (hydrogel-TTFCOOH) to test the viability of the resulting hydrogels-TTFCOOH (Fig. 5.8).

| pure hydrogel | hydrogel-TTFCOOH 1.6:1 | hydrogel-TTFCOOH 3.5:1 | hydrogel-TTFCOOH 7:1 |
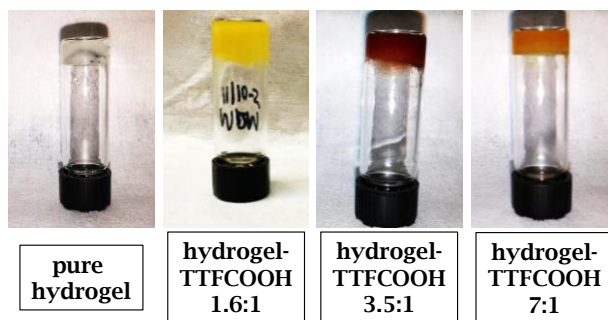
Fig. 5.8 Pictures of (from the left to the right) pure hydrogel and hydrogel-TTFCOOH with a content of Guan:TTFCOOH units 1.6:1, 3.5:1 and 7:1.

Hydrogel-TTFCOOH with a *Guan*:TTFCOOH ratio of 1.6:1 could be achieved, with a resulting change of color provided by the TTFCOOH perfectly incorporated to the matrix. Contrastingly, decreasing the relative content of *Guan* and extensively, increasing the free ionic sites, resulted in a system with two phases, the gel and particulate TTFCOOH dispersed on it. Surprisingly, when the ratio of functional groups increased up to 7:1, a consistent orange and single-phase hydrogel-TTFCOOH was obtained, being the last one the more promising sample.

Once the concentration of the ratio *Guan*:TTFCOOH was established at 7:1, the subsequent hydrogel-TTFCOOH system was analyzed by Fourier Transform Infrared Spectroscopy (FTIR) and compared with the pure precursors TTFCOOH, *Guan* and *Sulf* (Fig. 5.9). First, the peak at 3421 cm^{-1} for the hydrogel-TTFCOOH was attributed to the N-H and O-H stretching vibrations from the compound. In the FTIR spectra of the copolyelectrolyte precursors, this signal appeared less intense, broader and little shifted, a shoulder at 3459 cm^{-1} for the TTFCOOH, for the *Guan* at 3392 cm^{-1} and for the *Sulf* at 3465 cm^{-1}. The

signal of the C=O stretching vibrations in the spectrum of TTFCOOH appeared at 1646 cm^{-1}, while in the *Guan* this signal corresponded to the bending vibrations from aliphatic amines. In *Guan, Sulf* and hydrogel-TTFCOOH FTIR spectra, the peak observed at 1110 cm^{-1} was associated to the C-O-C stretching vibrations of the alkyl chain of the PEG block and also to the functional chain-endings of *Guan* and *Sulf*. Observed variations would suggest that the hydrogen bonding between the carboxylic acid of the TTFCOOH and the secondary amine of the *Guan* took place and the hydrogel-TTFCOOH was formed.
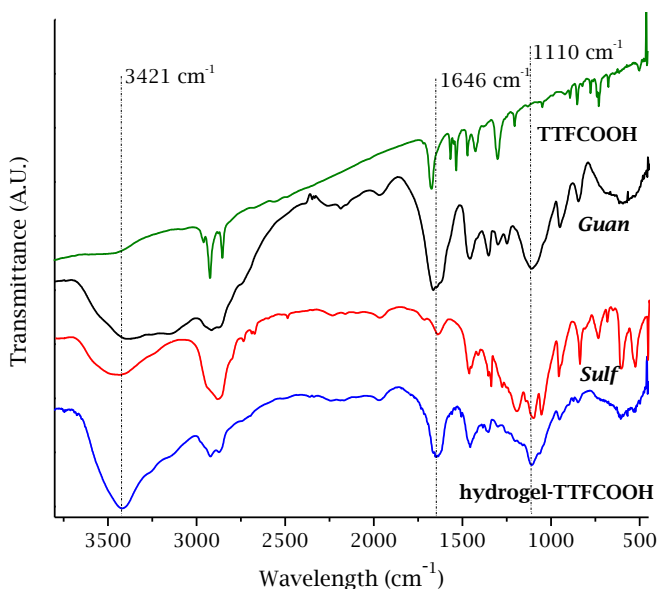
Fig. 5.9 *FTIR spectra of pure TTFCOOH,* Guan, Sulf *and hydrogel-TTFCOOH. Samples were prepared and analyzed in KBr pellets.*

Additionally, Diffusion-Ordered Nuclear Magnetic Resonance (DOSY NMR) experiments were performed to analyze the hydrogen bonding between the TTFCOOH and the *Guan*-TTFCOOH. DOSY NMR is a 2D NMR-based technique used for the correlation of the diffusion coefficient of a single-compound and multi-compound systems due to the self-diffusion behavior of individual molecules.[62] Diffusion values are characteristic of individual compounds so, DOSY NMR allows discerning the effectiveness of coordination, complexation or covalent-bonding reactions in many systems. Only a slight change from $2.48 \cdot 10^{-6}$ cm^2/s for the pure TTFCOOH to $2.31 \cdot 10^{-6}$ cm^2/s for the *Guan*-TTFCOOH in the

diffusion coefficient values could be observed by DOSY NMR (Fig. 5.10). The decrease of the diffusion when the TTFCOOH was incorporated to the *Guan* to form *Guan*-TTFCOOH compound was related to the increase of the volume of the resulting hydrogen bonded system. Even though, this slight change in the diffusion value could be associated to external factors, such as deviations in the preparation and/or analysis of the sample. To overcome this, an additional DOSY NMR study of the hydrogel-TTFCOOH sample was conducted. The diffusion value associated to the hydrogel-TTFCOOH compound, was found at $2.10 \cdot 10^{-6}$ cm^2/s, a decreasing respect to the pure TTFCOOH and the functionalized compound of *Guan*-TTFCOOH that agreed with the observed tendency. Thus, the functionalization of the hydrogel through the incorporation of the TTFCOOH by hydrogen bonding to the *Guan* part to form the hydrogel-TTFCOOH could be demonstrated.
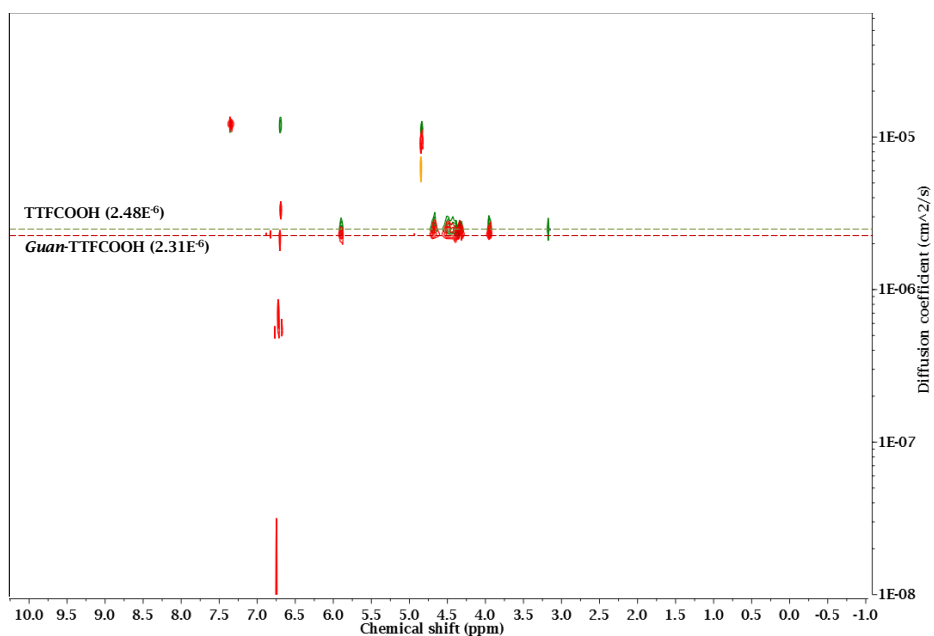
Fig. 5.10 *DOSY NMR spectra of TTFCOOH (green) and* Guan*-TTFCOOH (red) compounds. Dashed lines highlight corresponding diffusion coefficient values.*

In the same way that the experiments performed for pure hydrogel, high and low concentrations (10%$_w$ and 1%$_w$, respectively) in bulk and after microfluidics of a sample hydrogel-TTFCOOH were compared by

SEM. The SEM images from the resulting hydrogel-TTFCOOH obtained in bulk at $10\%_w$ (Fig. 5.11) showed a differentiated microstructure compared with the same sample for pure hydrogel (Fig. 5.3). The incorporation of TTFCOOH promoted a random packing of the arrangement of the fibers, similarly as a 'jacquard pattern'. Regardless, the fibrous matrix was at the same time an evidence of the crosslinking of polyelectrolytes and the size of the fibers also confirm that.
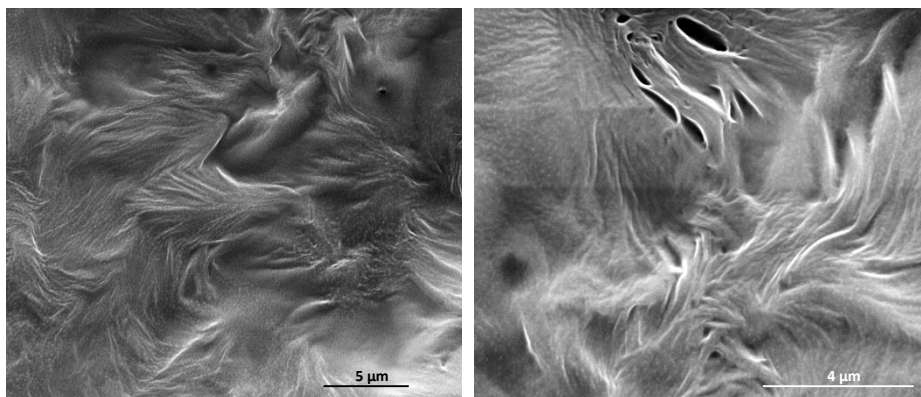
Fig. 5.11 *SEM images of hydrogel-TTFCOOH obtained from bulk conditions at a concentration of $10\%_w$.*

Consecutively, a test at a concentration of $1\%_w$ of hydrogel-TTFCOOH in bulk was also conducted. The SEM images of the hydrogel-TTFCOOH revealed two separated phases (Fig. 5.12). The phase corresponding to the pure hydrogel formed aggregates with the characteristic 'houndstooth pattern' according to the previous observations. Large crystals embedded in the hydrogel could be also observed, these with a similar shape to pure TTFs crystals,[63, 64] confirming the presence of the TTFCOOH, however not the formation of a homogenous hydrogel.
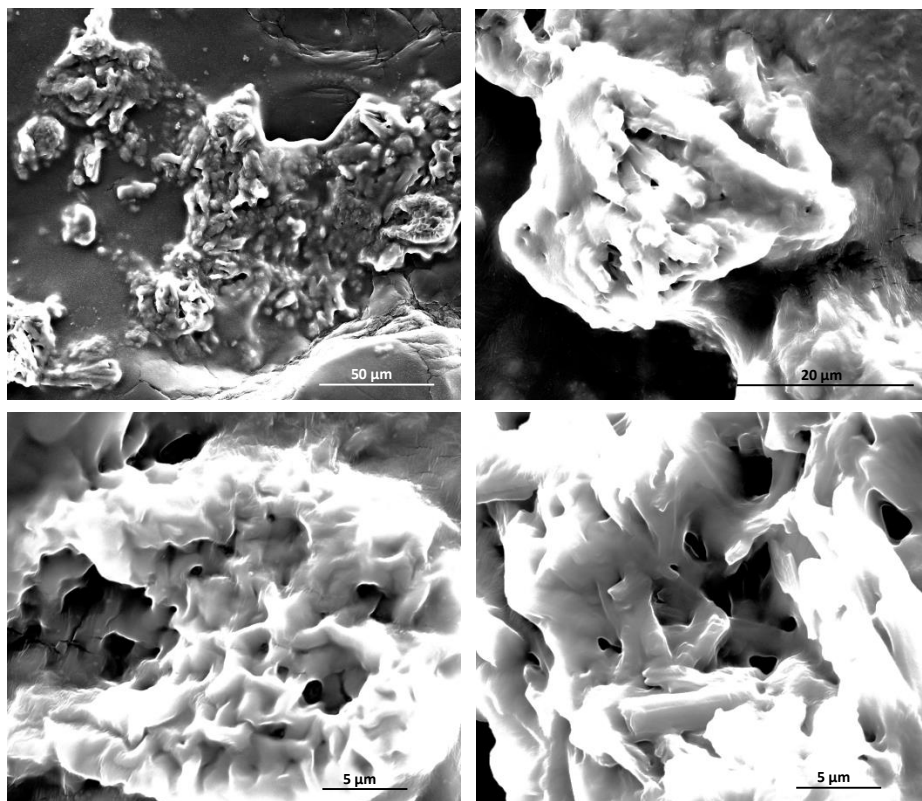
Fig. 5.12 *SEM images of hydrogel-TTFCOOH obtained from bulk at a concentration of 1%$_w$.*

Taking these results in account and order to demonstrate that the microfluidics could also have influence in the microstructure of the hybrid compound of *Guan*-TTFCOOH as it was seen for the pure hydrogel, a new microfluidics experiment was designed using the pre-mixture *Guan*-TTFCOOH with ratio 7:1 (*Guan*:TTFCOOH functional groups) as one of the feeding streams (Fig. 5.13).
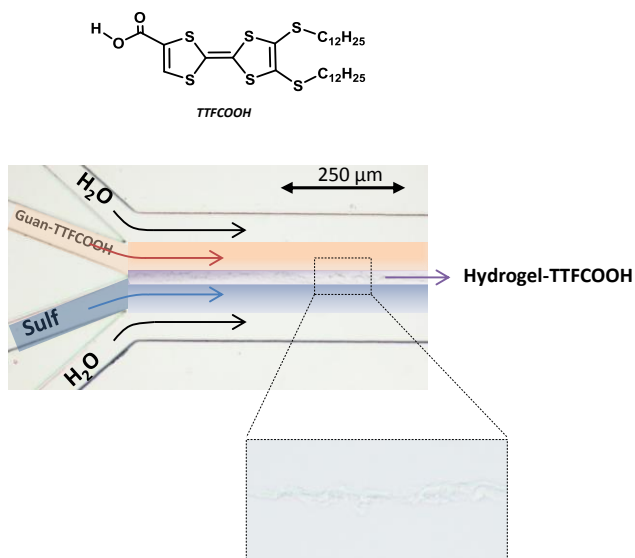
Fig. 5.13 *Structure of TTFCOOH and layout of the microfluidic experiments.*

To perform the experiments using microfluidics, a hydrogel-TTFCOOH at a concentration of $1\%_w$ was prepared using microfluidics with high flow rates (400 μl/min). SEM images revealed a smooth, uniform and single phase hydrogel-TTFCOOH, confirming the effect of the enhancement of the microstructure by flow focusing and indicating a better integration of the blocks (Fig. 5.14). Surprisingly, the width and alignment of the fibers were similar to the pure hydrogel samples obtained from bulk (both in high and low concentrations, Fig. 5.2 and Fig. 5.7). This suggested that TTFCOOH certainly hindered in some way the encountering of the ionic domains (even in microfluidics) and resulting samples were comparable to the pure hydrogel in bulk (but not pure hydrogel from microfluidics), in were randomly disposed copolyelectrolytes with long macromolecular chains have to react. Moreover, the formation of a single phase in the hydrogel-TTFCOOH sample when microfluidics was used, confirmed the effect of the influence of the hydrodynamic flow focusing in the microstructure of the functionalized gel. For the sample of hydrogel-TTFCOOH in bulk at the same low concentration (Fig. 5.12), isolated clusters or islands of matter and consequently, the formation of two separated phases were obtained, suggesting the independent formation of hydrogel and TTFCOOH crystals.
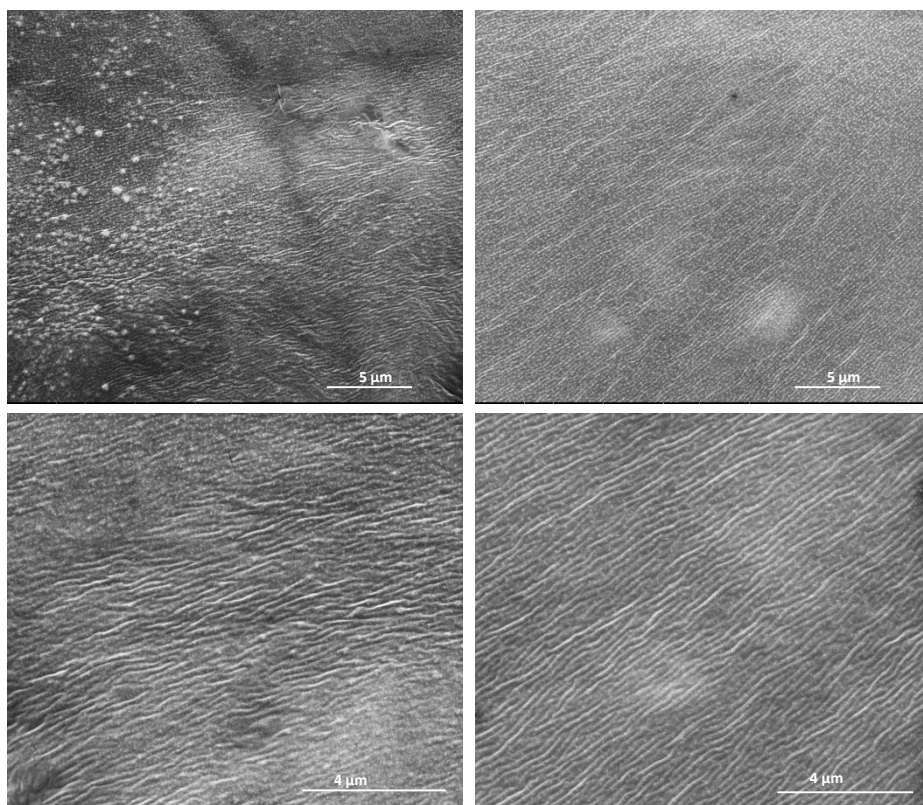
Fig. 5.14 *SEM images of hydrogel-TTFCOOH obtained from microfluidics at a total flow rate of 400 µl/min.*

Finally and with the aim to obtain a hydrogel with redox properties, the doping of the TTF derivative in the hydrogel-TTFCOOH system was followed by UV-Vis absorption spectroscopy. Undoped hydrogel-TTFCOOH at $1\%_w$ was compared with doped hydrogel-TTFCOOH $1\%_w$ obtained from bulk and from microfluidics. The doping procedure was performed by spreading material on standardized quartz slides and exposing the samples to I_2 vapors for 1 hour in a sealed container. UV-Vis absorption spectroscopic measurements were conducted immediately after 1 hour of uninterrupted doping and one week after the treatment, observing a decrease of the intensity of the bands associated to oxidized TTFCOOH, but still stable (here shown one week after doping) (Fig. 5.15).
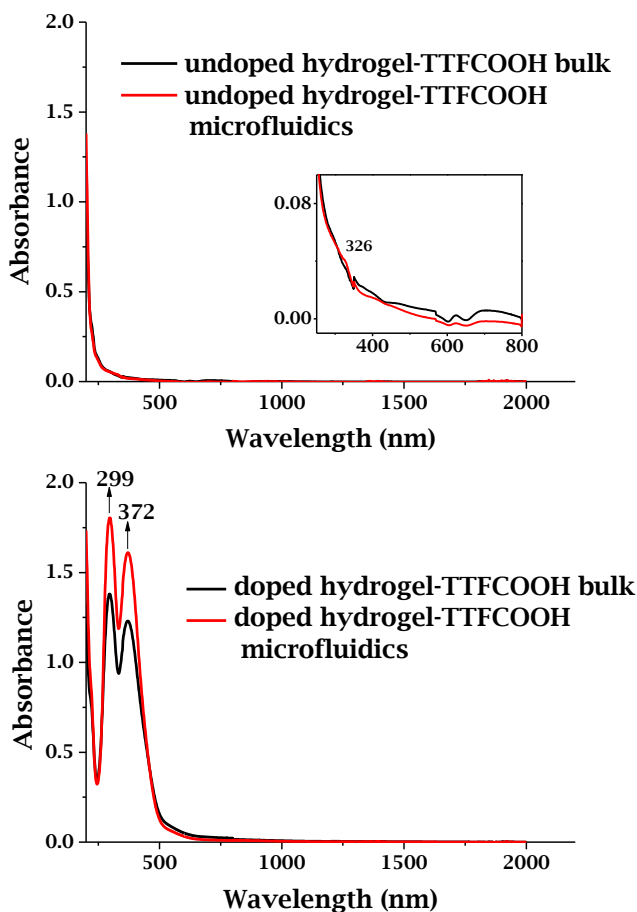
Fig. 5.15 *UV-Vis absorption spectra of undoped hydrogel-TTFCOOH from bulk and microfluidics (on the top) and doped hydrogel-TTFCOOH from bulk and microfluidics (on the bottom).*

Previous reported works of electroactive TTF-based organogelators based on the functionalization of aminoacids with TTF, in where neighboring aminoacids could interlink by hydrogen bonding, allowed obtaining and forming fibrous gelators. Moreover, TTF could be oxidized and formed ordered domains with charge-transfer properties.[46] In the case of undoped hydrogel-TTFCOOH (Fig. 5.15), the UV-Vis absorption spectra for bulk and microfluidics hydrogel-TTFCOOH depicted a low-intensity band at 326 nm, associated to the TTFCOOH hydrogen-bonded to the *Guan* part of the hydrogel. Then, when they were doped, this band shifted to 372 nm and appeared one at 299 nm indistinctly manifested in bulk and microfluidics prepared hydrogels. Kitamura *et al.* attributed the band

at 372 nm to intramolecular transitions of TTF cation radical and the appearance of charge transfer bands at higher wavelength values. In the hydrogel-TTFCOOH, charge transfer bands did not appear probably due to the spatial separation between the doped TTFCOOH units that could not allow the charge transportation along the fibers. Regardless, UV-Vis absorption spectroscopy demonstrated the presence of TTF moieties and the possibility to oxidize them individually up to, at least, the cation radical state.

5.2.2. Immobilization of ionically-driven coacervated hydrogels on surface by micro-contact printing

With the objective to immobilize hydrogel-TTFCOOH on surface and to have a control of the organization of the TTFCOOH units, μcP was employed. The immobilization process involved several steps, starting with the imidazole-functionalization of glass surfaces following the procedure described by Hsu and coworkers.[54] Then, the μcP of *Guan* and *Sulf*, as control experiments, was conducted by firstly immobilizing a full monolayer of imidazole on glass, followed by the patterning of the copolyelectrolytes of *Guan* or *Sulf* at concentrations of $10\%_w$ in water. The results of the immobilization of pure *Guan* and pure *Sulf* were separately carried out. The resulting micro-patterned surfaces were analyzed by SEM and Atomic Force Microscopy (AFM) (Fig. 5.16 and Fig. 5.17). In the control experiments, only in the immobilization of *Guan* was achieved, as it was expected due to the reactivity of the imidazole-functionalized surfaces towards amine-terminated compounds. SEM and AFM topography images could not confirm the immobilization of the *Guan* probably due to a lack of sensitivity of both equipment, although the AFM phase image depicted the circular pattern, suggesting the formation of the inverse pattern (block copolymer outside the dots).

Imidazole monolayer

Patterned Guan surface
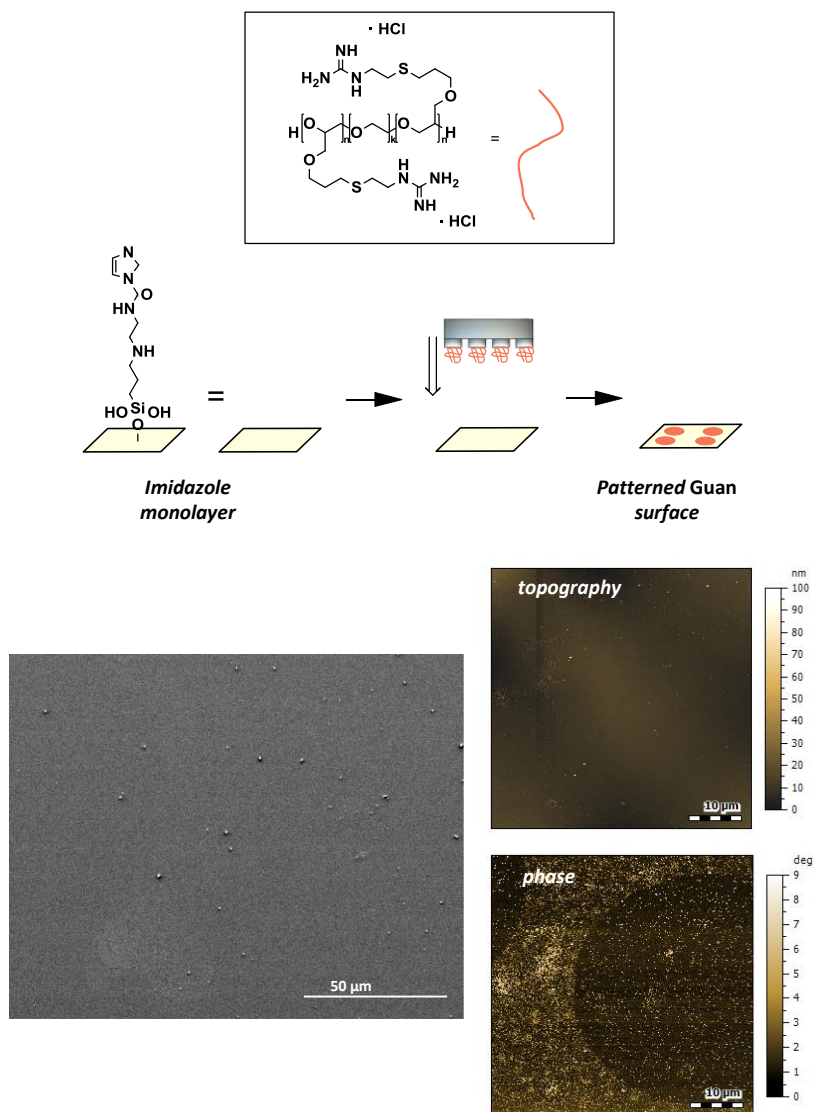
topography

phase

Fig. 5.16 *(On the top) Scheme of the μcP of Guan, (on the bottom-left) SEM image of patterned glass surface and (on the bottom-right) AFM topography and phase images of the same sample.*
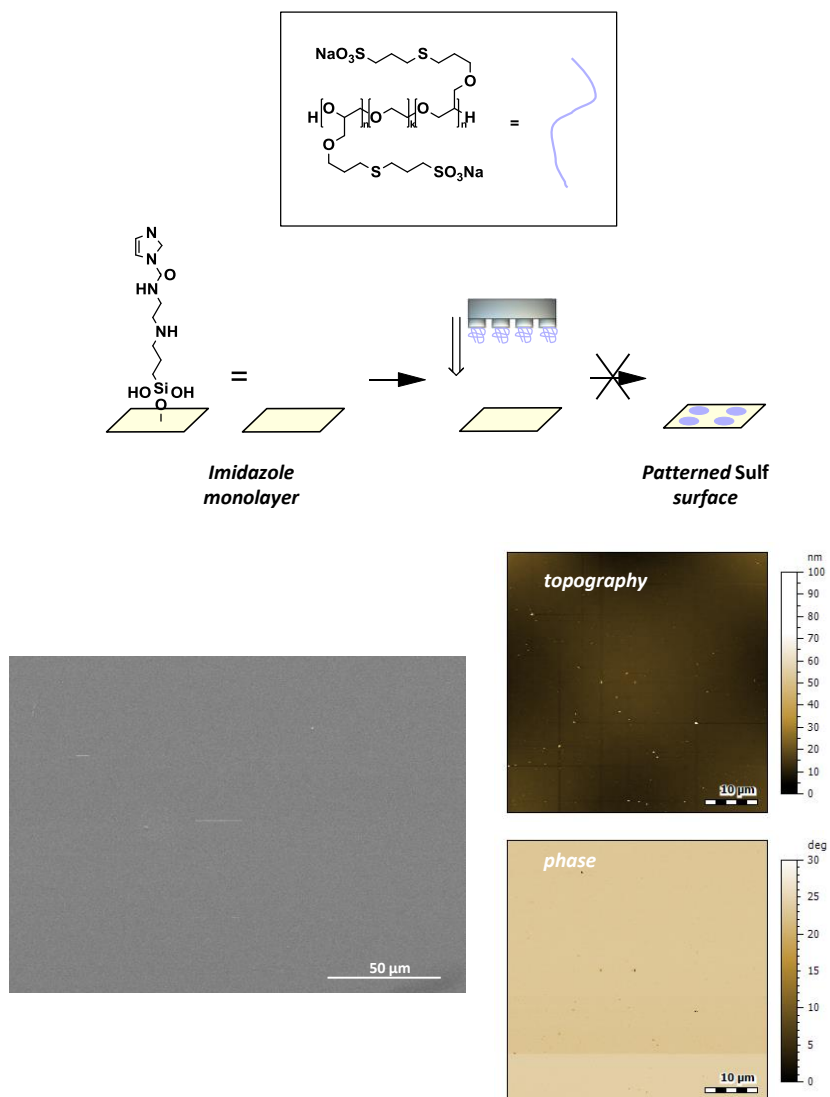
Fig. 5.17 *(On the top) Scheme of the µcP of Sulf, (on the bottom-left) SEM image of patterned glass surface and (on the bottom-right) AFM topography and phase images of the same sample.*

Finally, the immobilization of the pure hydrogel was performed according to the results of the control experiments, so the *Guan* was firstly patterned on a glass surface, followed by an immersion in an aqueous solution of *Sulf* towards the formation of hydrogel by ionic interactions (Fig. 5.18). Resulting surfaces were imaged by SEM and AFM.
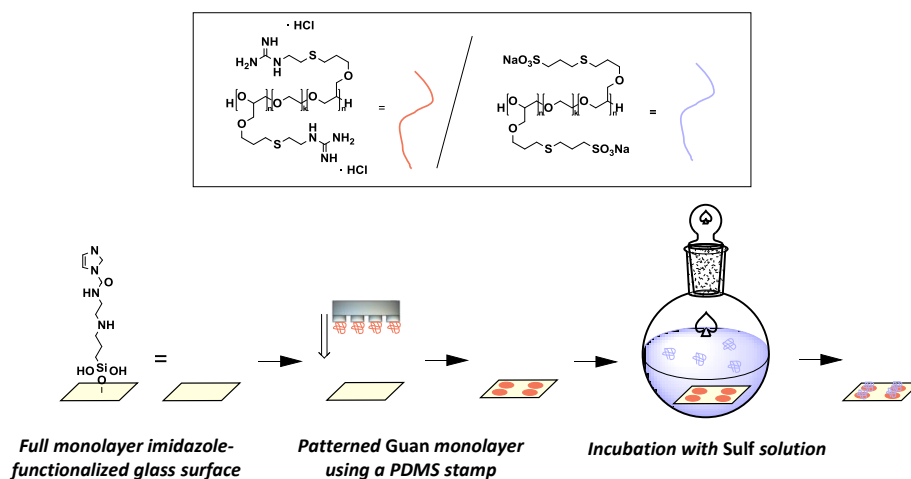
Fig. 5.18 *Scheme of the procedure followed to immobilize hydrogel on glass surfaces.*

Interestingly, in the full process of micro-patterning of the hydrogel, a highly-contrasted image of the dotted pattern compared to the precursors could be captured by SEM (Fig. 5.19), an unequivocally evidence that hydrogel was immobilized. Consequently AFM images showed the dotted pattern as well (Fig. 5.19).
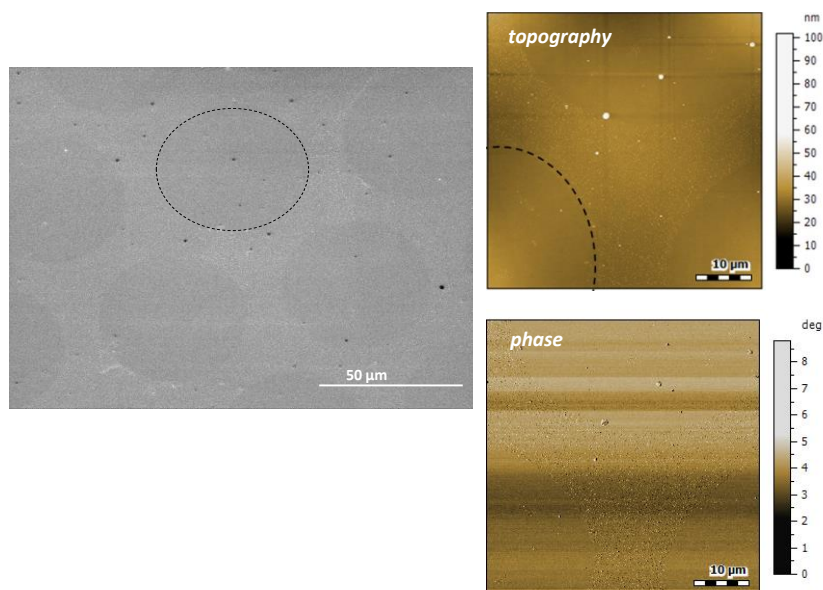
Fig. 5.19 *SEM image of patterned hydrogel on glass surface (left), AFM images of the topography and phase of the same sample (right) (dashed circle was drawn to localize the dotted pattern)*

Further attempts to immobilize hydrogel-TTFCOOH realizing different approaches were performed although not conclusive results could be obtained.

5.3.   CONCLUSIONS AND OUTLOOK

In this chapter the gelation and the control of the microstructure of a PEG-based P(AGE-*b*-EG-*b*-AGE) hydrogel obtained by ionic coacervation has been achieved by using microfluidics at concentrations 10 times lower than in bulk. It has been demonstrated the effect of the hydrodynamic flow focusing in the better contact of the compounds using low concentrated solutions without by-products, due to the larger surface-to-volume ratio compared to bulk conditions. The use of microfluidics resulted in hydrogels with a more aligned and fibrous microstructure when higher flow rates were applied, indicating a major effect of the confinement and shear forces inside the channel. Moreover, the functionalization of *Guan* ionic triblock copolymer with the redox-responsive TTFCOOH (*Guan*-TTFCOOH) has also been demonstrated as well as the possibility to later form the corresponding hydrogel-TTFCOOH by the ionic coacervation with the *Sulf* part. In this way, microfluidics also promoted the encountering between *Guan*-TTFCOOH with the counter-ionic streams of the *Sulf*, providing a more uniform (single-phase), homogeneous and ordered microstructure of the hydrogel-TTFCOOH system compared to the bulk. The possibility to dope the TTFCOOH moieties of the hydrogel-TTFCOOH has been demonstrated too, although redox-responsive units of TTFCOOH could not act as charge-carriers because the spatial separation between doped neighbouring units. With this, microfluidics can be concluded one more time, a powerful technique in where the microstructure of compounds can be easily and well-controlled and reproduced by modifying the hydrodynamic flow focusing parameter.

In a further step, it has been showed the possibility to immobilize on glass surfaces the ionically-driven coacervated hydrogel by the soft lithography technique of micro-contact printing. Although several attempts in the patterning of the redox system hydrogel-TTFCOOH were performed, not concluding results could be extracted and opened a research pathway for future studies.

5.4.   EXPERIMENTAL PART

Guan- and **Sulf-** functionalized **P(AGE-*b*-EG-*b*-AGE):** the polymerization degree of P(AGE-*b*-EG-*b*-AGE) (A_n-*b*-B_k-*b*-A_n) *Guan* and *Sulf* copolymers was n = 3.5k and k = 10k.

FTIR measurements: the FTIR analyses of the different compounds were performed by milling until getting a fine powder and mixing them with potassium bromide (KBr) to obtain pellets. KBr pellets were stored at the oven for several hours in order to remove the humidity traces before used.

DOSY NMR analysis: TTFCOOH and *Guan*-TTFCOOH were dissolved in a mixture of deuterated-H_2O/deuterated-THF in a ratio 1:2v/v. With the objective to appreciate changes in the diffusion values, the molar ratio *Guan*:TTFCOOH used was of 1:1, due to the smaller relative volume of the TTFCOOH respect to the *Guan*. The corresponding hydrogel-TTFCOOH sample was prepared firstly by following the same procedure than for *Guan*-TTFCOOH and secondly, by adding the necessary amount of a solution of *Sulf* in deuterated-H_2O/deuterated-THF in a ratio 1:2v/v to reach the ratio *Guan:Sulf* 1:1v/v.

Microfabrication of the microfluidics chip: microfluidics chips were obtained by replica molding technique (soft lithography).[65, 66] The microchannels were fabricated by transferring the complementary structure of a silicon wafer master to poly(dimethyl siloxane) (PDMS)

(curing on a hot plate at 150ºC for 10 minutes) and bonding the latter to glass. The silicon wafer master had previously been fabricated by standard photolithography of SU-8 epoxy resist on top of a silicon substrate (the same procedure of replica molding described in Chapter 4).

Microfluidics experimental details: fluids were introduced to the chip using a flexible Teflon® tubing system, including an extra short piece of tube connected to the outlet to facilitate sample collection. Flow rates were controlled using separate syringe pumps for each fluid. The concentrations of feeding solutions of *Guan* and *Sulf* were each of 10 mg/ml and the calculated concentration at the outlet by the dilution effect of lateral solvent streams was of 2.5 mg/ml. Calculated residence times for experiments 1 and 2 were of 18.7 ms and 187.5 ms, respectively ($Q = v/t$, being $v = w \cdot h \cdot l$, in where Q = total flow rate, v = volume, t = time, w = width, h = height and l = length).

SEM measurements: pure hydrogels, hydrogels-TTFCOOH and patterned glass surfaces were analyzed after sputter-coating with gold. High vacuum conditions, working distances ranging from 7 to 10 mm and spot values from 3 to 3.5 were used depending on the sample.

Functionalization of glass surfaces: [54] glass or silicon oxide slides were cleaned with piranha solution (H_2SO_4/H_2O_2 (30%); $3:1_{v/v}$) for 30 min, rinsed thoughtfully with ultrapure water and dried under a N_2 stream flow before their use. Then, surfaces were amino-terminated- functionalized using vapours of N-([3-(trimethoxysilyl)propylethylenediamine (TPEDA, 97% Sigma Aldrich) in a dome overnight. Later on, surfaces were rinsed with sequentially ethanol and dichloromethane to eliminate unreacted amino groups, and dried with N_2. At the same time, a saturated solution of *N,N*-carbonyldiimiazole (CDI, ≥97.0% Sigma-Aldrich) in dry tetrahydrofuran (THF) was prepared and the substrates were immersed and let incubating overnight under argon atmosphere. Afterwards substrates were rinsed with dry THF and dried under a N_2 flow. µcP was immediately performed due to the reactivity of the functional groups on surface.

µcP details: PDMS stamps were obtained from mixing a ratio 10:1$_{w/w}$ of polymer:curing agent (Sylgard® 184 elastomer kit from Dow Corning), degassing the mixture, spreading it on patterned silicon wafers and cured for 16 h at 60 ºC in the oven. Cured PDMS was diced, following the distribution of the different patterns and were activated by a treatment of UV/O$_3$ for 30 min.[67] As inking solutions, 0.6 mg/ml in ultrapure water *Guan* and *Sulf* solutions were used and, and 0.5 mg/ml of *Sulf* aqueous solution as incubating solution. 10 min inking and 10 min of printing exerting 30 g of pressure were the conditions used for µcP.

5.5.   REFERENCES

1.   Z.-M. Huang, Y. Z. Zhang, M. Kotaki and S. Ramakrishna, *Composites Science and Technology*, 2003, **63**, 2223-2253.
2.   S. B. Clough, A. Blumstein and E. C. Hsu, *Macromolecules*, 1976, **9**, 123-127.
3.   C. R. Bohn, J. R. Schaefgen and W. O. Statton, *Journal of Polymer Science*, 1961, **55**, 531-549.
4.   B. Langeveld-Voss, R. Janssen, M. Christiaans, S. Meskers, H. Dekkers and E. Meijer, *Journal of the American Chemical Society*, 1996, **118**, 4908-4909.
5.   Z. Hu, M. Tian, B. Nysten and A. M. Jonas, *Nature materials*, 2009, **8**, 62-67.
6.   S. Asperger, *Chemical Kinetics and Inorganic Reaction Mechanisms*, Springer US, 2011.
7.   A. Shamiri, M. Chakrabarti, S. Jahan, M. Hussain, W. Kaminsky, P. Aravind and W. Yehye, *Materials*, 2014, **7**, 5069.
8.   T. Mitamura, M. Daitou, A. Nomoto and A. Ogawa, *Bulletin of the Chemical Society of Japan*, 2011, **84**, 413-415.
9.   P. Theato and H. A. Klok, *Functional Polymers by Post-Polymerization Modification: Concepts, Guidelines and Applications*, Wiley, 2013.
10.   H. Pan, L. Li, L. Hu and X. Cui, *Polymer*, 2006, **47**, 4901-4904.
11.   Q. Li, *Liquid Crystals Beyond Displays: Chemistry, Physics, and Applications*, Wiley, 2012.
12.   M. Gruttadauria and F. Giacalone, *Catalytic Methods in Asymmetric Synthesis: Advanced Materials, Techniques, and Applications*, Wiley, 2011.
13.   V. V. Terekhin, A. V. Zaitseva, O. V. Dement'eva and V. M. Rudoy, *Colloid J*, 2013, **75**, 720-725.
14.   J. L. Brédas, *Conjugated Oligomers, Polymers, and Dendrimers : From Polyacetylene to DNA: Proceedings of the Fourth International Francqui Symposium, 21-23 October 1998, Brussels*, De Boeck Supérieur, 1999.
15.   X. Zhao, Q. Wang, Y.-I. Lee, J. Hao and H.-G. Liu, *Chemical communications*, 2015, DOI: 10.1039/C5CC05548B.

16. T. Luo, S. Lin, R. Xie, X.-J. Ju, Z. Liu, W. Wang, C.-L. Mou, C. Zhao, Q. Chen and L.-Y. Chu, *Journal of Membrane Science*, 2014, **450**, 162-173.

17. G. Gupta, C. R. Singh, R. H. Lohwasser, M. Himmerlich, S. Krischok, P. Müller-Buschbaum, M. Thelakkat, H. Hoppe and T. Thurn-Albrecht, *ACS Applied Materials & Interfaces*, 2015, **7**, 12309-12318.

18. J. Lu, F. S. Bates and T. P. Lodge, *Macromolecules*, 2015, **48**, 2667-2676.

19. K. Amundson, E. Helfand, D. D. Davis, X. Quan, S. S. Patel and S. D. Smith, *Macromolecules*, 1991, **24**, 6546-6548.

20. C. C. Kathrein, W. K. Kipnusu, F. Kremer and A. Böker, *Macromolecules*, 2015, **48**, 3354-3359.

21. R. L. Vekariya, D. Ray, V. K. Aswal, P. A. Hassan and S. S. Soni, *Colloids and Surfaces A: Physicochemical and Engineering Aspects*, 2014, **462**, 153-161.

22. B. Sarkar and P. Alexandridis, *Progress in Polymer Science*, 2015, **40**, 33-62.

23. C. Hu, J. Yu, J. Huo, Y. Chen and H. Ma, *Composites Part A: Applied Science and Manufacturing*, 2015, **78**, 113-123.

24. C. Park, J. Yoon and E. L. Thomas, *Polymer*, 2003, **44**, 6725-6760.

25. L. Tsarkova, in *Trends in Colloid and Interface Science XXIII*, Springer Berlin Heidelberg, 2010, vol. 137, ch. 1, pp. 1-4.

26. A.-C. Shi and B. Li, *Soft Matter*, 2013, **9**, 1398-1413.

27. R. M. Jendrejack, D. C. Schwartz, M. D. Graham and J. J. de Pablo, *The Journal of Chemical Physics*, 2003, **119**, 1165-1173.

28. H. Zhang, E. Tumarkin, R. M. A. Sullan, G. C. Walker and E. Kumacheva, *Macromolecular rapid communications*, 2007, **28**, 527-538.

29. A. G. Toh, Z. P. Wang, C. Yang and N.-T. Nguyen, *Microfluid Nanofluid*, 2014, **16**, 1-18.

30. B. G. Chung, K.-H. Lee, A. Khademhosseini and S.-H. Lee, *Lab on a Chip*, 2012, **12**, 45-59.

31. M. Vasudevan, E. Buse, D. Lu, H. Krishna, R. Kalyanaraman, A. Q. Shen, B. Khomami and R. Sureshkumar, *Nature materials*, 2010, **9**, 436-441.

32. H. Andersson and A. v. d. Berg, *Lab on a Chip*, 2004, **4**, 98-103.

33. N. K. Inamdar and J. T. Borenstein, *Current Opinion in Biotechnology*, 2011, **22**, 681-689.

34. S. Kobel and M. P. Lutolf, *Current Opinion in Biotechnology*, 2011, **22**, 690-697.

35. P. Domachuk, K. Tsioris, F. G. Omenetto and D. L. Kaplan, *Advanced materials*, 2010, **22**, 249-260.

36. A. S. Sawhney, C. P. Pathak and J. A. Hubbell, *Biomaterials*, 1993, **14**, 1008-1016.

37. J. Chang, Y. Tao, B. Wang, X. Yang, H. Xu, Y.-r. Jiang, B.-h. Guo and Y. Huang, *Polymer*, 2014, **55**, 4627-4633.

38. S. J. Buwalda, K. W. Boere, P. J. Dijkstra, J. Feijen, T. Vermonden and W. E. Hennink, *Journal of controlled release : official journal of the Controlled Release Society*, 2014, **190**, 254-273.

39. S. Ishii, J. Kaneko and Y. Nagasaki, *Macromolecules*, 2015, **48**, 3088-3094.

40. K. C. Remant Bahadur, S. R. Bhattarai, S. Aryal, M. S. Khil, N. Dharmaraj and H. Y. Kim, *Colloids and Surfaces A: Physicochemical and Engineering Aspects*, 2007, **292**, 69-78.

41. H. Bohidar, *Journal of Surface Science and Technology*, 2008, **24**, 105-124.

42. J. N. Hunt, K. E. Feldman, N. A. Lynd, J. Deek, L. M. Campos, J. M. Spruell, B. M. Hernandez, E. J. Kramer and C. J. Hawker, *Advanced materials*, 2011, **23**, 2327-2331.

43. E. Gomar-Nadal, L. Mugica, J. Vidal-Gancedo, J. Casado, N. J.T.L., J. Veciana, C. Rovira and D. B. Amabilino, *Macromolecules*, 2007, 7521-7531.

44. J. Puigmartí-Luis, E. E. Laukhina, V. N. Laukhin, Á. Pérez del Pino, N. Mestres, J. Vidal-Gancedo, C. Rovira and D. B. Amabilino, *Advanced Functional Materials*, 2009, **19**, 934-941.

45. J. Puigmarti-Luis, V. Laukhin, A. Perez del Pino, J. Vidal-Gancedo, C. Rovira, E. Laukhina and D. B. Amabilino, *Angewandte Chemie International Edition English*, 2007, **46**, 238-241.

46. T. Kitamura, S. Nakaso, N. Mizoshita, Y. Tochigi, T. Shimomura, M. Moriyama, K. Ito and T. Kato, *Journal of the American Chemical Society*, 2005, **127**, 14769-14775.

47. C. M. Nimmo and M. S. Shoichet, *Bioconjugate Chemistry*, 2011, **22**, 2199-2209.

48. S. Ahadian, R. B. Sadeghian, S. Salehi, S. Ostrovidov, H. Bae, M. Ramalingam and A. Khademhosseini, *Bioconjugate Chemistry*, 2015, **26**, 1984-2001.

49. L. Sola, P. Gagni, M. Cretich and M. Chiari, *Journal of Immunological Methods*, 2013, **391**, 95-102.

50. Y. Xia and G. M. Whitesides, *Angewandte Chemie International Edition*, 1998, **37**, 550-575.

51. O. Roling, A. Mardyukov, J. A. Krings, A. Studer and B. J. Ravoo, *Macromolecules*, 2014, **47**, 2411-2419.

52. H. Nandivada, H. Y. Chen, L. Bondarenko and J. Lahann, *Angewandte Chemie International Edition English*, 2006, **45**, 3360-3363.

53. Z. Nie and E. Kumacheva, *Nature materials*, 2008, **7**, 277-290.

54. S.-H. Hsu, D. N. Reinhoudt, J. Huskens and A. H. Velders, *Journal of Materials Chemistry*, 2008, **18**, 4959.

55. W. M. Lackowski, P. Ghosh and R. M. Crooks, *Journal of the American Chemical Society*, 1999, **121**, 1419-1420.

56. T. Kaufmann and B. J. Ravoo, *Polymer Chemistry*, 2010, **1**, 371.

57. M. R. Hynd, J. P. Frampton, M. R. Burnham, D. L. Martin, N. M. Dowell-Mesfin, J. N. Turner and W. Shain, *Journal of biomedical materials research. Part A*, 2007, **81**, 347-354.

58. G. Csucs, R. Michel, J. W. Lussi, M. Textor and G. Danuser, *Biomaterials*, 2003, **24**, 1713-1720.

59. A. G. Castano, V. Hortiguela, A. Lagunas, C. Cortina, N. Montserrat, J. Samitier and E. Martinez, *RSC Advances*, 2014, **4**, 29120-29123.

60. M. S. Turner and M. E. Cates, *Journal of Physics: Condensed Matter*, 1992, **4**, 3719.

61. W. Chen, Y. Yang, C. H. Lee and A. Q. Shen, *Langmuir : the ACS journal of surfaces and colloids*, 2008, **24**, 10432-10436.

62. C. S. Johnson Jr., *Progress in Nuclear Magnetic Resonance Spectroscopy*, 1999, 203-256.

63. K. Tanaka, T. Kunita, F. Ishiguro, K. Naka and Y. Chujo, *Langmuir : the ACS journal of surfaces and colloids*, 2009, **25**, 6929-6933.

64. J. Puigmartí-Luis, D. Schaffhauser, B. R. Burg and P. S. Dittrich, *Advanced materials*, 2010, **22**, 2255-2259.

65. A. Jahn, S. M. Stavis, J. S. Hong, W. N. Vreeland, D. L. DeVoe and M. Gaitan, *ACS Nano*, 2010, **4**, 2077-2087.

66. S. Marre and K. F. Jensen, *Chemical Society reviews*, 2010, **39**, 1183-1202.

67. B. Kim, E. T. K. Peterson and I. Papautsky, *26th Annual International Conference of the IEEE EMBS*, 2004, 5013-5016.

CHAPTER 6

Supramolecular Porphyrin-Block

Copolymer Systems

6.1.   INTRODUCTION AND OBJECTIVES

Synthetic supramolecular chemistry had a relevant impact in the polymers field because the potential applications in the construction of new materials, with unique structures and functionalities.[1] For example, polymer aggregation can be controlled by using the array of recognition of strategic elements in macromolecular chains.[2] This results very attractive for complex polymer systems, such as amphiphilic block copolymers. By definition, amphiphilic block copolymers are composed of a hydrophobic part covalently bonded to a hydrophilic part (forming blocks of distinctly matter properties), those parts formed by repeating units of polymers. Each part of these copolymers has the tendency to stay aggregate with subjects of similar nature (driven by Van der Waals interactions), creating generally well-defined structures at the interfaces due to the inherent immiscibility of the two blocks. Hence, the intervention of supramolecular chemistry and the role of functional groups has been the starting point of many studies.[3-7]

The continuous development of new materials has led the generation of forefront polymer-based systems such as the case of the introduction of the nanorotors or molecular rotors. Nanorotors are molecular structures that exhibit internal mechanical motion (random, flipping, concerted geared) at the nanoscale. In the particular case of solid molecular rotors, the part in movement is referred to an stationary part.[8] Gaub and coworkers explored the application of that concept of motion to stimuli-responsive polymers.[9, 10] From another point of view, Cnossen *et al*. prepared molecular motors with rotatory motion based on the light sensitivity of a tri-substituted palladium-coordinated metalloporphyrin.[11]

In this way, porphyrins in general have been in the supramolecular chemistry spotlight.[12] Porphyrins and their derivative systems have been widely studied due the inherent and exceptional optical and electronic properties that make them suitable for applications such as solar cells preparation in general,[13-15] and more specifically light-harvesting systems,[20, 21] and for dye-sensitizing[16, 17]. Their electrochemical and photophysical characteristics can be modified by changing the different

groups linked to the periphery of the porphyrin ring[18, 19] as well as by the introduction of a metal ion in the core of the macrocycle.[20-24] Free-base- and metallo-porphyrins can ensemble in supramolecular ordered structures by a combination of non-covalent interactions such as hydrogen-bonding, van der Waals and π-π stacking between porphyrin cores, but also the coordination of the metal ion in the core of the porphyrin with a ligand can influence the self-assembly of the chromophore.[25-29] Metalloporphyrins have been receiving great attention recently because their applications in metal-organic frameworks (MOFs)[30-33] and, as it has been mentioned, their use in molecular rotors.[8, 34, 35] An interesting study performed by Puigmartí-Luis *et al.* conducted a bottom-up self-assembled monolayer of a pre-complexed zinc (II) porphyrin with a pyridyl group on a gold surface, establishing and approach for supramolecular rotors (Fig. 6.1).[36] Concretely, zinc-porphyrins provide single units capable to coordinate with axial ligands as nitrogen-content compounds[37, 38] for example polymers that contain in its structure pyridine groups as a coordinating ligand.[39] On the other hand, the relatively ease of functionalizing and/or modifying the groups located in the periphery of porphyrin rings offers countless possibilities of modification. For example, introducing chiral properties through the linked groups to the central ring can change the self-assembly nature of the porphyrin, inducing certain orientation in its self-organization[40, 41] or by interaction with surfaces.[12, 42, 43]
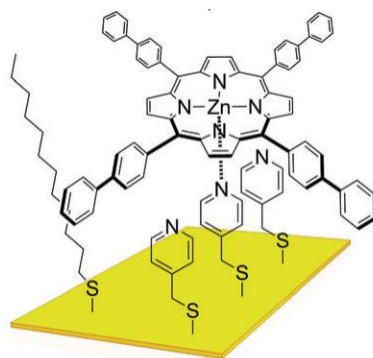
Fig. 6.1 *Bottom-up self-assembled monolayer of zinc (II) porphyrin on gold as approach towards molecular rotor.[36]*

This chapter gathers a study based on the supramolecular chemistry opportunities that offers poly(styrene-*b*-4-vinyl pyridine) (PS-*b*-P4VP) block copolymer (BCP) and a zinc(II)-coordinated metalloporphyrin (Zn-porphyrin) with four-substituted functional chains in the periphery. PS-*b*-P4VP is a versatile organic polymer due to the amphiphilic character and can easily be functionalized through the P4VP subunit block.[44-47] From the Zn-porphyrin part, the zinc metal ion located in the center position of the core of the porphyrin unit provided the possibility of coordination with the fourth position of the nitrogen of each single pyridyl unit[48] of the BCP, resulting in a supramolecular assembled system. The influence of the chirality was also tested through the role played by the four-substituted functional chains at the Zn-porphyrin periphery. For this, the Zn-porphyrins studied included, on the one hand, a porphyrin containing four chiral amide groups (Zn-(*R,R,R,R*)-1) and, on the other, its achiral homologue (Zn-2) (Fig. 6.2). Additionally to the coordination through the pyridine groups of the PS-*b*-P4VP and zinc (II) metal ion in the core of the porphyrin, amide groups on the periphery could drive the self-assembly by coordination of the carbonyl group of the amide with the zinc of an adjacent metalloporphyrin.[49] The chirality transfer from chiral metalloporphyrin monomer to the PS-*b*-P4VP Zn-(*R,R,R,R*)-1 superstructure was studied by circular dichroism (CD) spectroscopy. Moreover, other techniques such as UV-Visible absorption spectroscopy (UV-Vis) and Diffusion-Ordered Nuclear Magnetic Resonance (DOSY NMR) were used to demonstrate the axial coordination between the pyridyl units of the PS-*b*-P4VP to the zinc (II) metal ion in the porphyrin ring. The morphology studies of the superstructure formed in solution were analyzed by Transmission Electron Microscopy (TEM) and Electrostatic Force Microscopy (EFM). In a further step, the performance of Zn-(*R,R,R,R*)-1 nanorotors by linking the porphyrin to a immobilized PS-*b*-P4VP on surface was also conducted and characterized by Atomic Force Microscopy (AFM) and Scanning Electron Microscopy (SEM).
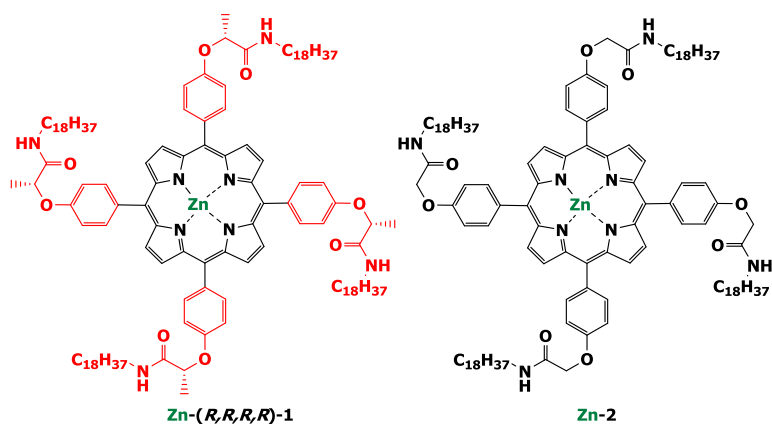
Fig. 6.2 *Target functionalized Zn-(R,R,R,R)-1 and Zn-2 porphyrins.*

6.2. RESULTS AND DISCUSSION

6.2.1. PS-*b*-P4VP-Zn(*R,R,R,R*)-1 and -Zn(2) coordination

Firstly and to ensure the viability of the coordination of the nitrogen from the pyridyl group of PS-*b*-P4VP BCP with the zinc (II) ion from either Zn(*R,R,R,R*)-1 or Zn(2), pure solutions of $5 \cdot 10^{-5}$ M Zn(*R,R,R,R*)-1 and $5 \cdot 10^{-5}$ M Zn(2) in chloroform were separately prepared. The solvent selected was chloroform because of its capacity to conserve the monomeric state (non-coordinated) of the chromophore part, avoiding the axial coordination between single Zn-porphyrins through competing carbonyl group coordination. The use of this solvent will guarantee that any change observed will be only product of the BCP-porphyrin binding.[49] The necessary volume of a freshly prepared $5 \cdot 10^{-4}$ M solution of PS-*b*-P4VP (molar ratio PS:P4VP 1:4) in chloroform to achieve the coordinating ratio P4VP:Zn-porhyrin 1:1 units was transferred to each porphyrin solution. All solutions were directly analyzed by UV-Vis absorption spectroscopy (UV-Vis) and the resulting spectra were compared with the spectra resulted from the same solutions after drop-casting them on standardized quartz

slides and allowing them to evaporate freely. In this way, coordination in the liquid and solid state could be compared (Fig. 6.3).
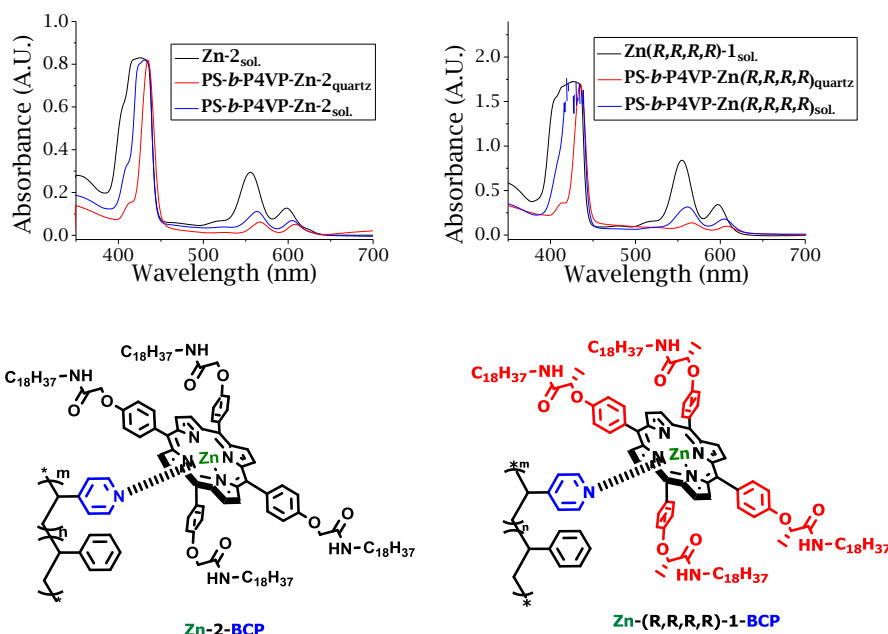
Fig. 6.3 *UV-Vis spectra of Zn-2 and Zn(R,R,R,R)-1 and their complexes with PS-b-P4VP in solution ('sol.') and on quartz (on the top) and, representation of the PS-b-P4VP-Zn-2 and -Zn(R,R,R,R)-1 complexed metallocompounds (on the bottom).*

A bathochromic shift of the Q bands in both coordinated complexes PS-*b*-P4VP-Zn-2 and PS-*b*-P4VP-Zn(*R,R,R,R*)-1 respect to the pure solutions of porphyrins was observed (Table 6.1). The absorption signal corresponding to Qα band of PS-*b*-P4VP-Zn-2 complex in solution ('PS-*b*-P4VP$_{sol.}$') evolved to lower energy compared with the metallocompound isolated in solution ('Sol.'), shifting from 556 to 564 nm. At the same time, the absorption signal associated to the Qβ band, also shifted from 598 to 605 nm in Zn-2 and PS-*b*-P4VP-Zn-2, respectively. The observed changes reflect the coordination of both elements through the pyridyl group with the zinc (II) metal ion in solution, as the character of the solvent was non-coordinating.[50-52] Analyzing the same complex casted on quartz ('PS-*b*-P4VP$_{quartz}$'), a similar bathochromic shift in Qα and Qβ bands experienced than in solution was revealed, being both of 11 nm. These results exhibited the viability to have the coordinated metallocompound PS-*b*-

P4VP-Zn-2 in solid state. On the other hand, PS-*b*-P4VP-Zn(*R,R,R,R*)-1 in solution ('PS-*b*-P4VP$_{sol}$') experienced a red-shift of the Qα band respect the pure porphyrin in solution ('Sol.') from 555 to 560 nm. In the same way, a bathochromic shift from 597 to 604 in Qβ band was spotted. According to the achiral homologue, these results indicated the coupling between the two compounds. Alike changes were observed when the coordinated system was in solid state ('PS-*b*-P4VP$_{quartz}$'). Few differences in the Q bands between the metallocompound in solution an in solid state were reflected in the spectra, indicating as well that chiral PS-*b*-P4VP-Zn(*R,R,R,R*)-1 was stable in solid state. The UV-Vis absorption signals corresponding to the Soret band of the porphyrins appeared in both complexed compounds at 420 nm, and the signal became saturated in solid and in solution states. Regardless, here only the Q-bands were followed. It needs to be highlighted that there is huge difficulty in controlling the exact concentration of the complexed systems in a drop when this was cast onto the quartz surface and moreover, the difficulty to control the distribution of the material on the substrate when solvent progressively evaporated. These could slightly affect the Q bands position due to some local stacking between neighboring free porphyrin units as a result of an increasing concentration by the evaporation of the chloroform (even is non-coordinating). Regardless, the equivalency of the shifts detected by UV-Vis absorption spectroscopy for PS-*b*-P4VP-Zn-2 and for PS-*b*-P4VP-Zn(*R,R,R,R*)-1 in solid and in solution state respect to the free metalloporphyrins attested the coordination (Table 6.1).[53]

Table 6.1   *Resume of the positions of absorption bands corresponding to the Q*
bands of the studied Zn-porphyrins in solution and on quartz.

| | Q bands position (nm) | | | |
| | Zn-2 | | Zn(*R,R,R,R*)-1 | |
Sample	Qα	Qβ	Qα	Qβ
Sol.	556	598	555	597
PS-*b*-P4VP$_{quartz}$	567	609	566	608
PS-*b*-P4VP$_{sol.}$	564	605	560	604

It was observed in a previous work, that metalloporphyrin Zn-
(*R,R,R,R*)-1 self-assembled in non-polar solvents through the coordination
between the carbonyl group of the amide and the zinc (II) metal ion of an
adjacent porphyrin forming a dimer aggregates.[49] The coordination
studies between the block copolymer PS-*b*-P4VP and the chiral
metalloporphyrin Zn-(*R,R,R,R*)-1 might allow the chiral amplification in the
supramolecular structure following sergeant and soldier effects[*,54-56] For
this reason and because the observed stability of the solid compound, a
study of the Circular Dichroism (CD) response of the PS-*b*-P4VP-Zn-
(*R,R,R,R*)-1 on a standardized quartz slide was performed (Fig. 6.4). The
CD principle is based in the absorption difference of the left- and right-
handed polarized light and, the CD signal intensity and position might be
affected by the perturbation in the surroundings of the chromophore.[57]
The sample was prepared following the same procedure and conditions
used in UV-Vis analyses for the solid state samples. Contrarily to the
results in solution[†], PS-*b*-P4VP-Zn-(*R,R,R,R*)-1 in solid state a noisy and
unclear CD signal response was recorded. The effect of the impossibility

---

[*] Sergeant and soldier effect is related to the amplification of the chirality conducted by
the cooperative action of individual small forces, for instance *via* incorporating
asymmetric centers in the sides of a macromolecular chain. See *J. Am. Chem. Soc.* 2001,
123, 10153-10163.

[†] See *Self-assembly of functional chromophores into chiral nanomaterials*, PhD. Thesis of
Cristina Oliveras-González, 2015.

to control the concentration in a drop as well as the effect of the progressive evaporation of the solvent inducing some kind of forced assembly (effect mentioned before but still not observed until now) hampered the visualization of the CD response in the solid chiral compound.
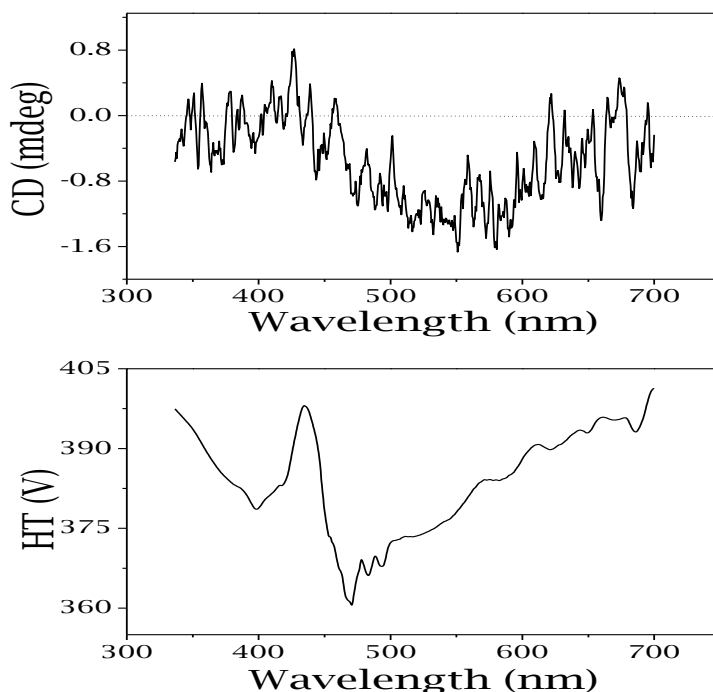
Fig. 6.4 *CD and High Tension (HT) spectra of solid PS-b-P4VP-Zn(R,R,R,R)-1 complex on a quartz surface.*

Apart from UV-Vis absorption spectroscopy, additional experiments by Diffusion-Ordered NMR (DOSY NMR) were performed to confirm the binding. The chiral compound was taken as reference and so, making extensible the results to the Zn-2. Zn(*R,R,R,R*)-1 porphyrin was analyzed individually and coordinated with the PS-*b*-P4VP in addition to the pure PS-*b*-P4VP solution. Samples were dissolved in deuterated chloroform and transferred to NMR glass tubes for further experiments. DOSY spectra (Fig. 6.5) clearly showed differentiated diffusion coefficients in the measurements involving the PS-*b*-P4VP-Zn(*R,R,R,R*)-1. Values of $4.18 \cdot 10^{-6}$ and $4.94 \cdot 10^{-7}$ cm^2/s were obtained for pure precursors Zn(*R,R,R,R*)-1 and PS-*b*-P4VP respectively, indicating a slower diffusion of

the BCP than the metallocompound alone under the same conditions. The block copolymer macromolecular chain was probably entangled forming an amorphous mesh oppositely favorable to diffusion through the medium, apart from a high molecular weight that hindered in part its dragging. The alkyl chains (C18) in the periphery of the porphyrin, and the phenylene groups linking the alkyl part to the core straightened in part peripheral substituents avoid a massive self-folding of the structure and facilitating the diffusion, apart from a lower molecular weight. Unlike the precursors, the diffusion coefficient of PS-*b*-P4VP-Zn(*R,R,R,R*)-1 resulted in a value of $8.91 \cdot 10^{-7}$ cm^2/s, an intermediate value between pure compounds, although more nearby to PS-*b*-P4VP. This could be explained because the molecular weight was the most relevant parameter so that observing a remarkable shift of the metallocompound diffusion spectrum respect to the BCP but more important respect to the porphyrin. With these results the coordination of PS-*b*-P4VP-Zn(*R,R,R,R*)-1 was demonstrated again.
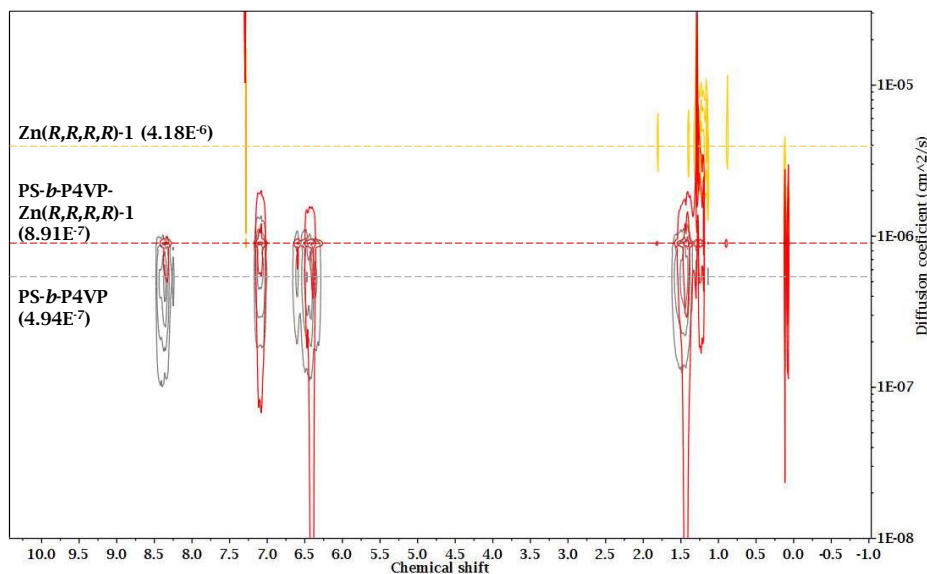
Fig. 6.5 *DOSY NMR spectra of Zn(R,R,R,R)-1 (orange), PS-*b*-P4VP (grey) and PS-*b*-P4VP-Zn(R,R,R,R)-1 (red) compounds. Dashed lines highlight corresponding diffusion coefficient values.*

6.2.2. Self-assembly of the coordinated PS-*b*-P4VP-Zn-2 and PS-*b*-P4VP-Zn(*R,R,R,R*)-1 complexes

With the aim to study the organization of the PS-*b*-P4VP-Zn-2 and PS-*b*-P4VP-Zn(*R,R,R,R*)-1 complexes at the microscopic level in the solid state, 0.5 ml of a Zn-2 solution in chloroform at a concentration of $2 \cdot 10^{-5}$M was mixed with 0.5 ml of a solution of PS-*b*-P4VP 0.48 M in chloroform. In parallel, another mixed solution of Zn(*R,R,R,R*)-1 with PS-*b*-P4VP at the same concentrations was prepared. A drop of each resulting mixed solutions was drop-cast separately on a HOPG (Highly Oriented Pyrolytic Graphite) surface and was analyzed by Atomic Force Microscopy (AFM) after the total free evaporation of the solvent at room temperature. Concurrently, an additional AFM control experiment with pure PS-*b*-P4VP prepared under same conditions was analyzed (Fig. 6.6). The AFM topography of PS-*b*-P4VP (Fig. 6.6a) showed an irregular holed layer, probably as a consequence of the free evaporation of the solvent, that created delocalized inhomogenities of concentration during the evaporation, leaving locally dewetted regions. Zooming-in the topography (Fig. 6.6b), indications of phase segregation from the continuous layer of polymer can be appreciated, although holes were too large to obtain better contrasted images. As a consequence of the large holes, not much information could be extracted from the phase image (Fig. 6.6c). Height profile (Fig. 6.6d) pointed a thin layer of PS-*b*-P4VP at the nanoscale was obtained, with crystal-like objects with ~10 nm in height. The nature of the crystal-like objects is unclear at present.

Fig. 6.6 *AFM images of PS-b-P4VP drop-casted on HOPG surface. a) Topography (scale bar 5 μm), b) topography of red-dashed area in a, (scale bar 1 μm), c) phase corresponding with b area (scale bar 1 μm), d) height profile of blue-dashed line in b.*

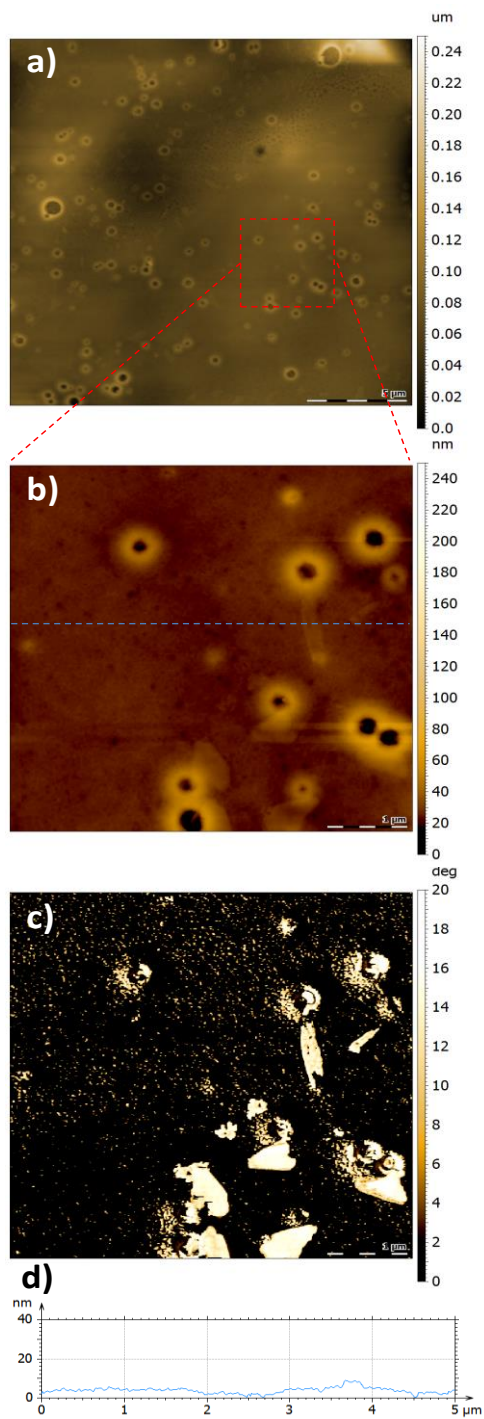On the other hand, AFM images of the topography of PS-*b*-P4VP-Zn-2 and PS-*b*-P4VP-Zn(*R,R,R,R*)-1 (Fig. 6.7a-e and b-f) showed a completely different structure: some flake-like objects appear uniformly across the surface, being larger in the chiral compound as well as small spherical-shaped objects, than for the achiral system.[58] Certainly the effect of the evaporation of the solvent can influence in some way the disposition of the sample on the surface as has been explained above, apart from some effect of the graphite in the disposition of the material on surface.[42] Taking into account the UV-Vis absorption spectroscopy measurements that demonstrated the binding in solid state it appears that the structures are directly related to the coordination of the block copolymer and metalloporphyrin. The influence of the chirality certainly had some effect in the self-assembly of the systems. Phase images showed better contrast than purely topographic micrographs (Fig. 6.7 c-g). In PS-*b*-P4VP-Zn-2 (Fig. 6.7c) two different phases were clearly appreciated, corresponding presumably to PS-*b*-P4VP-Zn-2 and to PS-*b*-P4VP in the role of matrix (assuming that not all porphyrin units were coordinated to the pyridyl groups). A similar situation was seen for the chiral homologue (Fig. 6.7g). Moreover, in both samples a very thin stripped phase in the flake-like structures could be distinguished. This might indicate the arrangement of the systems, presumably having the long alkyl chains of side-to-side coupled porphyrins to the polymeric structure a preferentially intermolecular interactions, similarly as Ikeda and coworkers earlier reported and Snitka *et al.* observed for a tetrakis(4-sulfonatophenyl) porphyrin (Fig. 6.8).[59-61] Both, height profiles of the achiral and chiral metalloporphyrin-based complexes showed that the flake-like structures were ~ 35 nm in height and small spherical-shaped solids had averaged diameters of ~50 nm in PS-*b*-P4VP-Zn-2 and of ~100 nm in PS-*b*-P4VP-Zn(*R,R,R,R*)-1, compared to the size of ~10 nm for the crystal-like objects observed in the pure polymer (Fig. 6.7 d-h).
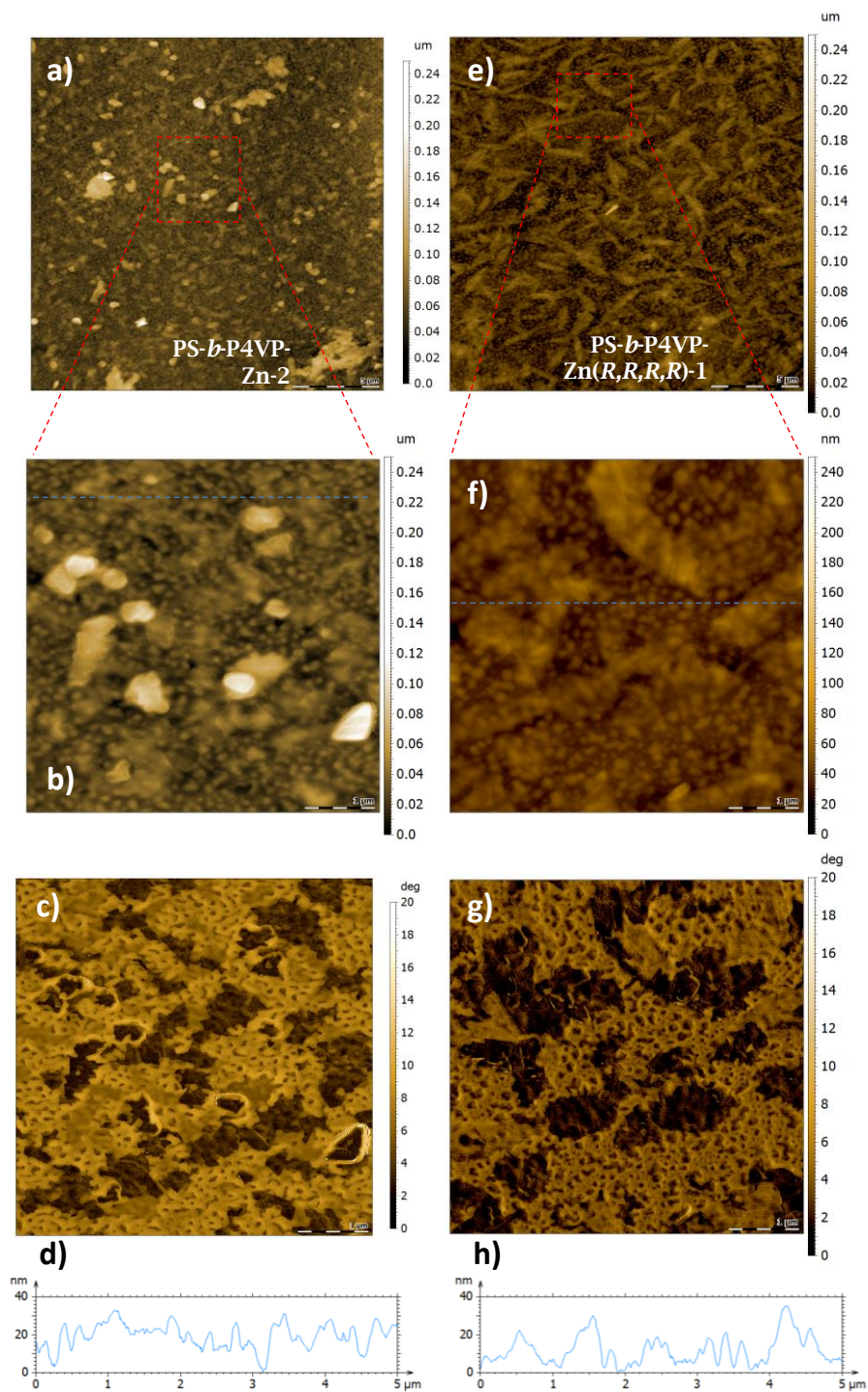
Fig. 6.7 *AFM images from PS-*b-*P4VP-Zn-2 (left column) and PS-*b-*P4VP-Zn(R,R,R,R)-1 coordinated compounds on HOPG surfaces. a, e) Images of the topography (scale bars 5 μm). b, f) Images of the topography of magnified*

areas from a, e (indicated with red dashed lines) (blue dashed lines indicate where the height profiles were taken from) (scale bars 1 µm). c, g) Phase images from b, f (scale bars 1 µm). d, h) Height profiles corresponding to horizontal dashed lines in b, f.
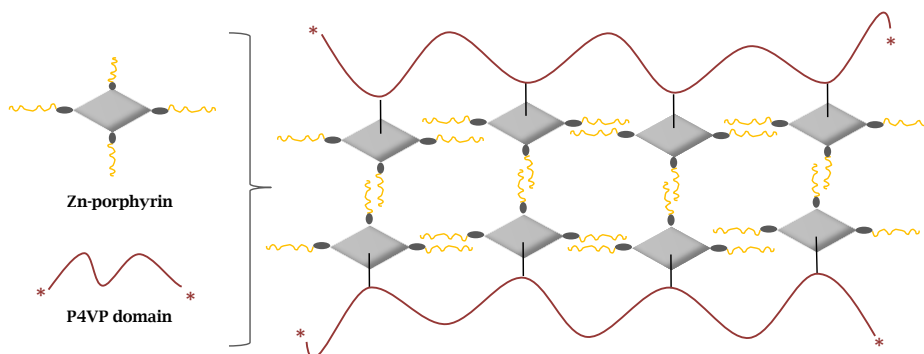
Fig. 6.8 *Representation of the proposed arrangement of the Zn-porphyrins coupled to P4VP macromolecular domains of the PS-b-P4VP.*

Transmission Electron Microscopy (TEM) was the technique used to determine the influence of the chirality of the metalloporphyrins in the phase segregation of the complexes. For this, PS-*b*-P4VP, PS-*b*-P4VP-Zn-2 and PS-*b*-P4VP-Zn(*R,R,R,R*)-1 solutions in chloroform were separately dried under vacuum for several hours until solid powders were afforded. These were separately embedded in an epoxy resin and cured at 60ºC for 2 days. Then, they were cut by using a microtome to finally obtain samples with a thickness of 70-100 nm. The different samples were collected in holey-carbon copper TEM grids and were also selective stained with iodine vapors for 1 hour in a sealed container. TEM image of pure block copolymer (Fig. 6.9) showed up disordered phase segregation in the PS-P4VP interface. Darker domains corresponded to P4VP block which was selectively stained with iodine vapors to enhance TEM contrast. The PS-*b*-P4VP-Zn-2 complex arranged in what could be either hexagonally packed cylinders or body-centered cubic system structures (would be necessary complementary techniques to elucidate it, such as Small-Angle X-ray Scattering, SAXS or synchrotron measurements). PS-*b*-P4VP-Zn(*R,R,R,R*)-1 chiral complex showed very defined domains, probably arranging either in body-centered cubic spheres (fm3m), gyroid (ia3d) or inverse discontinuous cubic structure (fd3m).[62-67] These evidences proved the

effect of the chiral groups located in the substituted periphery porphyrin chains in the self-assembly of the supramolecular PS-*b*-P4VP complex, resulting in strongly segregated conformations. The chiral characteristic, given only by a single methyl group in each substituted alkyl chain, enlarged significantly the space domains between PS and P4VP probably because a higher steric hindrance between neighboring metalloporphyrin units anchored to the pyridyl groups.
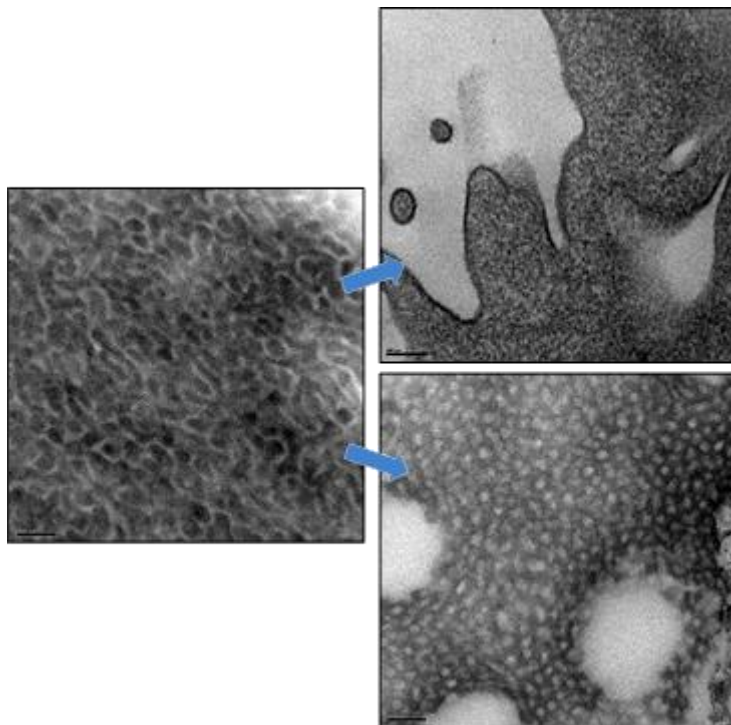
Fig. 6.9 *TEM images of PS-b-P4VP (on the left), PS-b-P4VP-Zn-2 (on the upper-right) and PS-b-P4VP-Zn(R,R,R,R)-1 (on the bottom-right). Scale bars correspond to 100 μm.*

All the foregoing results endorsed the viability of the chiral and achiral metalloporphyrin polymer-based complexes. For this reason and due to the amphiphilic character of PS-*b*-P4VP, it was thought they were suitable systems for tailored self-assembled approaches, i.e. inducing target arrangements by the role of the solvent. Tuning PS-*b*-P4VP phase segregation *via* annealing treatments[68-71], adjusting volume fraction of blocks[62, 72-74] and/or modifying the polarity of solvents[75-77] are well-known techniques and are widely described. Li and coworkers reported core-shell

micelles based on the electrostatic interaction between poly(ethylene glycol)-*b*-poly(4-vinyl pyridine) block copolymer and achiral free-based tetrakis(4-sulfonatophenyl) porphyrin, resulting in a chiral arrangement on the shell of micelles.[78]

Non-selective solvents for PS-*b*-P4VP (dissolving) are chloroform and tetrahydrofuran (THF), PS selective solvents are toluene and dioxane and to solubilize P4VP ethanol or dimethylformamide (DMF) are good.[70, 71, 79] As starting point, 0.04 mM solutions of Zn-2 and Zn(*R,R,R,R*)-1 and 0.02 mM dispersion of PS-*b*-P4VP all in ethanol were prepared. Then, 1 ml of each solutions of Zn-2 or Zn(*R,R,R,R*)-1 were mixed with 1 ml of PS-*b*-P4VP, respectively. Pure and mixed porphyrin-based solutions were drop-cast on carbon coated copper TEM grids for further analyses. The TEM measurements (Fig. 6.10a) revealed a compact packing of porphyrins, forming what it looked slices. Individual units of the metallocompound could not be found after checking all samples. Thus, indicating a considerable tendency of keeping the aggregated state in the presence of ethanol. The incorporation of PS-*b*-P4VP to Zn-2 with the aim of forming PS-*b*-P4VP-Zn-2 resulted in large holed membranes of the complex without a determined structure as indicated diffraction analysis (Fig. 6.10 c-e). It was assumed that darker regions belonged to P4VP-Zn-2 domains since samples were not stained, similar to the observations of Yao *et al.* in aggregated chiral compound with achiral polymers.[64] On the other hand, in the TEM images of chiral Zn(*R,R,R,R*)-1 (Fig. 6.10b), a more dispersed matter could be spotted, even though some slice-like parts (less compacted) were observed. Zn(*R,R,R,R*)-1 tended to keep more aggregated forming fibrous coiled elements compared to the Zn-2 porphyrin, presumably as a result of the chiral character of the sample. In PS-*b*-P4VP-Zn(*R,R,R,R*)-1 complex (Fig. 6.10d), well-defined 'cauliflower'-shaped structures were depicted. Concretely, in the case of PS-*b*-P4VP-Zn(*R,R,R,R*)-1 compound, results suggested that polymer embraced coiled Zn(*R,R,R,R*)-1 compound, conducting twisted fibrous meshes, as diffraction pattern showed (Fig. 6.10f).
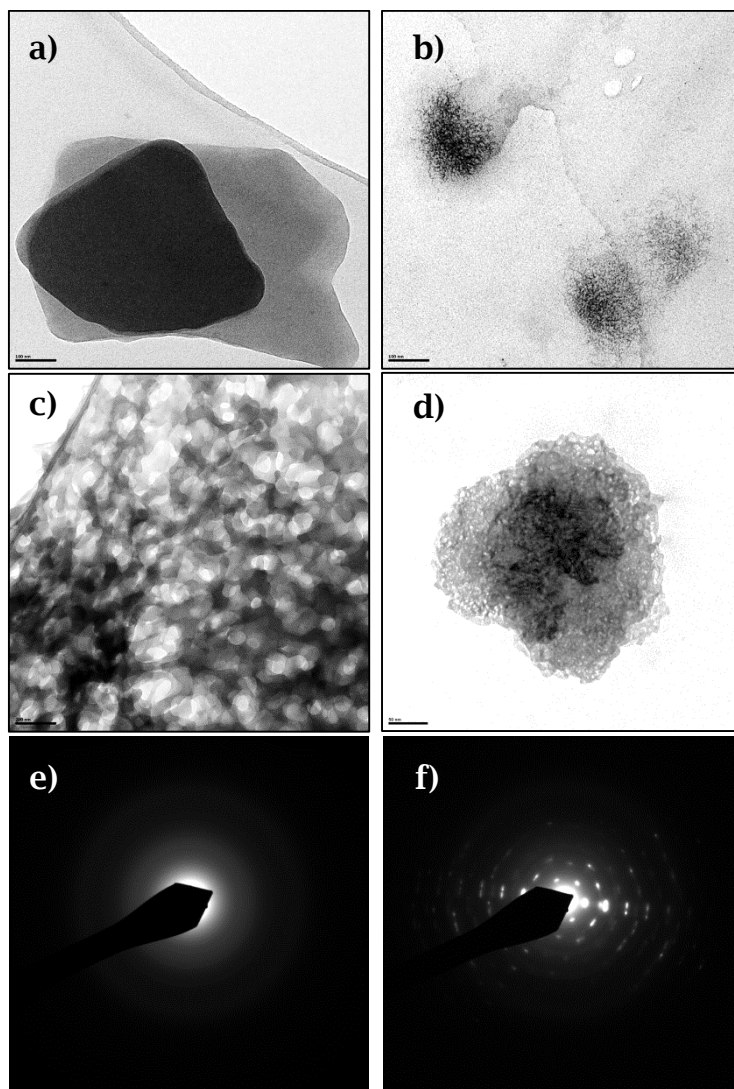
Fig. 6.10 *TEM images of Zn-porphyrins and their complexes with PS-b-P4VP obtained from solutions in ethanol. a) Zn-2 (scale bar 100 nm), b) Zn(R,R,R,R)-1 (scale bar 100 nm), c) PS-b-P4VP-Zn-2 (scale bar 200 nm), d) PS-b-P4VP-Zn(R,R,R,R)-1 (scale bar 50 nm), e) diffraction pattern from c and, f) diffraction pattern from d.*

Other concentrations and methodologies were tested to corroborate their effect on the resulting samples and also to obtain further evidence of the chiral packing. Therefore, 0.3 ml of a 0.09 mM solution of PS-*b*-P4VP was mixed with 0.3 ml of a solution 0.2 mM of Zn(*R,R,R,R*)-1, both in ethanol. The resulting mixed solution was analyzed in two ways by TEM: (i) a drop of it was cast on a holey-carbon copper TEM

grid and directly analyzed, (ii) an aliquot of the solution was dried and then was embedded in an epoxy resin, the resin was cured and then cut using microtome in thin slices (70-100 nm) and analyzed by TEM without staining and, (iii) the same procedure as (ii) but the sample was stained with I_2 vapours for 1 hour in a sealed container before TEM imaging (Fig. 6.11).
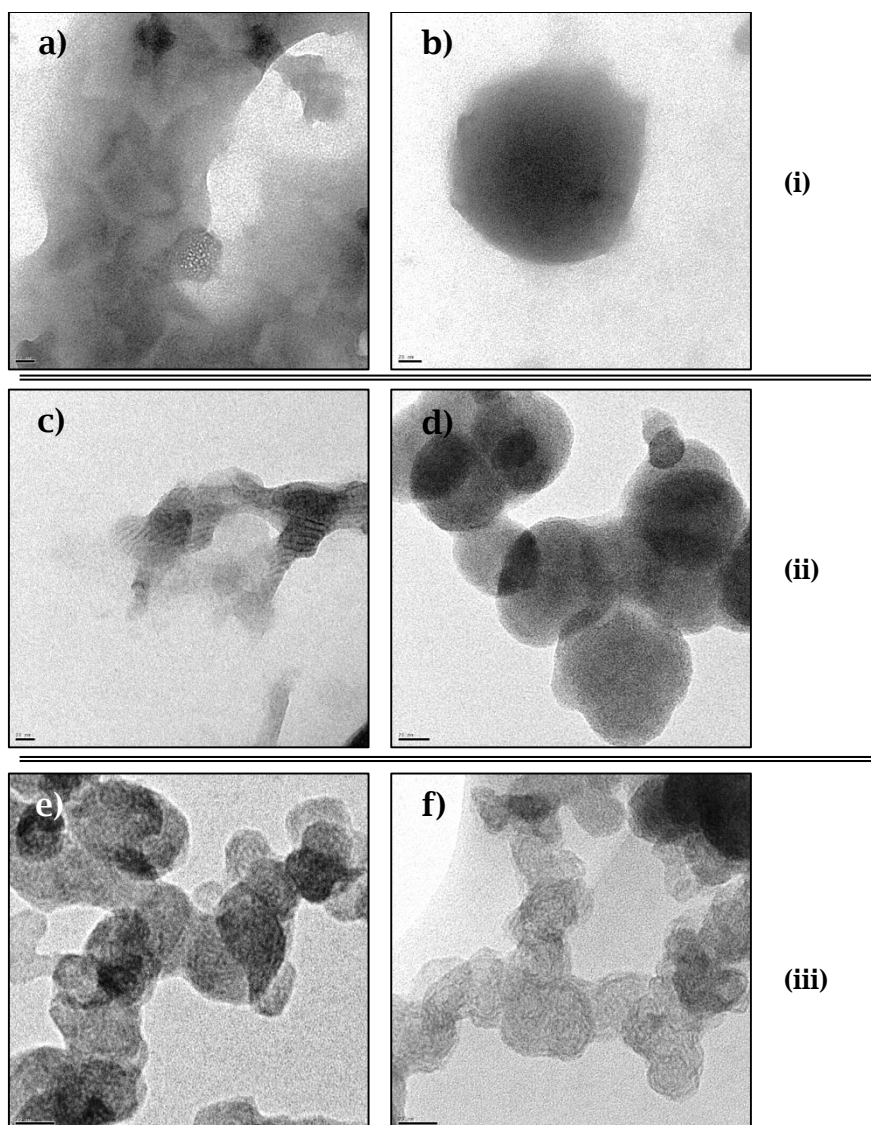
Fig. 6.11 *TEM images of PS-b-P4VP-Zn(R,R,R,R)-1 sample prepared in ethanol. a) and b) from a drop of the mixed solution without staining, c) and d) from the dried mixed solution embedded in an epoxy resin without staining and,*

e) and f) from dried mixed solution embedded in an epoxy resin stained with I₂ vapours. Scale bars of all images correspond to 50 nm.

From the drop of mixed solution PS-*b*-P4VP-Zn(*R,R,R,R*)-1 directly analyzed by TEM (Fig. 6.11 a-b) some regions with agglomerated matter and spherical aggregates with blurred perimeter were appreciated. The majority of the observed micelle-like objects were small but within a broad range of sizes, around 300 nm for the spherical objects. A few distorted micelles might suggest a chiral assembly in their coronas, as it was appreciated in Fig. 6.11a, similarly to Li *et al.*, who observed chiral porphyrin-based micelles, where they assumed that dark regions were from porphyrin-based stacks.[78] On the other hand, in the polymeric metallocompound PS-*b*-P4VP-Zn(*R,R,R,R*)-1 obtained from the sample prepared with epoxy resin, self-assembled Zn(*R,R,R,R*)-1 porphyrin domains (Fig. 6.11c), at the same time that aggregated micelles could be easily spotted (Fig. 6.11d). It was assumed that the observed dark regions in Fig. 6.11c corresponded to pure Zn(*R,R,R,R*)-1 porphyrin, because the sample was not selectively stained. After enhancing the contrast by selectively staining P4VP domains with I₂ vapours the distribution of the block copolymer in the PS-*b*-P4VP-Zn(*R,R,R,R*)-1 micelles could be clearly appreciated (Fig. 6.11 e-f). Images illustrated a possible twisted rope-like structure which could belong to P4VP domains, coiled by the chiral effect of the porphyrin.[78]

With the aim to elucidate whether obtained the self-assembled complex in the corona of micelles in ethanol corresponding to the PS-*b*-P4VP-Zn(*R,R,R,R*)-1 complex possessed chiral properties, a measurement of the CD signal of the complex in solution was performed. The analyzed ethanolic solution was the same as used in TEM experiments after diluting to $5 \cdot 10^{-3}$ mM. Neither the CD signal recorded from the pure metallocompound nor from the complexed system, a response derived from the chirality that could suggest a chiral packing was observed and moreover, the non-coordinative behaviour of the ethanol for that porphyrinic system could be confirmed (Fig. 6.12). These results rule out chiral arrangement on the corona of the micelles or even in the first sublayer (assuming a multi-layer conformation) probably due to either an

inhomogenous distribution or amorphous arrangement of the block copolymer that distorted it.
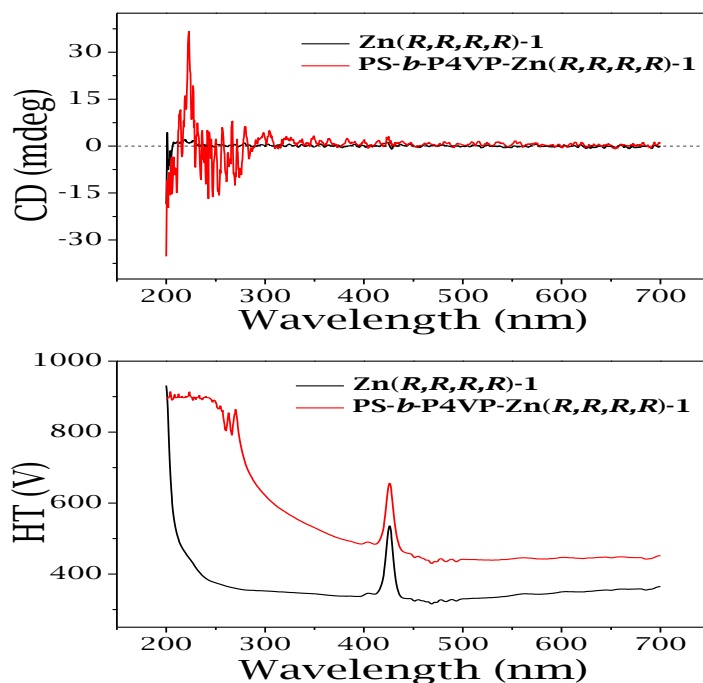
Fig. 6.12 *CD and High Tension (HT) spectra of PS-b-P4VP-Zn(R,R,R,R)-1 complex in ethanol solution.*

The next goal of this study was achieving polymer-based micelles by the interchange of solvent, i.e. by solvent exchange methodology.[80-82] The solvent exchange procedure involves firstly dissolving the amphiphilic copolymer in a non-selective solvent and secondly, adding slowly a selective solvent, for example a polar one, until the latter is in excess. Then the non-selective solvent is removed (usually by evaporation), in this way exchanging one solvent for another one. During the process of the progressive evaporation of the non-selective component, hydrophobic part of the copolymer will start to collapse and finally will form a micelle, with hydrophilic tails on the outskirts and hydrophobic in the core. To prove this in the present systems, organic-to-selective polar solvent exchange was tested. 3 mg of PS-*b*-P4VP and 0.25 mg of Zn-2 were dissolved in 1 ml of THF. Then, 4 ml of ultrapure water was added dropwise and THF was removed from the mixture by evaporation. In parallel, the inverse process,

organic-to-selective organic solvent, was also tested by preparing a solution of 3 mg of PS-*b*-P4VP and 0.25 mg of Zn-2 in THF, then adding 4 ml of 1,4-dioxane dropwise and removing the THF by simple evaporation. Both experiments (organic-to-selective polar and organic-to-selective organic solvents) were also performed with the chiral homologue Zn(*R,R,R,R*)-1-based metallocompound. Additionally control experiments for each solvent exchange process with pure PS-*b*-P4VP, Zn-2 and Zn(*R,R,R,R*)-1 under same conditions and following the same procedures were performed. A drop of each test mentioned above was separately analyzed by TEM using holey-carbon copper grids.
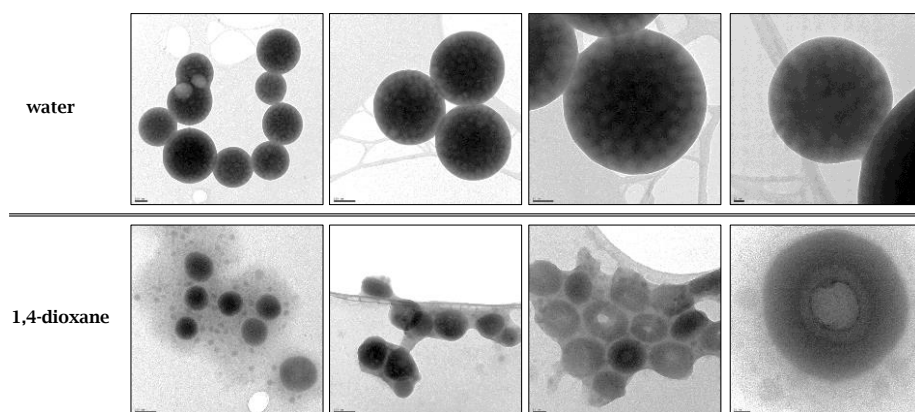
Fig. 6.13 *TEM images of pure PS-b-P4VP micelles obtained by water (upper) and 1,4-dioxane (bottom). Scale bars from the left to the right (for both samples), 100 μm, 100 μm, 50 μm and 20 μm. Samples were stained with I$_2$ vapours.*

TEM images of PS-*b*-P4VP in water (Fig. 6.13) revealed well-defined round micelle-like objects with a narrow range of sizes, comprised between ~150-400 nm. The P4VP phase was selectively stained with iodine vapours and appeared as dark regions. Similar micelles of PS-*b*-P2VP were obtained following same procedure by Klinger *et al.*[83] When the solvent inducing the micellar assembly was 1,4-dioxane, a core of P4VP surrounded by a PS corona was expected.[84] From TEM images collected for the mentioned sample (Fig. 6.13), smaller micellar structures were obtained and moreover, looked as though they were surrounded by poorly defined matter that appeared blurred. Because the sample was also stained to enhance the contrast, darker regions would correspond to P4VP domains, these being spherical dark regions and the surrounding matter

might be attributed to the PS block, probably swollen as a result of the contact with 1,4-dioxane and consequently forming a blurred matter in their surrounds.[85] Remarkably, the volume fraction of the blocks forming the PS-*b*-P4VP used in this study (PS:P4VP of 1:4), could be also a factor that probably affected the resulting sizes, distributions and behavior of micelle-like objects in the different solvents due to the selectivity of each block.

Conversely, TEM image of pure Zn-2 in water (Fig. 6.14a) showed that the metallocompound self-assembled in straight, planar and large ribbons induced by a presumably H-aggregation of porphyrin units, similarly to Ogi and coworkers observations.[58] Zn-2 in 1,4-dioxane (Fig. 6.14b) self-assembled forming mixed structures, both 'slices' as previously observed in ethanol and wider ribbons. The coordinative character of 1,4-dioxane is known, as shown for instance, by Mikhalitsyna *et al.* who used this solvent to coordinate Zn-porphyrin-based complexes axially.[86] TEM images from the chiral Zn(*R,R,R,R*)-1 in water (Fig. 6.14c) showed little and larger panel-shape or sliced aggregates of metallocompound, very different to the achiral homologue. When the solvent was 1,4-dioxane (Fig. 6.14d), similar sliced aggregated were found out, although a larger surface was apparent.

	Zn-2	Zn(*R,R,R,R*)-1
water	a)	c)
1,4-dioxane	b)	d)
	Zn-2	Zn(*R,R,R,R*)-1
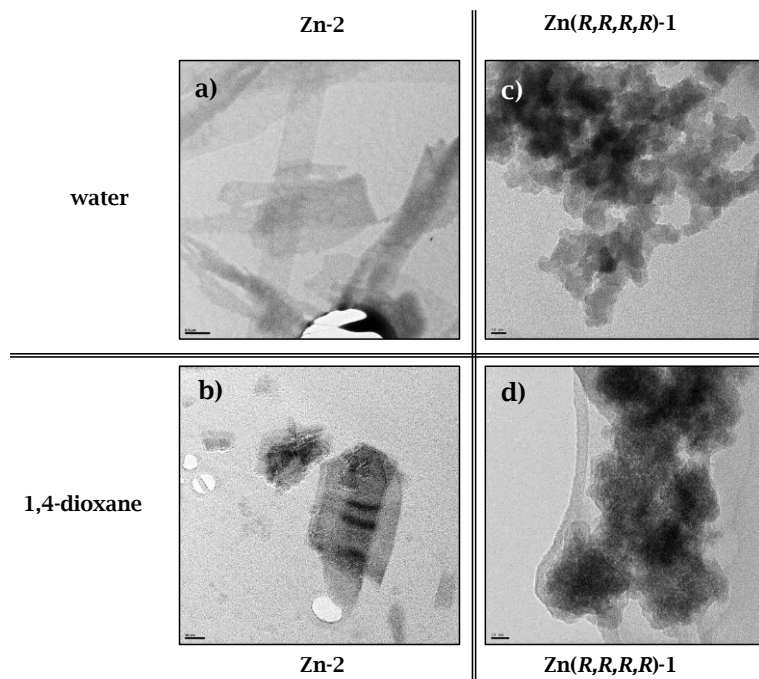
Fig. 6.14 *TEM images of Zn-2 in water a) (scale bar 0.5 µm) and in 1,4-dioxane b) (scale bar 50 nm), Zn(R,R,R,R)-1 in water c) (scale bar 20 nm) and in 1,4-dioxane d) (scale bar 20 nm).*

Images of PS-*b*-P4VP-Zn-2 organic-to-selective polar solvent exchange sample showed that very defined, round and filled spheres were obtained (Fig. 6.15 a-b). While PS-*b*-P4VP-Zn-2 was increasingly concentrated in water by the THF evaporation, the hydrophobic parts (PS block and porphyrin alkyl chains) is progressively relegated to the solvent shielded part of the spheres, leaving the hydrophilic part on the outer edge. Darker spots were also seen inside the spheres, assuming local inhomogenities of the quantity of matter and/or a proof of the location of the Zn-2 distribution. This might suggest a multiple layer or onion-like micelles as Fan and Jin earlier reported from precipitated micelles from aqueous solutions of PS-*b*-P2VP.[76] Going from the outer to the inner part of micelles, the 'skin' of the micelle was probably formed by a layer of the P4VP block, as was the part directly in contact with water, followed by the linked Zn-2 that was inhomogenously distributed due to the different sized dark spots and, in the more internal part, a combination of PS domains and the long alkyl chains from the Zn-2, oriented to the

hydrophobic part. The suggested assembling could be appreciated in a magnified image of a single sphere (Fig. 6.15b) where perforated regions showed up different internal levels, leaving the core exposed, formed by PS domain (white). Contrarily, when PS-*b*-P4VP-Zn-2 was obtained by organic-to-selective organic solvent exchange, rougher and smaller micelles were appreciated (Fig. 6.15 c-d). In this case inverse conformed micelles were expected, the corona being composed of PS domains and probably the alkyl chains of the Zn-2 oriented to the outside through a PS mesh (resulting in blurred profiles), followed by layer of Zn-2 and lately the P4VP domains in the core. An increased tendency of aggregation between micelles was appreciated, probably due to the affinity between projected alkyl chains of neighboring packed systems. The possible influence of the volume fraction of each block forming the BCP has to be taken into account, here the molar ratio of PS:P4VP in the BCP was of 1:4, thereby resulting in smaller and probably much greater quantity of micelles when PS was in the outer part. Moreover, the color of the solutions could also be indicative of the coordination state between BCP and porphyrin. BCP and Zn-porphyrin in individual solutions were colorless and intense violet, respectively, and after mixing them, solutions turned to greenish, an evidence of the coordination. Consequently, due to the color of the solution (pale rose) and to the results, the solvent 1,4-dioxane was not as suitable for the coordination of the compounds as water was.
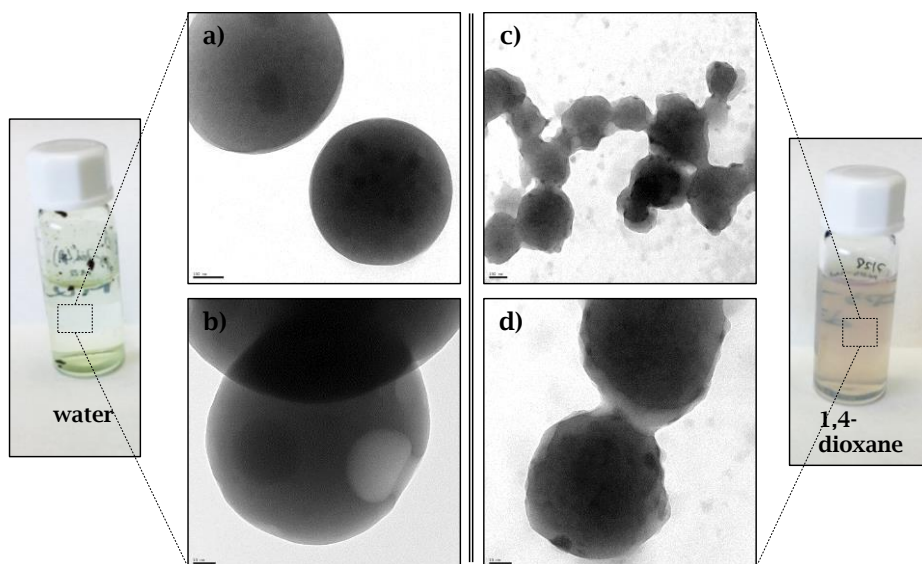
Fig. 6.15 Pictures of PS-b-P4VP-Zn-2 solutions in water (greenish) and in 1,4-dioxane (pale rose). TEM images of PS-b-P4VP-Zn-2 micelles in water a) and b) (scale bars 100 and 50 nm, respectively) and, in 1,4-dioxane c) and d) (scale bars 100 and 50 nm, respectively).

On the other hand, PS-*b*-P4VP-Zn(*R,R,R,R*)-1 in water (Fig. 6.16 a-b) displayed well defined micelles, similar to its achiral homologue. So for extension, images suggested a similar ordering, not evidencing a clear effect of the chirality. Contrarily, when the chiral metallocompound was immersed in 1,4-dioxane (Fig. 6.16 c-d), there was not micellar aggregation, even polymer phase segregation in the background in combination with some stripped aggregates could be discerned (Fig. 6.16 c). The sample contained a high proportion of the mentioned stripped aggregates, isolated or forming large areas. For this reason and as the color of the solution evidenced (pretty similar to the pure Zn(*R,R,R,R*)-1), it could be concluded that there was no coordination between the PS-*b*-P4VP and Zn(*R,R,R,R*)-1 as a result probably of a preferential axial coordination through the zinc (II) of the porphyrin and to the 1,4-dioxane.[86] Snitka and coworkers observed similar striped structures (they called them molecular ribbons) in aggregates of tetrakis(4-sulfonatophenyl)porphyrin, so this supported as well the theory that precursors were uncoupled not complexed.[61]
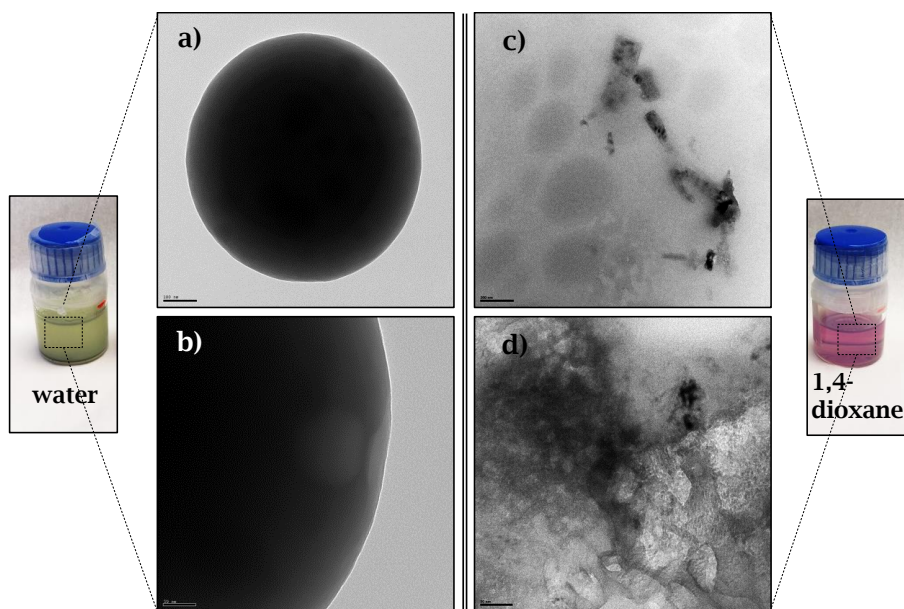
Fig. 6.16 *Pictures of PS-b-P4VP-Zn(R,R,R,R)-1 solutions in water (greenish) and 1,4-dioxane (pink) and TEM images of: a) and b) PS-b-P4VP-Zn(R,R,R,R)-1 micelles in water (scale bars 100 and 50 nm, respectively) and, c) and d) PS-b-P4VP-Zn(R,R,R,R)-1 mixed compound in 1,4-dioxane (scale bars 100 and 50 nm, respectively).*

6.2.3. An approach towards polymeric supramolecular rotors: surface immobilization of PS-*b*-P4VP-Zn(*R,R,R,R*)-1

Porphyrins, metalloporphyrins and their derivatives are well-known as components in photosynthetic reaction centers.[8] In a further step in nature mimicking, efforts in the control and understanding of the molecules motion have been made, for instance in the developing of molecular rotors. In this way, porphyrins and their derivatives have been widely described as their potential applications as molecular machines.[11, 87-89] Ikeda and coworkers could design, capture and demonstrate the motion of a cerium-coordinated porphyrin-based molecular rotor by controlling the photochemical redox states of the metal.[34, 35] Sauvage *et al.* reviewed the developments in porphyrin-based rotaxanes as molecular machine applications and their future perspectives.[90]

In view of the potential opportunities and tunability of the studied system, it was thought the immobilization of the polymeric part on surface to have stuck and free pending sites in were Zn-porphyrin could settle down and be anchored by coordination and ease the rotational motion of the porphyrin. Viability of rotors on surface was previously studied, and Kottas and coworkers in 2005 reviewed the work on the field so far.[8] Cyclodextrins (CyDs) are suitable compounds as linking agents between surface and PS-*b*-P4VP. Huskens and Reinhoudt led several studies using CyDs as linking agents on surface employing soft lithography, what they called molecular printboards[91, 92] CyDs, for their part, are widely known compounds because they constitute an important building block for supramolecular systems, as they can form complexes by host-guest interactions with other molecules due to their shape of cage/container (cyclic oligosaccharides).[93] For this, they have been on the focus of numerous studies based in drug delivery[94, 95], supramolecular polymers[96, 97], bioactive materials[98] or in the solubilization of hydrophobic materials.[99, 100] Typical CyDs can contain a number of glucose monomers ranging from six to eight units in a ring and their properties differ slightly: α-CD (6-memebered sugar ring molecule), β-CD (7-membered sugar ring molecule) and γ-CD (8-membered sugar ring molecule). The manipulation of hydrophobic-guest interactions between CyDs and polymers has been studied abundantly.[101-107]

From all the literature reported, the work performed by Storsberg and Ritter was of special interest for the present study, because they demonstrated the inclusion of a PS polymer into a β-CD by only mixing them together in an aqueous solution.[108] Subsequently, the immobilization of a derivative CyD on surface was another objective established. With this, CyD will create available inclusion sites to later incorporate the PS of the amphiphilic PS-*b*-P4VP by hydrophobic-guest interactions, having in this way, the P4VP part free for the coordination with Zn-porphyrin.[109] At this point the major challenge would be the demonstration of the inclusion of the PS instead of the hydrogen bonding coordination of P4VP with sugar-based units conforming CyD. Thiol-functionalized β-CD (per-6-thio-β-CD, β-CDSH) self-assembled monolayers (SAMs) on gold were prepared following the reported procedure.[110, 111] Then, an aqueous

dispersion of PS-*b*-P4VP was used with the aim to include it into *β*-CD cage and lately, chiral Zn(*R,R,R,R*)-1 was coordinated. Micro-contact printing (µcP) was the soft lithography[112] technique used to create patterns of the PS-*b*-P4VP on gold *β*-CDSH SAMs.[113-115]

There were several routes to be explored related with the best pathway to achieve the final objective, so here the routes that were tested have been classified in two subsections according to the first step of the processes: (6.2.3.1) *β*-CDSH full monolayer and (6.2.3.2) µcP of *β*-CDSH.

6.2.3.1. *β*-CDSH full monolayer

All the different variations in the procedure of the experiments gathered in this subsection had a common starting point, the creation of an entire (or full) monolayer of *β*-CDSH on a gold surface. To perform this, gold surfaces were firstly immersed in a freshly prepared piranha solution (H_2SO_4/H_2O_2 (30%); $3:1_{v/v}$) for 10-15 s and extensively washed with ultrapure water and dried in a stream of N_2. At this point gold surfaces were ready to be used. Concomitantly, 0.1 mM solutions of *β*-CDSH in different solvents were prepared to incubate into the cleaned gold surfaces under argon overnight.

In the first attempt, the solvent used to prepare *β* -CDSH incubating solution was ethanol. After being incubated overnight, gold surfaces were removed from *β*-CDSH solution and rinsed generously with ethanol, in order to remove physisorbed material, and then dried with a flow of nitrogen. Prior to µcP, poly(dimethyl siloxane) (PDMS) stamps[116] were prepared by curing a mixture polymer:curing agent $10:1_{w/w}$ in the oven at 60ºC for 16 hours on silicon master wafers that contained different sized motifs engraved. The activation of the PDMS stamps was performed by exposition to UV/O_3 (ultraviolet/plasma) treatment for 30 minutes. The inking solution in this experiment (solution containing the target to interact with *β*-CDSH monolayer) was a $9·10^{-3}$ mM solution of PS-*b*-P4VP in a solvent mixture of 1,4-dioxane/ethanol ($1:4_{v/v}$) (non-selective mixture). The µcP proceed by covering activated PDMS stamps with the inking solution and wait for 10 minutes. Then, the excess of liquid on the

stamps were dried with a stream of N_2 and it was put into contact with the β-CDSH SAMs for 10 minutes applying 30 g/cm^2 of pressure and finally the surfaces were rinsed with ethanol and dried with a flow of nitrogen (Fig. 6.17). The process was repeated four times printing different dots of 5, 10, 50 and 100 µm of diameter, with the aim to observe whether the size of the motifs had any implication on the effectiveness of the patterning. Samples were directly analyzed by SEM.
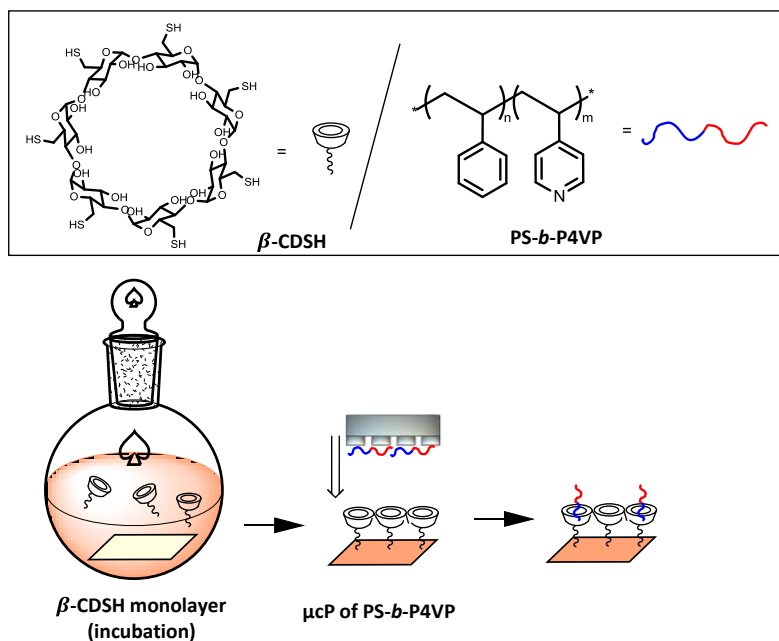
Fig. 6.17 *First procedure followed to immobilize PS-b-P4VP copolymer on gold surface.*

SEM images (Fig. 6.18) revealed different degree of effectiveness of the µcP. In the image of the sample a pattern of 5 µm printed dots could be clearly distinguished (Fig. 6.18a), contrarily to the rest of the samples. The dotted PS-*b*-P4VP pattern with motifs of 10 µm (Fig. 6.18b), was not vividly distinguished. In Fig. 6.18c corresponding to dots of 50 µm, an irregularly distributed pattern was observed and in the case of circular motifs of 100 µm (Fig. 6.18d) a pattern was again seen. It has to be mentioned that SEM could not provide enough resolution to contrast the little differences in height and in composition of the samples;

consequently µcP could perfectly succeed even if patterns were not strongly depicted.
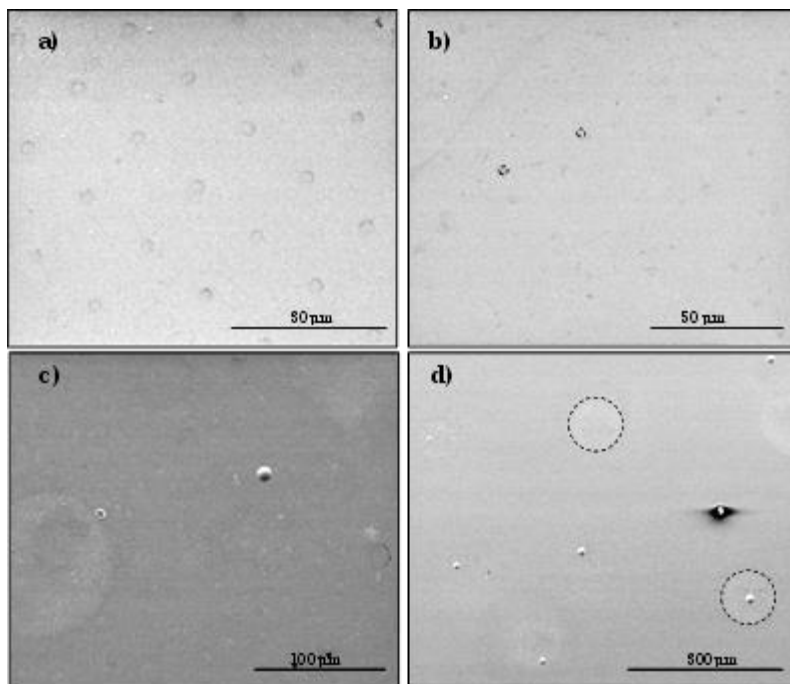
Fig. 6.18 *SEM images of micro-patterned PS-b-P4VP from 1,4-dioxane/ethanol solution on a full monolayer of β-CDSH on gold surfaces. Each image correspond to patterns of different dot sizes, a) dots of 5 µm, b) dots of 10 µm, c) dots of 50 µm and d) dots of 100 µm.*

The key factor of the solvent could highly affect to the obtained results, so the use of a non-selective solvent (as a result of a mixture of selective) could difficult the desired hydrophobic-guest interaction between the copolymer and the CyD. Because of this, in the second attempt, the same procedure performed above was followed but with some variations. Instead of using a mixture of solvents, in the present case inking solutions of $9 \cdot 10^{-3}$ mM of PS-*b*-P4VP, apart from additional control inking solutions PS and P4VP homopolymers at the same concentration were prepared in ethanol. Patterns selected were dots of 5 and 10 µm in diameter. The SEM images of the µcP of the PS-*b*-P4VP, showed in all cases circular patterns, meaning than there was material on surface (Fig. 6.19). Contrarily to preliminary expectation, the more promising sample was the homopolymer of P4VP in where clearly dots

were depicted. Double-ring shape of all motifs, could be an indication that an overpressure was applied, leaving this characteristic print. Another conceivable explanation was that matter was attached outside the dots (inverse pattern), indicating that the polymer might be physisorbed by pressure, even though the sample was rinsed thoroughly after printing. As mentioned before, P4VP can be bonded to CyD by hydrogen bonding through the hydroxyl groups remaining at the rim of the cage.

Fig. 6.19 *SEM images of micro-patterned homo- and copolymer from ethanol solution on a full monolayer of β-CDSH on gold surfaces. a) Dots of 5 μm of PS-b-P4VP, b) dots of 10 μm of PS-b-P4VP, c) dots of 5 μm of PS and, d) dots of 10 μm of P4VP. Some circular motifs of the pattern were highlighted with dashed circles to facilitate its location.*

After being concluded that pressure could also affect the results, a third attempt reproducing the same conditions was performed, avoiding the application of pressure during μcP process. Additionally to μcP samples of PS-*b*-P4VP (PS:P4VP of 1:4), PS and P4VP, an extra sample of PS-*b*-P4VP with molar ratio PS:P4VP of 1:1 was as well prepared as inking solution at the same concentration. The printing process was the same as it has been described in Fig. 6.17. In this exploratory path, PDMS stamps

with circular motifs of 5, 10, 50 and 100 µm in diameter were selected. SEM images revealed that the pressure was an important parameter to take in account as the dotted patterns appeared in all samples (Fig. 6.20). Micro-patterned sample of PS-*b*-P4VP with molar ratio PS:P4VP 1:4, turned out very different compared with previous results obtained, probably because without applying pressure matter was only located filing the motifs, evidencing a successful µcP process (Fig. 6.20a). Varying the volume fraction of the blocks forming the copolymer from 1:4 to 1:1, meaning an increase of the relative amount of PS units and vice versa for P4VP, a light-dark pattern showed up (Fig. 6.20b). Comparing samples of PS-*b*-P4VP 1:4 and 1:1 it might be concluded that a double contribution of PS and P4VP to the β-CDSH was taking place, i.e. that PS block was probably included into CyD cage while at the same time P4VP block was hydrogen-bonded in some way to the oligosaccharide groups. On the other hand, a sample of µcP PS appeared even lighter than the PS-*b*-P4VP 1:1, suggesting a possible inclusion by hydrophobic interactions into β-CDSH (Fig. 6.20c). The patterned surface with P4VP appeared as a combination of filled and unfilled dots, denoting a low homogeneity in the process. So at this point, the viability of immobilization of PS-*b*-P4VP on functionalized surface was demonstrated.
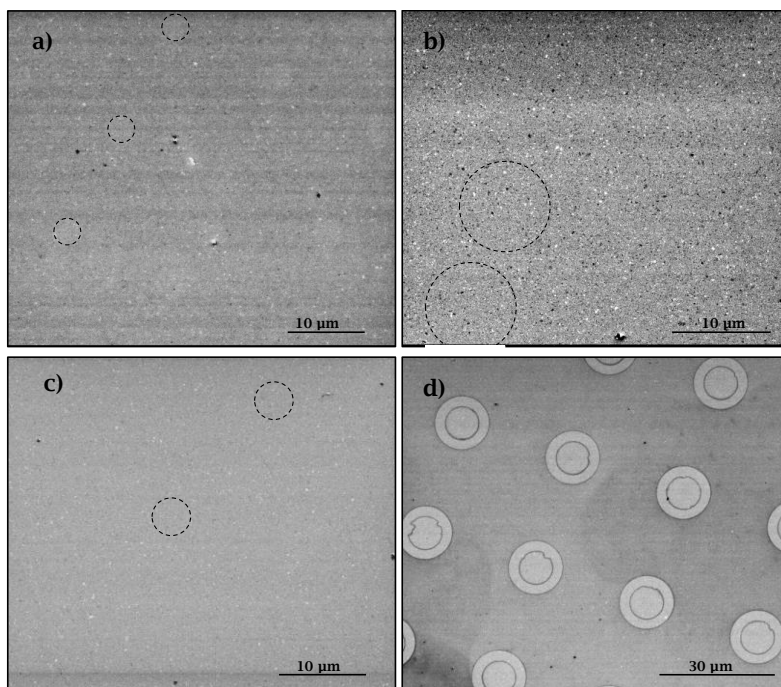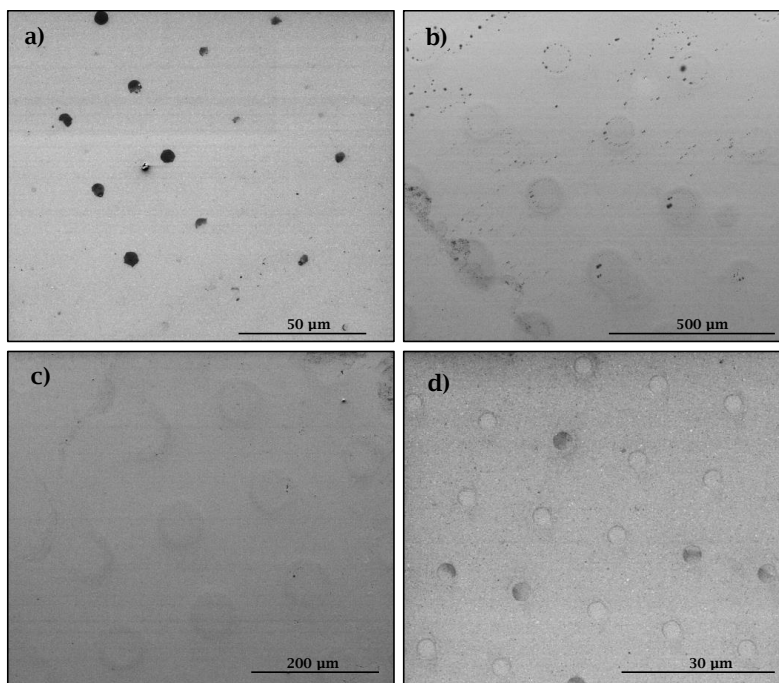
Fig. 6.20 *SEM images of micro-patterned homo- and copolymer from ethanol solution on a full monolayer of β-CDSH on gold surfaces without pressure. a) Dots of 10 μm of PS-b-P4VP 1:4, b) dots of 100 μm of PS-b-P4VP 1:1, c) dots of 50 μm of PS and, d) dots of 5 μm of P4VP.*

One of the objectives of this section was to achieve the coordination between the chiral Zn(R,R,R,R)-1 and the surface-immobilized PS-*b*-P4VP to make an approach to molecular rotors. For this, was directly printed to *β*-CDSH SAMs gold. The procedure followed was the same as described in Fig. 6.17, using the complexed polymer PS-*b*-P4VP-Zn(R,R,R,R)-1 as inking solution. Thus, 0.3 ml of a 0.09 mM solution of PS-*b*-P4VP was mixed with 0.3 ml of a solution 0.2 mM of Zn(R,R,R,R)-1, both in ethanol, and two experiments of μcP were planned, with and another without applying pressure. 50 and 100 μm were the diameters of the circular motifs used. Surfaces were analyzed as well by SEM.
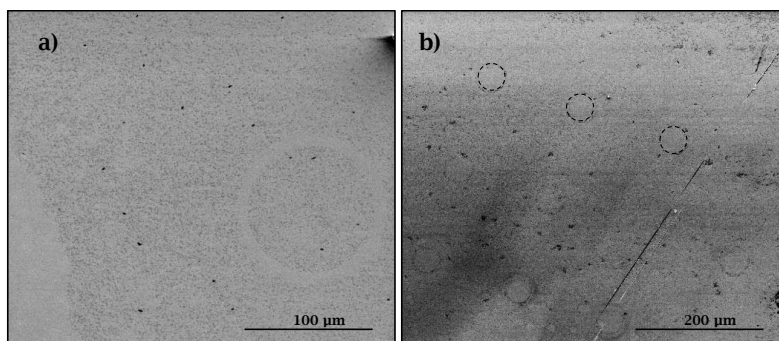
Fig. 6.21 *SEM images of micro-patterned PS-b-P4VP-Zn(R,R,R,R)-1 on β-CDSH-functionalized gold surface without a) and with b) pressure (dotted circles were to localize the pattern).*

SEM images of the μcP of the PS-*b*-P4VP-Zn(*R,R,R,R*)-1 complex with and without pressure, did not denote much differences and the pattern surrounded by aggregated material was appreciable in both cases (Fig. 6.21 a-b). This probably indicated the formation of micellar aggregates physisorbed on the surfaces (as has been presented in prior experiments, Fig. 6.11), excepting the areas in direct contact with the stamp (circles).

6.2.3.2.   μcP of β-CDSH

As using full monolayers of β-CDSH the μcP PS-*b*-P4VP-Zn(*R,R,R,R*)-1 complex did not show clear results, additional approaches were also tested. In this section the μcP methodology developed was firstly the local functionalization of the gold surfaces with a 0.1 mM solution of β-CDSH in ethanol (inking solution) by μcP, followed by an incubation of the β-CDSH patterns in a PS-*b*-P4VP-Zn(*R,R,R,R*)-1 complex solution (Fig. 6.22).
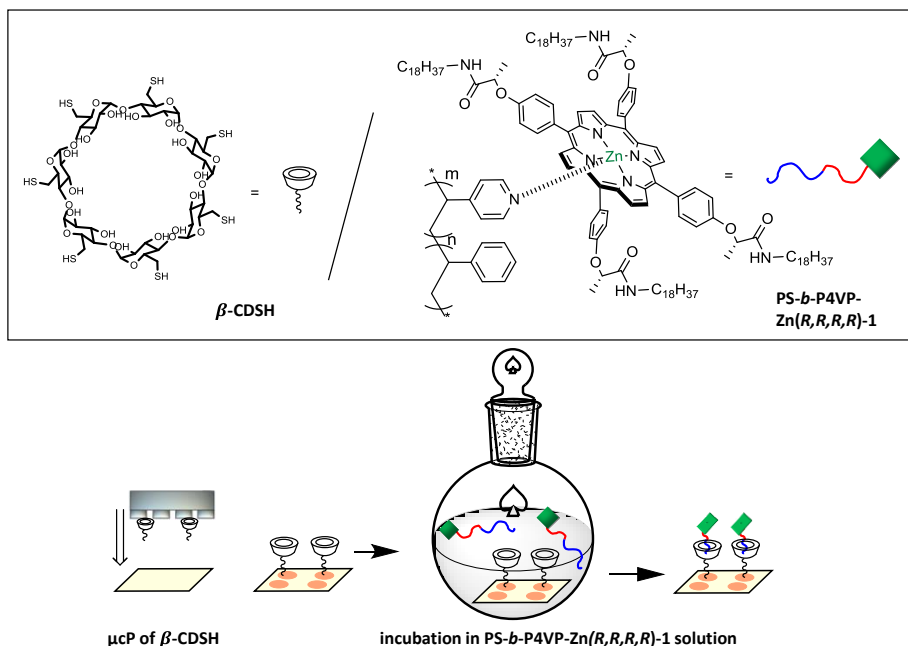
Fig. 6.22 *Methodology developed to immobilized on surface PS-*b*-P4VP-Zn(*R,R,R,R*)-1 complex.*

SEM images of incubated surfaces with and without applying pressure during the µcP process, did not show appreciable differences (Fig. 6.23 a-b). Marks derived from PDMS stamps could be denoted in both samples, even not pressure was applied and, moreover, no sign of micellar aggregates of PS-*b*-P4VP-Zn(*R,R,R,R*)-1 attached on surface were spotted. A possible explanation for this is that the polymer-based metallocompounds cannot be attached on the surface, being removed after rinsing the surfaces with ethanol. Moreover, unspecific physisorption of the polymer can also occur due to the free spacers between the *β*-CDSH patterns.
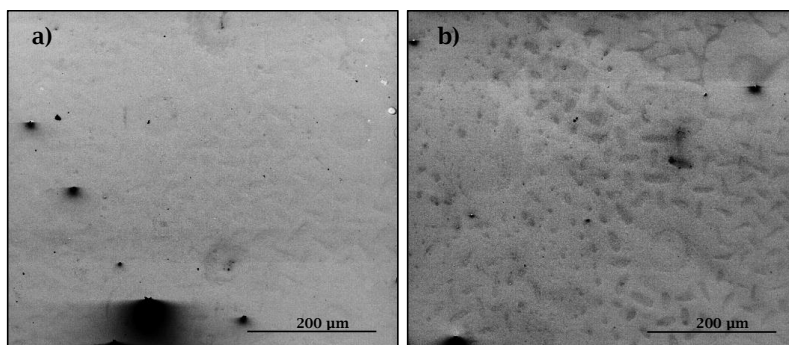
Fig. 6.23 *SEM images of incubated PS-b-P4VP-Zn(R,R,R,R)-1 solution on micro-patterned β -CDSH-functionalized gold surface without a) and with b) pressure.*

To avoid the unspecific adsorption of the PS-*b*-P4VP-Zn(*R,R,R,R*)-1 to the unpatterned β-CDSH areas, these areas were blocked by incubating patterned β-CDSH surfaces in a solution of 0.02 M 1-dodecanethiol in ethanol (Fig. 6.24). The resulted functionalized surfaces were then incubated in steps were the same as the previous experiments PS-*b*-P4VP in molar ratios PS:P4VP of 1:1, 1:4, 4:1 solutions were first immobilized followed by a consecutive incubation in a 0.02 mM Zn(*R,R,R,R*)-1 solution in ethanol. One sample after blocking gold surface was stepped apart for further comparisons. Stamps with dotted motifs of 10 and 50 µm in diameter were chosen.
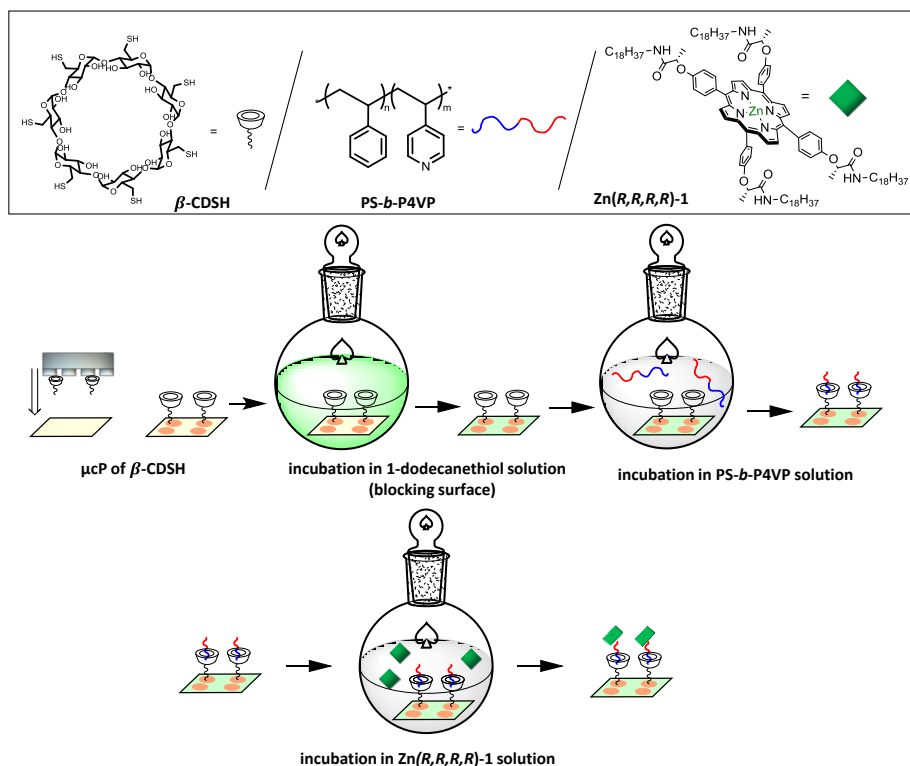
Fig. 6.24 *Procedure of the immobilization PS-b-P4VP-Zn(R,R,R,R)-1 on surface by blocking the β-CDSH patterned surfaces with 1-dodecanethiol, incubation in a PS-b-P4VP solution, followed by and another incubation with Zn(R,R,R,R)-1 solution.*

Firstly, PS-*b*-P4VP immobilized samples were analyzed. SEM image of the µcP *β*-CDSH immediately after the surface blocking with 1-dodecanethiol revealed light-contrasted dotted pattern (Fig. 6.25a). Furthermore, comparing the results obtained with the immobilized PS-*b*-P4VP surfaces with different block copolymer molar ratios (Fig. 6.25 b-d), differences in the intensity of patterns and in the location of the polymer could be clearly seen. Well-defined and dark dots were imaged in samples where the molar ratio PS:P4VP 1:1 (Fig. 6.25b), probably due to a preferential attachment or interaction of the PS-*b*-P4VP to the *β*-CDSH, contrarily to what it was displayed for the 1:4 molar ratio sample (Fig. 6.25c). For the PS-*b*-P4VP with molar ratio of 1:4 (Fig. 6.25c), the inverse pattern was spotted, material on the surface excepting where *β*-CDSH was printed, suggesting a preferential interaction of the material for the areas where the 1-dodecanethiol was attached. This suggested that the

hydrophobicity character of the 1-dodecanethiol influenced to the attachment of the PS domains. PS-*b*-P4VP surface with a molar ratio PS:P4VP 4:1 illustrated, as well as in 1:1 ratio sample, high-contrasted dotted pattern (high concentration of material on them), being the dots darker than the unpatterned regions of the surface (Fig. 6.25d). In concordance to what it has been mentioned, samples with high PS content that showed dark matter could be considered included into the β-CD.

Fig. 6.25 SEM images of immobilization PS-b-P4VP on β -CDSH functionalized gold surface blocked with 1-dodecanethiol followed by incubation with PS-b-P4VP solution. a) Control sample of micro-patterned β -CDSH on gold surface after its blocking with 1-dodecanethiol (dots of 10 μm) (drawn dashed circles were to localize the dotted pattern). PS-b-P4VP samples with PS:P4VP molar ratios of b) 1:1 (dots of 10 μm), c) 1:4 (dots of 50 μm) and, d) 4:1 (dots of 50 μm).

After being analyzed, PS-*b*-P4VP immobilized samples and the control sample of β-CDSH surfaces were incubated in the Zn(*R,R,R,R*)-1 solution overnight. Then, surfaces were removed and rinsed with ethanol thoughtfully and dried in a N_2 stream. The SEM image of the control surface did not show remarkable changes respect to sample before porphyrin incubation (Fig. 6.26a), probably meaning that Zn(*R,R,R,R*)-1 compound cannot be bonded or included to the β-CD by itself. The sample PS-*b*-P4VP-Zn(*R,R,R,R*)-1 containing a molar ratio PS:P4VP 1:1 did also not present significant changes respect to the analyzed in the previous step

(Fig. 6.26b). It was possible that the equimolar ratio of the polymeric blocks hindered the encountering between pyridyl units and zinc (II) from the core of the porphyrin when they were under incubation, without forgetting the probability that polymer chains would not be straight for the coordination with the porphyrin. On the other hand, a large quantity of agglomerated material on the sample representing the fraction 1:4 mostly appeared outside the dots. (Fig. 6.26c). As PS and 1-dodecanethiol had a preferential interaction, with this image it could be concluded that peripheral alkyl chains of the substituted porphyrins might also interact to those regions. The dotted pattern of PS-*b*-P4VP-Zn(*R,R,R,R*)-1 with a molar ratio of 4:1 PS:P4VP experienced slight changes (Fig. 6.26d). In this case the uniform colored dark dots observed in the previous step, faded forming a more complex draw/matter distribution, with a thin external ring delimiting the dot perimeter and an internal filled circle with dark matter on the center. It has to be mentioned that the technique could be considered equally successful, even though no notable changes were appreciated since SEM was not powerful enough to detect slight changes in the composition of a thin layer. Assuming that this last sample was the more promising, at least from the SEM images collected, an elemental analysis with Energy-Dispersive X-ray spectroscopy (EDAX) of the patterned dots of PS-*b*-P4VP-Zn(*R,R,R,R*)-1 with molar fraction PS:P4VP 4:1 was performed.
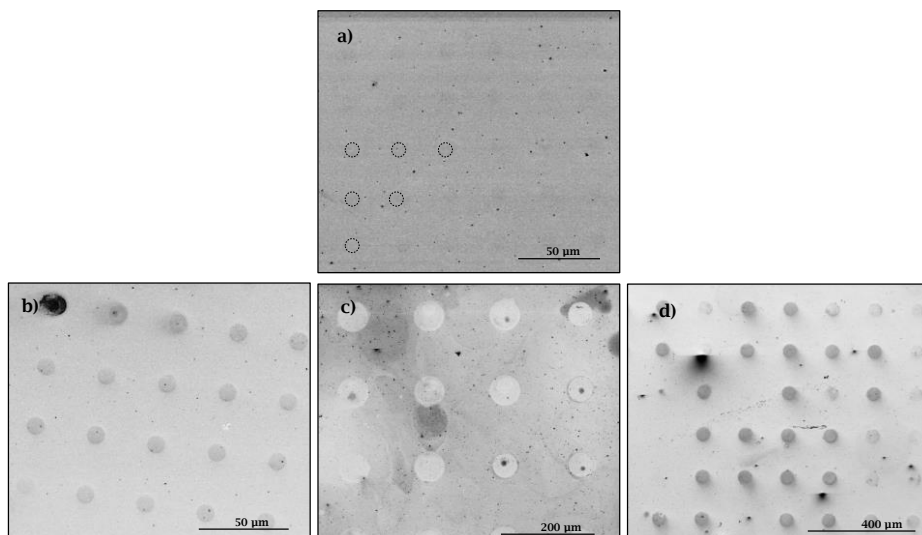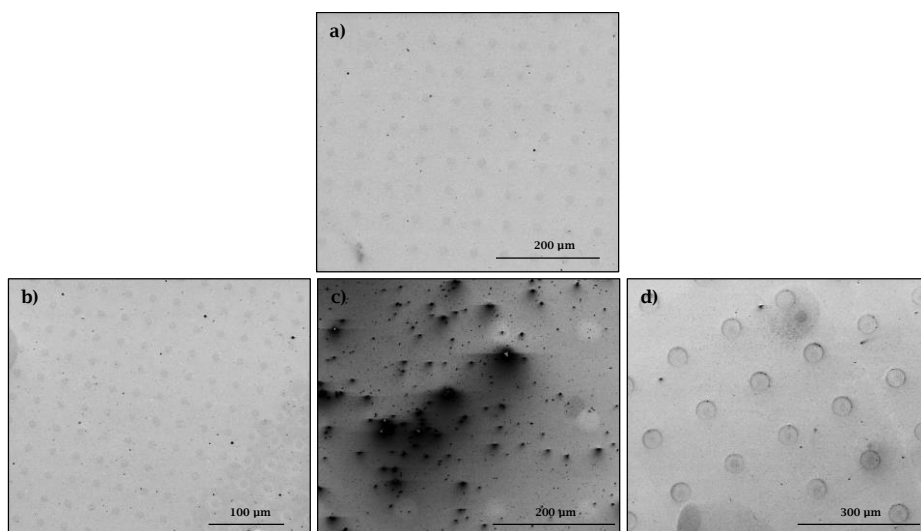
Fig. 6.26 *SEM images of immobilization PS-b-P4VP-Zn(R,R,R,R)-1 on β -CDSH functionalized gold surface blocked with 1-dodecanethiol followed by incubation with PS-b-P4VP solution. a) Control sample of micro-patterned β-CDSH on gold surface after its blocking with 1-dodecanethiol and incubated with Zn(R,R,R,R)-1 (dots of 10 µm). PS-b-P4VP-Zn(R,R,R,R)-1 samples with PS:P4VP molar ratios of b) 1:1 (dots of 10 µm), c) 1:4 (dots of 50 µm) and, d) 4:1 (dots of 50 µm).*

An EDAX analysis of the area encompassing a single dot was performed (Fig. 6.27 a-b). The resulting spectrum revealed a notable presence of zinc as well as nitrogen in the dot. Zinc represented the most distinguishable and characteristic element from porphyrin (because of its exclusivity) and nitrogen would represent in some way the presence of the polymer (P4VP), although Zn(R,R,R,R)-1 contained them (amide groups in peripheral chains and porphyrin core). Towards a better understanding concerning the possible binding, a map of the composition in nitrogen and zinc was performed in the same area (Fig. 6.27 d-e). In the mapping image of nitrogen (Fig. 6.27 d), a major presence of that atom on the center of the image could be appreciated, indicating that either PS-*b*-P4VP, Zn(R,R,R,R)-1 or PS-*b*-P4VP, Zn(R,R,R,R)-1 might be on surface. Moreover, in the image in where the zinc was analyzed (Fig. 6.27 e) an unclear distribution was detected, being a bit strong the signal in the same region in where the nitrogen was detected. With this, it could be confirmed the presence of the Zn(R,R,R,R)-1 on the surfaces, though gathering all previous observations it was assumed the validity of the technique as a

first approach to obtain molecular rotors based on PS-*b*-P4VP-Zn(*R,R,R,R*)-1 immobilized on surface.
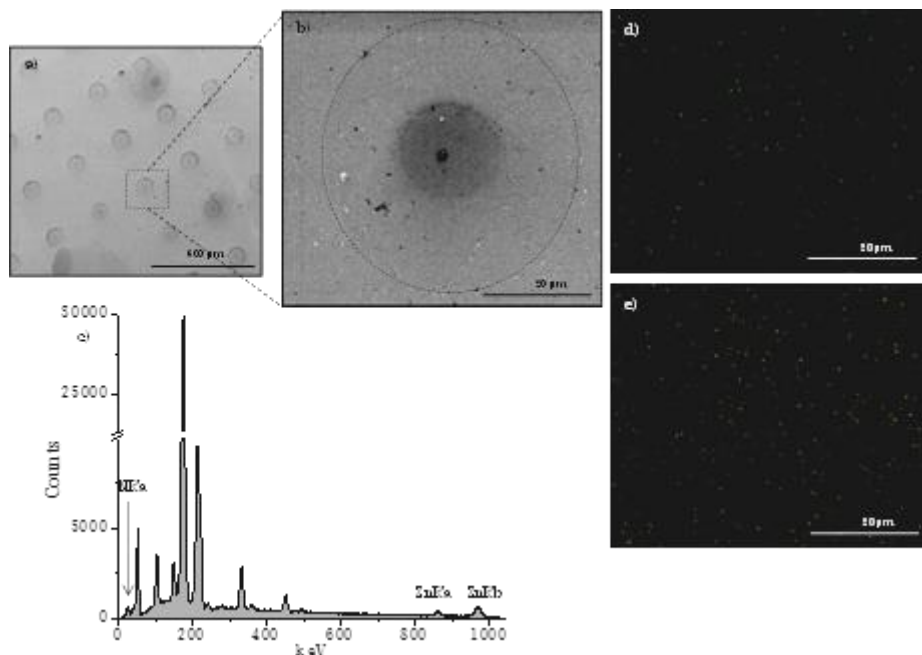
Fig. 6.27 *SEM image of a) PS-b-P4VP-Zn(R,R,R,R)-1 in molar ratio 4:1 PS:P4VP immobilized on surface and b) magnified dot of the area enclosed in a dashed square in a) in where EDAX was performed (dot perimeter was highlighted with a dashed circle). Results from EDAX measurements, c) spectrum of the detected elements in the analyzed area, d) mapping of elemental analysis corresponding to the detected nitrogen and e) mapping of elemental analysis corresponding to the detected zinc.*

6.3.   CONCLUSIONS AND OUTLOOK

In this chapter the supramolecular coordination between an achiral zinc (II) porphyrin derivative, Zn-2, and its chiral homologue, Zn(*R,R,R,R*)-1, and the amphiphilic block copolymer PS-*b*-P4VP was achieved through the zinc (II) of the porphyrin and the nitrogen of the pyridyl groups of the P4VP block. The binding of both metallocompounds to the polymer was separately achieved in solution in a non-coordinating

solvent (chloroform) and the stability of this bonding could also be demonstrated in the solid state, resulting the complexed systems PS-*b*-P4VP-Zn-2 and PS-*b*-P4VP-Zn(*R,R,R,R*)-1. Nonetheless the chiral effect of the solid PS-*b*-P4VP-Zn(*R,R,R,R*)-1 obtained after drying the chloroform-based solution was not clearly observed by circular dichroism (CD) spectroscopy. The noisy CD signal was attributed to the impossibility to control the homogeneity in the distribution of the material on surface while it was drying. Moreover, the complexed material resulted very concentrated in tiny areas, impeding the same homogeneous packing than the system could adopt in solution. Atomic Force Microscopy (AFM) measurements supported that idea, where no remarkable differences between achiral and chiral complexed metallocompounds self-assembled structures were observed. Even though well-differentiated segregated phases between PS-*b*-P4VP-Zn-2 and PS-*b*-P4VP-Zn(*R,R,R,R*)-1 were spotted by Transmission Electron Microscopy (TEM), elucidating the effect of the chirality in the self-arrangement of the polymer as well the porphyrins.

In a further step, the role of the solvent interplayed in the packing of the complexed system was presented, demonstrating the possibility of obtaining complex micelles, opening a broad range of possibilities of PS-*b*-P4VP-Zn-2 and PS-*b*-P4VP-Zn(*R,R,R,R*)-1 configurations with the easy control of the solvent.

Finally, PS-*b*-P4VP-Zn(*R,R,R,R*)-1 could be immobilized on a surface *via* soft lithography, concretely micro-contact printing (μcP). Cyclodextrin-functionalized gold surfaces were used as 'harbouring'-template to anchor the polymeric metallocompound. After several attempts and improvements of the procedure, the viability of the technique was demonstrated and, in this way, achieving molecular imprinted putative supramolecular rotors.

6.4.   EXPERIMENTAL PART

Materials: iodine (≥99.99% trace metal basis), β-CD (≥97%), triphenylphosphine (≥99.99%), thiourea (ACS reagent, ≥99.%), potassium bisulfate (≥99%, KHSO$_4$) and 1-dodecanethiol (≥98.%) were purchased to Sigma-Aldrich. Dimethylformamide (DMF, HPLC grade) was purchased to Severn Biotech Ltd. Poly(dimethyl siloxane) (PDMS) Sylgar® 184 elastomer kit was supplied by Dow Corning.

Synthesis of PS-*b*-P4VP: synthesis of PS-*b*-P4VP in all the PS:P4VP molar fractions studied in this chapter are described and characterized in detail in chapter 3.

Synthesis of Zn-2 and Zn(*R,R,R,R*)-1: 5,10,15,20-[4-N-octadecylacetamido phenoxy] zinc porphyrin (Zn-2) and 5,10,15,20-[4-(*R,R,R,R*)-2-N-octadecylamideethyloxyphenyl] zinc porphyrin (Zn(*R,R,R,R*)-1) were synthetized and characterized in a previous study leaded by a member of our research group following the literature.[43, 49, 117-119]

UV-Vis absorption spectroscopy: to perform experiments in liquid, standardized quarts cuvettes of 1 mm of optical path were used. In solid experiments standardized quartz slides were used. Quartz surfaces were cleaned with piranha solution (H$_2$SO$_4$/H$_2$O$_2$ (30%); 3:1$_{v/v}$) for 30 min prior their use.

TEM measurements: images were acquired at 120 kV. TEM supports used were holey carbon coated copper grids (200 lines/inch). Only samples containing pure PS-*b*-P4VP were selectively stained with iodine vapors and the process was by placing the samples in a sealed container in a iodine vapors atmosphere for 1 hour.

Solid samples: a dome to reach vacuum conditions was used to obtain solid samples for TEM analyses of the phase segregation and micellar aggregation.

β-CDSH synthesis: the synthesis of the per-6-thio-β-cyclodextrin (β-CDSH) was following two-step procedure described by Gadelle and

Rojas.[121, 122] 552.2 mg of β-CD were dried at 80ºC under vacuum for several hours. Meanwhile, 2.6 g of iodine were dissolved in10 ml of DMF and 2.7 g of triphenylphosphine were added. The mixture was stirred and sealed under argon atmosphere for several hours. Then, the mixture was transferred in a round-bottom flask containing β-CD. When all compound were dissolved, the solution was kept stirring at 80ºC for 15 hours under argon, resulting in per-6-iodo-β-cyclodextrin. 0.6 g of thiourea was added to the dried per-6-iodo-β-cyclodextrin and the mixture was dissolved with 15 ml of DMF under inert conditions. The reaction kept at 70ºC for 19 hours, to obtain an oily solution after removing the solvent. 50 ml of ultrapure water were added sequentially to 0.2 g of sodium hydroxide and the mixture was stirred and refluxing for 1 hour. Then, an aqueous solution of potassium bisulfate was added until reached pH of 3-4. Later on the mixture was cooled down by using an ice bath and was filtered, washed with ultrapure water and the solid was recovered and dried. Finally and to remove the last traces of DMF, the product was suspended in ultrapure water (20 ml) and the mixture was stirred for 20 min. The necessary amount of potassium hydroxide was added to neutralize the compound (pH = 10) and a milky suspension was obtained. The mixture was again cooled down with an ice bath and it was acidified by adding potassium bisulfate until pH was 1-2. The fine powder precipitated was filtered and dried.

µcP specifications: gold surfaces used were from Sense bv type SPR gold 1.25x12.5x1 mm. All incubations were performed under an argon atmosphere into sealed container provided with special fabricated glass holders that kept samples vertically tilted. Silicon master wafers were fabricated by standard photolithography of SU-8 epoxy resin on top of a silicon substrate.

SEM and EDAX specifications: 5 kV, a working distance of 10 mm, a spot of 3.5 and high vacuum were the conditions used to acquire SEM images. EDAX was assembled to SEM microscope, and to collect information 15 kV and analyzing times of ~ 2500 s were the fixed conditions.

6.5.   REFERENCES

1.   A. Harada, *Supramolecular Polymer Chemistry*, Wiley-VCH Verlag GmbH & Co. KGaA, 2011.
2.   R. J. Thibault and V. M. Rotello, in *Molecular Recognition and Polymers*, John Wiley & Sons, Inc., 2008, DOI: 10.1002/9780470384053.
3.   S. Förster and M. Antonietti, *Advanced materials*, 1998, **10**, 195-217.
4.   C. S. Kim, C. Randow and T. Sano, *Hybrid and Hierarchical Composite Materials*, Springer International Publishing, 2015.
5.   A. C. Miller, R. D. Bennett, P. T. Hammond, D. J. Irvine and R. E. Cohen, *Macromolecules*, 2008, **41**, 1739-1744.
6.   A. C. Miller, A. Bershteyn, W. Tan, P. T. Hammond, R. E. Cohen and D. J. Irvine, *Biomacromolecules*, 2009, **10**, 732-741.
7.   K. Letchford and H. Burt, *European Journal of Pharmaceutics and Biopharmaceutics*, 2007, **65**, 259-269.
8.   G. S. Kottas, L. I. Clarke, D. Horinek and J. Michl, *Chemical reviews*, 2005, **105**, 1281-1376.
9.   T. Hugel, N. B. Holland, A. Cattani, L. Moroder, M. Seitz and H. E. Gaub, *Science*, 2002, **296**, 1103-1106.
10.   N. B. Holland, T. Hugel, G. Neuert, A. Cattani-Scholz, C. Renner, D. Oesterhelt, L. Moroder, M. Seitz and H. E. Gaub, *Macromolecules*, 2003, **36**, 2015-2023.
11.   A. Cnossen, L. Hou, M. M. Pollard, P. V. Wesenhagen, W. R. Browne and B. L. Feringa, *Journal of the American Chemical Society*, 2012, **134**, 17613-17619.
12.   J. A. A. W. Elemans, R. van Hameren, R. J. M. Nolte and A. E. Rowan, *Advanced materials*, 2006, **18**, 1251-1266.
13.   N. Zhang, B. Zhang, J. Yan, X. Xue, X. Peng, Y. Li, Y. Yang, C. Ju, C. Fan and Y. Feng, *Renewable Energy*, 2015, **77**, 579-585.
14.   X. Huang, C. Zhu, S. Zhang, W. Li, Y. Guo, X. Zhan, Y. Liu and Z. Bo, *Macromolecules*, 2008, **41**, 6895-6902.
15.   A. C. Aragonès, N. Darwish, W. J. Saletra, L. Pérez-García, F. Sanz, J. Puigmartí-Luis, D. B. Amabilino and I. Díez-Pérez, *Nano letters*, 2014, **14**, 4751-4756.
16.   B. Louahem M'Sabah, M. Boucharef, J. Warnan, Y. Pellegrin, E. Blart, B. Lucas, F. Odobel and J. Boucle, *Physical Chemistry Chemical Physics*, 2015, **17**, 9910-9918.
17.   Y. Liang, X. Xue, W. Zhang, C. Fan, Y. Li, B. Zhang and Y. Feng, *Dyes and Pigments*, 2015, **115**, 7-16.
18.   I. Goldberg, *Chemical communications*, 2005, DOI: 10.1039/B416425C, 1243-1254.
19.   S. George, S. Lipstman, S. Muniappan and I. Goldberg, *Crystal Engineering Communications*, 2006, **8**, 417-424.
20.   T. Umeyama and H. Imahori, *Journal of Materials Chemistry A*, 2014, **2**, 11545-11560.
21.   L. Pengxia, Z. Du, D. Wang, Z. Yang, H. Sheng, S. Liang, H. Cao, W. He and H. Yang, *ChemPhysChem*, 2014, **15**, 3523-3529.
22.   P. J. Chmielewski and L. Latos-Grażyński, *Coordination Chemistry Reviews*, 2005, **249**, 2510-2533.
23.   J. Wojaczyński and L. Latos-Grażyński, *Coordination Chemistry Reviews*, 2000, **204**, 113-171.
24.   L. Baldini and C. A. Hunter, in *Advances in Inorganic Chemistry*, ed. A. G. Sykes, San Diego, 2002.

25. R. F. Pasternack, J. I. Goldsmith, S. Szép and E. J. Gibbs, *Biophysical Journal*, 1998, **75**, 1024-1031.
26. O. Ohno, Y. Kaizu and H. Kobayashi, *The Journal of Chemical Physics*, 1993, **99**, 4128-4139.
27. R. F. Pasternack, A. Giannetto, P. Pagano and E. J. Gibbs, *Journal of the American Chemical Society*, 1991, **113**, 7799-7800.
28. S. Ikeda, T. Nezu and G. Ebert, *Biopolymers*, 1991, **31**, 1257-1263.
29. Z. Wang, C. J. Medforth and J. A. Shelnutt, *Journal of the American Chemical Society*, 2004, **126**, 15954-15955.
30. Z. Guo, D. Yan, H. Wang, D. Tesfagaber, X. Li, Y. Chen, W. Huang and B. Chen, *Inorganic chemistry*, 2015, **54**, 200-204.
31. W.-Y. Gao, M. Chrzanowski and S. Ma, *Chemical Society reviews*, 2014, **43**, 5841-5866.
32. K. Wang, D. Feng, T.-F. Liu, J. Su, S. Yuan, Y.-P. Chen, M. Bosch, X. Zou and H.-C. Zhou, *Journal of the American Chemical Society*, 2014, **136**, 13983-13986.
33. L. Xu, J. Wang, Y. Xu, Z. Zhang, P. Lu, M. Fang, S. Li, P. Sun and H.-K. Liu, *Crystal Engineering Communications*, 2014, **16**, 8656-8659.
34. S. Ogi, T. Ikeda, R. Wakabayashi, S. Shinkai and M. Takeuchi, *Chemistry – A European Journal*, 2010, **16**, 8285-8290.
35. T. Ikeda, T. Tsukahara, R. Iino, M. Takeuchi and H. Noji, *Angewandte Chemie International Edition*, 2014, **53**, 10082-10085.
36. J. Puigmarti-Luis, W. J. Saletra, A. Gonzalez, D. B. Amabilino and L. Perez-Garcia, *Chemical communications*, 2014, **50**, 82-84.
37. L. Mei, T. Ming, L. Rong, S. Jie, Y. Zhong and L. Liang, *J Chem Sci*, 2009, **121**, 435-440.
38. R. Patiño, M. Campos and L. A. Torres, *Inorganic chemistry*, 2007, **46**, 9332-9336.
39. V. F. Slagt, P. C. J. Kamer, P. W. N. M. van Leeuwen and J. N. H. Reek, *Journal of the American Chemical Society*, 2004, **126**, 1526-1536.
40. C. M. Drain, A. Varotto and I. Radivojevic, *Chemical reviews*, 2009, **109**, 1630-1658.
41. I. Beletskaya, V. S. Tyurin, A. Y. Tsivadze, R. Guilard and C. Stern, *Chemical reviews*, 2009, **109**, 1659-1713.
42. P. Iavicoli, M. Simon-Sorbed and D. B. Amabilino, *New Journal of Chemistry*, 2009, **33**, 358-365.
43. P. Iavicoli, H. Xu, L. N. Feldborg, M. Linares, M. Paradinas, S. Stafström, C. Ocal, B. Nieto-Ortega, J. Casado, J. T. López Navarrete, R. Lazzaroni, S. D. Feyter and D. B. Amabilino, *Journal of the American Chemical Society*, 2010, **132**, 9350-9362.
44. D. M. Guldi, G. M. A. Rahman, S. Qin, M. Tchoul, W. T. Ford, M. Marcaccio, D. Paolucci, F. Paolucci, S. Campidelli and M. Prato, *Chemistry – A European Journal*, 2006, **12**, 2152-2161.
45. A. Arulkashmir, R. Y. Mahale, S. S. Dharmapurikar, M. K. Jangid and K. Krishnamoorthy, *Polymer Chemistry*, 2012, **3**, 1641-1646.
46. G. Bottari, G. de la Torre, D. M. Guldi and T. Torres, *Chemical reviews*, 2010, **110**, 6768-6816.
47. J. Liu, M. Chen, D.-J. Qian and M. Liu, *RSC Advances*, 2014, **4**, 5678-5682.
48. A. Tsuda, Y. Nagamine, R. Watanabe, Y. Nagatani, N. Ishii and T. Aida, *Nature chemistry*, 2010, **2**, 977-983.
49. L. N. Feldborg, W. J. Saletra, P. Iavicoli and D. B. Amabilino, *Journal of Porphyrins and Phthalocyanines*, 2011, **15**, 995-1003.
50. B. Gao, R. Wang and R. Du, *Journal of Porphyrins and Phthalocyanines*, 2010, **14**, 235-243.
51. C. Y. Huang and Y. O. Su, *Dalton transactions*, 2010, **39**, 8306-8312.

52. C. Ikeda, E. Fujiwara, A. Satake and Y. Kobuke, *Chemical communications*, 2003, DOI: 10.1039/b211434h, 616-617.

53. K. M. Kadish, K. M. Smith and R. Guilard, *The Porphyrin Handbook: Inorganic, organometallic and coordination chemistry*, Academic Press, 2000.

54. M. M. Green, M. P. Reidy, R. D. Johnson, G. Darling, D. J. O'Leary and G. Willson, *Journal of the American Chemical Society*, 1989, **111**, 6452-6454.

55. T. W. Anderson, J. K. M. Sanders and G. D. Pantos, *Organic & Biomolecular Chemistry*, 2010, **8**, 4274-4280.

56. L. J. Prins, P. Timmerman and D. N. Reinhoudt, *Journal of the American Chemical Society*, 2001, **123**, 10153-10163.

57. G. Gottarelli, S. Lena, S. Masiero, S. Pieraccini and G. P. Spada, *Chirality*, 2008, **20**, 471-485.

58. S. Ogi, K. Sugiyasu, S. Manna, S. Samitsu and M. Takeuchi, *Nature chemistry*, 2014, **6**, 188-195.

59. T. Ikeda, M. Asakawa, K. Miyake and T. Shimizu, *Chemistry Letters*, 2004, **33**, 1418-1419.

60. T. Ikeda, M. Asakawa, M. Goto, K. Miyake, T. Ishida and T. Shimizu, *Langmuir : the ACS journal of surfaces and colloids*, 2004, **20**, 5454-5459.

61. V. Snitka, M. Rackaitis and R. Rodaite, *Sensors and Actuators B: Chemical*, 2005, **109**, 159-166.

62. F. S. Bates and G. H. Fredrickson, *Physics Today*, 1999, **52**, 32.

63. W. van Zoelen and G. ten Brinke, *Soft Matter*, 2009, **5**, 1568-1582.

64. L. Yao, X. Lu, S. Chen and J. J. Watkins, *Macromolecules*, 2014, **47**, 6547-6553.

65. G. M. Grason, *ACS Macro Letters*, 2015, **4**, 526-532.

66. C. V. Kulkarni, *Nanoscale*, 2012, **4**, 5779-5791.

67. H.-Y. Hsueh, C.-T. Yao and R.-M. Ho, *Chemical Society reviews*, 2015, **44**, 1974-2018.

68. B. K. Kuila, P. Formanek and M. Stamm, *Nanoscale*, 2013, **5**, 10849-10852.

69. A. Rahikkala, A. J. Soininen, J. Ruokolainen, R. Mezzenga, J. Raula and E. I. Kauppinen, *Soft Matter*, 2013, **9**, 1492-1499.

70. E. B. Gowd, M. Böhme and M. Stamm, *IOP Conference Series: Materials Science and Engineering*, 2010, **14**, 012015.

71. E. B. Gowd, T. Koga, M. K. Endoh, K. Kumar and M. Stamm, *Soft Matter*, 2014, **10**, 7753-7761.

72. B. K. Kuila, C. Chakraborty and S. Malik, *Macromolecules*, 2013, **46**, 484-492.

73. S. Rangou, K. Buhr, V. Filiz, J. I. Clodt, B. Lademann, J. Hahn, A. Jung and V. Abetz, *Journal of Membrane Science*, 2014, **451**, 266-275.

74. J. I. Clodt, V. Filiz, S. Rangou, K. Buhr, C. Abetz, D. Höche, J. Hahn, A. Jung and V. Abetz, *Advanced Functional Materials*, 2013, **23**, 731-738.

75. M. Štěpánek, P. Matějíček, J. Humpolíčková, J. Havránková, K. Podhájecká, M. Špírková, Z. Tuzar, C. Tsitsilianis and K. Procházka, *Polymer*, 2005, **46**, 10493-10505.

76. H. Fan and Z. Jin, *Soft Matter*, 2014, **10**, 2848-2855.

77. L. A. Connal, N. A. Lynd, M. J. Robb, K. A. See, S. G. Jang, J. M. Spruell and C. J. Hawker, *Chemistry of Materials*, 2012, **24**, 4036-4042.

78. J. Li, Y. An, X. Chen, D. a. Xiong, Y. Li, N. Huang and L. Shi, *Macromolecular rapid communications*, 2008, **29**, 214-218.

79. W.-H. Huang, P.-Y. Chen and S.-H. Tung, *Macromolecules*, 2012, **45**, 1562-1569.

80. D. Klinger, C. X. Wang, L. A. Connal, D. J. Audus, S. G. Jang, S. Kraemer, K. L. Killops, G. H. Fredrickson, E. J. Kramer and C. J. Hawker, *Angewandte Chemie International Edition*, 2014, **53**, 7018-7022.

81. M. J. Robb, L. A. Connal, B. F. Lee, N. A. Lynd and C. J. Hawker, *Polymer Chemistry*, 2012, **3**, 1618-1628.

82. D. V. Krogstad, N. A. Lynd, S.-H. Choi, J. M. Spruell, C. J. Hawker, E. J. Kramer and M. V. Tirrell, *Macromolecules*, 2013, **46**, 1512-1518.

83. D. Klinger, M. J. Robb, J. M. Spruell, N. A. Lynd, C. J. Hawker and L. A. Connal, *Polymer Chemistry*, 2013, **4**, 5038-5042.

84. B. Bharatiya, J.-M. Schumers, E. Poggi and J.-F. Gohy, *Polymers*, 2013, **5**, 679.

85. S. P. Nunes, M. Karunakaran, N. Pradeep, A. R. Behzad, B. Hooghan, R. Sougrat, H. He and K.-V. Peinemann, *Langmuir : the ACS journal of surfaces and colloids*, 2011, **27**, 10184-10190.

86. E. A. Mikhalitsyna, V. S. Tyurin, S. E. Nefedov, S. A. Syrbu, A. S. Semeikin, O. I. Koifman and I. P. Beletskaya, *European Journal of Inorganic Chemistry*, 2012, **2012**, 5979-5990.

87. K. P. Ghiggino, J. A. Hutchison, S. J. Langford, M. J. Latter, M. A. P. Lee, P. R. Lowenstern, C. Scholes, M. Takezaki and B. E. Wilman, *Advanced Functional Materials*, 2007, **17**, 805-813.

88. A. Guenet, E. Graf, N. Kyritsakas and M. W. Hosseini, *Chemistry – A European Journal*, 2011, **17**, 6443-6452.

89. C. Joachim and G. Rapenne, *Single Molecular Machines and Motors: Proceedings of the 1st International Symposium on Single Molecular Machines and Motors, Toulouse 19-20 June 2013*, Springer International Publishing, 2015.

90. J. P. Sauvage and P. Gaspard, *From Non-Covalent Assemblies to Molecular Machines*, Wiley, 2011.

91. T. Auletta, B. Dordi, A. Mulder, A. Sartori, S. Onclin, C. M. Bruinink, M. Peter, C. A. Nijhuis, H. Beijleveld, H. Schonherr, G. J. Vancso, A. Casnati, R. Ungaro, B. J. Ravoo, J. Huskens and D. N. Reinhoudt, *Angewandte Chemie International Edition English*, 2004, **43**, 369-373.

92. M. W. J. Beulen, J. Bügler, M. R. de Jong, B. Lammerink, J. Huskens, H. Schönherr, G. J. Vancso, B. A. Boukamp, H. Wieder, A. Offenhäuser, W. Knoll, F. C. J. M. van Veggel and D. N. Reinhoudt, *Chemistry – A European Journal*, 2000, **6**, 1176-1183.

93. B. V. K. J. Schmidt, M. Hetzer, H. Ritter and C. Barner-Kowollik, *Progress in Polymer Science*, 2014, **39**, 235-249.

94. J. Zhou and H. Ritter, *Polymer Chemistry*, 2010, **1**, 1552-1559.

95. J. Zhang and P. X. Ma, *Advanced drug delivery reviews*, 2013, **65**, 1215-1233.

96. A. Harada, Y. Takashima and H. Yamaguchi, *Chemical Society reviews*, 2009, **38**, 875-882.

97. A. E. Tonelli, *Polymer*, 2008, **49**, 1725-1736.

98. Y. Chen and Y. Liu, *Chemical Society reviews*, 2010, **39**, 495-505.

99. M. Hetzer, B. V. K. J. Schmidt, C. Barner-Kowollik and H. Ritter, *Journal of Polymer Science Part A: Polymer Chemistry*, 2013, **51**, 2504-2517.

100. B. V. K. J. Schmidt, M. Hetzer, H. Ritter and C. Barner-Kowollik, *Macromolecules*, 2011, **44**, 7220-7232.

101. A. Bertrand, M. Stenzel, E. Fleury and J. Bernard, *Polymer Chemistry*, 2012, **3**, 377-383.

102. X. Li, J. Li and K. W. Leong, *Polymer*, 2004, **45**, 6845-6851.

103. C.-C. Tsai, S. Leng, K.-U. Jeong, R. M. Van Horn, C.-L. Wang, W.-B. Zhang, M. J. Graham, J. Huang, R.-M. Ho, Y. Chen, B. Lotz and S. Z. D. Cheng, *Macromolecules*, 2010, **43**, 9454-9461.

104. Z. Huang, X. Liu, S. Chen, Q. Lu and G. Sun, *Polymer Chemistry*, 2015, **6**, 143-149.

105. S. Wang, Q. Shen, M. H. Nawaz and W. Zhang, *Polymer Chemistry*, 2013, **4**, 2151.

106. E. Doganci, M. Gorur, C. Uyanik and F. Yilmaz, *Journal of Polymer Science Part A: Polymer Chemistry*, 2014, **52**, 3406-3420.
107. G. Chen and M. Jiang, *Chemical Society reviews*, 2011, **40**, 2254-2266.
108. J. Storsberg and H. Ritter, *Macromolecular rapid communications*, 2000, **21**, 236-241.
109. J. Wang, X. Wang, F. Yang, H. Shen, Y. You and D. Wu, *Langmuir : the ACS journal of surfaces and colloids*, 2014, **30**, 13014-13020.
110. A. Gadelle and J. Defaye, *Angewandte Chemie International Edition in English*, 1991, **30**, 78-80.
111. M. T. Rojas, R. Koeniger, J. F. Stoddart and A. E. Kaifer, *Journal of the American Chemical Society*, 1995, **117**, 336-343.
112. Y. Xia and G. M. Whitesides, *Angewandte Chemie International Edition*, 1998, **37**, 550-575.
113. Z. Nie and E. Kumacheva, *Nature materials*, 2008, **7**, 277-290.
114. G. Csucs, R. Michel, J. W. Lussi, M. Textor and G. Danuser, *Biomaterials*, 2003, **24**, 1713-1720.
115. M. Wang, H. G. Braun, T. Kratzmüller and E. Meyer, *Advanced materials*, 2001, **13**, 1312-1317.
116. J. N. Lee, C. Park and G. M. Whitesides, *Analytical Chemistry*, 2013, 6544-6554.
117. M. Minguet, D. B. Amabilino, J. Vidal-Gancedo, K. Wurst and J. Veciana, *Journal of Materials Chemistry*, 2002, **12**, 570-578.
118. A. D. Adler, F. R. Longo and W. Shergalis, *Journal of the American Chemical Society*, 1964, **86**, 3145-3149.
119. P. Rothemund, *Journal of the American Chemical Society*, 1936, **58**, 625-627.

CHAPTER 7

Techniques and Description

7.1.   INTRODUCTION

This chapter gathers a brief description of the techniques and details of the equipment used. The aim of the chapter is to provide a background and settle the fundamentals of the characterization techniques used in this study.

7.2.   GEL PERMEATION CHROMATOGRAPHY (GPC)[1]

Chromatography is a separation methodology which is simply based on the affinity of the molecules to be separated for the solvent. The general and common layout consists of a stationary phase which not moves during the analysis whereas a mobile phase moves through the container. The separation occurs when the molecules that have major affinity to the stationary phase remain longer into the container. Gases, liquids or solids in simple mixture or complex blends of widely differing chemicals can be separated. To cover all these types of analysis, there are several analytical techniques as gas chromatography (GC) and liquid chromatography (LC). GPC is included in the LC type and it is also indistinctly named as size-exclusion chromatography (SEC).

GPC involves a stationary solid phase and a liquid as a mobile phase; however the separation mechanism relies on the size of the polymer molecules in solution in the mobile phase (Fig. 7.1). The stationary phase is based on beads with a certain size pore packed into a column in where the polymer solubilized in a solvent is forced to flow through. The molecules with higher sizes will not enter into the bead pores and will leave firstly the column, followed by the mid-size molecules and ending by the smaller size molecules. Elution times and molecular

sizes and be correlated so that molecular size distribution, polydispersity and even separation of oligomers and undesired discrete fractions from the main polymer can be obtained.

polymer   🖋 = larger molecules   ⅃ = mid-size molecules

⅃ = smaller molecules

Elution time (min)
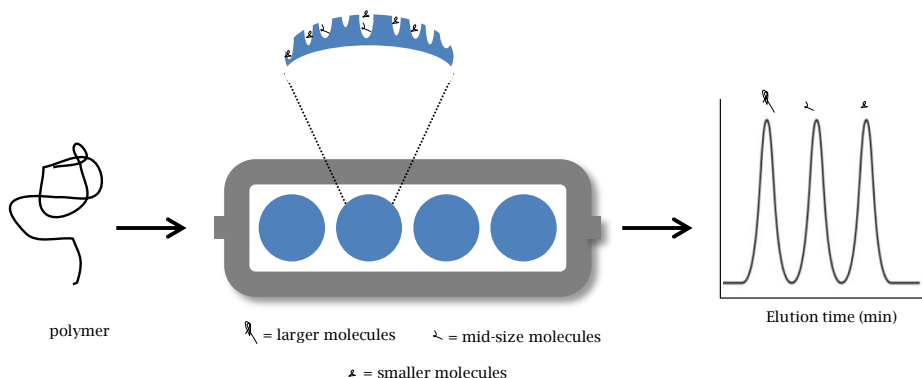
Fig. 7.1 *Scheme of the size separation mechanism of GPC. A polymer solubilized in an eluent (mobile phase) and is injected into a bead-filled column (stationary phase). Reprinted from Agilent Technologies (http://www.agilent.com/home).*[1]

Equipment: analysis were performed in a high performance liquid chromatograph from Hewlett Packard, model HP 1100 series equipped with a QuatPump pump, ultraviolet detector with a deuterium arc lamp and an injection pre-chamber. THF was the solvent used as eluent. Poly(styrene) standardized buffers were supplied by Supelco Inc. (PS standard kit).

7.3. NUCLEAR MAGNETIC RESONANCE (NMR)

Nuclear magnetic resonance spectroscopy (NMR) is a non-destructive and popular technique used in the study of the structure of molecules, the interactions between them, the kinetics and/or dynamics of molecules and the composition of mixtures of biological or synthetic solutions or composites.[2]

NMR is based on the physical phenomenon occurred when the nuclei of certain atoms absorb and re-emit an electromagnetic radiation after being exposed to a magnetic field. The emitted energy is associated to a specific resonance frequency and is depending on both, the strength of the magnetic field applied and on the properties of the isotope of the atoms. The isotopes have an intrinsic magnetic moment and angular momentum (non-zero spins) so, after the alignment of the spins induced by a magnetic field, the radiation emitted after the relaxation of them is which the equipment measures. NMR exploits this to characterize different molecules present in samples and the most commonly studied nuclei are ^1H, ^{13}C, ^{15}N, ^{31}P and ^{19}F.[3]

Equipment: a spectrometer Bruker Avance II 300 equipped with two probes, a QNP-z ($^1H/^{13}C/^{19}F/^{31}P$) for routine experiments, and for inverse detection ($^1H/^{31}P/^{109}Ag$) with an accessory for low temperature was used.

7.3.1.   Diffusion-Ordered NMR (DOSY)

Diffusion-ordered NMR spectroscopy (DOSY) introduces a second frequency dimension through the use of pulse sequences having two independent precession periods. This allows the introduction of additional NMR dimensions not included in spin Hamiltonians which are depending on molecular properties such as size, shape, mass and charge. In some particulars cases, longitudinal and/or transverse relaxations can differ for same nuclei in different surroundings due to diverse molecular local motions, providing valuable information about, for instance, size dependent molecular reorientation. DOSY-NMR implements transport properties of molecules and ions taking in account the translational motion, correlating in two-dimensional (2D) NMR spectra with diffusion values of the different substances present in the sample.[4] The measuring signal of DOSY experiments decays exponentially due to the self-diffusion behavior of individual molecules, thus allowing the correlation between the diffusion coefficient of single-compound and multi-compound systems.[5] As diffusion values are characteristic of individual compounds,

DOSY has been a quick, clean and non-destructive methodology to discern the effectiveness of coordination, complexation or covalent-bonding reactions in the block copolymers field.

Equipment: the spectrometer used in DOSY experiments was a Bruker 500 MHz equipped with a cryoprobe CryoFIT TCI of 5 mm.

7.3.2. Electron Paramagnetic Resonance (EPR)

Electron Paramagnetic Resonance (EPR) or Electron Spin Resonance (ESR) is a non-destructive technique applied in the characterization samples with unpaired electrons. The basis of EPR relies in the spin of an unpaired electron and its associated magnetic moment. When a magnetic field is applied to an electron, this electron has two possible spin states with different energies (Zeeman effect). The higher energy state takes place when the magnetic moment of the electron is aligned with the magnetic field (-1/2) and the lower energy states occurs when the magnetic moment is aligned against the magnetic field (+1/2) (Fig. 7.2).[6]
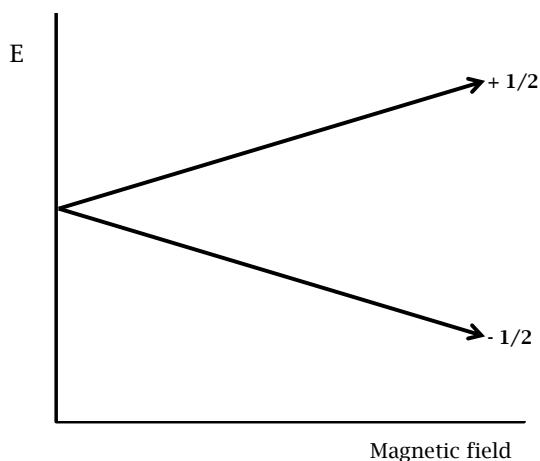

Fig. 7.2 *Scheme of the projection of the energies of electron spin states under a magnetic field in EPR spectroscopy.*

EPR spectrum is obtained by holding the frequency of radiation constant and varying the magnetic field until the difference of energy

between spins is equal to the radiation and so then, is when the radiation is absorbed by the sample.[6]

EPR allows the characterization of oxidation and reduction processes, bi-radicals and triplet state molecules, reaction kinetics as well as numerous additional applications in biology, medicine and physics.

Equipment: a Bruker ELEXYS E500 X band EPR spectrometer equipped with a variable temperature unit, a field frequency (F/F) lock accessory, and built in NMR Gaussmeter was used to measure EPR spectra.

7.4.   SPECTROSCOPIC TECHNIQUES

This section gathers a brief description and some details of the spectroscopic techniques used in the study.

7.4.1.   Ultraviolet-visible Spectroscopy (UV-Vis)

Ultraviolet-visible Spectroscopy (UV-Vis) is a spectroscopic technique based on the absorption or reflectance of liquid or solid samples in the ultraviolet-visible spectral region. The technique relies on the Beer-Lambert[*] law which relates the attenuation of light passing through a sample to the optical properties of the material due to molecules containing π-electrons or n-electrons can absorb energy to

---

[*] Beer-Lamber law claims that the absorbance of a solution is directly proportional to the concentration of the absorbing species in the solution and the path length. The equation defining the law is: $A = \varepsilon \cdot c \cdot L$, where A is the measured absorbance, ε is the molar absorptivity constant or extinction coefficient, c is the concentration of the absorbing species and, L is the path length through the sample. At high concentration solutions, the Beer-Lamber law cannot be applied due to the saturation of the sample that causes important deviations of the absorbance signal.

excite these electrons to higher molecular orbitals. The wavelengths of absorption peaks can be correlated with the types of bonds in a given molecule and are valuable in determining the functional groups within a molecule. UV-Vis technique can comprise low-energy wavelengths from the near-infrared (NIR) to high-energy levels ultraviolet (UV) (from 2,000 to 200 nm respectively) depending on the light source used to irradiate the sample.

Equipment: for NIR-range experiments a Varian Cary 5000 spectrophotometer with operational range of 190-3300 nm was used, while some of the UV-Vis-range experiments were measured in a Varian Cary 5 spectrophotometer. For liquid samples cuvettes of 1 mm path length quartz cuvettes were used while in solid samples (films) 1 mm path length quartz slides were used.

7.4.2. Fourier Transform Infrared Spectroscopy (FTIR)

Fourier Transform Infrared Spectroscopy (FTIR) is a characterization technique that measures the energy absorbed or transmitted in a sample at a range of infrared wavelengths (usually between 500 and 4,000 cm^{-1}). The light beam reaches the sample (solid, liquid or gas), and the detector records the data and processes them to obtain an infrared spectrum for that sample. Infrared spectrum is the result from transitions between quantized vibrational energy states. Molecular vibrations can range from simple coupled motion of the two atoms of diatomic molecule to the much more complex motion of each atom in a large polyfunctional molecule. Every molecule has slightly different vibrational modes from all other molecules (excepting enantiomers). Thus, the infrared spectrum of a given molecule is unique and can be used to identify that molecule and it gives also detailed information of the presence or absence of certain functional groups.[7]

The importance of the technique relies mostly in the sample preparation procedure. There are several standardized ways to prepare

samples depending whether are liquid or solid. For liquid samples, the use of potassium bromide (KBr, transparent to infrared wavelengths) plates is the widest known methodology. In the case of solid samples can be used either KBr plates by placing the solid sample with a drop of Nujol (a mineral oil) between them or, perform a KBr pellet containing the solid sample dispersed into it.

Attenuated Total Reflection (ATR) is a variation of FTIR whereby the sample is placed in contact with a sensing element and a spectrum is recorded as a result of that contact. Unlike FTIR which the radiation is transmitted though the sample, in ATR is based in the refractive/reflective indices of compounds. One of the reasons because ATR is more straightforward than FTIR is because there is practically no need of sample preparation, but a good contact sample-sensing element is mandatory.[7]

Equipment: spectra were recorded in a Spectrometer Perkin-Elmer Spectrum One with an energy range of 450-4000 cm^{-1}. Samples were measured in KBr pellets and using a Universal Attenuated Total Reflectance accessory (U-ATR) for powder samples, films, polymers, etc.

7.4.3. Circular Dichroism spectroscopy (CD)

Circular Dichroism Spectroscopy (CD) is based in differences in the absorption of left-handed circularly polarized light (L-CPL) and right-handed circularly polarized light (R-CPL) in a molecule containing one or more chiral chromophores (light-absorbing groups) (Fig. 7.3). Chiral molecules exist as pairs of mirror-image isomers. These mirror image isomers are not super-imposable and are known as enantiomers. The physical and chemical properties of a pair of enantiomers are identical with two exceptions: the way they interact with polarized light and the way they interact with others chiral molecules.[8]

CD can be defined as: $\Delta A(\lambda) = \Delta A(\lambda)_{L-CPL} - \Delta A(\lambda)_{R-CPL}$, where λ is the wavelength and, the phenomena only occurs at wavelengths of light that can be absorbed by the chiral molecule. A primary use of CD is in

analyzing the secondary structure or conformation of macromolecules, which in the particularly case of proteins one can observe differences in dissimilar environments or conditions. So, structural, kinetic and thermodynamic information about macromolecules can be derived from CD spectroscopy.[8]
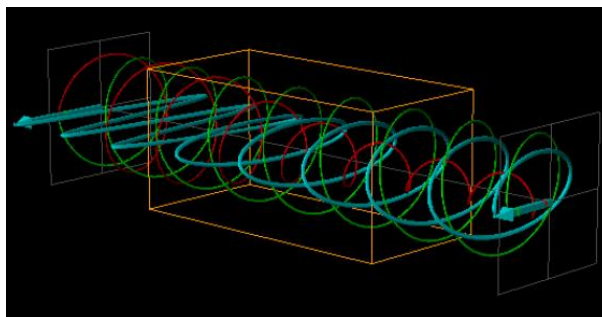

Fig. 7.3 Circular dichroism- The orange cuboid represents the sample. *Reprinted from Department of Chemistry from University of California, Irvine.* [8]

Equipment: a dichroic circular polarizer J-715 from JASCO that can work in a range of 165-900 nm. The polarized was equipped with a Peltier thermo-controlled module that permitted perform analysis at different temperatures.

7.5. MICROSCOPIC TECHNIQUES

7.5.1. Optical Microscopy (OM)

Optical microscopy (OM) employs optical microscopes (or also named light microspores) equipped with a visible light source with the aim detect small objects through a system of lenses to magnify them. Currently, the majority of devices are coupled with charge-coupled device (CCD) cameras that allow the capture of digital images of the sample. There are several optical configurations commercially available.

Equipment: the microscope used was an Olympus IX71 equipped with a polarizer U-POT and an halogen lamp supply TH4-200.

7.5.2. Scanning Electron Microscopy (SEM) / Energy-Dispersive X-ray Spectroscopy (EDX)

Scanning electron microscopy (SEM) is a microscope technique based on the imaging of objects at the micro- and nanoscale by an electron source that focuses the beam on the surface of the object. The use of an electron beam source allows the visualization of objects that would not be possible to see through an optical microscopy because the limitation of the wavelength of the visible light and even the lenses. The electrons of the beam hit the sample and later, the detection of the signal of that electrons can be translated in information related for instance with the topography and composition. One limitation of SEM is that the analyzed specimens must be electrically conductive (at least the surface) and to prevent accumulation of electrostatic charge, they should be grounded. There are several methodologies of sample preparation to overcome this, for example solid samples are usually stuck on a sticky carbon tape, or samples are commonly processes by sputter coating with the aim to cover the specimen with a conductive metal thin layer of gold, gold/palladium alloy, platinum, graphite, etc.

Energy-Dispersive X-ray spectroscopy (EDX) is usually a complementary and useful analytical technique coupled to SEM microscopes that allows chemical characterization by an elemental analysis of the sample. Through the interaction of X-ray source exciting the electrons with the sample, permits collect information of the composition of the measured specimen.

Equipment: a SEM QUANTA FEI 200 FEG-ESEM microscope equipped with a field emission gun (FEG) for optimal spatial resolution was used. The instrument can be used in high vacuum mode (HV), low-vacuum mode (LV) (water vapour injection), and environmental SEM mode

(ESEM), depending on the stability of samples. This makes it possible to study samples in pressures up to 5 Torr. The microscope is equipped with an Energy Dispersive X-ray (EDX) system for chemical analysis. In the case of non-conductive or low-contrasted samples, these were coated with gold using a K550 sputter coater, resulting in 5-20 nm thickness gold layers.

7.5.3. Transmission Electron Microscopy (TEM)

Transmission Electron Microscopy (TEM) is a microscope technique based on the same basic principles as SEM, i.e. using an electron source instead of light. In TEM, unlike SEM, the electrons pass through the sample, so the image is formed from the interaction of the electrons transmitted through the specimen. Samples are held on standard-sized copper or gold (among other metals) grids.

Equipment: A 120 KV JEOL 1210 TEM microscope with a high angular range (Tilt X= ± 60o, Tilt Y= ± 30o) for exploring large volumes of the reciprocal lattice by electron diffraction with a resolution below 3.2 Å was used in TEM images.

7.6. CONTACT ANGLE

Contact angle is a non-destructive technique used to determine the interaction of a liquid to a solid surface. The technique measures wettability of that liquid by measuring the angle created by a drop of liquid in the liquid/vapor/solid interface, permitting its quantification (Fig. 7.4). Every system has a unique equilibrium contact angle and the obtained values allow a simple way to characterize a surface and/or liquid. In practical terms, it is common to calculate the contact angle

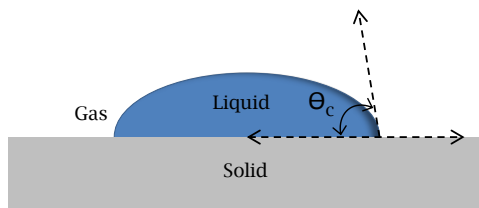hysteresis, which is the difference between the advancing (maximal) and the receding (minimal) contact angle.[9]

Fig. 7.4 *Scheme of contact angle sessile drop measurement.*

There exist different methodologies to measure the contact angle, such as, the static sessile drop, the pendant drop, dynamic sessile drop, and dynamic Wilhelmy method among others.[9]

Equipment: contact angle measurements were made following the static sessile drop methodology and to determine the surface tension of liquids the pendant drop method was used. For both analyses a DSA 100 system from KRÜSS was used.

7.7. ELLIPSOMETRY

Ellipsometry is an optical technique that in this study was used to characterize the thickness of thin films, although can as well be used to investigate composition, roughness, crystallinity, doping concentration and electrical conductivity among other properties. In the measurement of thickness, the change in polarization of an incident radiation which interacts with the material (reflecting, absorbing, scattering or transmitting) is measured.[10] By the difference of the reflection angle of the beam between a neat surface and the same surface containing the studied thin film, one can deduce the thickness of it.

Equipment: a GES5E Optical Platform ellipsometer from Sopra allowed various measurement modes from standard ellipsometry to

generalized ellipsometry going thru photometric measurements (in Transmission and Reflection), scatterometry, and luminescence measurements. The standard spectral range of it was 230-900 nm and the measurement angles ranged from 10º to 90º. All the measurements were made in a conditions-controlled room, a clean room 10,000 class.

7.8.   SCANNING PROBE MICROSCOPY (SPM)

7.8.1.   Atomic Force Microscopy (AFM)

Atomic Force Microscopy (AFM) is a high resolution technique with which information at the surface related with the topography and roughness, among others, is acquired. Generally, it operates by the use of a small cantilever that ends with a sharp tip which traces the surface of the sample. There are two operational modes, contact and non-contact tip-to-surface although the commonly used is the non-contact. The cantilever vibrates in resonance when the tip is approached down to the cantilever deflects and vibrates in resonance with the sample due to interaction forces. This deflection is assigned as setpoint (related with the height of the sample) and the equipment forced to maintain. When the tip scans an area of the specimen, differentiated deflection values/heights can be recorded in a photodetector and processed as image (Fig. 7.5).
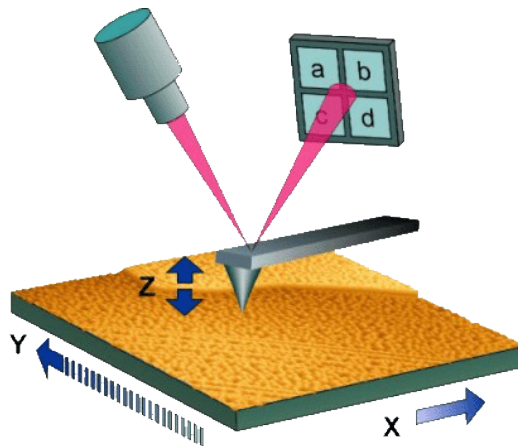
Fig. 7.5 *General scheme of how AFM operates. Extracted from* Encyclopedia of Nanotechnology, *ed. B. Bhushan, Springer Netherlands, 2012.*[11]

Equipment: 5100 SPM system from Agilent Technologies AFM measurements in tapping mode with FORT-50 SPM silicon tips from AppNano.

7.8.2. Electrostatic Force Microscopy (EFM)

Electrostatic Force Microscopy (EFM) is based on the principle of AFM but measures electrostatic inhomogeneities enclosed on a semiconductive or charge-carrier surface of the specimen (Fig. 7.6). The sample is grounded to a conductive holder and a sequentially positive and negative bias between the holder and the tip of the cantilever is created in order to record the cantilever deflection when this scans the charged surface. EFM works in two modes simultaneously, the first scans the sample and the equivalent information to AFM analysis is acquired, while in the second mode electrostatic response is processed.
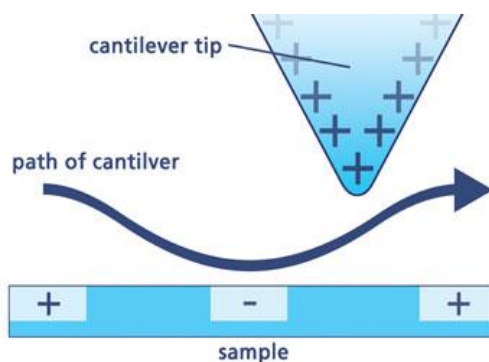
Fig. 7.6 *Principle of operation of EFM. Extracted from Nanowerk.*[12]

Equipment: A 5500LS SPM system from Agilent Technologies was used to conduct EFM measurements. All measurements were made with Nano World Pointprobe silicon SPM sensor tips, provided with a force constant of 2.8 N/m, a coating tip side of Pt/Ir, and a coating detector side of Pt/Ir.

7.9.   SMALL-ANGLE   X-RAY   SCATTERING (SAXS)

Small-Angle X-ray Scattering (SAXS) is an analytical method that uses radiation in the determination of the structure of particle systems, such as averaged particle sizes or shapes. SAXS allows the analyses of solid or liquid samples, they containing solid, liquid or gaseous domains of the same material or in combination with others. In the case of polymers, this technique is the great interest because permits the quantification of the conformation of phase-segregated systems, without the need of growing crystals. In general, the basic components of all SAXS instruments comprise a source, a collimation system, a sample holder, a beam stop and a detection system. Firstly, the source irradiates the sample and the detector measures the radiation coming from the sample in a certain range of angles. The function of the collimator is the makes

the beam narrow and to define the zero-angle position. The beam stop component prevents that the intense incident beam hit the detector.[13] When the X-rays interact with the matter, a fraction of them will pass through, another fraction will be absorbed and transformed into other forms of energy (e.g. heat, fluorescence radiation, etc.) and the rest will be scattered into other directions of propagation. From the collected data, the equipment can extract parameters related with the form, the structure, orientation and order of samples.[13] It is very valuable as complementary technique with TEM, overall in the determination of the self-assembly packing of polymers and copolymers.

Equipment: SAXS measurements were carried out using a small-angle Kratky camera (m-Braun) coupled to a Siemens K-760 generator, operating at 50 kV and 40 mA. The wavelength corresponding to the Cu $K\alpha$ line (1.542 Å) was used. The linear detector was a PSD-OED 50 M (m-Braun) and the temperature controller was a Peltier KPR AP PAAR model working at 25 ± 0.1 °C.

7.10. REFERENCES

1. A. Technologies, http://www.agilent.com/home, (accessed 07/05, 2015).
2. B. Corporation, https://www.bruker.com/, (accessed 2015/07/17).
3. J. P. Hornak, The Basics of NMR, https://www.cis.rit.edu/htbooks/nmr/, (accessed 2015/07/17).
4. C. S. Johnson Jr., *Progress in Nuclear Magnetic Resonance Spectroscopy*, 1999, 203-256.
5. Y. Bakkour, V. Darcos, S. Li and J. Coudane, *Polymer Chemistry*, 2012, **3**, 2006.
6. A. University of Texas, http://www.utexas.edu/, (accessed 2015-08-03).
7. Peter R. Griffiths and J. A. d. Haseth, *Fourier Transform Infrared Spectrometry*, Wiley-Interscience, John Wiley & Sons, Inc., Publication, New Jersey, 2nd edition edn., 2007.
8. U. o. C. Department of Chemistry, Irvine, http://www.chem.uci.edu/, (accessed 2015-08-02).
9. J. N. Israelachvili, *Intermolecular and Surface Forces*, Elsevier Inc., Oxford, 2011.
10. J. A. W. Co., http://www.jawoollam.com/, (accessed 2015-08-14).

11. H. Hölscher, in *Encyclopedia of Nanotechnology*, ed. B. Bhushan, Springer Netherlands, 2012, DOI: 10.1007/978-90-481-9751-4_33, ch. 33, pp. 99-99.
12. Nanowerk, http://www.nanowerk.com/, (accessed 2015/09/27).
13. H. Schnablegger and Y. Singh, *Journal*, 2011.

CHAPTER 8

Summary

This thesis has been focused on the study of the control of the self-assembly of organic-based materials and their final microstructure. First, supramolecular functionalization of homo- (P4VP) and block copolymer (PS-*b*-P4VP) by different supramolecular strategies such as, functionalization with electron-donor molecules (TTFCOOH) and the effect of doping processes in polymeric hybrid thin films have been presented. Then, using the effect of the hydrodynamic flow focusing of microfluidics platforms in the self-assembly and organization of macromolecules and hydrogels have been studied. Finally, the effect in the arrangement of block copolymers meditated by the coordination with chiral and achiral metallocompounds have also been explored. The conclusions extracted from each one of the conducted studies are summarized below.

Functional Supramolecular Tetrathiafulvalene-Based Films with Mixed Valence States: The supramolecular functionalization of the homopolymer P4VP with TTFCOOH through hydrogen bonding (P4VP-TTFCOOH) has been demonstrated as viable strategy for the preparation of stable thin films, which incorporate redox active components. Polymeric hybrid thin films of P4VP-TTFCOOH with mixed valence states of TTFCOOH^0-TTFCOOH$^+$ and TTFCOOH$^-$-TTFCOOH^{2+} have been obtained. Moreover, their electrostatic response due to the charge transportation as a result of the assembly and doping processes of the TTFCOOH units have been observed using EFM. Finally, the controlled growing of TTF-based crystals from a P4VP polymer matrix has corroborated that P4VP can be used as support or template for crystallisable-organic conductive materials.

Electrostatic Response Dependence on Tetrathiafulvalene-Based Block Copolymer Thin Films: It has been demonstrated that the self-packing configuration of PS-*b*-P4VP amphiphilic block copolymer is dependent on the molar fraction of the blocks of both polymers and can be influenced by the introduction of TTFCOOH units. Pure PS-*b*-P4VP block copolymers at different molar fractions of PS and P4VP provide disordered domains while after the introduction of TTFCOOH units, the resulting PS-*b*-P4VP-TTFCOOH films presented an ordering in the self-arrangements at the interfaces. The electrostatic response and

consequently, semiconductivity of the PS-*b*-P4VP-TTFCOOH hybrid films has been demonstrated to be dependent on the phase segregation conformations and on the molar fraction of PS and P4VP block content.

Electrostatic Responsiveness of a Hierarchically Self-Assembled C_3-Symmetric Tetrathiafulvalene: The obtaining of redox-responsive coiled C_3-symmetric tris(TTF) self-assembled microstructures has been obtained depending on the solvent used. The mixed valence state TTF^0-$TTF^{+\cdot}$ of the structures has been achieved using a solution of $Fe(ClO_4)_3$. The reversibility of the oxidizing process was studied using a solution of trimethylamine (TEA). The use of 1,4-dioxane has allowed obtaining fibers, whereas using acetonitrile a different self-assembled flake-like aggregates with some fibrillate regions was spotted. To control the microstructure, the hydrodynamic flow focusing parameter of microfluidics, has been demonstrated a powerful technique in the self-assembly of the C_3-TTF depending on the flow rate used, being more controllable than the bulk and resulting in fibrillary aggregates with acetonitrile using a total flow rate of 400 µl/min. Finally, an easy one-step method has been proposed to characterize electrostatically active organic compounds, reducing the cross-talking levels below respect to the regular EFM and bimodal-AFM analyses.

Microfluidics as a Platform to Design Tetrathiafulvalene-Based Ionically-Driven Coacervated Hydrogels and to Enhance their Microstructure: The gelation and microstructure of an ABA triblock copolymer PEG-based hydrogel obtained by ionic coacervation has been achieved by using microfluidics. The effect of the hydrodynamic flow focusing provided on the one hand, a better contact of the reactants and, on the other, its effect on the microstructure resulting in an aligned hydrogel has been demonstrated using lower concentrations respect to the same hydrogel under bulk conditions. Microfluidics has offered hydrogels with a more aligned and fibrous microstructure when higher flow rates were applied, indicating a major effect of the confinement and shear forces inside the channel. Furthermore, the ABA triblock hydrogel has been functionalized with TTFCOOH (hydrogel-TTFCOOH) and the control of its microstructure has been achieved using a total flow rate of

400 µl/min. Moreover, the hydrogel has been achieved to be immobilized on functionalized glass surfaces using the soft lithography technique of micro-contact printing, demonstrating in this way the possibility of organizing macromolecules on different substrates.

Supramolecular Porphyrin-Block Copolymer Systems: The supramolecular coordination between an achiral zinc (II) porphyrin derivative, Zn-2, and its chiral homologue, Zn(*R,R,R,R*)-1, and the amphiphilic block copolymer PS-*b*-P4VP has been achieved through the coordination of the zinc (II) of the porphyrins with the pyridyl groups of the P4VP block. Well-differentiated segregated phase segregation of PS-*b*-P4VP-Zn-2 and PS-*b*-P4VP-Zn(*R,R,R,R*)-1 could be observed, elucidating the effect of the chirality in the self-arrangement of the polymer. Moreover, the role of the solvent interplayed in the packing of the complexed system has been presented, demonstrating the possibility of obtaining complex micelles, opening a broad range of possibilities of PS-*b*-P4VP-Zn-2 and PS-*b*-P4VP-Zn(*R,R,R,R*)-1 configurations with an easy control of the solvent. Finally, a first approach towards supramolecular rotors based on PS-*b*-P4VP-Zn(*R,R,R,R*)-1 has been successfully conducted using micro-contact printing.